

**Discrete Element Method Modelling of Complex Granular  
Motion in Mixing Vessels: Evaluation and Validation**

By

Michele Marigo

A thesis submitted to the School of Chemical Engineering of the University  
of Birmingham for the degree of  
DOCTORATE IN ENGINEERING EngD

School of Chemical Engineering

Faculty of Engineering

The University of Birmingham

B12 2TT, UK

UNIVERSITY OF  
BIRMINGHAM

**University of Birmingham Research Archive**

**e-theses repository**

This unpublished thesis/dissertation is copyright of the author and/or third parties. The intellectual property rights of the author or third parties in respect of this work are as defined by The Copyright Designs and Patents Act 1988 or as modified by any successor legislation.

Any use made of information contained in this thesis/dissertation must be in accordance with that legislation and must be properly acknowledged. Further distribution or reproduction in any format is prohibited without the permission of the copyright holder.

## **Abstract**

In recent years, it has been recognised that a better understanding of processes involving particulate material is necessary to improve manufacturing capabilities and product quality. The use of Discrete Element Modeling (DEM) for more complicated particulate systems has increased concordantly with hardware and code developments, making this tool more accessible to industry.

The principal aim of this project was to study DEM capabilities and limitations with the final goal of applying the technique to relevant Johnson Matthey operations. This work challenged the DEM numerical technique by modelling a mixer with a complex motion, the Turbula mixer. The simulations revealed an unexpected trend for rate of mixing with speed, initially decreasing between 23 rpm and 46 rpm, then increasing between 46 rpm and 69 rpm. The DEM results were qualitatively validated with measurements from Positron Emission Particle Tracking (PEPT), which revealed a similar pattern regarding the mixing behaviour for a similar system. The effect of particle size and speed on segregation were also shown, confirming comparable results observed in the literature. Overall, the findings illustrated that DEM could be an effective tool for modelling and improving processes related to particulate material.

## **Table of contents**

### **Chapter 0 Business needs**

0.1 Introduction: Johnson Matthey Plc	1
0.2 Particle technology in catalysis	2
0.3 DEM as investigation tool in particle technology: rotating mixer system	6
0.4 References	8

### **Chapter 1 An introduction to solid mixing**

1.1 Introduction to particulate materials and powder mixing	10
1.2 Mixing mechanisms	11
1.3 Segregation mechanisms	12
1.4 Definitions: mixing time and mixing rate	15
1.5 Type of industrial mixers	20
1.6 Turbula laboratory mixer	20
1.7 Conclusions	22
1.8 References	23

### **Chapter 2 Theoretical background DEM (EDEM)**

2.1 Introduction: modelling granular material	29
2.2 Discrete Element Modelling (DEM)	30
2.2.1 Examples of DEM applications for particle motion	32
2.3 DEM Numerical model	34
2.4 Current limitations for DEM modelling techniques	44

2.5 Examples of current limitations	46
2.5.1 Packing of pellets: poor particle shape representation leads to incorrect packing results	47
2.5.2 Pan coater: influence of particle shape and choice of input parameters on the simulation time	49
2.5.3 Choice of correct input parameters can have a major influence on the simulations results: simulation of Flodex	52
2.6 Particle DEM input parameters and typical particle characterisation techniques	56
2.6.1 Examples for the determination of the coefficient of restitution	59
2.6.2 Examples for the determination of particle mechanical properties: elastic modulus, plastic yield, particles strength and hardness	62
2.6.3 Examples for the determination of particle friction properties	63
2.6.4 Comparison of the magnitude of interparticle forces for small particles	66
2.7 Conclusions	68
2.8 References	71

### **Chapter 3 Mechanical properties of ZSM5 zeolite particles**

3.1 Introduction: ZSM5 zeolite particles	84
3.2 Particle size and shape	84
3.2.1 Scanning Electric Microscopy (SEM)	85
3.2.2 Laser light diffraction	89
3.3 Particle flowability (Hausner ratio, Carr index and flow function)	91
3.3.1 Definition of Hausner ratio (HR) and Carr's Index (CI)	92
3.3.2 Hausner ratio and Carr's index: ZSM5 zeolite sample	95
3.3.3 Definition of flow function ( <i>ffc</i> ): Schulze ring tester	96
3.3.3.1 Flow function ( <i>ffc</i> ): ZSM5 zeolite sample	99
3.4 Single particle compression: reduced Young's modulus and strength of single particle	104
3.4.1 Diametrical compression of single zeolite particles	105
3.5 Nanoindentation: hardness and reduced Young's modulus	114
3.5.1 Nanoindentation of zeolite particles	116
3.6 Powder bulk compression	119

3.6.1 Bulk powder compaction: tests results for zeolite ZSM5	121
3.6.2 The Heckel model	126
3.6.3 The Kawakita model	128
3.6.4 The Adams model	129
3.6.5 Heckel, Kawakita and Adams plots for zeolite ZSM5	131
3.7 Conclusions	137
3.8 References	139

## **Chapter 4 Turbula mixer motion measurement and reconstruction using Positron Emission Particle Tracking (PEPT)**

4.1 Introduction: Positron Emission Particle Tracking technique (PEPT)	150
4.1.1 Positron Emission Particle Tracking	150
4.1.2 Improvements: Multiple Positron Emission Particle Tracking	154
4.2 Experimental set-up: Turbula mixer motion measurement	155
4.2.1 Experimental set-up for the motion measurement	155
4.3 Data processing: solid body translational and rotational motion reconstruction	157
4.4 Results and discussion	162
4.5 Conclusions	165
4.6 References	166

## **Chapter 5 DEM modelling of particle motion in a Turbula mixer**

5.1 Introduction: uni-axis and multiple-axes blender motion	172
5.2 Simulation conditions and DEM input parameters	173
5.2.1 Definition of vessel motion in EDEM package	177
5.2.2 Data processing	183
5.2.3 Definition of the segregation (mixing) index	185
5.2.4 Definition of coefficients of dispersion: particle dynamic analysis	187
5.3 Results: DEM mixing studies bed size ratio $R=1$	188
5.3.1 Axial loading patterns: influence of rotational speed on the mixing rate	189
5.3.2 Transverse loading patterns: influence of rotational speed on the mixing rate	200
5.3.3 Particle movement in axial direction	201

5.3.4 Particle speed analysis	209
5.4 Results: DEM mixing studies influence of rotational speed for a particle bed size ratio R=1.4 (bimodal particles)	212
5.4.1 Effect of baffle design: mixing improvement in case of bidisperse particle (R=1.4)	219
5.5 Conclusions	221
5.6 References	224

**Chapter 6 A DEM numerical comparison of mixing efficiencies of solids in a cylindrical vessel subject to a range of motions: rotating drum, hoop mixer and Turbula mixer**

6.1 Introduction: cylindrical vessels moving with different motion types	228
6.2 Geometry and simulations conditions	229
6.3 Results and discussion	231
6.3.1 Rotating drum	231
6.3.2 Hoop mixer	236
6.3.3 Turbula mixer	238
6.3.4 Comparison of characteristic number of rotations for a rotating drum, hoop mixer and Turbula mixer	239
6.5 Conclusions	242
6.6 References	244

**Chapter 7 Particle motion inside the Turbula mixer: PEPT mixing experiments for a system with irregular moving boundaries**

7.1 Introduction: mixing studies and experimental techniques for powder mixing	248
7.2 Materials	249
7.3 Experimental set-up: relating particle position with vessel moving boundaries	250
7.3.1 Step A: tracking irregular moving boundaries	254
7.3.2 Step B: reconstruction of the tracer position relative to the coordinate system fixed to the vessel	258

7.4 Results and discussion	263
7.4.1 Axial displacement analysis for glass bead tracer particle	263
7.4.2 Occupancy plots for glass beads	268
7.4.3 Dispersion coefficients for glass bead tracer	273
7.4.4 Occupancy plots for zeolite	275
7.4.5 Dispersion coefficient for zeolite bead tracer	280
7.5 Conclusions	281
7.6 References	284

## **Chapter 8    Input parameters sensitivity analysis for the comparison of Turbula mixer                   DEM simulations and PEPT mixing experiments**

8.1 Introduction: comparison between DEM simulation and PEPT experimental results for the Turbula mixer	286
8.1.1 Comparison of DEM and PEPT axial and radial dispersion coefficients, $D_x$ and $D_r$	287
8.1.2 Comparison of particle movement in axial direction: peak frequency distribution and average plateau periods length	289
8.2 DEM input parameters sensitivity analysis for operating 3 speeds: 23, 46 and 69 rpm	292
8.2.1 Effect of input parameters on distribution of $x'-x$ and $r'-r$	293
8.2.2 Effect of input parameters on the segregation index $S$	300
8.3 Conclusions	305

## **Chapter 9    Conclusion and future work**

9.1 Results.....	307
9.2 Summary.....	311

## **Appendix    List of publications**

## **Overview of the thesis**

**DVD** contains the videos from the simulation of the Turbula mixer. The reader is invited to watch these videos when reading Chapter 4 and Chapter 5.

**Chapter 0** contains a brief overview on particle technology in Johnson Matthey and the main business reasons for this work. The flow of particles is fundamental in many Johnson Matthey processes and there is a need to improve the fundamental understanding regarding particle technology. The main goal for this work is to understand if and how particle flow modelling Discrete Element Method (DEM) could be applied as a possible tool.

**Chapter 1** is an introduction of some of the basic concepts about powder mixing and different type of mixers. A broad literature review is given especially in terms of rotating drums in order to show the typical problems.

**Chapter 2** is a presentation of DEM numerical modelling and a description of the commercial package used in this work. The Hertz Mindlin contact model implemented into the software has been described. Typical current limitations have been addressed especially in terms of measurement or collection of the material properties in order to setup a DEM numerical model.

**Chapter 3** reports a list of typical powder characterization techniques used in order to characterise Zeolite catalyst support material.

**Chapter 4** reports the description of the Positron Emission Particle Tracking technique (PEPT) and the Multiple Emission Particle Tracking (Multiple-PEPT). This chapter also describe Turbula mixer motion and reconstruction.

**Chapter 5** contains the results of DEM simulation of the Turbula mixer. In particular regarding different operational speeds and different loading patterns. The effect of operational speed on segregation for a particles size ratio has also been studied. The effect of adding a baffle to avoid segregation has been investigated.

**Chapter 6** reports a numerical comparison on mixing between the Turbula mixer and other mixers with a simpler motion such as rotating drum and hoop mixer.

**Chapter 7** contains mixing studies on the Turbula using the PEPT technique. One single particle located inside the moving vessel has been tracked. The motion reconstruction of the single particle with respect of the moving boundaries of the mixer has been reported. Results have been compared with the ones form the DEM numerical simulations from Chapter 5.

**Chapter 8** reports the comparison between the DEM numerical results and the PEPT experimental results for the Turbula mixer. Qualitatively agreements are shown between the simulations and the experiments. Quantitative values differences are investigated by sensitivity parametric study of the DEM input parameters.

**Chapter 9** includes the conclusion regarding this work and future work that will be carried out in particular regarding the determination of input parameters for DEM numerical simulation for mixing and coating of cylindrical pellets.

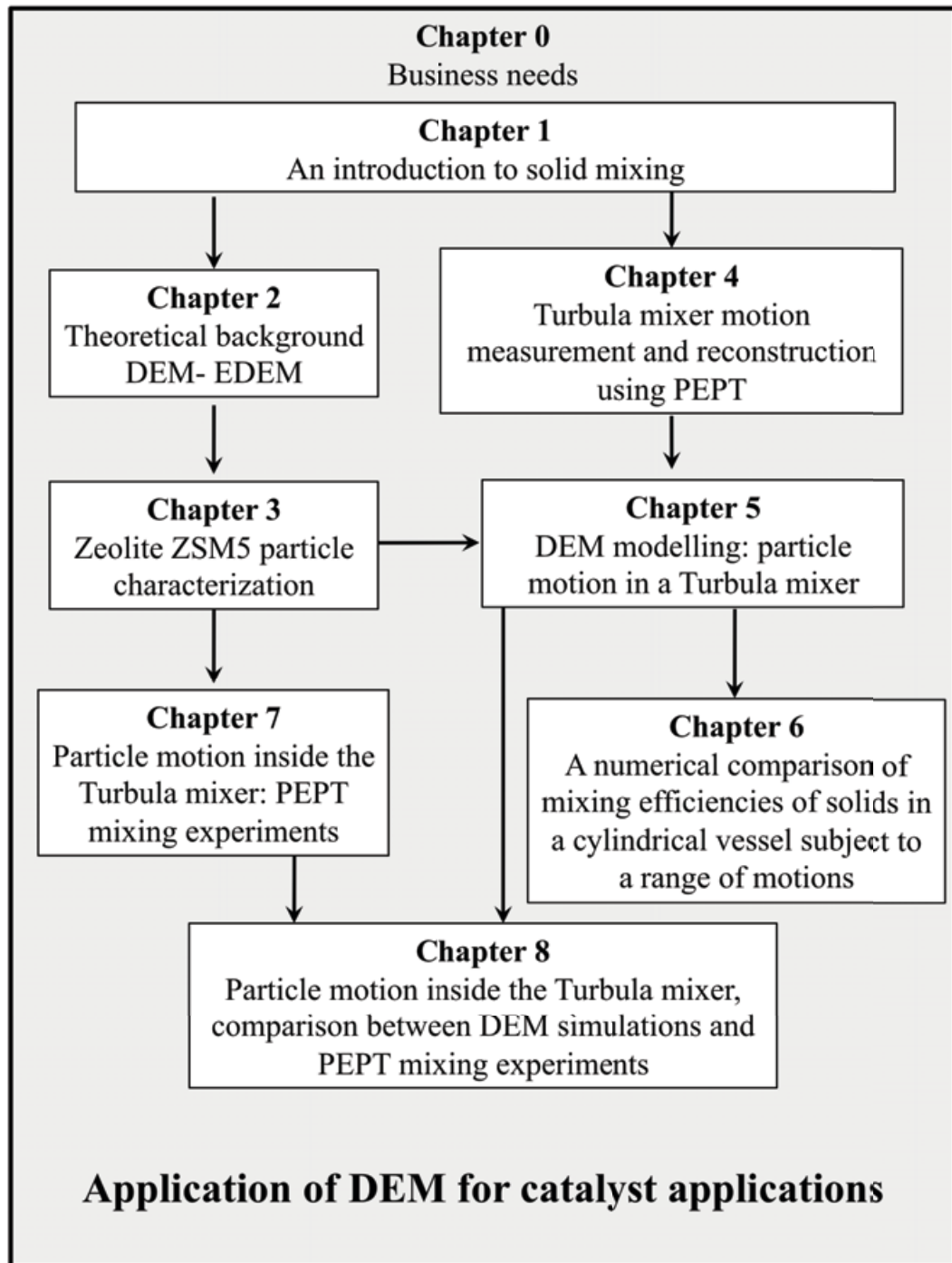


Figure I: Thesis structure.

## List of Figures

### Chapter 0

Figure 0.1: Figure 0.1: Typical catalyst shape and size: typically made by, granulation, pelleting and extrusion.

Figure 0.2: Typical heterogeneous catalyst production route.

### Chapter 1

Figure 1.1: Mixing mechanisms: convection and dispersion.

Figure 1.2: Representation of mixedness equal proportions of black and white particles.

Figure 1.3: Segregation mechanisms.

Figure 1.4: A typical mixing plot, with relative standard deviation (RSD) of the samples concentration plotted against number of revolutions.

Figure 1.5: Turbula T2F shaker-mixer.

### Chapter 2

Figure 2.1: (a) Photo-elasticity picture of the granular assembly of discs: force transmission pattern. (b) Force transmission pattern numerically simulated by DEM.

Figure 2.2: Number of publications related to discrete particle simulation between 1993-2011 from Science Direct website.

Figure 2.3: DEM numerical algorithm.

Figure 2.4: Contacts between particle  $i$  with particle  $j$ .

Figure 2.5: Kelvin-Voigt contact model: spring  $k$ , damper  $\eta$  and slider  $\mu$ .

Figure 2.6: Modified Hertz Mindlin contact model .

Figure 2.7: Clusters of interpenetrating spheres.

Figure 2.8: (a) typical real particle shape. (b) first approximation with one sphere. (c) multiple-sphere representation.

Figure 2.9: Cylindrical pellet packing: a) Poor pellets representation formed (10: 2.7 mm diameter particles). b) Improved pellets representation (10: 2.7 mm diameter particles plus 76: 0.35 mm diameter particles).

Figure 2.10: Mixing of particle in a pan coater, spherical particles and Raschig rings.

Figure 2.11: DEM simulation time for a pan coater in case of spherical and Raschig ring shape particles. Raschig rings made as assembly of 540 spherical particles.

Figure 2.12: Discharge of spherical particles from a 3D cylindrical container.

Figure 2.13: Effect of shear modulus on discharge rate.

Figure 2.14: Effect of shear modulus  $G$  on computational time to model container discharge.

Figure 2.15: Effect of particle-particle coefficient of friction  $\mu_{s-pp}$  on the discharge rate.

Figure 2.16: Effect of rolling particle-particle coefficient friction  $\mu_{r-pp}$  on the discharge rate

Figure 2.17: Typical experimental particle dropping setup for impact tests.

Figure 2.18: (a) Compression single sodium benzoate granule. (b) Micromanipulation technique University of Birmingham (UK). (c) Schematic representation of nanonindentation.

Figure 2.19: Schematic Pin-on-disk tribometer.

Figure 2.20: Setup for measuring coefficient of rolling friction for pharmaceutical tablets using a slope of height  $h$  and measuring the distance  $d$  travelled on a flat plane.

Figure 2.21: Nanotribological AFM measurements for friction.

Figure 2.22: Size dependency of inter-particles interaction force such as liquid bridges, Van der Waals, Coulombic and gravity forces for two equally sized spheres (in air).

### Chapter 3

Figure 3.1: Picture of tablets formed by using zeolite material.

Figure 3.2: Schematic representation of SEM apparatus.

Figure 3.3: SEM images of spray dried ZSM5 zeolite.

Figure 3.4: Distribution of sphericity values for ZSM5 zeolite sample from SEM.

Figure 3.5: Schematic of a laser diffraction instrument.

Figure 3.6: Particle size distribution for the zeolite sample.

Figure 3.7: Yield locus and Mohr's circles.

Figure 3.8: Set-up of the Schulze shear cell, for particle internal friction and wall friction tests.

Figure 3.9: Zeolite yield locus for the normal load at pre-shear equals to 2000 (purple), 4000 (red), 6000 (black) Pa.

Figure 3.10: Zeolite unconfined yield strength  $\sigma_c$  versus consolidation stress  $\sigma_l$  and flow function  $ffc$ .

Figure 3.11: Zeolite bulk density  $\rho_b$  versus consolidation stress  $\sigma_l$ .

Figure 3.12: Zeolite wall shear stress in a wall friction test.

Figure 3.13: Characteristic plate-particle contact during single particle compression.

Figure 3.14: Stable Microsystems analyser.

Figure 3.15: Typical force displacement curve for the zeolite sample. Crushing measurement on particles by the Stable Microsystems analyser.

Figure 3.16: Data for single particle compression (a) local displacement (b) data plotted according the Hertz contact theory and linear fitting.

Figure 3.17: Reduced elastic modulus and critical force for individual zeolite particle.

Figure 3.18: Nominal rupture stress of single zeolite particle.

Figure 3.19: Cumulative distribution function for the zeolite sample, determination of the Weibull modulus  $m$  (dashed line).

Figure 3.20: Schematic of a typical load–displacement curve during indentation test.

Figure 3.21: Typical load and unload curves for a zeolite particles with different levels of indentation depth: 1, 4, 5 and 6  $\mu\text{m}$ . A loading, B hold, C unloading, D hold, E no load.

Figure 3.22: Typical load versus time for a zeolite particles with different levels of indentation depth: 4, 5 and 6  $\mu\text{m}$ . A loading, B hold, C unloading, D hold, E no load.

Figure 3.23: (a) Reduced Young's modulus and (b) hardness during indentation of ZSM5 particles.

Figure 3.24: Typical sequences of mechanisms during powder compression.

Figure 3.25: Schematic representation set-up of the bulk compression machine Instron 5500.

Figure 3.26: Nominal pressure  $P$  against punch displacement curves for the bulk compression for different punch speed.

Figure 3.27: Bulk compression for zeolite particles for different punch speed.

Figure 3.28: Single tablet multiple compression loading and unloading cycles. Powder bed is subsequently loaded and unloaded for different cycles. (a) only the loading curves are shown for clarity. (b) the change in bulk density is shown.

Figure 3.29: Typical Heckel plot for Eudragit® polymer particles.

Figure 3.30: Typical Kawakita plot for Eudragit® polymer particles.

Figure 3.31: Typical Adams plot for Eudragit® polymer particles.

Figure 3.32: Heckel compression curve for tablet T1.

Figure 3.33: (a) Kawakita compression curve for tablet T1 (b) degree of compression as function of the applied pressure.

Figure 3.34: Adams compression curve for tablet T1.

Figure 3.35: Linear fitting compression curves for table T1 up to 2000 N normal load. (a) Heckel relationship. (b) Kawakita relationship.

Figure 3.36: Linear fitting compression curves for table T1 up to 12000 N normal load, Adams relationship.

Figure 3.37: Effect of aspect ratio A.R. on  $\tau'_o$  and  $\alpha'$  parameters from the Adams model.

## Chapter 4

Figure 4.1: Positron ADAC Forte camera.

Figure 4.2: Schematic representation of PEPT (Positron Emission Particle Tracking) camera.

Figure 4.3: Categories of valid and invalid gamma pairs.

Figure 4.4: Schematic representation of the experimental measurement of the Turbula motion by PEPT.

Figure 4.5: Measured position  $x,y,z$  for the tracers fixed at position  $\mathbf{P}_A$ ,  $\mathbf{P}_C$  and  $\mathbf{P}_D$  by Multiple-PEPT at 23 rpm for one shaft rotation.

Figure 4.6:  $x,y,z$  positions for point  $\mathbf{P}_A$ ,  $\mathbf{P}'_C$  and  $\mathbf{P}'_D$  from Multiple-PEPT at 23 rpm for one shaft rotation.

Figure 4.7: Definition of the vessel fixed unit vector coordinate system ( $\mathbf{l}, \mathbf{m}, \mathbf{n}$ ) Schematic representation of the experimental measurement of the Turbula motion by PEPT.

Figure 4.8: Components for the unit vector  $\hat{\mathbf{l}}$ .

Figure 4.9: Components for the unit vector  $\hat{\mathbf{m}}$ .

Figure 4.10: Components of the angular velocity  $\boldsymbol{\omega}$ .

Figure 4.11: Components of the linear velocity  $\mathbf{v}$ .

Figure 4.12: Coding for translations and rotations into EDEM.

## Chapter 5

Figure 5.1: The container, located in the centre of the cage in the Turbula mixer.

Figure 5.2: Initial loading patterns: (a) Axial. (b) Transverse.

Figure 5.3: Definition of list of translations and rotations into EDEM at each motion timestep.

Figure 5.4: Steps in EDEM software to define the translational and rotational movements for the cylindrical geometry.

Figure 5.5: Schematic explanation of vessel motion and idea of inversion.

Figure 5.6: Definition of the coordinate system  $x,y,z$  fixed with the vessel geometry from the  $X,Y,Z$  coordinate system from DEM.

Figure 5.7: Comparison between unit vectors  $\hat{l}, \hat{m}$  from the simulation at different rotational speeds.

Figure 5.8: Typical particle position  $(x,y,z)$  with respect to the vessel coordinate system.

Figure 5.9: Schematic representation of contacts between particles for the definition of the segregation index based on contacts between particles of different species.

Figure 5.10: Segregation index as a function of rotational speed and blender revolutions  $N_R$ . Example of fitted curve for 46 rpm.

Figure 5.11: Characteristic number of rotations and characteristic mixing times (to achieve 63.2% mixing) as function of shaft rotation speed.

Figure 5.12: Snapshots of particles within the vessel as mixing proceeded from the 2<sup>nd</sup> to the 5<sup>th</sup> shaft rotation at 23, 46 and 69 rpm.

Figure 5.13: Snapshots of vessel position during the first complete Turbula shaft rotation at 23 rpm.

Figure 5.14: Snapshots of vessel position during the first complete Turbula shaft rotation at 46 rpm.

Figure 5.15: Snapshots of vessel position during the first complete Turbula shaft rotation at 69 rpm.

Figure 5.16: Axial and radial dispersion coefficients  $D_x$  and  $D_r$  as a function of the rotational speed.

Figure 5.17: Cylindrical vessel binned in axial  $x$  direction every 10 mm and orientation of the vessel.

Figure 5.18: Average number of particles during the 15 rotations inside each bin.

Figure 5.19: Axial dispersion coefficient  $D_x$  calculated considering in which bin the particle are before each rotation.

Figure 5.20: Characteristic number of rotations for the two loading patterns as a function of rotational speed.

Figure 5.21: 10 particles selected for “bucket” analysis.

Figure 5.22: Plot of  $x$  position against number of rotation for one of the ten particles particle at 23, 46 and 69 rpm for 15 shaft rotations (left) and plot for the first 3 rotations (right), definition of peak.

Figure 5.23: Plot of  $x$  position for one of the ten particles during the motion between rotation 1 and 2 with the corresponding orientation for the vessel at the same rotation fraction.

Figure 5.24: Length of average plateau periods in axial direction for the ten particles selected as a function of speeds.

Figure 5.25: Number of peaks divided by total number of peaks during the 15 shaft rotations at different shaft rotational speeds.

Figure 5.26: Particles average speed  $v_{particle}$  increases with the increase of the operating speed.

Figure 5.27: Normalised axial average particles velocity.

Figure 5.28: Normalised transverse average particle velocity.

Figure 5.29: (a) Initial loading pattern, (b) final pattern and (c) section after 18 rotations for monodisperse and bidisperse simulations at 23 rpm and  $R=1.4$ .

Figure 5.30: 1 mm doped beads with 0.35 mm undoped beads  $R=2.8$  at 23rpm. Segregation of small particles in the centre of the bed (white area).

Figure 5.31: Trends for the segregation index for monodisperse ( $R=1$ ) and bidisperse particles ( $R=2.8$ ) at 22 rpm. Redrawn from [7].

Figure 5.32: Trends for the segregation index from DEM simulations for monodisperse ( $R=1$ ) and for bidisperse particles ( $R=1.4$ ) at 23 rpm.

Figure 5.33: Trends for the segregation index from DEM simulations for bidisperse particles ( $R=1.4$ ) at different mixer speeds.

Figure 5.34: Trends for the segregation index from DEM simulations for monodisperse ( $R=1$ ) and bidisperse particles ( $R=1.4$ ) at 69 rpm.

Figure 5.35: Ultimate level of segregation index as a function of mixer speed [7].

Figure 5.36: Ultimate level of segregation index versus rotation speed from DEM simulations after 23 rotations.

Figure 5.37: Simple baffle design, two opposite cones with a cube into the centre.

Figure 5.38: Comparison segregation index  $S$  at different rotational speeds of 23, 46, 69 rpm with and without baffle.

Figure 5.39: Comparison segregation index  $S$  at 23 rpm with baffle and no baffle.

## Chapter 6

Figure 6.1: (a) Transverse filling. (b) Axial filling.

Figure 6.2: Comparison of the segregation index for a rotating drum at different rotational speeds 23, 46, 69 rpm.

Figure 6.3: Magnitude of velocity in a rotating drum operating at different rotational speeds.

Figure 6.4: Schematic of a rotating drum operating in rolling mode showing the active and passive regions.

Figure 6.5: Plot of calculated x-direction velocity  $u$  against y-direction distance from the bed surface.

Figure 6.6: Comparison of particle angular velocity  $\omega_{particle}$  with drum angular velocity  $\omega_{drum}$  for particles in the passive layer along the bisector line at 10 mm distance from the wall.

Figure 6.7: Magnitude of velocity in a of hoop mixer. The direction of the flow for a particular drum position is highlighted in black.

Figure 6.8: Comparison mixing rates for a hoop mixer at 23, 46, 69 rpm.

Figure 6.9: Comparison of the segregation index in a Turbula mixer for different rotational speeds for axial and transverse filling.

Figure 6.10: Comparison of rate of mixing for a rotating drum, hoop mixer and Turbula mixer at different rotational speed.

## Chapter 7

Figure 7.1: Schematic diagram of the experimental system setup the mixing study.

Figure 7.2: General scheme for the methodology used to locate a tracer within the vessel with the moving boundaries. Larger graphs for the steps A-2, A-3, A-4, B-2 are reported in the next paragraph.

Figure 7.3: Schematic representation of the experimental measurement of the Turbula motion by PEPT.

Figure 7.4: Setup for the vessel boundaries orientation measurement.  $X, Y, Z$  directions PEPT coordinate system direction.

Figure 7.5: Vessel geometry. Points  $A, B$  and  $C$ , where tracer was located for the vessel motion measurement.

Figure 7.6:  $X, Y, Z$  positions for the point  $A$  determined over 3 minutes time (here only first 5 seconds are reported).

Figure 7.7: (a)  $X, Y, Z$  positions for the point  $A$  averaged over 3 minutes time and full  $360^\circ$  angle. (b) discontinuous data collection.

Figure 7.8:  $X, Y, Z$  positions for the point  $A$  after interpolation and  $fft$ .

Figure 7.9: Point  $A, B, C$  used to define a unit vector coordinate system  $\hat{\mathbf{i}}, \hat{\mathbf{m}}$  fixed with the vessel geometry (the normal vector  $\hat{\mathbf{n}}$  is given by  $\hat{\mathbf{i}} \times \hat{\mathbf{m}}$ ).

Figure 7.10: Tracer located inside the cylindrical vessel during the PEPT mixing experiments (e.g. glass beads).

Figure 7.11: Typical particle position ( $X, Y, Z$ ) with respect to the PEPT coordinate system for glass beds at 22, 46 and 67 rpm.

Figure 7.12: Typical particle position ( $x, y, z$ ) with respect to the vessel coordinate system for glass beds at 22, 46 and 67 rpm.

Figure 7.13: Typical particle position ( $x, y, z$ ) with respect to the vessel coordinate system for zeolite particle at 22, 46 and 67 rpm.

Figure 7.14: Plot of  $x$  position against number of rotation for the tracer particle at 22 rpm for 15 shaft rotations (left) and only for the first 3 rotations (right), definition of peak and plateau.

Figure 7.15: Peaks frequency distribution during PEPT experiment for glass beads at different speed.

Figure 7.16: Length of average plateau periods in axial direction for the tracer particle as functions of speeds.

Figure 7.17: Occupancy plots (20 min) for glass bead tracer particle at different speeds.

Figure 7.18: Dispersion coefficient  $D_x$  and  $D_r$  for glass beads particle at different speeds.

Figure 7.19: Occupancy plots (20 min) for zeolite tracer particle at different speeds.

Figure 7.20: Dispersion coefficient  $D_x$  and  $D_r$  for zeolite particle at different speeds.

## Chapter 8

Figure 8.1: Comparison of axial and radial dispersion coefficients,  $D_x$  and  $D_r$ , for DEM and PEPT as a function of speed.

Figure 8.2: Peak frequency distribution for DEM simulations and PEPT experiments.

Figure 8.3: Average length of plateau periods for DEM simulations and PEPT experiments.

Figure 8.4:  $D_x$  and  $D_r$  from rotation 2 and 15 for the “base” case.

Figure 8.5: Comparison of  $x'-x$  and  $r'-r$  distributions, DEM simulations and PEPT at 23 rpm.

Figure 8.6: Comparison of  $x'-x$  and  $r'-r$  distributions, DEM simulations and PEPT at 46 rpm.

Figure 8.7: Comparison of  $x'-x$  and  $r'-r$  distributions, DEM simulations and PEPT at 69 rpm.

Figure 8.8: Comparison of  $x'-x$  distributions for DEM simulations (*case E*) and PEPT.

Figure 8.9: Comparison of  $r'$ - $r$  distributions for DEM simulations (*case E*) and PEPT.

Figure 8.10: Effect of DEM parameters on  $\ln(S_{fit}-S_\infty)$  with number of rotation  $N_R$  for 23 rpm.

Figure 8.11: Effect of DEM parameters on  $\ln(S_{fit}-S_\infty)$  with number of rotation  $N_R$  for 46 rpm.

Figure 8.12: Effect of DEM parameters on  $\ln(S_{fit}-S_\infty)$  with number of rotation  $N_R$  for 69 rpm.

Figure 8.13: Effect of DEM input parameters for the axial and radial coefficient of dispersions,  $D_x$  and  $D_r$ , against characteristic number of rotations for different operating speeds. The dotted line represents the PEPT experimental values for  $D_x$  and  $D_r$ .

## List of Tables

### Chapter 1

Table 1.1: Indices for binary mixture based on statistical analysis.

Table 1.2: Example of mixers for solid material.

### Chapter 2

Table 2.1: Pan coater DEM input parameters.

Table 2.2: Flodex DEM simulation input parameters values.

### Chapter 3

Table 3.1: Particle size distribution for the zeolite sample.

Table 3.2: Classification of flowability by Hausner Ratio HR.

Table 3.3: Classification of flowability by Carr's index.

Table 3.4: Measured zeolite flow properties: Hausner ratio, Carr's index and flow function.

Table 3.5: Classification of the flowability function  $ff_c$ .

Table 3.6: Results of the measurements for the zeolite at different values of normal load at pre-shear.

Table 3.7: Comparison between bulk density, tapped, density and bulk density from the Schulze ring test.

Table 3.8: Values of the kinematics angle of wall friction.

Table 3.9: Mean rupture force, stress and strain, with standard deviation.

Table 3.10: Average values for the reduced Young's modulus  $E^*$  and hardness  $H$  for each indentation depth with standard deviation.

Table 3.11: Bulk compaction conditions.

Table 3.12: Average values of bulk compression parameters from Heckel, Kawakita and Adams models compared with single particles compression test and Nanoindentation. Only the apparent strength from the Adams model is comparable with single particle strength data.

### Chapter 5

Table 5.1: Turbula mixer EDEM simulation conditions.

Table 5.2: Physical parameters and their values used in the EDEM simulations.

Table 5.3: Summary for the predicted EDEM (version 2.3, 2 processors) simulation time for 45 s total simulation time (23 rpm) if input parameters were chosen were same as those measured for zeolite particles in Chapter 3.

Table 5.4: Values for the segregation index  $S$ .

Table 5.5: EDEM simulations conditions for  $R=1.4$ .

## **Chapter 6**

Table 6.1: Parameters used in the simulations.

## **Chapter 8**

Table 8.1: list of equation used to calculate axial and radial dispersion coefficients in DEM simulations and PEPT mixing experiments.

Table 8.2: EDEM input parameters for sensitivity analysis.

Table 8.3: Summary dispersion coefficients  $D_x$  and  $D_r$  from sensitivity analysis.

# Chapter 0

## Business needs

### 0.1 Introduction: Johnson Matthey Plc

Johnson Matthey is a chemical company with core skills in catalysis, precious metals, fine chemicals and process technology. The company is organised in three main divisions [1], namely:

1. *Environmental technologies division* supplies catalysts to customers globally as well as related technologies for applications, which benefit the environment such as pollution control, cleaner fuel, more efficient use of hydrocarbon and the hydrogen economy. The division is organised into three businesses:
  - Emission Control Technologies (ECT);
  - Process Technologies;
  - Fuel Cells.
2. *Precious metals division* markets, distributes, refines and recycles platinum group metals. They also refine gold and silver and fabricate products using precious metals and related materials. The division is organised into four businesses:
  - Platinum Marketing and Distribution;
  - Noble Metals;
  - Catalysts, Chemicals and Refining;
  - Colour Technologies.

3. *Fine chemicals division* supplies active pharmaceutical ingredients, fine chemicals and other speciality chemical products and services to a range of chemical and pharmaceutical industries as well as industrial and academic research organisations.

The division is organised into three businesses:

- Macfarlan Smith
- Pharmaceutical Materials and Services
- Research Chemicals

## **0.2 Particle technology in catalysis**

Particle technology is very important in the process and chemical industry. 75% of manufacturing processes involve the use of solid particles [2]. Improvements and a better design and handling of such operations can make an economic difference. Particles are also critical in the catalyst industry and catalysts are essential to the chemical industry. Heterogeneous catalysts are inherently solid and either particulate in form or made via particle processing. The catalyst industry is expanding and the world catalyst demand is expected to grow by 6%/year, to \$16.3 billion, through 2012 [3].

Catalysts are needed to decrease the activation energy and the temperature required for the reactions and increase the rate of reaction. Example of catalyst products with various shapes and sizes are shown in Figure 0.1.

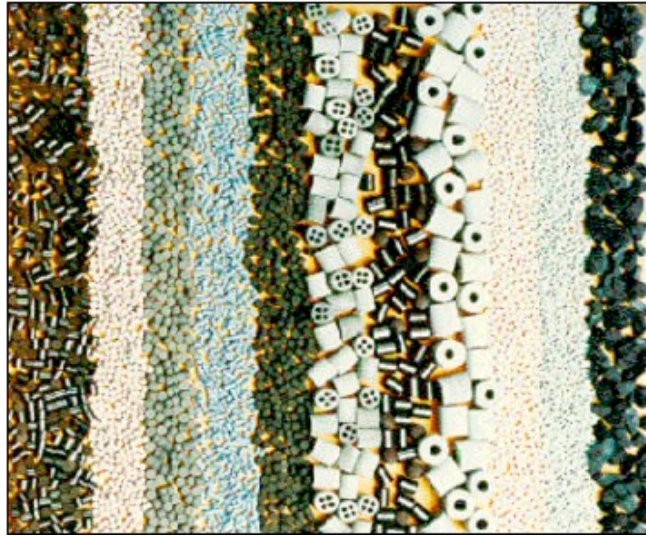


Figure 0.1: Typical catalyst shape and size: typically made by, granulation, pelleting and extrusion.

The morphology of the catalyst is important for the following reasons [4,5].

- Ease of homogeneous packing;
- Guaranteed constant temperature along the tube wall;
- Guaranteed constant low pressure drop along the tube;
- Surface area per unit volume of material to guarantee the desired conversion;
- Economical to fabricate;
- Necessary structural strength to resist crushing and abrasion in operation and during handling.

Particle processing technology is thus important in catalyst manufacture. For example considering the production of heterogeneous catalysts, Figure 0.2, the catalysts are produced either by precipitation of the active and support components, or by impregnation (cone blenders) of the active components onto a pre-existing support. This will then go through a post-processing sequence that may involve one or more of the following operations: filtering, washing, drying (rotary drum, fluid bed, spray drying) and thermal processing (rotary drum).

Ultimately the catalyst is prepared in its final form. In some cases this may simply be the powder produced in the first step. Alternatively this may involve pelleting, extrusion, granulation or coating onto a preformed substrate.

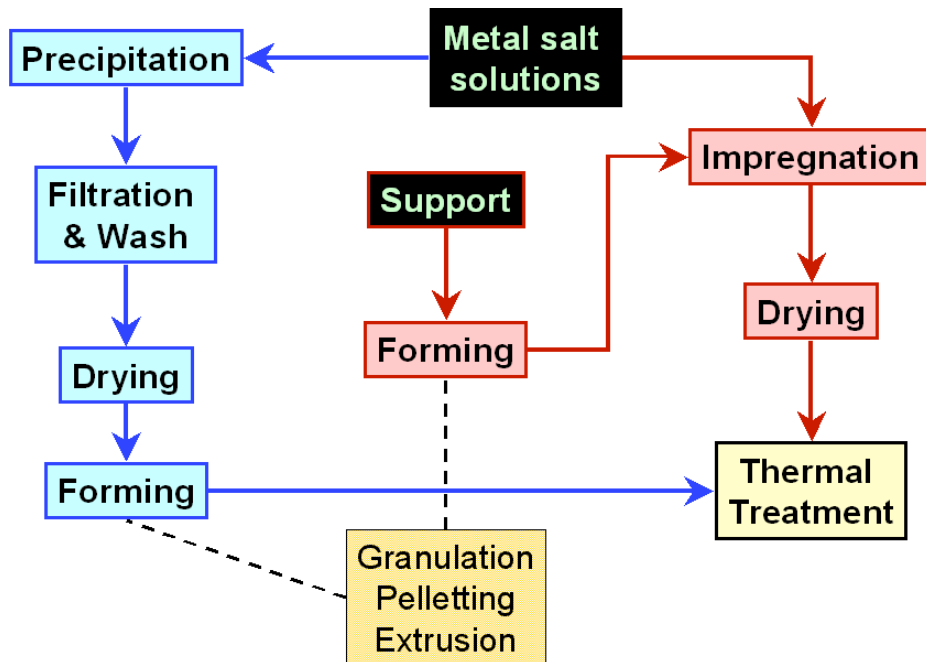


Figure 0.2: Typical heterogeneous catalyst production route.

The following equipment types are among those used for handling particles during manufacturing operations:

- Rotary drum
- Cone blender
- Fluidised bed
- Spray drier
- Compaction press
- Extruder
- Granulator

All these operations involve particles, sometimes in the gas or liquid phase. By understanding these processes, improvements in product manufacture can be achieved. Research in these equipment types therefore helps to resolve the problems associated with them, such as:

- Product performances
- Ability to achieve design performances for mass or heat transfer
- Need for a pilot plant stage
- Need of over-design
- Reduction of energy consumption
- Ability to maintain product quality
- Loss of production time
- Mechanical failures of plants

In the past research into particulate solids was perceived as a low-tech sector, and moreover not easy to define mathematically. In the last decade, however, the necessity to understand particles has been heightened as the demand for durable products is driving the industry due to increasing competition. In many fields it has been realised that a better understanding is a key task to gain benefit in terms of improvements in predictive design and manufacturing capability. Lack of understanding of powder flow can lead to a considerable loss of money. Some simple data from the *Institute of Scientific Information* proves that in different fields there has been a huge interest in this matter over the last few years [6]. This data shows that the number of the papers with the key words *granular matter*, *granular material* and *granular materials*. Between 1982-1988 is 1, 27 and 93 respectively. The corresponding numbers for the period 1995-2001 are 40, 593 and 795. For the terms particulate system and particle system the number of papers published are 205 in the period 1982-1988 and 724 in the period 1995-2001, showing the increase of interest in such topics.

### **0.3 DEM as investigation tool in particle technology: rotating mixer system**

As a consequence of increasing computer power and more readily useable commercial codes, the Discrete Element Method (DEM) is being used in an increasing range of applications to simulate increasingly complex processes, often for evaluation of machinery prototypes. This presents the additional challenge of analysis of results, in particular mixing to extract flow and mixing mechanisms with a view to improving design or operation. In the past few years, a great deal of DEM modeling simulation research has been devoted to this domain, giving rise to constructive numerical approaches to study the behaviour of granular material in different systems. Rotating vessels of a range of shapes and motions are widely used for granular mixing in many industries, such as chemical, pharmaceutical, ceramic and food. Given the difficulty and poor reliability of measurement, granular mixing is however still poorly understood [7]. In recent years, advancement in computer speed power has opened the way to model complex granular flow using the Discrete Element Method (DEM), originally presented by Cundall and Strack in 1979 [8], in which the particulate system is modelled as an assembly of individual discrete and interacting particles. DEM can provide much needed insight into the mechanisms governing particle flow and is a powerful tool for optimising mixing processes since the complete trajectory of every particle relative to all other particles and the equipment can be calculated.

In this work attention will be focusing on rotating mixers. These are typical equipment used within Johnson Matthey PLC for: pellet and powder impregnation, spray coating of tablets, thermal processing of catalyst as well as for hydration of final pharmaceutical product forms. In this thesis the first numerical model of the Turbula mixer has been carried out using DEM. This is part of a larger piece of work in which the motion of the modelled particles is compared with real experimental data in order to validate the model. This will be used to

identify uncertainties in the model and highlight critical input parameters from experimental and DEM modelling research.

#### 0.4 References

- [1] Johnson Matthey, (2010). Corporate website [online]. Available: <http://www.matthey.com> [accessed January 2010].
- [2] R.D. Nelson, (1999). Why Study Particle Science [online]. Available: <http://www.erpt.org/misc/whystudy.htm>, [accessed June 2010].
- [3] R. Coons, (2009). Catalysts seeking the next big thing, Chemical Week [online]. Available: [http://www.chemweek.com/sections/cover\\_story/Catalysts\\_18634.html](http://www.chemweek.com/sections/cover_story/Catalysts_18634.html), [accessed January 2010].
- [4] M.V. Twigg, Catalyst handbook, second ed., 1996, Manson, London ,1979.
- [5] S. Afandizadeh, A. Foumeny, Design of packed bed reactors: guides to catalyst shape, size, and loading selection, *Applied thermal engineering* **21** (2001), pp. 669-682.
- [6] J.M. Ottino, D.V. Khakhar, Fundamental research in heaping, mixing, and segregation of granular materials: challenges and perspectives, *Powder Technology* **121** (2001), pp. 117-122.
- [7] A.W. Roberts, Particle Technology—Reflections and Horizons: An Engineering Perspective, *Chemical Engineering Research and Design* **76** (1998), pp. 775-796.
- [8] P.A. Cundall, O.D.L.Strack, A discrete numerical model for granular assemblies, *Geotechnique* **29** (1979), pp. 47–65.

## **Chapter 1**

### **An introduction to solid mixing**

*Particulate materials are of great importance in a wide range of engineering applications, and within a number of industry sectors including pharmaceutical, chemical, powder metallurgy, and food. Particle technology is a relatively new discipline and in the past few decades there has been a considerable growth in understanding of the way powders and bulk solids behave during the variety of processing and handling operations used [1]. Powder mixing is one of the most widely used operation across different industries, but research on the fundamental understanding of the behaviour of granular materials and mixing mechanisms remains difficult.*

## **1.1 Introduction to particulate materials and powder mixing**

Recently, there has been increased interest in the behaviour of particulate materials, both from an experimental and modelling viewpoint. Granular materials play an important role in engineering and they can be considered as conglomerations of single discrete particles in contact surrounded by voids. A powder consists of a group of discrete particles of any solid material with a maximum dimension of less than 1000  $\mu\text{m}$  [2]. A particle is therefore considered as small object having precise physical boundaries in all directions. The overall bulk constitutive relationships are considered to be determined by the individual characteristics of all these single particles, and also by the contact interactions that take place between adjoining particles [3]. All these interactions can generally be expressed by relationships, which can be more or less complicated. Granular material can behave quite differently from any of the other standard familiar forms of matter such as solid or liquid. The overall geometrical structure defined by the local particles can result in a complex non-linear overall bulk behavior [4]. Granular material should therefore be considered as an additional state of matter. Generally, granular material is divided into two categories, free-flowing and cohesive mixtures, which can show erratic behaviour under certain circumstances.

Particulate material is important in many industries and a variety of manufacturing operations. For example, solids mixing is extensively employed in the manufacture of ceramics, plastics, fertilizers, detergents, glass, pharmaceuticals, processed food and animal feeds and in the powder metallurgy industry [5]. In some industries mixing is a critically important operation, since the amount of the active ingredient in a formulation can be imperative. For example in the pharmaceutical industry where a product with too low active ingredient may be ineffective and a product with too high active ingredient content may be lethal [6]. Often, granular materials are mixed for subsequent operations such as compaction where lubricants or flow

aids are added. Lubricants also have an effect on the compaction behaviour of a bulk material, with a direct influence on the properties of the final compact [7]. The mixing of particulate material is therefore an important operation to reach the desired final product quality or the right manufacturing conditions, however, often it can be difficult to mix particles homogeneously. Understanding and controlling the mixing mechanisms is a key task to achieve the desired characteristics of a final product. The mixing mechanisms are determined by the different forms of movement for the solid material inside the mixer, which can vary due to different mixer designs.

In many instances powder mixing is still an empirical discipline. Often, technology is largely based on experience and application of academic mixing theories that involve the use of simpler non-cohesive binary particulate systems [8]. Real industrial applications, however, have to deal with more complex cohesive multi-component systems.

An important aspect in powder mixing regards the selection or design of the correct mixing device. Usually, mixing operation is batch-wise, however in certain cases it can be a continuous process [9]. Moreover selection of the correct way to assess the state of the resulting mixture is essential.

## **1.2 Mixing mechanisms**

Three types of mechanisms are often used to describe the mixing process [6]:

- 1) *Convection*: when movements, or regions, of the mixture are moved as bulk material to different areas, Figure 1.1.a, (also referred as *macromixing*).
- 2) *Dispersion*: when in an expanded bed of free flowing material particles can change their position with random movements, Figure 1.1.b, (also referred as *micromixing*)

3) *Shear*: mixing occurs along the slip planes or discontinuities in the velocity distribution between regions of particles. This third mechanism is often considered a combination of the two previous processes [10].

All the mechanisms can exist in a single mixer, but one could predominate with respect to the others at a given time point. The relative importance of these mechanisms can change during the mixing process [11]. The selection of the mixer should be related with the type of material that must be mixed.

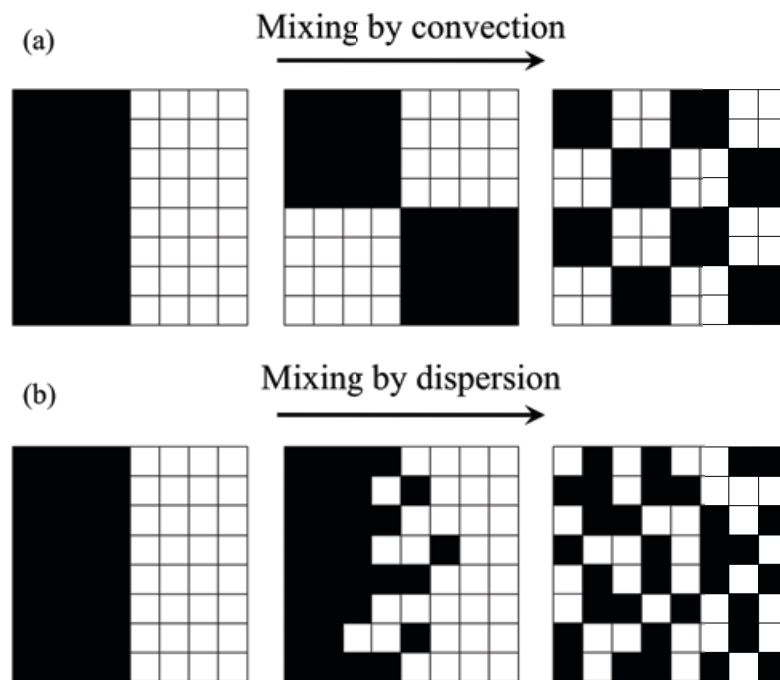


Figure 1.1: Mixing mechanisms: convection and dispersion.

### 1.3 Segregation mechanisms

Poor mixing is characterised by segregation, which consists of the separation of particles due to differences of physical properties [12]. Typical factors that can lead to segregation are: differences in particle size, shape, density, surface roughness, forces of attraction and friction

[13]. Particle segregation can be difficult to describe and therefore there are difficulties in predicting it quantitatively [14]. The segregation of free-flowing granular material has been extensively investigated in the literature [15,16,17] but segregation of cohesive material is neither fully understood or well described [18].

When material is blended the final result can assume different configurations depending on the nature of the product and the mixing conditions. It is usually not a regular arrangement. For example a simple binary system, like in Figure 1.2, which illustrates different possible mixing arrangements. These depend on the particle nature and mixing conditions.

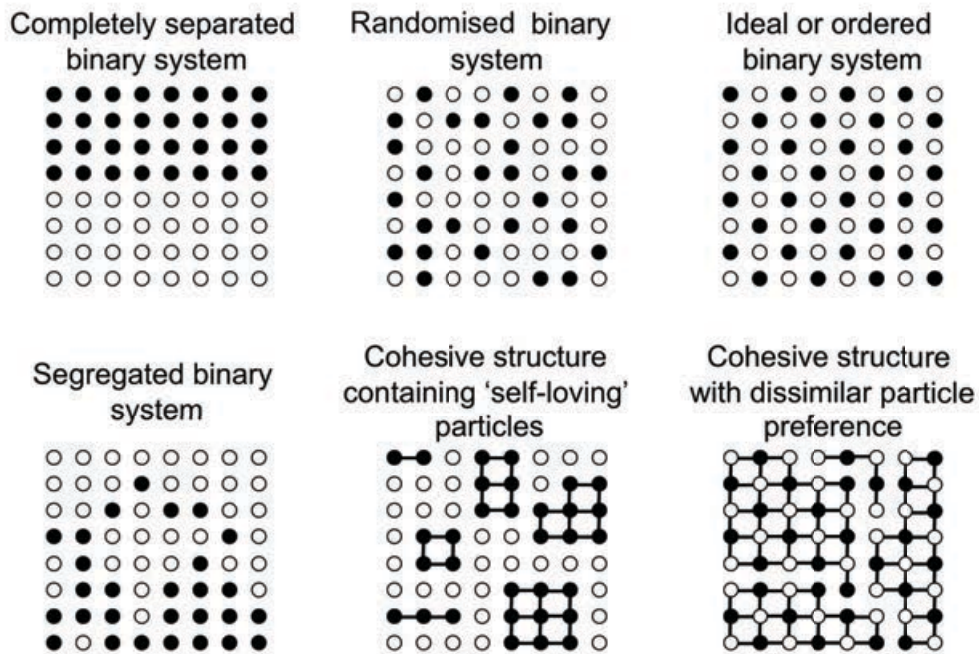


Figure 1.2: Representation of mixedness equal proportions of black and white particles, each circle represents particles of the two different components. Redrawn from [19].

Before mixing, the two components in the system might be completely segregated as shown in Figure 1.2. The randomized binary system is the best mixture that can be achieved by using any real blender [9] and it corresponds to the situation when the probability of finding a

particle of a constituent in every point is identical [20]. In the ideal or ordered binary system each particle of a constituent is near a particle of another type. The probability of obtaining this situation in real industrial mixers is practically equal to zero. In the case of cohesive materials particles can aggregate and bond together and then a randomly structured powder will result. This is a typical example of “self loving” particles, where particles tend to bond with similar particles or in the case of “dissimilar particles preferences” where particles tend to bond with dissimilar particles.

Three principal mechanisms for segregations are schematically described in Figure 1.3, and they are listed as follows [21]:

- 1) *Trajectory segregation*: results from different travelling distances of particles with varying particle size or density projected with velocity into a fluid.
- 2) *Percolation segregation*: is induced when in a multi-size component mixture, fine particles can move freely through the voidage created by dilation of the bulk of solids material when flow occurs (when incipient flow occurs the bed of material is dilated).
- 3) *Vibration segregation (also know as Brazil nut effect)*: Under the influence of vibrations, a mixture of granular materials tends to segregate. Mixtures of particles with different sizes or particles identical in size but with different densities tend to stratify in layers. Smaller particles or heavier particles move downward, if the bulk of solid is vibrated or shaken. When the bulk solid is vibrated the small or lighter particles tend to run through the larger or heavier particles, and eventually these the larger or heavier particles can be made to migrate to the surface.

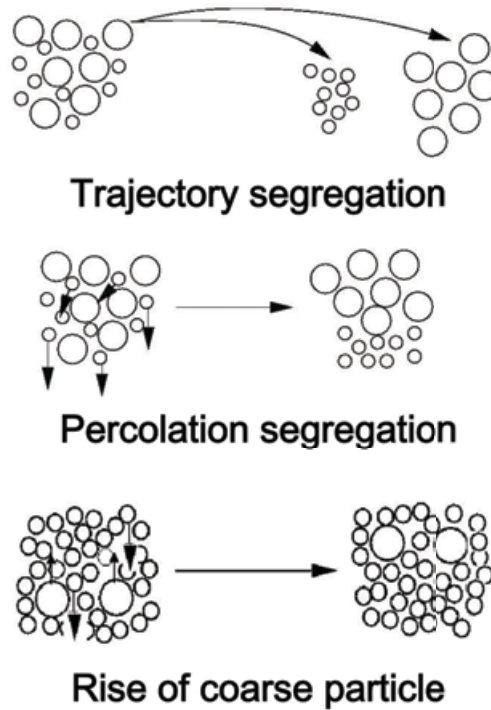


Figure 1.3: Segregation mechanisms [22].

In process design, the solution to a segregation problem can be resolved in two ways. The process can be modified to accommodate segregation patterns caused by the various mechanisms or changes can be made to the process to reduce the cause of segregation. In either case, understanding the segregation mechanisms is fundamental for developing and controlling the mixing process where segregation can occur.

#### 1.4 Definitions: mixing time and mixing rate

The degree of mixedness or homogeneity in a system is defined by measuring a mixing index.

In a binary mixture a general rule to define mixing is given as follows [11]:

$$M = \frac{\text{amount of mixing that has occurred}}{\text{amount of mixing that could occur}} \quad (1.1)$$

In the literature different mixing indices  $M$  have been proposed by different authors to define the quality of homogeneity between components in the system [10]. The most common way of assessing the performance of a mixer is to withdraw a number of samples and to use statistical analysis of the variance of the concentration of these samples as a measure of mixture quality [23]. For a binary system a few examples of mixing indices based on statistical analysis of *sample variance*  $\sigma$ , variance of a completely segregated system  $\sigma_o$  and *variance of perfectly random system*  $\sigma_R$ , are given in Table 1.1.

Table 1.1: Indices for binary mixture based on statistical analysis [10].

Author	Expression	$M$ for $\sigma = \sigma_o$	$M$ for $\sigma = \sigma_R$
Kramers	$M = \frac{\sigma_o - \sigma}{\sigma_o - \sigma_R}$	=0	1
Lacey	$M = \frac{\sigma_o^2 - \sigma^2}{\sigma_o^2 - \sigma_R^2}$	0	1
Ashton and Valentin	$M = \sqrt{\frac{\log \sigma_o^2 - \log \sigma^2}{\log \sigma_o^2 - \log \sigma_R^2}}$	0	1
Valentin	$M = \frac{\log \sigma_o - \log \sigma}{\log \sigma_o \log \sigma_R}$	0	1
Miles	$M = 1 - \frac{\sigma^2}{\sigma_o^2}$	0	<1
Rose and Robinson	$M = 1 - \frac{\sigma}{\sigma_o}$	0	<1
Smith	$M = \frac{\sigma_o}{\sigma}$	1	>1
Yano	$M = \frac{\sigma}{\sigma_o}$	1	<1
Lacey	$M = \frac{\sigma_R}{\sigma}$	<1	1
Lexis	$M = \frac{\sigma}{\sigma_R}$	>1	1

The time required to achieve a desired level of mixture homogeneity depends on the rate of mixing which is a function of the dominating mixing mechanisms. The mixing time is therefore defined as the period of time when the mixing index reaches a stationary final

condition. The rate of mixing is generally described by an exponential decay relationship. In Figure 1.4 for example the relative standard deviation (RSD) of the sample concentrations is plotted against the number of revolutions in the case of a bin blender. Initially the impact of the convective (bulk flow) mixing mechanisms is the dominant factor on the measured variable, RSD. This is then followed by a slower period where the dispersion (individual particle motion) or shear mechanisms are the controlling mechanisms [24].

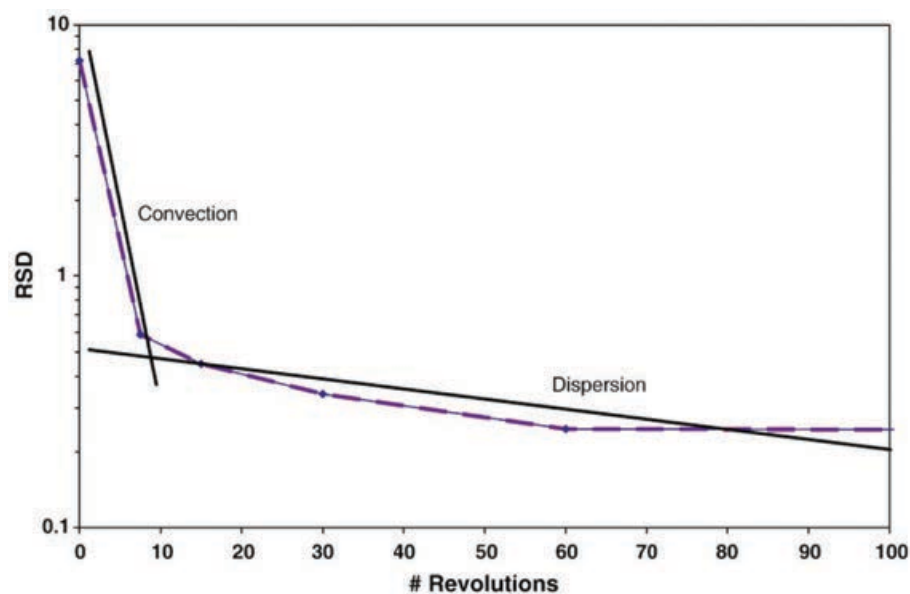


Figure 1.4: A typical mixing plot, with relative standard deviation (RSD) of the samples concentration plotted against number of revolutions. The two solid lines show the two distinctive mixing regimes for a bin blender [24].

Different techniques can be used to assess powder mixing and the homogeneity of a mixture. For example, sampling is a common method; this involves the positioning of thief probes inside the mixing vessel, which are used to withdrawal samples from the mixture. Difficulties can arise withdrawing a representative sample from the mixture since errors can influence the probing result [25]. Inserting a thief probe into a mixture can cause extensive disturbance of

the mixture structure dragging particles along the path of the thief and therefore, the sample collected is likely to contain particles from all position along this path [26]. Usually, one sample is not enough and normally many samples are necessary to describe the mixture structure. Moreover, the size of the sample and the location of withdraw can have an influence on the magnitude of the results since segregation can occur during blending.

Alternatively the homogeneity is sometimes measured by solidifying the bed structure after the mixing experiment by the use of a binder solution, which penetrates through the bed voidage and “freezes” that bed structure by evaporation of the solvent. Subsequently, the bed is sliced and the local composition is studied with image analysis techniques [26].

Non-invasive imaging techniques such as X-ray computer tomography (CT) and magnetic resonance imaging (MRI) can also be used to give useful insights into the internal “structure” of powder beds. Computed Tomography is a non-invasive radiological imaging technique that can measure density variations within objects using X-rays. In the case of mixing studies, material mixing patterns are measured by analyzing the differences in material density obtained by inserting materials with different X-ray attenuation coefficient within the blender. Computed Tomography is therefore used to reconstruct non-destructive cross-sectional stationary images [27]. This technique has also been used on a scaled-down model of a commercial double-cone blender as a method of investigating catalyst impregnation variables as function of mixing mechanisms. The concentration of particles of a given colour in the granular bed were quantified for 1/16 inch diameter pellets and nominally 100 mm diameter spherical particles [28]. CT has also been applied to study the mixing of Pb-impregnated microcrystalline cellulose particles used in pharmaceutical processes [29]. These mixing studies conducted with a model V-blender show that particle size and initial loading configuration of the mixing components alter the mixing efficiency.

MRI can be utilised to plot high-resolution three-dimensional images of flowing particles, and can also be used to obtain information such as velocity and local concentration by voxel analysis. Phase separation and state of mixing between multi-component systems is determined by using differences in MRI from atomic resonance relaxation, resonance frequency or diffusivity [30]. The three-dimensional evolution of the segregation phenomena in a rotating drum filled with a binary mixture of spherical particles has been described using MRI [31]. The authors highlighted the development of a radial core of small particles along the axis of the cylinder, which evolves to axially segregated bands. Mixing of free flowing sugar beads in a cylindrical vessel within a Turbula mixer and quantification of homogeneity has also been studied by this method [32].

Any method used for assessing mixture quality should, however, account for a number of requirements [33]:

- a. have some physical significance with regard to the process under investigation or to the mixture application;
- b. be sufficiently sensitive to changes in the state of mixing (scale of scrutiny);
- c. be unambiguous;
- d. be applicable to different systems, as far as possible;
- e. cause no disturbance of the mixture under investigation;
- f. require the minimum of experimental effort;
- g. be mathematically and statistically rigorous.

Numerical simulations can have the advantage that the system being studied is not affected by the sampling technique, which can affect systems during experimental methods. Simulations should therefore provide reliable information on mixing efficiency. For example, the degree of mixedness for a system operating under different conditions can be studied in terms of

contact numbers and coordination numbers directly obtained from simulations [34,35]. The mixing time and number of revolutions necessary for uniform mixing of solids (steady state of the number of contacts between particles) obtained from simulation were in agreement with experimental results in the case of a rotating drum [35].

### 1.5 Type of industrial mixers

A variety of solid mixers are available in industry, which can be divided into two categories: mixers with rotating vessels and mixers with fixed vessels. Mixers can also be grouped depending on the predominant mixing mechanisms [10,19], as listed in Table 1.2.

Table 1.2: Example of mixers for solid material [10,19].

Type of mixer	Predominant mechanisms
Rotating drum	Shear - Dispersive [10] Dispersive [19]
Double cone mixer	Shear – Dispersive [10] Dispersive [19]
V-mixer	Dispersive [19]
Y-mixer	Dispersive [19]
Ribbon mixer	Convective [10,19]
Orbiting vertical screw mixer	Convective – Dispersive [10] Convective [19]
Air mixer	Convective – Dispersive [10] Convective [19]

### 1.6 Turbula laboratory mixer

A three-dimensional movement of a cylindrical container can be achieved in the Turbula mixer, Figure 1.5. This is a laboratory scale mixer that is largely used in industry for the development or testing of new products. The model T2F considered in this work has a mixing chamber that can hold a container with a capacity up to 2 L. The rotational speed can be

varied from 22 to 100 rpm. The mixing container, located in the mixer chamber, is subjected to intensive, periodically translational and rotational pulsating movements, which simulate the pattern of agitation achieved by manual shaking [32]. This extremely complicated movement is composed of two rotations of the container and a horizontal translation. In addition to these traditional principal motions of rotation and translation there is a third fundamental motion of inversion based on the Schatz inversion principle [36]. This particular motion subjects the contents to two alternating, rhythmic pulsating motions, which have the effect of continuously compressing and thinning material. Hence the particle bed moves within the vessel with a periodical behaviour.

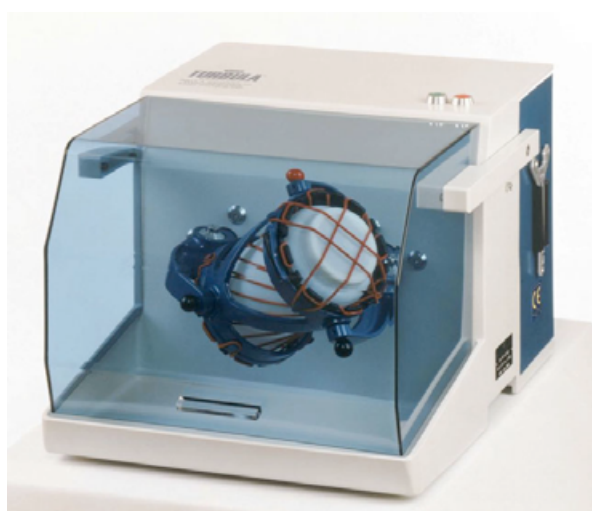


Figure 1.5: Turbula T2F shaker-mixer (reproduced with the kind permission of Willy A. Bachofen AG Switzerland).

Despite its widespread use as a laboratory scale blender in the catalyst and pharmaceutical industries, only a few mixing studies using the Turbula have been reported in the literature. For example, Magnetic Resonance Imaging (MRI) studies [32, 37] are the only studies in the literature where the mixing process for free flowing non-cohesive material has been

characterised under different conditions. In the present work the rate of mixing of particles with monomodal and bimodal size distributions was quantified using a segregation index.

## **1.7 Conclusions**

Studying granular materials is a complicated subject. Granular materials are not simple and it is difficult to define a set of properties to predict their behaviour, unlike other forms of matter, like liquid or gas. The influence of granular matter on industrial manufacturing is tremendous, hence many applications such as mixing in the chemical, construction material, pharmaceutical, drug and food industries, have been investigated. One of the most common industrial operations is powder blending. Often such an operation needs to be controlled to achieve the right mixing conditions or to avoid conspicuous particle separation. Understanding the mixing mechanism is essential, especially in systems involving complicated geometries or multi dimensional motions, such as the Turbula mixer. Due to the complications involved in such systems, understanding mixing and segregation processes requires the use of several tools, both experimental and modelling techniques.

## 1.8 References

- [1] A.W. Roberts, Particle Technology—Reflections and Horizons: An Engineering Perspective, *Chemical Engineering Research and Design* **76** (1998), pp. 775-796.
- [2] BSI (1993). BS 2955:1993, Glossary of terms relating to particle technology. BSI - British Standards Institution. <http://www.bsonline.bsi-global.com>. 30pp.
- [3] M. Oda, K. Iwashita, An introduction Mechanics of Granular Materials, *A.A. Balkema*, Rotterdam, 1999.
- [4] F. Nicot, F. Darve, RNVO Group: Natural Hazards and Vulnerability of Structures A multi-scale approach to granular materials, *Mechanics of Materials* **37** (2005), pp. 980-1006.
- [5] L.T. Fan, Y.-M. Chen, F.S. Lai, Recent developments in solids mixing, *Powder Technology* **61** (1990), pp. 255–287.
- [6] R. Holdich, Fundamentals of Particle Technology, *Midland Information Technology & Publishing*, 2002.
- [7] U. Klemm, D. Sobek, Influence of admixing of lubricants on compressibility and compactibility of uranium dioxide powders, *Powder Technology* **57** (1989), pp. 135-142.
- [8] J.A. Hersey, Powder mixing: theory and practice in pharmacy, *Powder Technology* **15** (1976), pp. 149-153.
- [9] L. Pernenkil, C.L. Cooney, A review on the continuous blending of powders, *Chemical Engineering Science* **61** (2006), pp. 720-742.
- [10] M. Poux, P. Fayolle, J. Bertrand, D. Bridoux, J. Bousquet, Powder mixing: Some practical rules applied to agitated systems, *Powder Technology* **68** (1991), pp. 213-234.

- [11] C.D. Rielly, D.L.O. Smith, J.A. Lindley, K. Niranjana, V.R. Phillips, Mixing Processes for Agricultural and Food Materials: Part 4, Assessment and Monitoring of Mixing Systems, *Journal of Agricultural Engineering Research* **59** (1994), pp. 1-18.
- [12] J.P.K Seville, U. Tuzun, R. Cliff, Processing of particulate solids, first ed., *Blackie academic & professional*, London, 1997.
- [13] R. Weinekötter, H. Gericke, Mixing of Solids Particle Technology, Kluwer Academic Publisher, 2000.
- [14] D. Schulze, Powders and Bulk Solids Behavior, Characterization, Storage and Flow, *Springer Berlin Heidelberg*, 2008.
- [15] G. Félix, V. Falk, U. D'Ortona, Segregation of dry granular material in rotating drum: experimental study of the flowing zone thickness, *Powder Technology* **128** (2002), pp. 314-319.
- [16] A. Alexander, T. Shinbrot, B. Johnson, F.J. Muzzio, V-blender segregation patterns for free-flowing materials: effects of blender capacity and fill level, *International Journal of Pharmaceutics* **269** (2004), pp. 19-28.
- [17] S.K. Hajra, T. Bhattacharya, J.J. McCarthy, Improvement of granular mixing of dissimilar materials in rotating cylinders, *Powder Technology* **198** (2010), pp. 175-182.
- [18] H. Li, J.J. McCarthy, Cohesive particle mixing and segregation under shear, *Powder Technology* **164** (2006), pp. 58-64.
- [19] N. Harnby, M.F. Edwards, A.W. Nienow, Mixing in the process industries, second ed., *Butterworth Heinmann*, 2001.
- [20] P.M.C. Lacey, Developments in the theory of particle mixing, *Journal of Applied Chemistry* **4** (1954), pp. 257-268.

- [21] J.C. Williams, The segregation of particulate materials. A review, *Powder Technology* **15** (1976), pp. 245-251.
- [22] H. Li, Impact of cohesion forces on particle mixing and segregation, PhD thesis, *University of Pittsburgh*, (2005).
- [23] M.H. Cooke, D.J. Stephens, J. Bridgwater, Powder mixing — a literature survey, *Powder Technology* **15** (1976), pp. 1-20.
- [24] A. Mehrotra, F.J. Muzzio, Comparing mixing performance of uniaxial and biaxial bin blenders, *Powder Technology* **196** (2009), pp. 1-7.
- [25] J. Bridgwater, Particle technology, *Chemical Engineering Science* **50** (1995), pp. 4081-4089.
- [26] F.J. Muzzio, P. Robinson, C. Wightman, D. Brone, Sampling practices in powder blending, *International Journal of Pharmaceutics* **155** (1997), pp. 153-178.
- [27] A.W. Chester, J.A. Kowalski, M.E. Coles, E.L. Muegge, F.J. Muzzio, D. Brone, Mixing dynamics in catalyst impregnation in double-cone blenders, *Powder Technology* **102** (1999), pp. 85-94.
- [28] A.W. Chester, J.A. Kowalski, M.E. Coles, E.L. Muegge, F.J. Muzzio, D. Brone, Mixing dynamics in catalyst impregnation in double-cone blenders, *Powder Technology* **102** (1999), pp. 85-94.
- [29] C.-Y. Yang, X.-Y. Fu, Development and validation of a material-labeling method for powder process characterization using X-ray computed tomography, *Powder Technology* **146** (2004), pp. 10-19.
- [30] L.F. Gladden, Magnetic resonance: ongoing and future role in chemical engineering research, *A.I.Ch.E. Journal* **49** (2003), pp. 2-8.
- [31] M. Nakagawa, S.A. Altobelli, A. Caprihan, E. Fukushima, NMRI study: axial

- migration of radially segregated core of granular mixtures in a horizontal rotating cylinder, *Chemical Engineering Science* **52** (1997), pp. 4423-4428.
- [32] N. Sommier, P. Porion, P. Evesque, B. Leclerc, P. Tchoreloff, G. Couarraze, Magnetic resonance imaging investigation of the mixing-segregation process in a pharmaceutical blender, *International Journal of Pharmaceutics* **222** (2001), pp. 243-258.
- [33] C. Schofield, The definition and assessment of mixture quality in mixtures of particulate solids, *Powder Technology* **15** (1976), pp. 169-180.
- [34] Y. Akao, H. Kunisawa, L.T. Fan, F.S. Lai, R.H. Wang, Degree of mixedness and contact number A study on the mixture of particulate solids and the structure of solid mixtures, *Powder Technology* **15** (1976), pp. 267-277.
- [34] M. Kwapinska, G. Saage, E. Tsotsas, Mixing of particles in rotary drums: A comparison of discrete element simulations with experimental results and penetration models for thermal processes, *Powder Technology* **161** (2006), pp. 69-78.
- [35] P. Schatz, Deutsches Reichspatent Nr. 589 452 in *Der allgemeinen Getriebeklasse* (1993). US Patent Nr. 2 302 804 (1942).
- [36] N. Sommier, P. Porion, P. Evesque, Mixing and Segregation Processes in Turbula Blender, *Material Research Society Symposium Proceedings* **627** (2000).

## Chapter 2

### Theoretical background DEM (EDEM)

*The Discrete Element Method (DEM) has been an increasingly recognised numerical tool for modelling granular systems since the original work of Cundall and Strack back in 1979 [1]. In DEM, the particulate material is modelled as an assembly of individual particles, which interact with each other or any other solid body such as the walls or moving blades of mixing equipment. The macroscopic behaviour of the assembly of particles is determined by microscopic interactions amongst particles and between particles and boundaries. The path and velocity of each particle is computed in discrete time steps. This provides a wealth of information such as the frequency of collisions and duration of contacts with neighbours. Movement of particles relative to bulk flow gives a measure of dispersion and is revealing about flow and mixing mechanisms at a scale and level of detail that is very difficult to achieve by experimental means.*

*DEM simulations in this work were performed using a commercial package (EDEM) based on the original algorithm proposed by Cundall and Strack. Commercial codes such as EDEM incorporate a powerful Graphical User Interface (GUI) that interfaces with CAD drawing packages. This and the readily available computational power allow complex mixing systems to be simulated. The reliability of DEM predictions depends entirely on the simplification of the physical models used to describe the microscopic interaction. Simplifications are necessary, and are widely used, to make complex problems solvable in sensible time frames,*

*yet there seems to be little validation work reported in the literature that probes beyond macroscopic flow features. If DEM is to fulfil its promise of becoming as important a design tool as Computational Fluid Dynamics (CFD), there is a need to quantify and validate the ability of DEM simulations to provide an insight into mixing mechanisms in equipment where flow is difficult to observe, let alone measure, on the granular scale.*

## **2.1 Introduction: modelling granular material**

Recently, there has been an increased awareness of the important role particle technology plays in many industry sectors. Granular materials are the object of studies in many disciplines, for example geotechnics, materials science, physics and soil mechanics. Granular materials are also produced and used in many manufacturing processes such as chemical, pharmaceutical, food industry and mining. For example, in the transport industry storage of materials can promote jamming of silos or pipes during pneumatic conveying. In soil mechanics problems regarding run-out of avalanche have been of interest. In the pharmaceutical and chemical industry material segregation can occur during mixing.

The study of particulate solids can be approached by treating the bulk solids as continuum or as a conglomerate of discrete particles. Regarding the second approach, a considerable amount of work has been carried out to study the physics of single particle interactions in recent years [2]. The reason why problems regarding granular materials appear to be complicated is that the traditional macroscopic continuum approach, utilized so far, is not completely adequate. In addition, time dependent microscopic mechanisms are not completely understood. In the past studies of micromechanical interactions between particles such as the tensional state within the material or force distribution within an assembly were not possible. Since micro-measurement experimental techniques, mathematical models or simulation capabilities were not available, micromechanical approaches were not extensively carried out. Photo-elastic experiments demonstrated the complexity and the discontinuous nature of granular materials by visualization of the force chain ramification within granular media formed by photoelastic sensitive disks as shown in Figure 2.1.a [3]. The two-dimensional disks with different diameters (from 8 to 20 mm) were stacked between two glass plates and loaded. The average stress and strain-rate tensors in the interior of particle assemblies were

determined by using the pattern of isochromatics, from which the forces that are transmitted through the contact points between the discs. At the end of the 70s the first numerical micromechanical simulation was presented by Cundall and Strack. This work considered a simple aggregate of disk elements subjected to a biaxial stress. The stress transmission pattern was numerically simulated and compared with the photoelastic experimental results on disk, as shown in Figure 2.1.b.

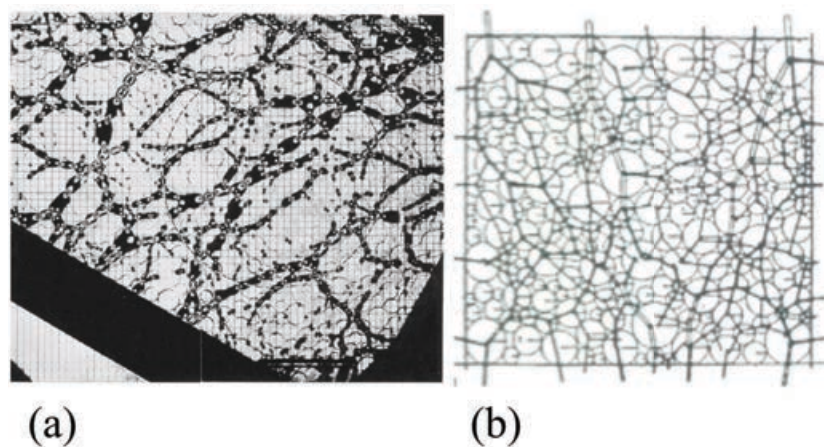


Figure 2.1: (a) Photo-elasticity picture of the granular assembly of discs: force transmission pattern [3]. (b) Force transmission pattern numerically simulated by DEM [1].

## 2.2 Discrete Element Modelling (DEM)

In recent years increasing computer power, development of academic DEM models and the availability of new user-friendly commercial software have led to DEM becoming a popular research tool in industry as well as academia. As a consequence DEM is being used in an increasing range of applications to simulate increasingly complex systems, often for evaluation of machinery prototypes. Compared with early years simulations, models can now consider large numbers of particles or increasing system complexities (dimension of the problem). 2D simulations have also evolved into more sophisticated 3D simulations giving

greater capability in the complexity of the system that can be studied. The interest and the effort into DEM research increased dramatically [4]. Figure 2.2 shows the number of publications related to discrete particle simulation between 1993 and 2011, obtained from ScienceDirect website with the following keywords: discrete element method/model, distinct element method/model, discrete particle simulation/method/model, and granular dynamic simulation.

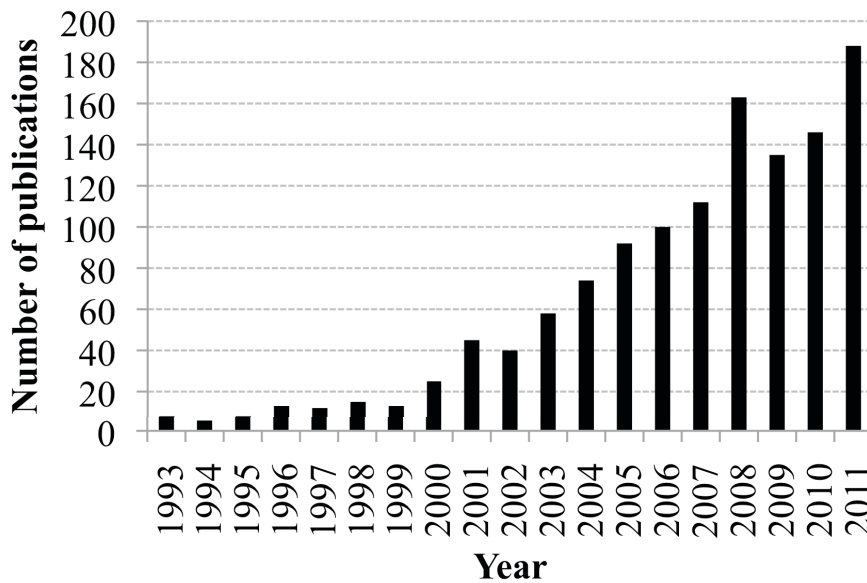


Figure 2.2: Number of publications related to discrete particle simulation between 1993-2011 from ScienceDirect website.

DEM modelling is providing insight into the mechanisms governing particle flow and it is a powerful tool for optimising a number of industrial processes. In DEM each particle is considered as a discrete element and the bulk mechanical behaviour of the assembly is related to individual particle properties and interactions. Because the output of DEM is the complete trajectory of every particle relative to all other particles and the equipment, such numerical simulations can enhance fundamental understanding of granular motion and can also help in

the improvement of design or operation of systems involving particulate material [5]. The value of DEM is demonstrated by the broad variety of applications reported in the literature.

### **2.2.1 Examples of DEM applications for particle motion**

The Discrete Element Method algorithm was originally presented by Cundall and Strack in 1979. Since then many other DEM simulations have been published in the literature studying the modelling of diverse granular processes as comminution [6,7,8,9,10,11], granulation [12,13,14], flow through hopper [15,16,17,18], die filling for tableting [19,20], fracture of agglomerates [21,22,23,24], packing of particles [25,26,27,28,29,30], bulk compression of particles [31,32,33,34,35] and flow in a screw extruder [36,37].

The motion of particles in blenders rotating around a one-fixed axis such as drum, double cone, bead mill and V-mixer has been extensively studied and modelled. For example, Muguruma *et al.* 1997 [38] investigated the three dimensional motion of particles in a rotating cylinder and showed how DEM simulations can be used as tool for design improvements in a particular system. The mixing rate was compared in case of different designs and the length/height ratio of the baffles was optimised. Simulations were validated against experimental results by visual comparison of mixing pattern for spheres with two different colours. Kwapinska *et al.* 2006 [39] used DEM to study transverse mixing of free flowing particles in horizontal rotating drums in terms of mixing time and number of drum rotations necessary to achieve uniform mixing. The authors explored the effect of a range of operating parameters such as drum diameter, rotational frequency and average particle diameter and compared the results with experimental data from literature. Good agreement was found in terms of mixing time and mixing number for the uniform mixing of the solids by comparing the DEM simulation with mixing experimental data from literature. Sarkara *et al.* 2009 [40]

showed the effect of operating conditions such as fill level and impeller rotation rate (Froude number) on axial mixing in a horizontal bladed continuous blender. The axial particle movement was shown to be strongly dependent on the operating conditions, with better mixing achieved at low Froude numbers for high fill levels and high Froude number for low fill levels.

The effect of the particle physical properties (density, size or friction) on the mixing behaviour (qualitative visual comparison of profile for the bed cross section) in a 2D rotating drum was shown by Xu *et al.* 2010 [41]. For their system, it was observed that for a specific rotational speed, differences in particle density and particle size were the principal factors affecting mixing behaviour whereas friction coefficient had less importance. It was also demonstrated that segregation due to large particle size ratio or density ratio can be suppressed (percolation effects) by including into the system particles with appropriate particle size distribution, for example, ternary- or multi-sized system). Industrially relevant tumbling blenders such as the double cone and V-blender have also received attention [42,43,44]. Investigations by Moakher *et al.* 2000 [42] presented 3D simulations of double cone and V-blenders containing both monodisperse and bidisperse grain sizes, comparing the results with visual experiments. It was shown that in case of bidisperse spheres in both systems, segregation rapidly reaches a steady state. Both mixers' typical mixing patterns showed that convection is the dominant mixing mechanism while axial dispersion across the symmetry plane is the dominant bottleneck. DEM modelling can therefore be helpful in designing new mixing systems with broken symmetries by using baffles or proper shapes for the vessels. Intermittent particle movement, repeated sequence of splitting and merging, observed in the V-blender results in more rapid mixing and segregation compared with the double-cone mixer, which operates almost continuously, with a nearly constant flow of

particles in a uniform surface layer. Kuo *et al.* 2008 [43] modelled the mixing of 3 mm monosized spheres and showed good semi-quantitative agreement of bulk velocity and axial dispersion coefficient between numerical and experimental results obtained by Positron Emission Particle Tracking (PEPT). It was shown that the choice of a wide range of input parameters such as restitution coefficient, normal stiffness, friction coefficients (both particle-particle and particle-wall) influences the velocity, speed and velocity fluctuation distributions, the exchange rate between the two arms and the circulation time in the mixer and dispersion at division and combination steps. An optimal selection of such parameters was necessary in order to achieve the semi-quantitative agreement with experimental results.

Typical DEM simulations consider a small number of particles involved, which typically is very different to the number of particles involved in an industrial application. Lemieux *et al.* 2008 [44] showed the possibility of using DEM numerical simulations in large-scale systems (225,000 particles over long time spans 2 minutes, up to 60 mixer revolutions) by modelling a V-blender over the period of few weeks of CPU time on a Beowulf cluster. The bed behaviour, for both monodisperse and bidisperse, was studied in terms of flow patterns, velocity fields, granular temperature and torque of the mixing system. The fact that DEM simulations are computationally intensive has led to an increase of effort into software developments such as software parallelization and algorithm optimisation.

### **2.3 DEM Numerical model**

DEM employed in this work uses the soft-sphere approach originally developed by Cundall and Strack. In this method, particles in contact are permitted to withstand small deformations, and these deformations are used to calculate forces acting between particles, as reported in the general numerical algorithm illustrated in Figure 2.3, [43].

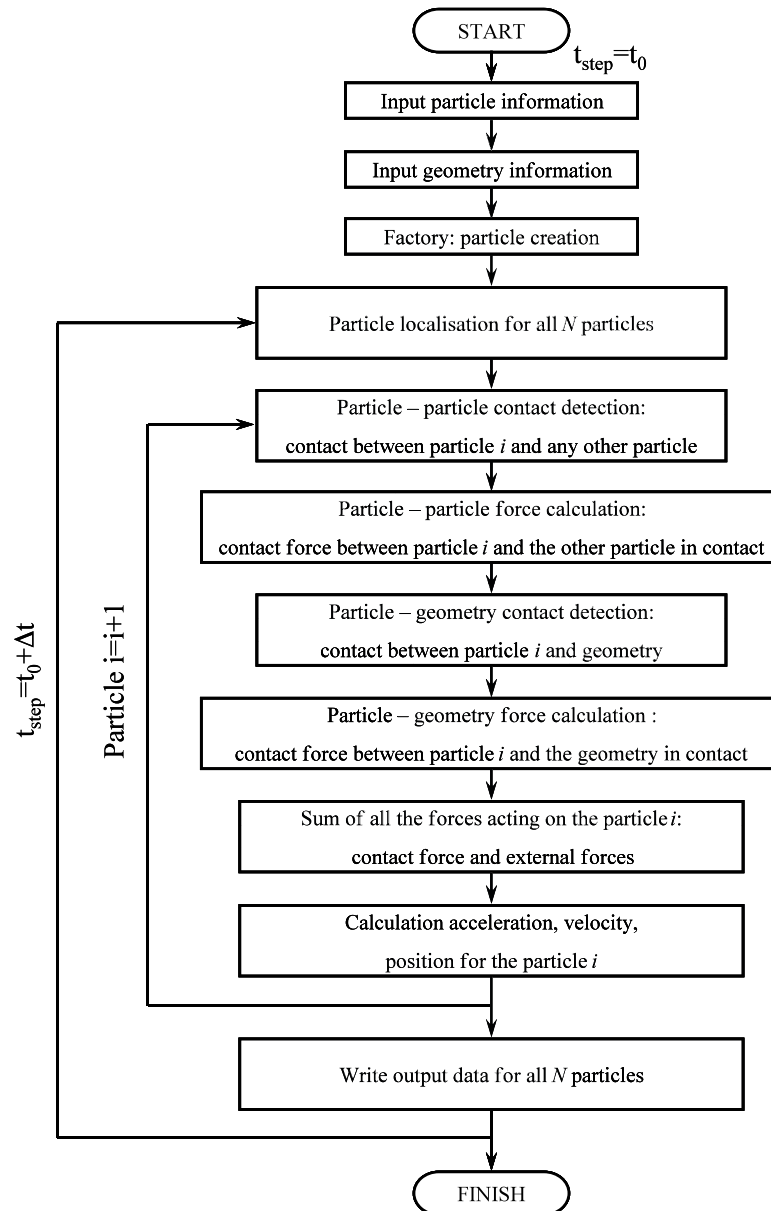


Figure 2.3: DEM numerical algorithm. Redrawn from [43].

The DEM numerical algorithm generally begins by placing the particles into the system. In order to calculate the contact force EDEM performs a contact detection search to account for the contact between each individual particle. The contact detection is the most time consuming, computationally demanding operation. Once the contact detection is complete the total force acting on each particle is determined and hence the translation and rotation motion

can be described by integrating the Newton's equations of motion Eq.(2.1) and Eq.(2.2). Calculations are performed in discrete time steps. Between each time-step, the particles move in a straight line according to the velocity and acceleration calculated in the preceding time step. These trajectories are used to calculate the positions of the particles at the next time step. Overlaps (i.e. contacts) are then used to calculate the forces acting on each particle, which determine its velocity and acceleration in the next time interval. Therefore the position, velocity and acceleration are obtained for all the particles at discrete time-steps. The force and torque are the sum of all forces and torques acting on each particle, including gravity, fluid drag, magnetic fields and electrostatic fields.

In this work the forces and torques due to gravity, collision and rolling friction are considered and the Newton's equations of motion for a particle  $i$  in contact with particle  $j$  assume the following form:

$$m_i \frac{d\mathbf{v}_i}{dt} = \sum (\mathbf{F}_{ij}^n + \mathbf{F}_{ij}^t) + m_i \mathbf{g} \quad (2.1)$$

$$I_i \frac{d\boldsymbol{\omega}_i}{dt} = \sum (\mathbf{R}_i \times \mathbf{F}_{ij}^t - \boldsymbol{\tau}_{ij}^r) \quad (2.2)$$

Where  $m_i$ ,  $I_i$ ,  $\mathbf{v}_i$  and  $\boldsymbol{\omega}_i$  are, respectively, the mass, moment of inertia, translational velocity and rotational velocity of particle  $i$ .  $\mathbf{F}_{ij}^n$  and  $\mathbf{F}_{ij}^t$  are the normal and the tangential forces due to contact between particle  $i$  and  $j$  at the current time-step as reported in Figure 2.4.  $\mathbf{R}_i$  is the vector between the centre of particle  $i$  and the contact point where the force  $\mathbf{F}_{ij}^t$  is applied.

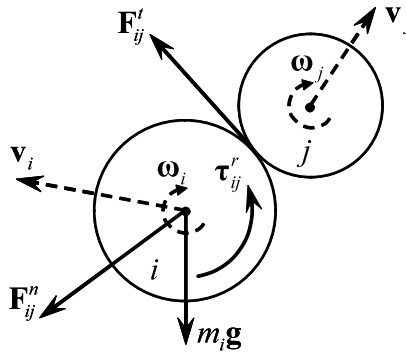


Figure 2.4: Contacts between particle  $i$  with particle  $j$ .

The term  $\tau_{ij}^r = -\mu_r R_i |\mathbf{F}_{ij}^n| \hat{\omega}_i$  in Eq.(2.2) is added to account for the torque caused by rolling friction. The parameter  $\mu_r$  is defined as the coefficient of rolling friction and  $\hat{\omega}_i$  is the unit angular velocity of the particle  $i$ . Rolling friction losses can arise from, for instance: making and breaking of surface bonds such as liquid or electrostatic bridges; hysteresis in deformation of the moving point of contact; and interlocking of asperities on the contacting surfaces [45,46,47,48]. So, while the causes of rolling resistance are understood in a general sense, the value of this friction coefficient is difficult to predict and to measure for granular material.

Considering Figure 2.4 the following notations are:

- $R_i$  = radius particle  $i$
- $R_j$  = radius particle  $j$
- $\mathbf{r}_i$  = position of particle  $i$  (location of centre)
- $\mathbf{r}_j$  = position particle  $j$  (location of centre)
- $\mathbf{v}_i$  = velocity particle  $i$
- $\mathbf{v}_j$  = velocity particle  $j$

The two particles are in contact if the following relation is valid:

$$|\mathbf{r}_i - \mathbf{r}_j| \leq R_i + R_j \quad (2.3)$$

The normal unit vector joining the centres of the two particles is defined as:

$$\mathbf{n}_{ij} = \frac{\mathbf{r}_j - \mathbf{r}_i}{\|\mathbf{r}_j - \mathbf{r}_i\|} \quad (2.4)$$

The relative velocity is defined as:

$$\mathbf{v}_{ij} = \mathbf{v}_i - \mathbf{v}_j \quad (2.5)$$

Therefore the relative velocity in the normal direction is given by:

$$\mathbf{v}_{ij}^n = (\mathbf{v}_{ij} \cdot \mathbf{n}_{ij}) \mathbf{n}_{ij} \quad (2.6)$$

The relative velocity in the tangential direction is given by:

$$\mathbf{v}_{ij}^t = \mathbf{v}_{ij} - \mathbf{v}_{ij}^n \quad (2.7)$$

The tangential unit vector is calculated as follows:

$$\hat{\mathbf{t}}_{ij} = \frac{\mathbf{v}_{ij} - \mathbf{v}_{ij}^n}{\|\mathbf{v}_{ij} - \mathbf{v}_{ij}^n\|} \quad (2.8)$$

A model is necessary to evaluate the force terms between particles and those between particles and any other solid body (e.g. wall boundaries) when they come into contact. A variety of contact models have been previously reported in the literature [49,50,51,52,53,54].

There is no general consensus on what is the best contact model since these models are not

equivalent and deal with particle contacts differently. For instance models based on Hertz theory consider particles that lead to elastic deformation, whereas the linear spring dashpot model considers that this deformation is viscoelastic [53]. All these models depend on parameters, the values of which must be included in the setup. It is very important to validate any DEM based model before using it. A careful validation strategy should always include an ultimate test between the numerical and experimental results.

The contact model used by Cundall and Struck is based on a Kelvin-Voigt model represented in Figure 2.5. A spring, damper and slider represent the contact model for the normal and the tangential direction. This model assumes the definition of the following parameters in normal and tangential directions:

- Stiffness  $k$
- Damping coefficient  $\eta$
- Friction coefficient  $\mu$

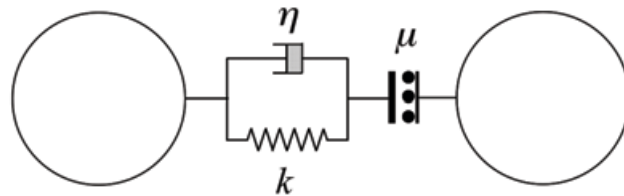


Figure 2.5: Kelvin-Voigt contact model: spring  $k$ , damper  $\eta$  and slider  $\mu$ .

Cundall and Strack defined Eq.(2.9) for the normal contact model and Eq.(2.10) for the contact force in tangential direction.

$$\mathbf{F}_{ij}^n = (-k_n \delta_{ij}^n - \eta_n \mathbf{v}_{ij}^n) \quad (2.9)$$

$$\mathbf{F}_{ij}^t = (-k_t \delta_{ij}^t - \eta_t \mathbf{v}_{ij}^s) \quad (2.10)$$

The stiffness parameters in normal and tangential directions ( $k_n, k_t$ ), damping parameters ( $\eta_n, \eta_t$ ), and the friction coefficient  $\mu_s$  must be defined in the simulation model.  $\delta_{ij}^n$  and  $\delta_{ij}^t$  are the particle normal and tangential displacement due to normal force and tangential force.  $\mathbf{v}_{ij}^s$  is the slip velocity at the contact point defined as follows:

$$\mathbf{v}_{ij}^s = \mathbf{v}_{ij} - (\mathbf{v}_{ij} \cdot \mathbf{n}_{ij}) \mathbf{n} + (R_i \omega_i + R_j \omega_j) \times \mathbf{n}_{ij} \quad (2.11)$$

Tsuji *et al.* 1997 [55] proposed a non-linear model from adaptation of the Cundall and Strack contact model, Figure 2.6.

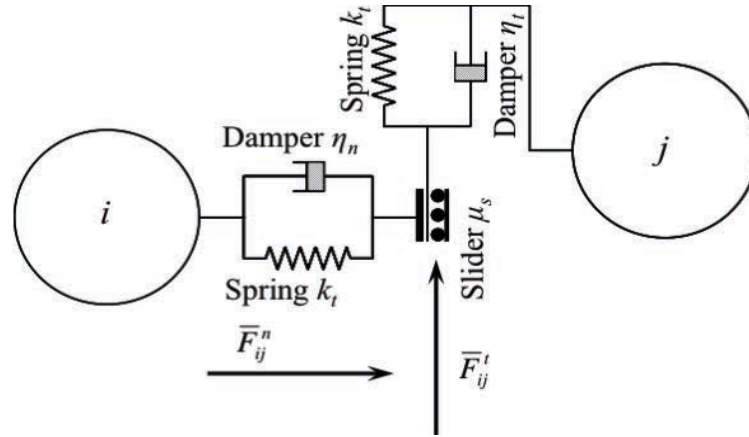


Figure 2.6: Modified Hertz Mindlin contact model described by Eq.(2.12, Eq.(2.13) and Eq.(2.15).

In this model the first term of Eq.(2.9) is substituted with a non-linear term to consider the Hertz theory for normal contact (ref. Chapter 3). For the tangential contact Tsuji proposed

[56] an adaptation of Eq.(2.9) to include a viscous dissipation term in Eq.(2.12). Therefore the modified contact model results as follows:

$$\mathbf{F}_{ij}^n = \left( -k_n \delta_{ij}^{n3/2} - \eta_n (\mathbf{v}_{ij} \cdot \mathbf{n}_{ij}) \mathbf{n}_{ij} \right) \quad (2.12)$$

$$\mathbf{F}_{ij}^t = \left( -k_t \delta_{ij}^t - \eta_t \mathbf{v}_{ij}^t \right) \quad (2.13)$$

where  $\mathbf{v}_{ij}^s$  slip velocity is substituted with the  $\mathbf{v}_{ij}^t$  relative tangential velocity. Sufficiently high tangential forces will cause particles to slip relative to each other or to surfaces with which they are in contact. Consider cohesionless particles subject to a constant normal force: the extent of slippage under tangential force is determined by:

$$|\mathbf{F}_{ij}^t| < \mu_s |\mathbf{F}_{ij}^n| \quad (2.14)$$

These equation represents a cut-off for the magnitude of the maximum tangential force for a given static friction coefficient  $\mu_s$ , and it is known as Coulomb's law of friction [50,57]. If Eq.(2.14) is satisfied, the effect of  $\mathbf{F}_{ij}^t$  is to cause a small relative movement, termed "microslip" and Eq.(2.13) is used as tangential force. If Eq.(2.14) is not satisfied the slip covers the entire area of contact and this can be referred as "gross sliding". In this case, the tangential force is given by Amontons' first law of friction as follows, where  $\hat{\mathbf{t}}_{ij}$  is the tangential unit vector:

$$\mathbf{F}_{ij}^t = -\mu_s |\mathbf{F}_{ij}^n| \hat{\mathbf{t}}_{ij} \quad (2.15)$$

EDEM software offers several different contact models and also has provision for user-defined models, if required. The modified Hertz Mindlin contact model is the default contact

model in EDEM software [58,59] and is based on the contact model proposed by Tusji *et al.* [56]. This is an extension of the damped linear spring contact force model of Cundall and Strack. The normal and tangential non-linear contact forces are represented by equations Eq.(2.16) and Eq.(2.17), and they result from a combination of the non-linear elastic Hertz model (1881) [60] in the normal direction, and the linear elastic Mindlin model (1949) [61] in the tangential direction with a dissipative term in tangential direction. For both normal and tangential directions a dissipative second term is applied to account for energy lost during collisions through inelastic deformation and friction.

In the Hertz Mindlin contact model employed in EDEM, the collision between two spheres  $i$  and  $j$ , the normal force,  $\mathbf{F}_{ij}^n$ , acting on each sphere is given by:

$$\mathbf{F}_{ij}^n = -\frac{4}{3} E^* \sqrt{R^*} \delta_{ij}^{n3/2} - 2\sqrt{\frac{5}{6}} \psi \sqrt{S_n m^*} \mathbf{v}_{ij}^n \quad (2.16)$$

where  $E^*$  is the equivalent Young's Modulus of the two colliding particles,  $R^*$  is the equivalent radius,  $\delta_{ij}^n$  is the normal particle displacement due to the normal force,  $m^*$  is the equivalent mass, the normal contact stiffness  $S_n = 2E^* \sqrt{R^*} \delta_n$  and  $\mathbf{v}_{ij}^n$  is the normal component of relative velocity. The damping ratio coefficient  $\psi$  is a function of the coefficient of restitution,  $\varepsilon$ , and assumes a value between 0 and 1 (fully viscous to fully elastic).

The tangential force,  $\mathbf{F}_{ij}^t$ , depends on the tangential displacement  $\delta_{ij}^t$ , the relative tangential velocity  $\mathbf{v}_{ij}^t$  and the tangential contact stiffness  $S_t = 8G^* \sqrt{R^*} \delta_n$ . In EDEM, the tangential force is still limited by the sliding condition defined by the Coulomb's law of friction.

$$\mathbf{F}_{ij}^t = -S_t \delta_{ij}^t - 2\sqrt{\frac{5}{6}} \psi \sqrt{S_t m^*} \mathbf{v}_{ij}^t \quad (2.17)$$

The damping ratio is a function of the coefficient of restitution and it is defined as:

$$\psi = -\frac{\ln e}{\sqrt{(\ln e)^2 + \pi^2}} \quad (2.18)$$

with  $e$  the coefficient of restitution. In the EDEM default Hertz-Mindlin contact model the coefficient of restitution  $e$  remains constant with impact speed, assuming other model parameters are constant.

For two spheres 1 and 2, the equivalent radius  $R^*$ , the equivalent mass  $m^*$ , the equivalent Young's modulus  $E^*$  and shear modulus  $G^*$  are defined as follows:

$$R^* = \left( \frac{1}{R_1} + \frac{1}{R_2} \right)^{-1} = \frac{R_1 R_2}{R_1 + R_2} \quad (2.19)$$

$$m^* = \left( \frac{1}{m_1} + \frac{1}{m_2} \right)^{-1} = \frac{m_1 m_2}{m_1 + m_2} \quad (2.20)$$

$$E^* = \left( \frac{1 - \nu_1^2}{E_1} + \frac{1 - \nu_2^2}{E_2} \right)^{-1} \quad (2.21)$$

$E_1$  and  $E_2$  are the Young's modulus of sphere 1 and 2.  $\nu_1$  and  $\nu_2$  are Poisson's ratio of sphere 1 and 2.

$$\frac{1}{G^*} = \frac{(2 - \nu_1)}{G_1} + \frac{(2 - \nu_2)}{G_2} \quad (2.22)$$

$G_1$  and  $G_2$  are the Young's modulus of sphere 1 and 2.

If the simple Hertz Mindlin contact model defined by Eq.(2.16) and Eq.(2.17) is employed, the following contact input parameter must be defined for the EDEM simulation model.

- Coefficient of static friction  $\mu_s$ : for both particle-particle  $\mu_{s-pp}$  and particle-wall  $\mu_{s-pw}$  contacts;
- Coefficient of rolling frictions  $\mu_r$ : for both particle-particle  $\mu_{r-pp}$ , and particle-wall  $\mu_{r-pw}$  contact;
- Coefficient of restitution  $e$ : for both particle-particle  $e_{pp}$ , and particle-wall  $e_{pw}$  contact.

#### **2.4 Current limitations for DEM modelling techniques**

Due to computing limitations there are some restrictions in current DEM software. There are also limitations regarding the determination of the input parameters necessary for the simulations. All these limitations lead to uncertain accuracy of the DEM modelling and often DEM simulations results are qualitative instead of quantitative.

Representation of real particle shapes is still one of the key issues with particle size and number of particles that can be modelled. A majority of DEM simulations consider only a small amount of particles with diameters in the order of mm and a maximum number of particles in the order of 10,000 to achieve a reasonable simulation time [44,62]. The simple spherical shape and the low number of particles that DEM can handle at the moment is not usually comparable with real industrial systems which consist of millions of small, irregular particles often with a particle size distribution. Therefore, modelling capabilities are mainly limited by high computational requirements as results of the explicit time integration scheme based on sequential calculations over the desired modelled time period, with low timestep. For example the simulation of one million non-spherical particles in a complex 3D geometry is not reasonably performed by a single processor. In real industrial mixing operations some

of the segregation phenomena that occur during mixing can take a long period of time, for example in the order of second or minutes. However, typical times that can be simulated currently in DEM are usually shorter, in the order of fractions of seconds. Clusters of parallel computing can give the required level of computational power necessary for larger DEM simulations. However, such systems are usually only available at academic levels. Though computer hardware is improving, in the future it should be possible to model complicated geometries with large numbers of non-spherical particles on readily available desktop multiprocessor units. The challenge for modellers at the moment is, therefore, to present simplified models that can be processed in a reasonable time scale while still being relevant to real systems that comprise many millions of irregularly shaped particles with a wide size distribution. A major challenge for DEM simulations is to simulate non-spherical particles in an efficient manner. Different methods of modelling complex shapes have been presented in literature, for example complex particles can be represented in DEM codes as clusters of inter-penetrating or non-penetrating spheres, polyhedra ellipses, ellipsoids or polygons [63]. Clusters of inter-penetrating or non-penetrating spherical particles with different or constant diameters are rigidly connected to form an approximation of any desired shape by using the multi-sphere (MS) method [64,65,66,67].

The development of non-spherical shapes to represent the real particle can be complicated since more sophisticated particle contact models must be developed rather than the usual simple sphere contact model. The detection of the contact and subsequent calculation of the forces and torques for edge-edge, edge-corner, corner-corner contacts can be complicated and computationally expensive in case of polygons and polyhedrons [63]. However, by using the multi-sphere method it is possible to ensure computational efficiency for contact detection and force calculation and many commercial DEM packages implement such methods [65]. A

drawback of this method is that to precisely represent a complex shape requires clustering of many spherical particles which increase computational memory. Also the contribution to the surface roughness becomes difficult to evaluate.

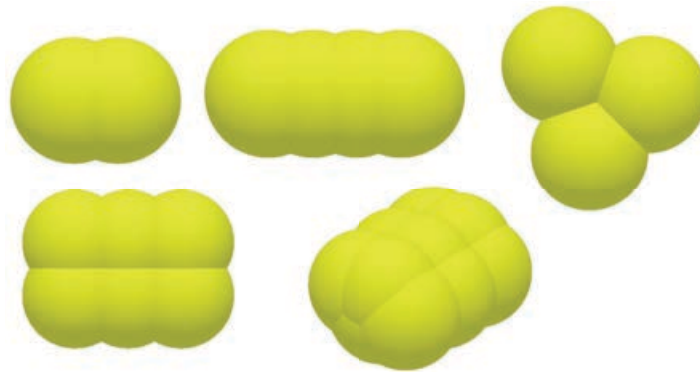


Figure 2.7: Clusters of interpenetrating spheres.

Another important key issue in the development of DEM to real industrial applications is the determination of DEM input material parameters. The simulation input parameters are often not measured and the values were sometimes assumed without proper justification since there is no robust method for their determination [68]. Thinking about predictivity, in order to interpret the simulation results confidently, correct input parameters should be selected [69] and simulations should also be validated against experimental results. However whilst DEM is increasingly used, experimental validations of the simulations are very rare [70,71].

## 2.5 Examples of current limitations

Many limitations and difficulties regarding the application of DEM for real industrial scale applications exist, some examples are given in this section. The first limitation regards the representation of particle shape: an example of the effect particle representation on packing of cylindrical pellets into a tube is given. Secondly there are limitations in terms of simulation

time, if values of DEM input parameters corresponding to real material properties are employed. Thirdly it was shown how the choice of the input parameters is an important aspect varying the final results: as example the discharge of particles from a container is used. Therefore the aim of the following paragraph is to show typical problems and uncertainties in the application of DEM as a possible predictive tool for industry. The EDEM version 1.3 provided by DEM-Solutions has been used.

### **2.5.1 Packing of pellets: poor particle shape representation leads to incorrect packing results**

The effect of particle shape can be important and it can be a dominant factor in many cases. In dynamic systems, for example mixing operations or hopper discharge, differences in particle shapes can have a significant effect since particle shape is one of the mechanisms that can promote segregation [72,73,74,75]. The unconfined yield strength, which is a factor that influences the bulk flow properties of a powder, is influenced by particle shape. The particle shape controls the number of contacts per adjacent particle and the direction of those contacts relative to a line passing through the centre of two adjacent particles [76]. Particle shape, in particular circularity, affects the packing characteristics in terms of void fraction and bed height [77].

In early DEM simulations particles were initially considered as a simple sphere for a first approximation Figure 2.8.b., however more recent literature work have concentrated on simulation with complex shaped particles. In EDEM software the multi-sphere (MS) approach is considered, where “complex” particles are created as conjoining particles [78], Figure 2.8.c.

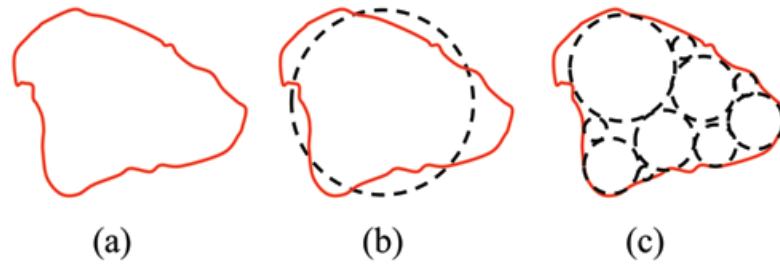


Figure 2.8: (a) typical real particle shape. (b) first approximation with one sphere. (c) multiple-sphere representation.

Representing complicated shapes by using a simple sphere can lead to some errors. Glued spheres clusters do not duplicate the overall non-spherical particle shape exactly. Although algorithms have been developed to approximate particle shapes using glued spheres, the fine details of the overall non-spherical particle surface remain irregular even with a large number of constituent spheres. The following example is given to show how a poor representation can lead to inaccurate results in case of a cylindrical pellet ( $D \times L = 3.42 \times 3.46$  mm). As shown in Figure 2.9.a, a poor particle shape representation (10: 2.7 mm diameter particles) can lead to artefacts and in this case clear errors in terms of the packing structure of pellets. The poor representation of the particles corners can lead to apparent overlaps due to the rounded corner. This inaccuracy can be improved by using for example an higher number of spheres with smaller diameters to achieve a better representation of the square sharp edge. By increasing the particle details (10: 2.7 mm diameter particles plus 76: 0.35 mm diameter particles), Figure 2.9.b, a better precision and more representation of the packing would be achieved. There should therefore be a right number and configuration of spheres that must be used to get a reasonable representation of shapes. However this considerably increases the computational time since in the multi-sphere (MS) a higher number of particles would be considered into the simulation.

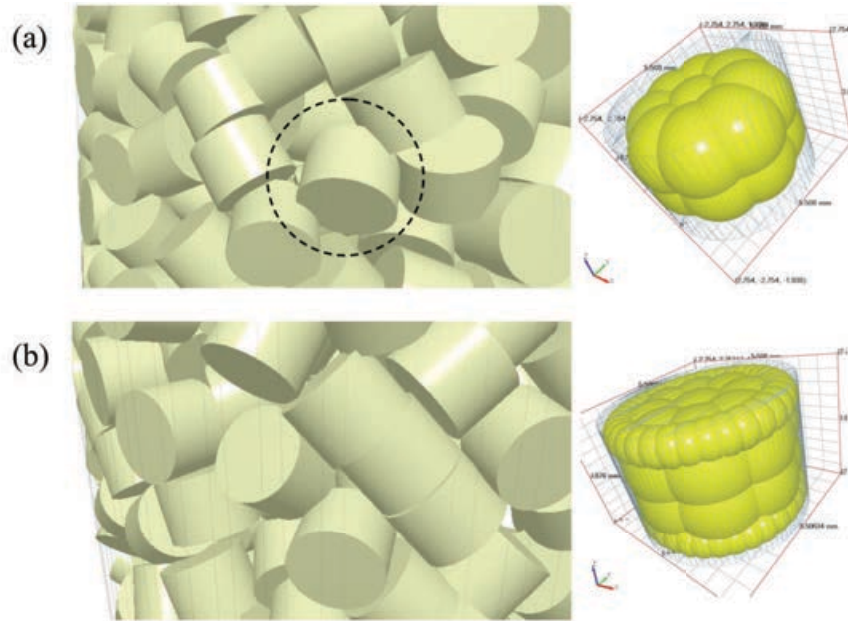


Figure 2.9: Cylindrical pellet packing: a) Poor pellets representation formed (10: 2.7 mm diameter particles). b) Improved pellets representation (10: 2.7 mm diameter particles plus 76: 0.35 mm diameter particles).

### 2.5.2 Pan coater: influence of particle shape and choice of input parameters on the simulation time

The problem of long simulation time related with the choice for the particle input parameters and particle shape representation is demonstrated by this simple example relevant to catalyst manufacture; the mixing of particles with different shapes inside the vessel in a pan coater. The DEM predicted simulation time to mix alumina Raschig rings in a laboratory scale pan coater by using an Intel Dual Core 2.66 GHz 4 GB of RAM machine is calculated. In this example only the mixing is modelled, the actual coating process is not considered.

Initially DEM simulations, reported in Figure 2.10, were run by filling the drum with 1500 spherical particles ( $d$ : 3 mm) and with 1400 Rashig rings ( $d_e, d_i, l$ : 5,3,5 mm) made by

conjoined spheres (540 spheres with 0.6 mm diameter per each Raschig ring), as shown in Figure 2.11.

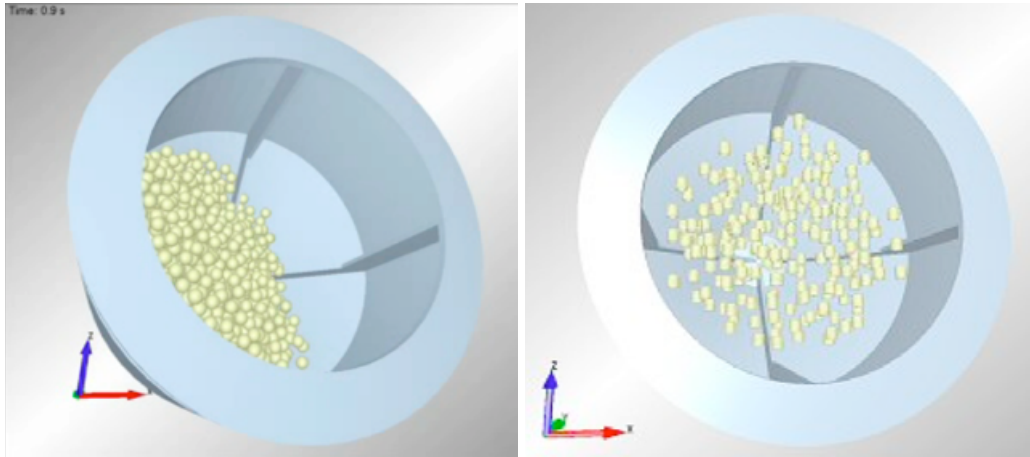


Figure 2.10: Mixing of particle in a pan coater, spherical particles and Raschig rings.

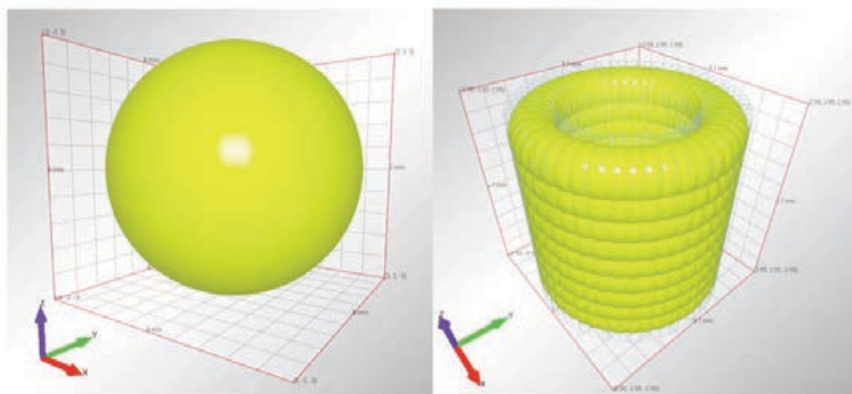


Figure 2.11: DEM simulation time for a pan coater in case of spherical and Raschig ring shape particles. Raschig rings made as assembly of 540 spherical particles.

The simulation parameters for the simulation are reported in Table 2.1. Alumina parameters, from literature [79], were used for some of the input parameters such as density, shear modulus and Poisson's ratio. The other parameters were initially assumed.

Table 2.1: Pan coater DEM input parameters.

Properties	Value
Density $\rho$ (Kg/m <sup>3</sup> )	2800 <sup>[79]</sup>
Shear modulus $G$ (Pa)	170e+09 <sup>[79]</sup>
Poisson's ratio $\nu$	0.25 <sup>[79]</sup>
Static friction coefficient $\mu_{s-pp}$	0.5 <sup>[79]</sup>
Static friction coefficient $\mu_{s-pw}$	0.35
Rolling friction coefficient $\mu_{r-pp}$	0.0006
Rolling friction coefficient $\mu_{r-pw}$	0.0005
Restitution coefficient $\varepsilon_{pp}$	0.9
Restitutions coefficient $\varepsilon_{pw}$	0.5

In the case of spherical particles the computational time was about 210 hours to model 7 seconds of mixing. For the highly detailed particle shapes (Rashig rings), the estimated by EDEM software computational was about 6100 hours with only 260 Rashig rings placed in to the system, the simulation was therefore stopped considering the impractical computational time. For the case of spherical particles the relatively long simulation time (210 hour) was mainly the result of the choice for input parameters, which according to Eq.(2.23) strongly influences the critical timestep and hence the total computational time. In the second case, the extreme detailed particle considered in the system represented by a high number of particles (1400x540=756,000) and small size (conjoined 0.6 mm spheres) resulted in an unacceptable computational time.

In the DEM simulation the timestep,  $\Delta T_{step}$ , is defined as the time between every iteration. A simulation is stable only if the timestep is less than a critical timestep  $\Delta T_{critical}$ , which is

generally defined as a fraction of the natural frequency of an equivalent mass-spring system [80]. The relation used to obtain the natural frequency can differ significantly between authors and in EDEM software the critical time step is defined as the critical Rayleigh timestep [58],  $T_R$  as follows:

$$\Delta T_{step} < \Delta T_{critical} = T_R = \frac{\pi R \sqrt{\frac{\rho}{G}}}{0.1631\nu + 0.8766} \quad (2.23)$$

where  $R$  is the particle's radius,  $\rho$  its density,  $G$  the shear modulus and  $\nu$  the Poisson's ratio. From Eq.(2.23) the shear modulus  $G$  is parameter that influences the timestep value the most. A choice of a shear modulus in the range of  $G = 10^8 - 10^{12}$  Pa would lead to a very small timestep and therefore computationally expensive simulations.

Generally the total computational time is a combination of multiple factors:

- Number of particles in the system: more data points to be calculated;
- Shape of the particles: usually “complex” shapes are described by conjoining particles which cause an increase in the number of particles within the system and therefore time;
- Size of the particles: smaller particles, smaller timestep;
- Choice of material properties: material properties influence the critical timestep;
- Total desired simulated time.

### **2.5.3 Choice of correct input parameters can have a major influence on the simulations results: simulation of Flodex**

The effect of input parameters on the DEM model is investigated in terms of discharge rate from the bottom of a simple system such as a 3D cylinder reported in Figure 2.12. The effect of the choice for the shear modulus  $G$  in terms of simulation time has been indicated, Table

2.2. The discharge rate was calculated by dividing the number of particles going through the orifice by the elapsed time.

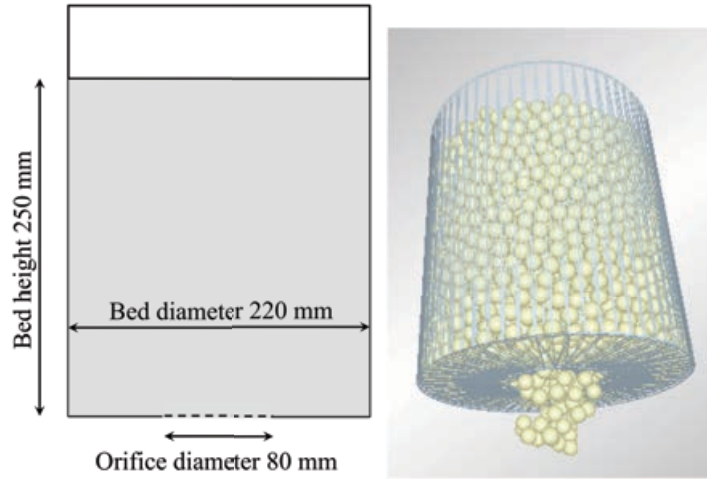


Figure 2.12: Discharge of spherical particles from a 3D cylindrical container.

Table 2.2: Flodex DEM simulation input parameters values.

Properties	Value
Diameter particle $d$ (mm)	13
Density $\rho$ (Kg/m <sup>3</sup> )	2500
Shear modulus $G$ (Pa)	$2e+04 - 2e+11$
Poisson's ratio $\nu$	0.3
Static friction coefficient $\mu_{s-pp}$	0.2 - 0.9
Static friction coefficient $\mu_{s-pw}$	0.1 - 0.9
Rolling friction coefficient $\mu_{r-pp}$	0.01 - 0.2
Rolling friction coefficient $\mu_{r-pw}$	0.005 - 0.1
Restitution coefficient $\epsilon_{pp}$	0.9
Restitutions coefficient $\epsilon_{pw}$	0.5

As observed from the following Figure 2.13 the effect of reducing  $G$  is negligible down to 2 MPa in terms of discharge rate.

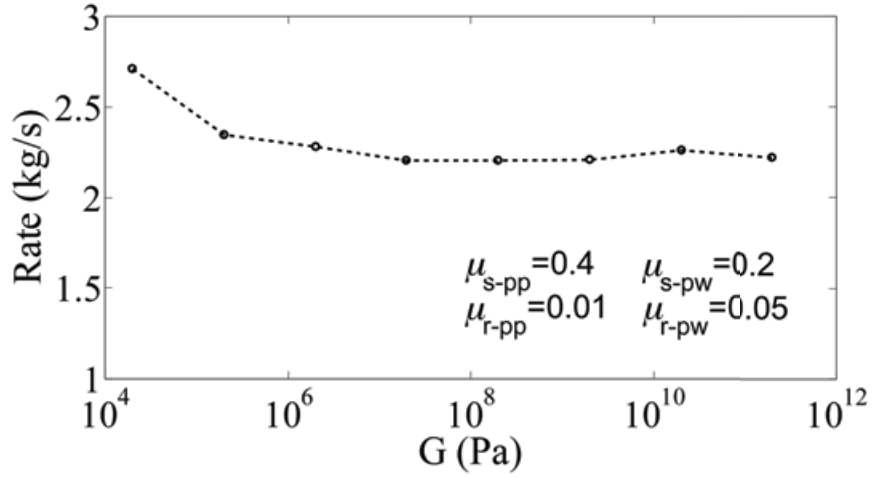


Figure 2.13: Effect of shear modulus on discharge rate.

In terms of computational time modifying the shear modulus leads to stunning decrease of the computational time, Figure 2.14, since a smaller timestep, Eq.(2.23), can be selected. Modifying particle properties to achieve reasonable simulation times is justifiable.

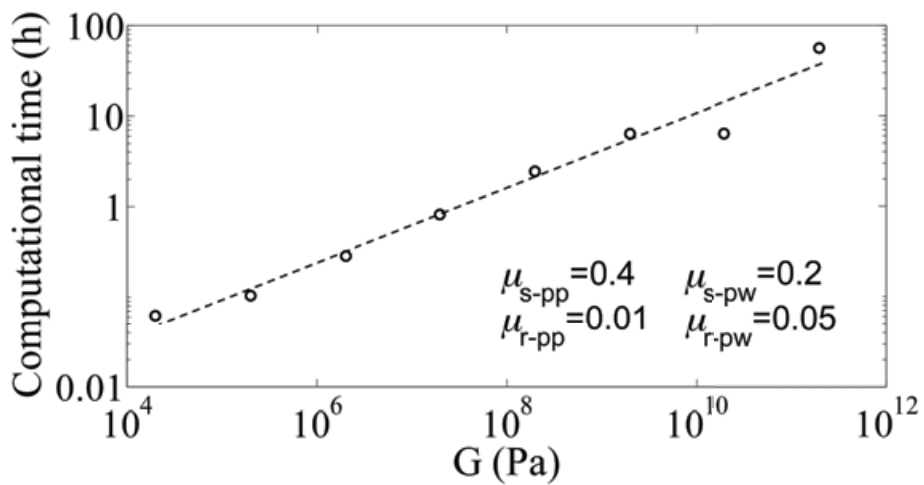


Figure 2.14: Effect of shear modulus  $G$  on computational time to model container discharge.

The effect of the other frictional parameters, particle-particle static friction  $\mu_{s-pp}$  and particle-particle rolling friction  $\mu_{r-pp}$  is investigated. The effect of such parameters on the discharge rate are illustrated in Figure 2.15 and Figure 2.16.

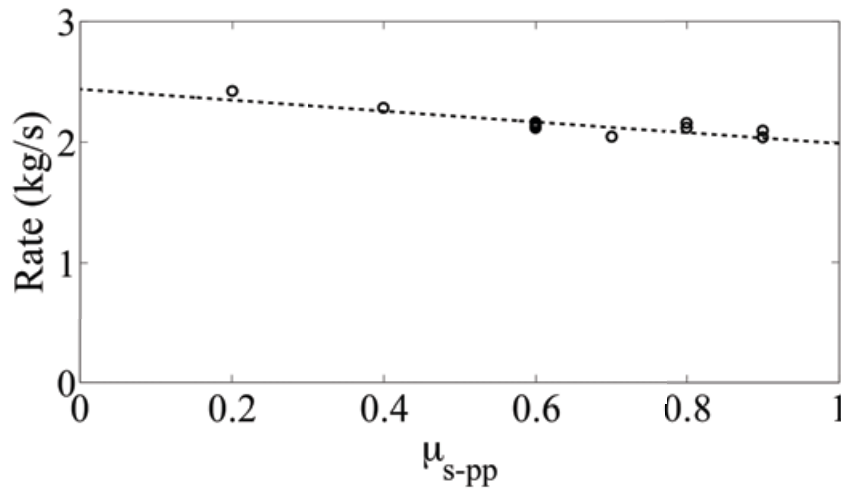


Figure 2.15: Effect of particle-particle coefficient of friction  $\mu_{s-pp}$  on the discharge rate.

From Figure 2.15 the effect of the particle-particle friction coefficient  $\mu_{s-pp}$  over a large range of values shows a small variation on the discharge rate. However in the case of the particle-particle rolling friction coefficient  $\mu_{r-pp}$ , this shows a major influence, as shown in Figure 2.16.

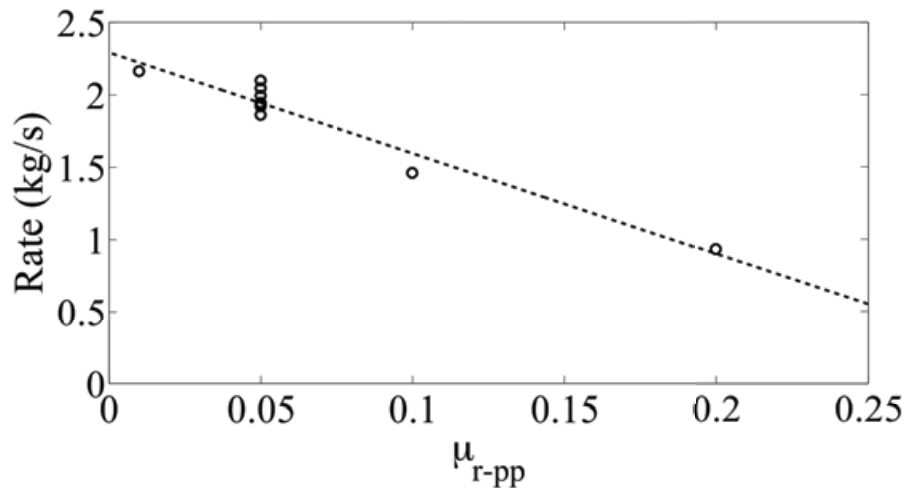


Figure 2.16: Effect of rolling particle-particle coefficient friction  $\mu_{r-pp}$  on the discharge rate.

This case clearly shows that the selection of the input parameters can be important. The question therefore is how the input parameters required for the DEM can be measured or determined.

## 2.6 Particle DEM input parameters and typical particle characterisation techniques

Considering the Hertz Mindlin contact model, employed in the EDEM software, if only gravity is considered as an external force particle characteristics and contact input parameters that must be defined are:

- Particle shape
- Particle size
- Particle density
- Particle shear modulus ( $G$ ) and Poisson's ratio ( $\nu$ )
- Coefficients of friction: static and rolling, between particle-particle and particle-wall material
- Coefficients of restitution: particle-particle and particle-wall material

Generally, for the definition of the DEM input parameters two main approaches have been attempted.

The first approach is widely employed and it involves the determination of DEM simulation parameters by comparing numerical results with experiments by input parametric studies. The influences on particle motion have been quantitatively compared between DEM numerical simulations and experiments using PEPT with radioactive tracer measurements of particle motion in a V-mixer [81] and a high-shear mixer [82] in the case of glass beads. In the DEM simulations, linear springs, dash-pots and frictional sliders were used to model the contact mechanics between the particles and between the particles and the walls. The effect of using different spring stiffness, restitution and friction coefficients was investigated. In case of the V-mixer [81] the effects of using different input parameters influences the quantitative results for comparisons between DEM and PEPT for the velocity, speed and velocity fluctuation distributions, the exchange rate between the two arms, the circulation time in the mixer, and dispersion at division and combination steps. Quantitative agreements between DEM and PEPT in the velocity and speed distributions were found using the following values for the particle–particle friction coefficient, 0.3, the particle–wall friction coefficient, 0.3, and the coefficient of restitution, 0.9. Although using similar simulation input parameters (normal stiffness =1000 and 10 000 N/m; coefficient of restitution =0.9; internal friction coefficient =0.2, 0.3 and 0.45; wall friction coefficient =0.2, 0.25 and 0.3) in the case of a high-shear mixer [82], the DEM predicted particle motion in the vertical-axis in terms of flow patterns and velocity were only qualitatively in agreement with experimental measurements results. Quantitative differences were predicted by DEM, particle velocities were approximately 50% higher than the measurement. A DEM parametric study has been carried out for the operation of a Freeman powder rheometer to understand how the measured force and torque values are

affected by key particle properties such as particle size and shape [67]. Numerical simulations based on the Hertz Mindlin contact model (EDEM commercial software) were compared with experimental results. Particle shape and material input parameters such as friction coefficients (sliding and rolling) were found to be important factors determining the force and the torque. DEM fitted input parameters for glass beads were different than those presented from literature and it was observed that good agreement with experimental results can be obtained for various combinations of particle shape, sliding and rolling friction coefficients. This suggests that since the parameters are identified by using macroscopic comparison, the parameters of the contact laws are not linked directly to measurable physical parameters of the powder material [83] and different combinations of input parameters can lead to similar results. These observations, somehow implies that the general approach behind these input parameters do not have a physical meaning but the input parameters are used as adjustable parameters.

The second approach involves the development of systematic methodology for the determination of the input parameters. Some of the necessary input parameters are easily measurable and some are not. The influence of particle size and shape is of course important as previously mentioned and their determination is relatively straightforward (ref. Chapter 3). Considering the other contact input properties, attempts have been presented in literature, but mainly regarding particles with diameters in the order of mm. A large body of work in the determination of DEM input parameters has been carried out recently in the literature especially in case of DEM simulations for pharmaceutical tablet processing operations.

Overall, it is clear that obtaining the input parameters for the real, unknown materials is a challenge especially if the particle size is small. Another important observation is that usually average values are used in DEM simulations as input parameters. However, particles can have

a size distribution and also an input parameters distribution. Hence there are some questions that need to be addressed. How or should this aspects be taken into account? Is it viable to use an average value for different discrete particles?

### 2.6.1 Examples for the determination of the coefficient of restitution

Particle-wall coefficients of restitution can be measured by using impact dropping techniques, Figure 2.17, [69,71,84,85].

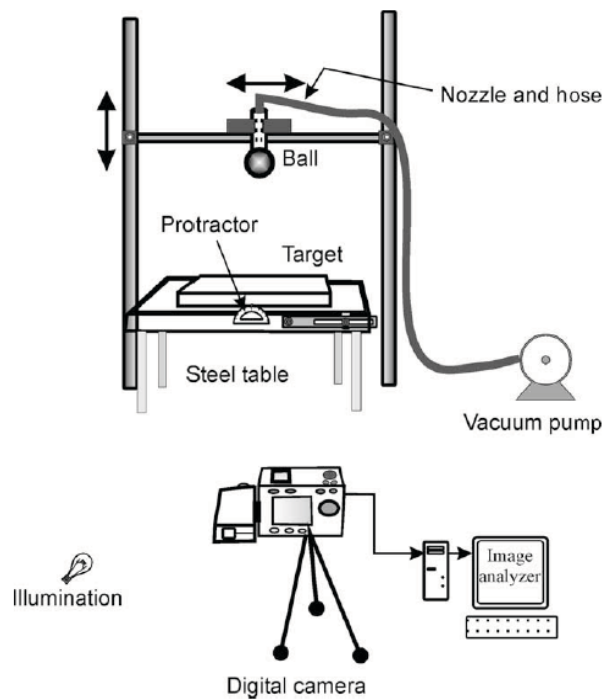


Figure 2.17: Typical experimental particle dropping setup for impact tests [69].

Parameters characterizing impacts in a quantitative way include coefficient of normal restitution, coefficient of tangential restitution, impulse ratio, and angular velocity. In the case of spherical particles the normal coefficient of restitution can be calculated as the ratio between the final velocity after the impact and the initial velocity before the impact. For non-

spherical particles, the impact results in a more complex trajectory involving particle rotation and therefore the description of such impact is more complicated [71]. Depending on the characteristic of the impacting bodies it was also found that the coefficient of restitution, in some cases, can vary quite dramatically with impact speed and therefore it can be a function of operating conditions.

Only the coefficient of restitution is needed to describe a collinear impact while the coefficient of tangential restitution and angular velocity are additionally necessary to fully describe an oblique impact. The effects of incident velocity, geometrical and material properties on the coefficient of restitution was studied in detail for a large sphere (steel ball, glass ball, malachite ball, cricket ball or billiard ball) impacting against a wall (steel or rubber) at different angles 0–60° [69]. The coefficient of normal restitution decreases slowly with an increase in incidence velocity but not as previously found from other studies in manner of  $e \propto v^{-1/4}$ . The speed ranges investigated are typical of tumbling mills, hence in this case it can be treated as a constant in DEM simulations.

The effect of formulation on the coefficient of normal restitution was investigated in case of pharmaceutical tablets as a function of material properties (elastic modulus and solid fraction) and collision conditions (type of substrate material and impact velocity) by using a drop impact tester [85]. In this case the coefficient of restitution generally increases with increasing compact solid fraction and, therefore, it was proved that is lower for more plastic collisions and higher for elastic collisions. It was also observed that the coefficient of restitution is dependent on the velocity at which the tablet impacts the substrate.

The dependency of the coefficient of restitution on impact velocity was also numerically demonstrated using finite element method (FEM) simulation by calculating the dissipated energy [86]. For impacts of an elastic spherical particle with an elastic substrate the

coefficient of restitution is a function of the thickness of the substrate material since the number of reflections of stress wave propagation vary during contact. In the case of a thin substrate the coefficient of restitution is very close to unity since in that case the number of reflections would be equal to or higher than one. For the impact with a thicker substrate there would not be any reflection and the energy is dissipated in wave propagation through the material. In this case the coefficient of restitution decreases as the impact velocity increases, indicating an increased proportion of kinetic energy is dissipated. The impact of an elastic-plastic surface involving plastic deformation the plastic deformation is the dominant energy dissipation mechanism, as the energy loss due to stress wave propagation is relatively small and hence the coefficient of restitution is found also to be dependent on the impact velocity.

It was also experimentally confirmed that for elastic-plastic materials, impact energy recovery is a function of impact velocity by using free-fall impact tests for different type of granules [87]. Therefore, the coefficient of restitution is often a function of the relative velocities of the two impacting bodies. In some cases it was found that the coefficient of restitution below a certain speed is almost constant and in other cases it varies quite dramatically with the speed and therefore it can be function of the operating conditions. However, the value of the coefficient of restitution is usually kept constant in the DEM simulations. Further, evidence of measurements of the coefficient of restitution are given for large particles and tablets with collisions against a particle-wall material substrate. Obtaining the particle-particle coefficient of restitution for small particles is still challenging since it is difficult to setup an experiment, which would achieve a perfect normal impact between two small particles.

## 2.6.2 Examples for the determination of particle mechanical properties: elastic modulus, plastic yield, particles strength and hardness

Determining input parameters regarding mechanical properties for different scales of particle size is well established and widely applied in literature. Single particle mechanical properties such as elastic properties, plastic yield, particle strength and hardness, can be calculated by application of contact mechanic theories and particle compression techniques, Figure 2.18, for large particles [71,88,89,90] or micromanipulation techniques [91,92] and indentation techniques [93,94,95] for small particles.

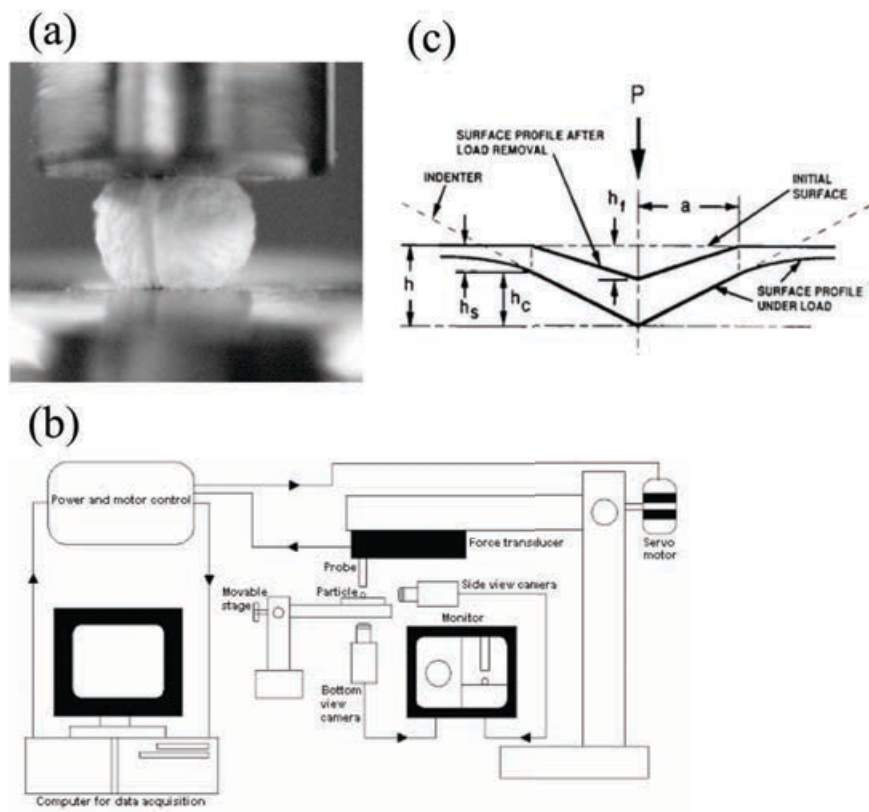


Figure 2.18: (a) Compression single sodium benzoate granule [88]. (b) Micromanipulation technique University of Birmingham (UK) [96]. (c) Schematic representation of nanonindentation [93].

Single particle compression and nanoindentation is extensively presented in Chapter 3 specifically on the determination of mechanical properties of ZSM5 zeolite particles. Single particle compression tests were used to measure the reduced elastic modulus and strength for single close-to-spherical zeolite particles assuming Hertzian contact and nanoindentation for determination of hardness and reduced elastic modulus.

With smaller scale experiments technique such as micromanipulation techniques (e.g. maximum transducer load ~100 g) can be used to determine mechanical strength and deformation behaviour for small and weak particles. Particles can be compressed between the flat end of a glass fibre (micromanipulation probe) and a glass surface (the bottom of a glass chamber containing the individual particles) by using micromanipulation techniques and application of contact mechanics theory to determine their mechanical properties. For example, small elastic-plastic pharmaceutical particles (diameter <200  $\mu\text{m}$ ) were compressed by micromanipulation to determine Young's modulus, hardness and nominal rupture stress were determined by micromanipulation [91]. Young's modulus as a function of compression speed and force relaxation were determined for even smaller viscoelastic agarose microspheres (mean diameter 15-22  $\mu\text{m}$ ) [92].

### **2.6.3 Examples for the determination of particle friction properties**

There are a limited number of studies considering the determination of friction coefficients as input parameters for DEM. For example, with the Hertz Mindlin contact model implemented into EDEM software, static and rolling friction values should be defined. The term static friction is the ratio of tangential force to the load applied in normal direction for two bodies in contact when the initial movement of contacting surfaces is being considered. The term kinetic friction (sliding friction) is the ratio of the steady-state tangential force to the load

applied in normal direction for the two surfaces already in reciprocal movement. Rolling friction relates to the interaction between two surfaces where one of them is rolling without slipping [97]. The coefficient of rolling friction accounts for the resistance of the rolling motion of a body in contact over another. This was initially implemented in DEM codes to account for the hysteric losses due to the contact between deformable materials. Now it is generally implemented to account for the rolling resistance due to the non-sphericity of particles [98].

By using a shear cell (ref. Chapter 3), the effective angle of internal friction and the internal coefficient of friction can be measured for both particle-particle and particle-wall materials. This is done by determining the yield locus generated by repetitive vertical loading of the bulk material by a normal stress and application of shear deformation. However, this is a bulk measurement under consolidation conditions and considering the definition of friction for DEM as static and rolling, the shear cell measures an amalgam of the two terms. By using such devices there is an issue as how to decouple the two and to “translate” this bulk measurement in semi-static conditions to the micro-level particle-particle or particle-wall coefficients.

Measurements for coefficient of kinetic friction and rolling friction have been developed for pharmaceutical tablets and capsules. A pin-on-disk tribometer was used to measure the kinetic inter-tablet friction and tablet substrate (metals or polymers) kinetic friction coefficients [97]. The system is depicted in Figure 2.19; the single tablet is glued on the vertical pin and is vertically loaded (5 N) against the rotating disk ( $1.0 \text{ cm s}^{-1}$ ). The shear force acting on the pin created through the sliding contact of the tablet with the disk is measured and it is used to calculate the coefficient of kinetic friction for any combination of materials.

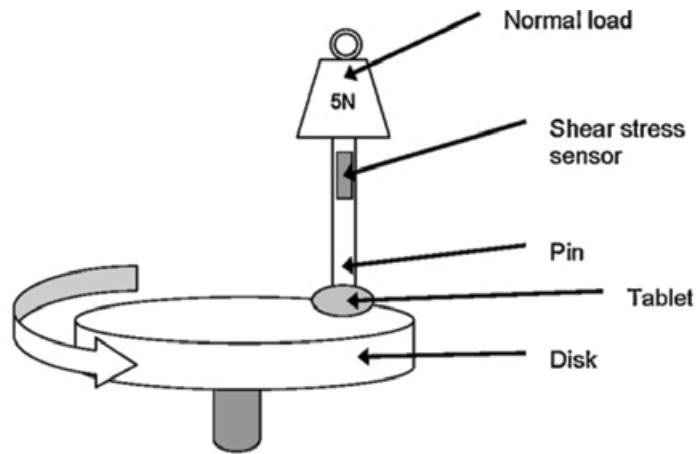


Figure 2.19: Schematic Pin-on-disk tribometer [97].

An experimental technique was developed for the determination of the coefficient of rolling friction for relatively large pharmaceutical tablets and other materials, such as glass beads and steel ball bearings [98]. The method is based on the conservation of energy of a body that rolls down an inclined plane onto a flat surface, Figure 2.20; the coefficient of rolling friction is calculated as the ratio ( $\mu_r = h/d$ ) between the initial body height  $h$  (potential energy) and distance travelled  $d$  (distance travelled) as result that the potential energy of the system at A is equal to the kinetic energy at B plus the losses from rolling A to B ( $loss_{AB}$ ).

$$mgh = \frac{1}{2}mv_B^2 + loss_{AB} \quad (2.14)$$



Figure 2.20: Setup for measuring coefficient of rolling friction for pharmaceutical tablets using a slope of height  $h$  and measuring the distance  $d$  travelled on a flat plane [98].

A more sophisticated tribological technique such as Atomic Force Microscopy (AFM), Figure 2.21, can be used to measure friction properties such as sliding and rolling frictions between small particles (micro and nano particles) and substrate materials.

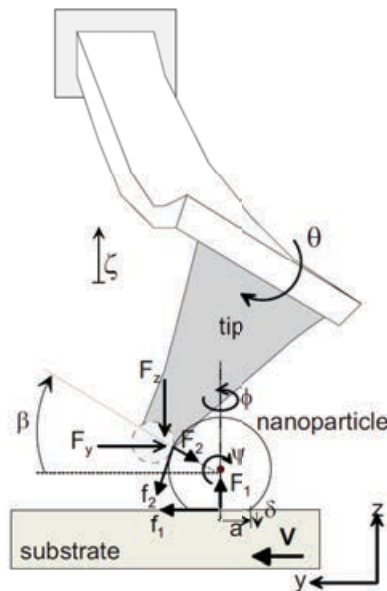


Figure 2.21: Nanotribological AFM measurements for friction [99].

For example, nano-particles (500 nm gold-coated latex particles) can be pushed over a substrate (silicon) by using a sharp AFM probe whose deflection measurements can give direct information regarding friction: sliding and rolling [99].

#### 2.6.4 Comparison of the magnitude of interparticle forces for small particles

From this review and examples of particle measurements it is clear that there are some issues in setting up a methodology or development of suitable equipment to directly measure DEM input parameters that need to be chosen in accordance with the contact model employed. A few examples are reported regarding the measurement of coefficient of restitution and frictional properties. For large particles or tablets and usually for the interaction between particle and

wall material. The set-up of such experiments is relatively straightforward. For small particles, however, the determination and setup of an experiment to determine particle-particle impact or particle-particle frictional properties is difficult since measurements on micro or nano-scale are difficult.

In addition, whereas gravity is usually the dominant force acting on the system in DEM simulations comprising of large particles, with small particles like those usually employed in real industrial operations, other forces acting at the microscopic level may affect the system's behaviour.

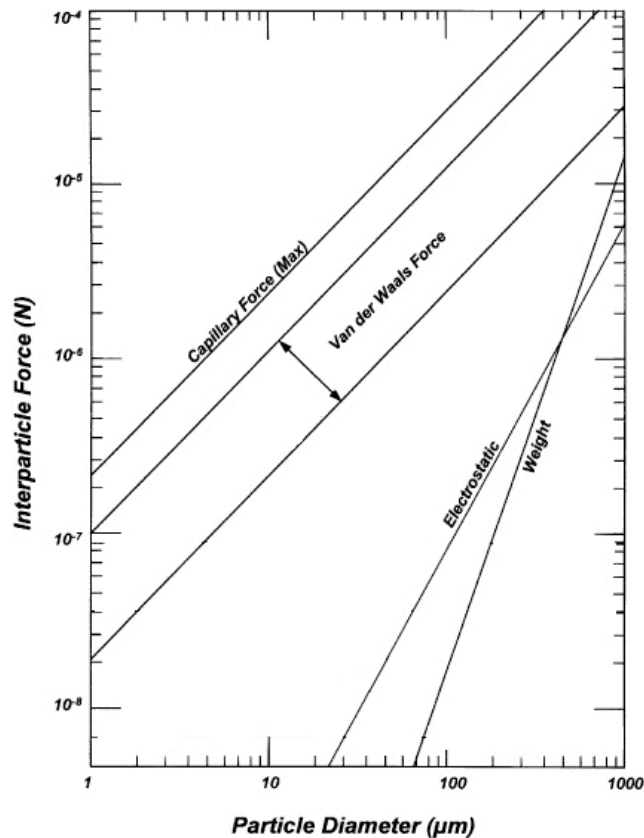


Figure 2.22: Size dependency of inter-particles interaction force such as liquid bridges, Van der Waals, Coulombic and gravity forces for two equally sized spheres (in air). Redrawn from [100].

Typical examples of inter-particle forces acting at the microscopic level are given as follows [4,57]:

- Van der Waals forces
- Liquid bridge forces
- Electrostatic Coulombic forces

A comparison of the theoretical values for the magnitude of these forces as a function of particle size is shown in Figure 2.22 along with the gravitational force (weight) for a contact between equal spheres (in air) [100], for particles closer to 1 mm size these values may not be representing the practical cases. However, It can be seen that for particles smaller than 1 mm the magnitude of the capillary, Van der Waals and electrostatic forces can be considerably higher than gravitational forces. Hence, for system considering small particles (diameter <1 mm) more complex contact models including these interparticle forces and definition of correct input parameters for the model are necessary.

## **2.7 Conclusion**

DEM is still in its infancy when compared to other modelling tools such as Computational Fluid Dynamics (CFD). However, the development of DEM and its increasing applications are following a similar pattern to those previously seen with CFD. Early developments of CFD occurred during the late 1950s and throughout the 1960s. This resulted in the innovation of new unique computational resources and increased interest from academic groups globally as they became aware of the potential benefit of applying the technique to a large number of applications. CFD was then used in industry from the 1980s, and its use continues to rise with increasing availability of computational resources. Similarly, thanks to advancing in computational power, DEM is becoming more and more accessible to academia and to

industry. At present, on commercially available desktop computers, simulations of up to a million particles can be performed. Only on very large clusters, the trajectories of millions of particles can be computed.

The aim of the present chapter is to provide an overview on discrete element method DEM techniques. Use of this modelling technique is expanding and it is being exploited in many applications. Despite this, as extensively reported and demonstrated, there are still some limitations that need to be addressed to use DEM as a possible full predictive tool for modelling real scale industrial systems. Some of these issues are highlighted as follows:

- DEM can be used to describe granular problems considering each particle as a discrete discontinuous element within the system. DEM simulations are widely reported in cases of large-scale particles. Limitations on the particle size are mainly due to computational limitations as results of the high number of particles to be considered resulting in a higher number of calculations necessary. In addition the computational effort increases dramatically with the decrease of particle size due to the smaller timestep, which results in an increased number of iterations necessary.
- Considering the limitation with the size dependency of some problems there is still a question on the formulation of the local constitutive contact laws to account for some of the important interparticle effects that could arise in case of small-scale particles.
- There are some limitations regarding the representation of particles with simplified spherical discrete elements. Different approaches using representation of complex shapes are being developed, however there is still a need of developing and validating relationships between the local constitutive laws depending on the shapes of the discrete elements. By using a multiple sphere approach there is a limitation on computational effort due to the increased complexity due to the large number of spheres considered in the

simulations.

- Clear limitations regarding the determination or the choice of the input parameters for the simulations in case of different materials still make DEM a tool for simplified systems which user consider “model” particles such as for example glass bead. A methodology for gathering the input parameters is not clearly defined especially in case of small particles.

Regardless of the issues reported above, this modelling technique for granular material is growing considerably, mainly in research but also for industry. Many DEM modelling results have shown that this kind of simulations reproduces well experimental results, giving new understanding on the behaviour of granular systems. This is mainly true for simpler systems that consider large spherical particles. However, new developments and advancements for both computer hardware and DEM software are resulting in a continuously more extensive application of this modelling technique for the exploration of more complex applications.

## 2.8 References

- [1] P.A. Cundall, O.D.L. Strack, A Discrete Numerical Model for Granular Assemblies, *Géotechnique*, **29** (1979), pp. 47-65.
- [2] A.W. Roberts, Particle technology - reflections and horizons: an engineering perspective. *Trans. IChemE* **76 A** (1998), pp. 775–796.
- [3] A. Drescher, G. de Josselin de Jong, Photoelastic verification of a mechanical model for the flow of a granular material, *Journal of the Mechanics and Physics of Solids* **20** (1972), pp. 337-340.
- [4] H.P. Zhu, Z.Y. Zhou, R.Y. Yang and A.B. Yu, Discrete particle simulation of particulate systems: Theoretical developments, *Chemical Engineering Science* **62** (2007), pp. 3378-3396.
- [5] P.W. Cleary, DEM prediction of industrial and geophysical particle flows, *Particuology* **8** (2010), pp. 106-118.
- [6] N. Djordjevic, F. N. Shi, R. D. Morrison, Applying discrete element modelling to vertical and horizontal shaft impact crushers, *Minerals Engineering* **16** (2003), pp. 983-991.
- [7] H. Mori, H. Mio, J. Kano, F. Saito, Ball mill simulation in wet grinding using a tumbling mill and its correlation to grinding rate. *Powder Technology* **143-144** (2004), pp. 230-239.
- [8] D. Gudin, R. Turczyn, H. Mio, J. Kano, F. Saito, Simulation of the movement of beads by the DEM with respect to the wet grinding process, *AIChE Journal* **10** (2006), pp. 3421–3426.
- [9] N. Djordjevic, R. Morrison, B. Loveday, P. Cleary, Modelling comminution patterns within a pilot scale AG/SAG mill, *Minerals Engineering* **19** (2006), pp. 1505-1516.

- [10] M.S. Powell, I. Govender, A.T. McBride, Applying DEM outputs to the unified comminution model, *Minerals Engineering* **21** (2008), pp. 744-750.
- [11] L.M. Tavares, R.M. de Carvalho, Modeling breakage rates of coarse particles in ball mills, *Minerals Engineering* **22** (2009), pp. 650-659.
- [12] A. Hassanpour, C.C. Kwan, B.H. Ng, N. Rahmanian, Y.L. Ding, S.J. Antony, X.D. Jia, M. Ghadiri, Effect of granulation scale-up on the strength of granules, *Powder Technology* **189** (2009), pp. 304-312.
- [13] J.A. Gantt, E.P. Gatzke, High-shear granulation modeling using a discrete element simulation approach, *Powder Technology*, **156** (2005), pp. 195-212.
- [14] H. Nakamura, Y. Miyazaki, Y. Sato, T. Iwasaki, S. Watano, Numerical analysis of similarities of particle behavior in high shear mixer granulators with different vessel sizes, *Advanced Powder Technology* **20** (2009), pp 493-501.
- [15] P.W. Cleary, M.L. Sawley, DEM modelling of industrial granular flows: 3D case studies and the effect of particle shape on hopper discharge, *Applied Mathematical Modelling* **26** (2003), pp. 89-111.
- [16] W.R. Ketterhagen, J.S. Curtis, C.R. Wassgren, B.C. Hancock, Predicting the flow mode from hoppers using the discrete element method, *Powder Technology* **195** (2009), pp. 1-10.
- [17] A. Anand, J.S. Curtis, C.R. Wassgren, B.C. Hancock, W.R. Ketterhagen, Predicting discharge dynamics from a rectangular hopper using the discrete element method (DEM), *Chemical Engineering Science* **63** (2008), pp. 5821-5830.
- [18] W.R. Ketterhagen, B.C. Hancock, Optimizing the design of eccentric feed hoppers for tablet presses using DEM, *Computers and Chemical Engineering* **34** (2010), pp. 1072-1081.

- [19] C.-Y. Wu, DEM simulations of die filling during pharmaceutical tableting, *Particuology* **6** (2008), pp. 412-418.
- [20] Y. Guo, C.-Y. Wu, K.D. Kafui, C. Thornton, Numerical analysis of density-induced segregation during die filling, *Powder Technology* **197** (2010), pp. 111-119.
- [21] D. Kafui, C. Thornton, Agglomerate fracture/fragmentation, In: Proc. 1st International Particle Technology Forum, AIChE, Denver, Colorado (1994), pp. 184-189.
- [22] C. Thornton, K.K. Yin, M.J. Adams, Numerical simulation of the impact fracture and fragmentation of agglomerates, *Journal of Physics D: Applied Physics*, **29** (1996), pp. 424-435.
- [23] Z. Ning, R. Boerefijn, M. Ghadiri, C. Thornton, Distinct element simulation of impact breakage of lactose agglomerates, *Advanced Powder Technology* **8** (1997), pp. 15-37.
- [24] L. Liu, K.D. Kafui, C. Thornton, Impact breakage of spherical, cuboidal and cylindrical agglomerates, *Powder Technology* **199** (2010), pp. 189-196.
- [25] H.G. Matuttis, S. Luding, H.J. Herrmann, Discrete element simulations of dense packings and heaps made of spherical and non-spherical particles, *Powder Technology* **109** (2000), pp. 278-292.
- [26] Z.P. Zhang, L.F. Liu, Y.D. Yuan, A.B. Yu, A simulation study of the effects of dynamic variables on the packing of spheres, *Powder Technology* **116** (2001), pp. 23-32.
- [27] M. Dutt, B.C. Hancock, A.C. Bentham and J.A. Elliott, An implementation of granular dynamics for simulating frictional elastic particles based on the DL\_POLY code, *Computer Physics Communications* **166** (2005), pp. 26-44.
- [28] K. Lochmann, L. Oger, D. Stoyan, Statistical analysis of random sphere packings with variable radius distribution, *Solid state science* **8** (2006), pp. 1397-1413.

- [29] X. Fu, M. Dutt, A.C. Bentham, B.C. Hancock, R.E. Cameron, J.A. Elliott, Investigation of particle packing in model pharmaceutical powders using X-ray microtomography and discrete element method, *Powder Technology* **167** (2006), pp. 134-140.
- [30] T. Aste, T. Di Matteo, A. Tordesillas, Granular and Complex Materials, *World Scientific Lecture Notes in Complex Systems* **8** (2007).
- [31] A. Samimi, A. Hassanpour, M. Ghadiri, Single and bulk compressions of soft granules: Experimental study and DEM evaluation, *Chemical Engineering Science* **60** (2005), pp. 3993-4004.
- [32] A. Mehrotra, B. Chaudhuri, A. Faqih, M.S. Tomassone, F.J. Muzzio, A modeling approach for understanding effects of powder flow properties on tablet weight variability, *Powder Technology* **188** (2009), pp. 295-300.
- [33] A. Hassanpour, M. Ghadiri, Distinct element analysis and experimental evaluation of the Heckel analysis of bulk powder compression, *Powder Technology* **141** (2004), pp. 251-261.
- [34] Y.Y. Foo, Y. Sheng, B.J. Briscoe, An experimental and numerical study of the compaction of alumina agglomerates, *International Journal of Solids and Structures* **41** (2004), pp. 5929-5943.
- [35] D. Markauskas, R. Kacianauskas, Compacting of particles for biaxial compression test by discrete element method, *Journal of Civil Engineering and Management* **12** (2006), pp. 153-161.
- [36] P.A. Moysey, M.R. Thompson, Modelling the solids inflow and solids conveying of single-screw extruders using the discrete element method, *Powder Technology* **153** (2005), pp. 95-107.

- [37] P.J. Owen, P.W. Cleary, Prediction of screw conveyor performance using the Discrete Element Method (DEM), *Powder Technology* **193** (2009), pp. 274-288.
- [38] Y. Muguruma, T. Tanaka, S. Kawatake, Y. Tsuji, Discrete particle simulation of a rotary vessel mixer with baffles, *Powder Technology* **93** (1997), pp. 261-266.
- [39] M. Kwapinska, G. Saage, E. Tsotsas, Mixing of particles in rotary drums: A comparison of discrete element simulations with experimental results and penetration models for thermal processes, *Powder Technology* **161** (2006), pp. 69-78.
- [40] A. Sarkara, C.R. Wassgren, Simulation of a continuous granular mixer: Effect of operating conditions on flow and mixing, *Chemical Engineering Science* **64** (2009), pp. 2672-2682.
- [41] Y. Xu, C. Xu, Z. Zhou, J. Du, D. Hu, 2D DEM simulation of particle mixing in rotating drum: A parametric study, *Particuology* **8** (2010), pp. 141-149.
- [42] M. Moakher, T. Shinbrot, F. J. Muzzio, Experimentally validated computations of flow, mixing and segregation of non-cohesive grains in 3D tumbling blenders, *Powder Technology* **109** (2000), pp. 58-71.
- [43] H.P. Kuo, Numerical and experimental studies in the mixing of particulate material, PhD thesis, School of Chemical Engineering, The University of Birmingham UK (2001).
- [44] M. Lemieux, G. Léonard, J. Doucet, L.-A. Leclaire, F. Viens, J. Chaouki, F. Bertrand Bertrand, Large-scale numerical investigation of solids mixing in a V-blender using the discrete element method, *Powder Technology* **181** (2008), pp. 205-216.
- [45] D. Tabor, The Mechanism of Rolling Friction. II. The Elastic Range, *Proceedings of the Royal Society London A* **229** (1955), pp. 198-220.
- [46] K.L. Johnson, Rolling resistance of a rigid cylinder on an elastic-plastic surface,

- International Journal of Mechanical Sciences* **14** (1972), pp. 145-146.
- [47] Y.C. Zhou, B.D. Wright, R.Y. Yang, B.H. Xu, A.B. Yu, Rolling friction in the dynamic simulation of sandpile formation, *Physica A*. **269** (1999), pp. 536–553.
- [48] R.Y. Yang, R.P. Zou, A.B. Yu, Microdynamic analysis of particle flow in a horizontal rotating drum, *Powder Technology* **130** (2003), pp. 138-146.
- [49] H. Kruggel-Emden, F. Stepanek, A. Munjiza, A study on adjusted contact force laws for accelerated large scale discrete element simulations, *Particuology* **8** (2010), pp. 161-175.
- [50] A. Di Renzo, F.P. Di Maio, Comparison of contact-force models for the simulation of collisions in DEM-based granular flow codes, *Chemical Engineering Science* **59** (2004), pp. 525-541.
- [51] A. Di Renzo, F.P. Di Maio, An improved integral non-linear model for the contact of particles in distinct element simulations, *Chemical Engineering Science* **60** (2005), pp. 1303-1312.
- [52] B.K. Mishra, A review of computer simulation of tumbling mills by the discrete element method: Part I—contact mechanics, *International Journal of Mineral Processing* **71** (2003), pp. 73-93.
- [53] F. Bertrand, L.-A. Leclaire, G. Levecque, DEM-based models for the mixing of granular materials, *Chemical Engineering Science* **60** (2005), pp. 2517-2531.
- [54] M. Oda, K. Iwashita, An Introduction Mechanics of Granular Materials, *A.A. Balkema*, Rotterdam, 1999.
- [55] Y. Tsuji, T. Tanaka, T. Ishida, Lagrangian numerical-simulation of plug flow of cohesionless particles in a horizontal pipe, *Powder Technology* **71** (1992), pp. 239-250.

- [56] Y. Tsuji, T. Kawaguchi, T. Tanaka, Discrete particle simulation of two-dimensional fluidized bed, *Powder Technology* **77** (1993), pp. 79-87.
- [57] J.P.K. Seville, U. Tuzun, R. Cliff, Processing of particulate solids, first ed., *Blackie academic & professional*, London UK, (1997).
- [58] EDEM user guide, DEM Solutions Limited, Edinburgh, UK. ([www.dem-solutions.com](http://www.dem-solutions.com)).
- [59] A.O. Raji, J.F. Favier, Model for the deformation in agricultural and food particulate materials under bulk compressive loading using discrete element method. I: Theory, model development and validation, *Journal of Food Engineering* **64** (2004), pp. 359-371.
- [60] H. Hertz, Ueber die Berührung fester elastischer Koerper, *Journal für die reine und angewandte Mathematik* **92** (1881), pp. 156-171.
- [61] R.D. Mindlin, Compliance of elastic bodies in contact, *Journal of Applied Mechanics (Trans. ASME)* **71** (1949), pp. 259–268.
- [62] S.-Y. Lim, Particle dynamics in rotating cylinders, PhD thesis, Department of Chemical engineering University of Cambridge UK (2002).
- [63] F.V. Donzé, V. Richefeu, S.-A. Magnier, Advances in Discrete Element Method applied to Soil, Rock and Concrete Mechanics, *State of the art of geotechnical engineering Electronic Journal of Geotechnical Engineering* **8** (2009), pp. 1-44.
- [64] J.F. Favier , M.H. Abbaspour-Fard, A.O. Raji, M. Kremmer, Shape Representation of Axi –Symmetrical Arbitrary Particles in Discrete Element Simulation Using Multi-Element Model Particles, *Engineering Computations*, **16** (1999), pp. 467-480.
- [65] H. Kruggel-Emden, S. Rickelt, S. Wirtz, V. Scherer, A study on the validity of the multi-sphere Discrete Element Method, *Powder Technology* **188** (2008), pp. 153-165.

- [66] M. Kodam, R. Bharadwaj, J. Curtis, B. Hancock, C. Wassgren, Cylindrical object contact detection for use in discrete element method simulations. Part I – Contact detection algorithms, *Chemical Engineering Science* **65** (2010), pp. 5852-5862.
- [67] R. Bharadwaj, W.R. Ketterhagen, B.C. Hancock, Discrete element simulation study of a Freeman powder rheometer, *Chemical Engineering Science* **65** (2010), pp. 5747-5756.
- [68] Z. Asaf, D. Rubinstein, I. Shmulevich, Determination of discrete element model parameters required for soil tillage, *Soil and Tillage Research* **92** (2007), pp. 227-242.
- [69] H. Dong, M. H. Moys, Measurement of impact behaviour between balls and walls in grinding mills, *Minerals Engineering* **16** (2003), pp. 543-550.
- [70] Y. Li, Y. Xu, C. Thornton, A comparison of discrete element simulations and experiments for ‘sandpiles’ composed of spherical particles, *Powder Technology* **160** (2005), pp. 219-228.
- [71] Y.-C. Chung, J.Y. Ooi, A study of influence of gravity on bulk behaviour of particulate solid, *Particuology* **6** (2008), pp. 467-474.
- [72] S.J. Roskilly, E.A. Colbourn, O. Alli, D. Williams, K.A. Paul, E.H. Welfare, P.A. Trusty, Investigating the effect of shape on particle segregation using a Monte Carlo simulation, *Powder Technology* **203** (2010), pp. 211-222.
- [73] M.J. Metzger, B. Remy, B.J. Glasser, All the Brazil nuts are not on top: Vibration induced granular size segregation of binary, ternary and multi-sized mixtures, *Powder Technology*, *In Press, Corrected Proof, Available online 3 September 2010*.
- [74] P.W. Cleary, M.L. Sawley, DEM modelling of industrial granular flows: 3D case studies and the effect of particle shape on hopper discharge, *Applied Mathematical Modelling* **26** (2002), pp. 89-111.

- [75] J. Li, P. A. Langston, C. Webb, T. Dyakowski, Flow of sphero-disc particles in rectangular hoppers-a DEM and experimental comparison in 3D, *Chemical Engineering Science* **59** (2004), pp. 5917-5929.
- [76] K. Johanson, Effect of particle shape on unconfined yield strength, *Powder technology* **193** (2009), pp. 246-251.
- [77] T. Miyajima, K.-I. Yamamoto, M. Sugimoto, Effect of particle shape on packing properties during tapping, *Advanced Powder Technology* **12** (2001), pp. 117-134.
- [78] J.F. Favier, M.H. Abbaspour-Fard, M. Remmer, A.O. Raji, Shape representation of axisymmetrical non-spherical particles in discrete element simulation using multi-element model particles *Engineering Computation* **16** (1999) pp. 467-480.
- [79] R.G. Munro, Evaluated material properties for high purity (99.5% or higher) alpha-Al<sub>2</sub>O<sub>3</sub>, *Journal American Ceramic Society* **80** (1997), pp. 1919-1928.
- [80] K.F. Malone, B.H. Xu, Determination of contact parameters for discrete element method simulations of granular systems, *Particuology* **6** (2008), pp. 521-528.
- [81] H.P. Kuo, P.C. Knight, D.J. Parker, Y. Tsuji, M.J. Adams, J.P.K. Seville, The influence of DEM simulation parameters on the particle behaviour in a V-mixer, *Chemical Engineering Science* **57** (2002), pp. 3621-3638.
- [82] H.P. Kuo, P.C. Knight, D.J. Parker, M.J. Adams, J.P.K. Seville, Discrete element simulations of a high-shear mixer, *Advanced Powder Technology* **15** (2004), pp. 297-309.
- [83] P.Pizette, C.L. Martin, , G. Delette, P. Sornay, F. Sans, Compaction of aggregated ceramic powders: From contact laws to fracture and yield surfaces, *Powder Technology* **198** (2010), pp. 240-250.

- [84] S.F. Foerster, M.Y. Louge, H. Chan, Measurements of the collision properties of small spheres, *Physics of Fluids* **6** (1994), pp.1108-1115.
- [85] R. Bharadwaj, C. Smith, B.C. Hancock, The coefficient of restitution of some pharmaceutical tablets/compacts, *International Journal of Pharmaceutics* **402** (2010), pp. 50-56.
- [86] C.-Y. Wu, L.-Y. Li, C. Thornton, Energy dissipation during normal impact of elastic and elastic–plastic spheres, *International Journal of Impact Engineering* **32** (2005), pp. 593-604.
- [87] C. Mangwandi, Y.S. Cheong, M.J. Adams, M.J. Hounslow, A.D. Salman, The coefficient of restitution of different representative types of granules, *Chemical Engineering Science* **62**, (2007), pp. 437-450.
- [88] R. Pitchumani, O. Zhupanska, G.M.H. Meesters, B. Scarlett, Measurement and characterization of particle strength using a new robotic compression tester, *Powder Technology* **143-144** (2004), pp. 56-64.
- [89] S. Antonyuk, J. Tomas, S. Heinrich, L. Mörl, Breakage behaviour of spherical granulates by compression, *Chemical Engineering Science* **60** (2005), pp. 4031-4044.
- [90] A. Samimi, A. Hassanpour, M. Ghadiri, Single and bulk compressions of soft granules: Experimental study and DEM evaluation, *Chemical Engineering Science* **60** (2005), pp. 3993-4004.
- [91] S.F. Yap, M.J. Adams, J.P.K. Seville, Z. Zhang, Single and bulk compression of pharmaceutical excipients: Evaluation of mechanical properties, *Powder Technology* **185** (2008), pp. 1-10.
- [92] Y. Yan, Z. Zhang, J.R. Stokes, Q.-Z. Zhou, G.-H. Ma, M.J. Adams, Mechanical characterization of agarose micro-particles with a narrow size distribution, *Powder*

- Technology* **192** (2009), pp. 122-130.
- [93] R. Roop Kumar, M. Wang, Modulus and hardness evaluations of sintered bioceramic powders and functionally graded bioactive composites by nano-indentation technique, *Materials Science and Engineering* **A338** (2002), pp. 230-236.
- [94] M. Skrzypczak, C. Guerret-Piecourt, S. Bec, J.-L. Loubet, O. Guerret, Use of a nanoindentation fatigue test to characterize the ductile–brittle transition, *Journal of the European Ceramic Society* **29** (2009), pp. 1021-1028.
- [95] M. Meier, E. John, D. Wieckhusen, W. Wirth, W. Peukert, Influence of mechanical properties on impact fracture: Prediction of the milling behaviour of pharmaceutical powders by Nanoindentation, *Powder Technology* **188** (2009), pp. 301-313.
- [96] S.F. Yap, M. Adams, J. Seville, Z. Zhang, Understanding the mechanical properties of single micro-particles and their compaction behaviour, *China Particuology* **4** (2006), pp. 35-40.
- [97] B.C. Hancock, N. Mojica, K. St.John-Green, J.A. Elliott, R. Bharadwaj, An investigation into the kinetic (sliding) friction of some tablets and capsules, *International Journal of Pharmaceutics* **384** (2010), pp. 39-45.
- [98] W.R. Ketterhagen, R. Bharadwaj, B.C. Hancock, The coefficient of rolling resistance (CoRR) of some pharmaceutical tablets, *International Journal of Pharmaceutics* **392** (2010), pp. 107-110.
- [99] B. Sumer, M. Sitti, Rolling and Spinning Friction Characterization of Fine Particles using Lateral Force Microscopy based Contact Pushing, *Journal of Adhesion Science and Technology* **22** (2008), pp. 481-506.
- [100] J.P.K. Seville, C.D. Willett, P.C. Knight, Interparticle forces in fluidisation: a review, *Powder Technology* **113** (2000), pp. 261-268.

## Chapter 3

### Mechanical properties of ZSM5 zeolite particles

*In Chapter 2 it was illustrated that there is no clear, defined and unified methodology to measure or to define the input parameters for the DEM model. In the literature there are numerous examples of different techniques for measuring particle material and particle mechanical properties but only a few examples are given with the aim of defining the DEM input parameters. This is mainly due to the difficulty of setting up experimental techniques, in particular in the case of small particles, or to directly relate the parameters obtained with such techniques with the definition of the input parameters required for DEM models.*

*In this chapter some of the typical mechanical properties for a widely used catalyst support material, ZSM5 zeolite particles, have been measured. Particle size distribution and shape of the powders were determined by laser diffraction, and Scanning Electron Microscopy (SEM) confirming the spherical shape for the spray dried particles. The high flowability of the material was assessed by typical flowability methods such as the Hausner ratio and the Carr's index. This was confirmed by bulk measurements of particle-particle and particle-wall material internal friction parameters using a Schulze shear cell. A single particle compression technique was used for characterising individual particle mechanical properties such as elastic modulus and strength by applying the Hertz contact mechanic theory. Nanoindentation was employed to measure particle surface mechanical properties such as hardness and elastic modulus. The two methods give different mechanical properties in terms*

*of reduced elastic modulus showing the mechanical non-homogeneity between the surface of the particle and the entire particle. Particle bulk compression was used to show the influence of single particle mechanical properties on bulk compression behaviour and the typical Heckel and Kawakita models showed to be unsuitable for the bulk compression in case of zeolite particles. The predicted Adams model parameter, apparent strength for the single particles, however, was in good agreement with the single particle strength determined by single particle compression test.*

### 3.1 Introduction: ZSM5 zeolite particles

A spray dried ZSM5 zeolite has been chosen in this work. Zeolite material is widely used in the catalyst industry. During manufacture and use the material goes through a series of mechanical operations which comprise for example blending and formation of final product by granulation, extrusion or compaction as shown in Figure 3.1. During such operations the particles are subjected to high stress and shear forces and different material properties play a different role during such operations. The zeolite particles have a skeletal material density (this is determined by considering the volume within the particle envelope minus volume of open pores) of about  $2.41 \text{ g cm}^{-3}$ , according to helium pycnometry and an average interparticle pore size of  $40 \text{ \AA}$  as measured by mercury porosimetry.



Figure 3.1: Picture of tablets formed by using zeolite material.

### 3.2 Particle size and shape

Different techniques can be used to gather information regarding particles size and shape for example, *scanning electron microscopy* (SEM) [1,2,3], *laser light diffraction* [4,5,6], *sedimentation* [7,8,9], *transmission electron microscopy* (TEM) [10,11] and *atomic force microscopy* (AFM) [12,13,14].

Usually particles are complex three-dimensional objects for which shape characterisation can be difficult. For most regular shapes at least three parameters should be given for a complete description: length, breadth and height. Only for a perfect sphere a single dimension, the diameter, is sufficient to describe the shape. Therefore, it is generally not possible to relate the particle size to a single dimension and a single measurement technique. However, most sizing techniques intrinsically assume that the materials being measured are perfect spheres.

In this work, the spray dried zeolite particle size distribution has been determined by laser scattering technique. Particle morphology has been characterized by scanning electron microscopy (SEM). In the following sections, the basic principles of these two techniques are described.

### **3.2.1 Scanning Electric Microscopy (SEM)**

Grain shape is one of the key factors affecting the flow properties of granular material. Therefore, the description of particle shape is an essential parameter that has to be taken in account to achieve realistic DEM simulations and representation of true particle flow behaviour. *Scanning electron microscopy* (SEM) is an imaging technique that can be used to record high-resolution images of a large number of individual particles. The technique can provide information regarding: size, shape and surface morphology, which are critical parameters for powder processing and development. SEM can reveal high levels of detail and complexity for micro-objects and micro-structures. In literature 90% of SEM applications are used to image surface topography [15]. An overview of electron microscopy methods employed for analysis of individual particles have previously been reported [16,17,18].

Attention must, however, be exercised when using image analysis to determine particle morphology since particles are three dimensional and micrograph analyses only give a two

dimensional representation of the particles and this simplification can lead to errors since the particle diameter is derived from a 2-dimensional projection. Different shape descriptors have been presented in literature to describe particle morphology based on image analysis. For example agglomerates of particles have been described by aspect ratio, clumpiness, concavity index, fractal dimension, heterogeneity, perimeter ratio and roundness [19]. Image analysis of SEM photographs have been used to quantify the morphology of sand grains by using three lower order complex Fourier shape descriptors (elongation, triangularity and squareness) whilst an additional descriptor, denoted “Asymmetry” provided a measure of particle irregularity [20]. Particles shapes were also characterised using a set of images of the particle projections in three mutually perpendicular directions and the circularity of the particles for each projection was used as descriptor for the particle shape. In addition a computer-based image analysis system was used to embed the particle shape into a DEM model for computer simulation studies [21].

SEM utilises a finely focused electron incident beam of high energy to create the magnified images instead of light waves that are used in optical microscopes. A schematic image showing the principle of SEM is shown in Figure 3.2. The electron beam is created from a filament loop, usually made from tungsten, which functions as the cathode. A voltage is applied to the loop and the filament is heated to a sufficient temperature to cause the release of a stream of electrons. The anode, which is positive with respect to the filament, forms powerful attractive forces causing the beam to travel downward through a series of magnetic lenses designed to focus the electron beam to a very fine spot on the sample surface. The interactions between electrons and atoms on the sample surface are used to produce the analytical signals for imaging reconstruction. The electron beam is passed across the surface of the specimen in an ordered pattern.

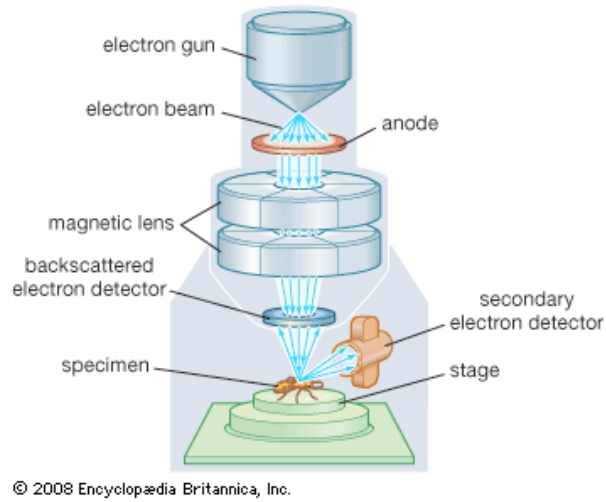


Figure 3.2: Schematic representation of SEM apparatus [22].

The silhouette image of the particles obtained by SEM imaging, shown in Figure 3.3, was used in this study to determine the sphericity of the zeolite particles. The majority of the spray dried powder particles had spherical or near-spherical morphology.

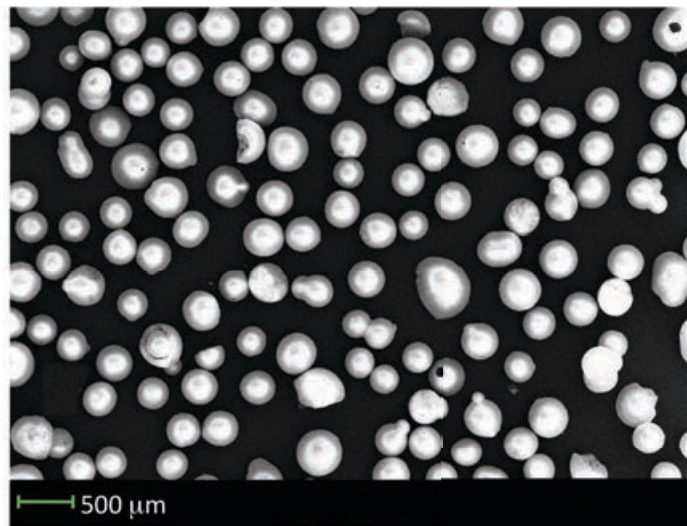


Figure 3.3: SEM images of spray dried ZSM5 zeolite.

The sphericity of a particle can be determined from SEM images by image analysis. The mean sphericity  $S$  of the sample of particle is calculated using Eq.(3.1), for each particle the projected area is used to represent the 3-dimensional particle shape. A perfect circle has sphericity of one while a very irregular object has sphericity closer to 0. The calculated value of sphericity is sensitive to both overall form (like elongation) and surface roughness (like convexity).

$$S = 4\pi \frac{A}{P^2} \tag{3.1}$$

where  $A$  and  $P$  are the projected area and perimeter of the single particle, determined by image analysis.

The particles considered in this work are spray-dried powders and the mean value of the sphericity calculated with Eq.(3.1) is reported in Figure 3.4. With a mean sphericity value of 0.84 the granules can be considered fairly spherical.

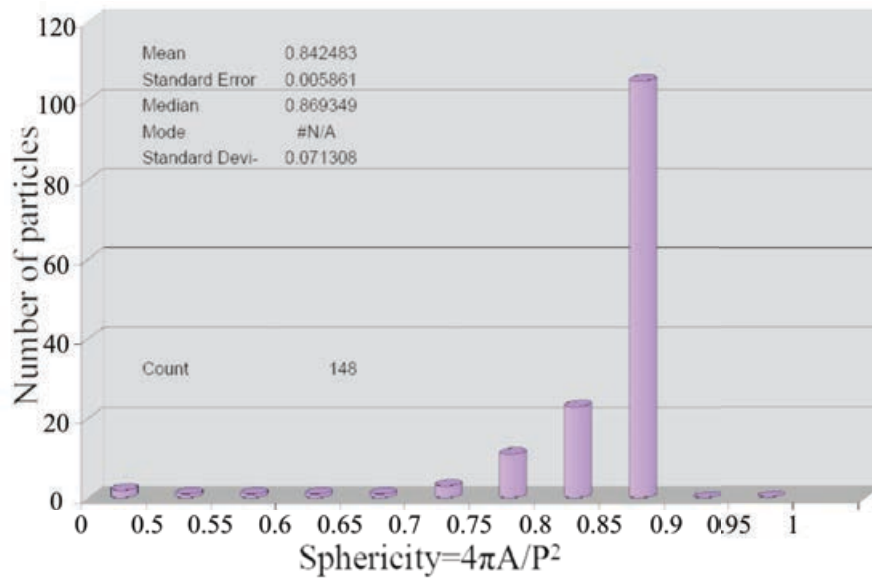


Figure 3.4: Distribution of sphericity values for ZSM5 zeolite sample from SEM.

### 3.2.2 Laser light diffraction

Laser light diffraction is an indirect measurement technique where the particle size distribution is inferred from light-scattering measurements modelled on, and calibrated from, the scatter caused by spherical particles. The technique of laser diffraction is based on the principle that particles passing through a laser beam will scatter light at an angle that is directly related to their size. Larger particles scatter light at narrow angles with high intensity whereas small particles scatter at wider angles but with lower intensity. A volume distribution is generated directly, which is equivalent to the weight distribution if the density is constant. The schematic operating principle is depicted in Figure 3.5.

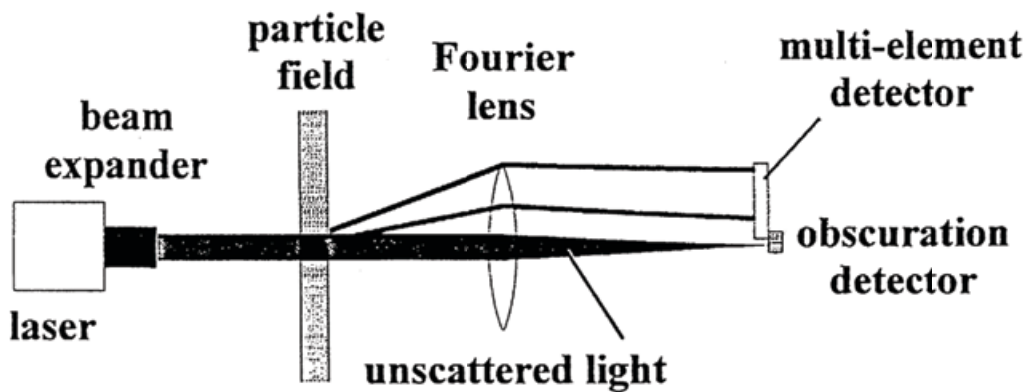


Figure 3.5: Schematic of a laser diffraction instrument. Redrawn from [23].

A laser diffraction instrument comprises the following elements:

- *Light source:* a laser of coherent intense light of fixed wavelength. He-Ne gas lasers ( $\lambda=0.63 \mu\text{m}$ ) are the most commonly used since they offer the best stability, especially in relation with temperature, and give better signal to noise ratios than the higher wavelength laser diodes.

- *Sample presentation system (particle field)*: a system that ensures that a stream of dispersed particles (in liquid or air) passes through the laser beam at an appropriate concentration.
- *Positive Fourier lens or set of lenses*: used to focus the laser beam onto the multi-element detector.
- *Multi-element detector*: a slice of photosensitive material with a number of discrete detectors to measure the intensity of the original or remaining light beam (obscuration) and the intensity of the scattered light by the particles at different angles.

The *Malvern Mastersizer 2000* laser light diffraction was used to gather information about the particle size distribution. The particles size distribution is summarised in Table 3.1 and Figure 3.6. The measurement was carried out in wet dispersion with a continuous ultrasonic level of 85%.

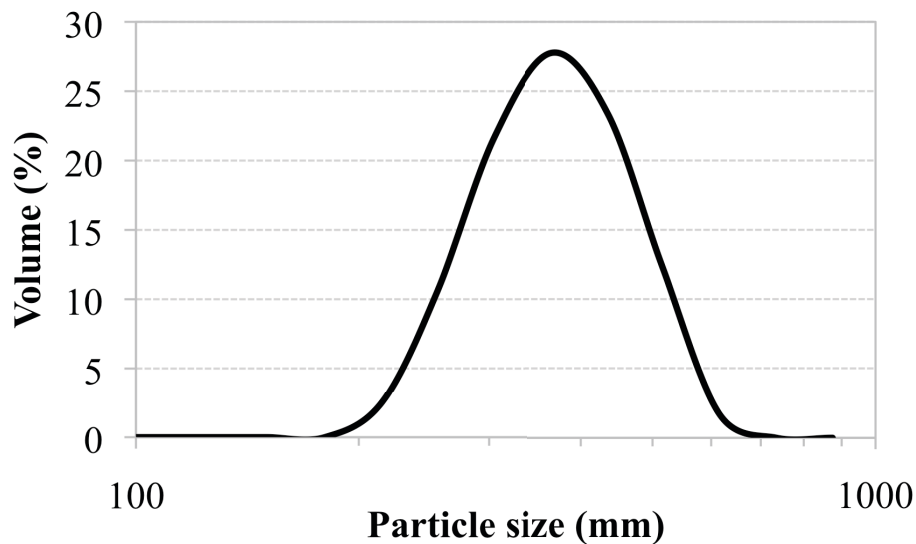


Figure 3.6: Particle size distribution for the zeolite sample.

Table 3.1: Particle size distribution for the zeolite sample.

<b><math>d_{0.1}</math> (<math>\mu\text{m}</math>)</b>	243.48
<b><math>d_{0.5}</math> (<math>\mu\text{m}</math>)</b>	338.05
<b><math>d_{0.9}</math> (<math>\mu\text{m}</math>)</b>	461.77

### 3.3 Particle flowability (Hausner ratio, Carr's index and flow function)

The flowability of a powder is important in many industrial manufacturing operations which involve particulate materials. The word flowability of a bulk of solid material refers to the plastic deformation of a bulk solid due to the loads acting on it and it depends on many factors. It is a combination of a) powder characteristics: particle size, particle shape, size distribution, packing, density, surface properties and b) process conditions, moisture contents, temperature, humidity, electric charge, fluidisation and applied shear/stress. All these factors influence the inter-particle forces acting between the particles. Accurate measurements of flowability should be carried out under representative conditions, which mimic the manufacturing process. The flowability of a powder depends on the relationship between adhesive forces to other forces acting on the bulk solid, and the magnitude of the load necessary for flow is a *measure of flowability*.

In the literature different methods have been reported to assess powder flowability. They can be grouped as *direct methods*, where powder properties are determined during flow in its consolidated state, or *indirect methods*, which are related to the powder flowability properties in its loosely packed state [24]. Certain bulk solids continue to gain strength under a constant compressive stress for an extended period of time and this effect is called time consolidation. Examples of indirect methods are: uniaxial testing [25], shear cells [26,27,28], e.g. Jenike cell [29,30,31], annular cells [26], Schulze cell [32], triaxial cells [33,34], and biaxial testers [35].

Examples of direct methods are: poured and tapped density [36,37], aeroflow [25], rheometer [28] static angle and dynamic angle of repose [38,39], discharge time [40]. All these methods are based on different principles and the choice of the appropriate technique should be related to the process conditions to be studied. Although all these tests can give a comparable numerical value for powders with different flowability it is difficult to relate such measurements with the DEM input particle parameters, as described in Chapter 2. In the literature these measurements techniques are sometimes used to validate or calibrate the DEM input parameters by comparing the results of bulk measurements with numerical modelling of the same bulk measurement techniques. For example, experimental values for flow in a horizontally aligned annular shear cell have been compared with DEM numerical simulations to match quantitatively the experimental data with the numerical model in terms of velocity, granular temperature, and solids fraction profiles [41]. Different contact mechanics force laws and a sensitivity analysis for different input material properties were carried out.

In this chapter powder bulk flowability for the ZSM5 zeolite, has been assessed by evaluation of packing properties (Hausner's ratio HR, Carr's compressibility index CI) and determination of the flow function  $ffc$  by Schulze ring tester.

### **3.3.1 Definition of Hausner ratio (HR) and Carr's Index (CI)**

The poured packing density and the tapped density of a powder can be used to assess the material flowability. The Hausner Ratio and Carr Index are two parameters that can be used to define the flowability of a granular material, and they are not theoretically derived parameters, but rather a practical numerical index of powder flowability. The classifications for assessing the flowability for a given material are presented in Table 3.2 and Table 3.3.

Table 3.2: Classification of flowability by Hausner Ratio HR [42].

<b>Flowability</b>	<b>HR</b>
Non flowing	>1.4
Cohesive	>1.4
Fairly free-flowing	1.25-1.4
Free-flowing	1-1.25
Excellent flowing	1-1.25
Aerated	1-1.25

Table 3.3: Classification of flowability by Carr's index [43].

<b>Flowability</b>	<b>CI</b>
Excellent	<10
Good	11-15
Fair	16-20
Passable	21-25
Poor	26-31
Very poor	32-37
Very, very poor	>38

The classification in Table 3.2 is based on empirical correlation from experimental data. It is interesting to observe that, the Hausner ratio for the extreme cases is not capable of discrimination between cohesive and not flowing and between excellent flowing and aerated.

The Hausner ratio is perhaps a good quick method for assessing powder flowability, but this single number shows clear limitation in giving a numerical value for the flowability.

The Hausner Ratio has been defined after the work by Hausner [44,45]. It was shown that for a dry powder there is a relationship between the Hausner Ratio and flow rate and also the angle of repose. The Hausner Ratio is given in Eq.(3.2), where  $\rho_{tapped}$  is the powder bulk density, and  $\rho_{bulk}$  is the powder tapped density.

$$HR = \frac{\rho_{tapped}}{\rho_{bulk}} \quad (3.2)$$

The *bulk density* of the powder (random loose packing) is defined as the ratio between the sample mass and its total volume, which includes the interstices between particles. Sometimes, the *bulk density* is also referred as *poured density*. The sample particles are loaded into a container and are allowed to settle under the influence of gravity. The *tapped density* (random dense packing) is the value of the bulk density after tapping the container a number of times. The following equations, Eq.(3.3) and Eq.(3.4) are used to calculate the bulk and tapped density where  $M$  is the mass of the poured material,  $V_o$  the volume of the poured material and  $V_N$  the volume of the material after tapping.

$$\rho_{bulk} = \frac{M}{V_o} \quad (3.3)$$

$$\rho_{tapped} = \frac{M}{V_N} \quad (3.4)$$

The Carr's Index or compressibility index is calculated as given in Eq.(3.5) [46].

$$CI = \frac{(\rho_{tapped} - \rho_{bulk})}{\rho_{bulk}} \cdot 100\% \quad (3.5)$$

### 3.3.2 Hausner ratio and Carr's index: ZSM5 zeolite sample

To determine the initial bulk volume,  $V_o$ , the sample was poured into a glass cylinder and the volume of the untapped bulk was determined. The sample was then subjected to a numbers of taps by using *Copley tap density volumeter model JV200* apparatus. The sample was tapped for a number of cycles until the volume stopped changing (in this case about N=1500 times). Values of bulk volume,  $V_N$ , for the powders were determined, and values of bulk density were calculated using the weight of the powders as follows. The results for the Hausner ratio and Carr's compressibility index are shown in Table 3.4 and illustrate that the material showed excellent flowability. The bulk poured and tapped densities reported in Table 3.4 are much lower than the skeletal density of the material measured by helium pycnometry as the latter excludes the micro and nano porosities of the particles and the voidage between the packed particles.

Table 3.4: Measured zeolite flow properties: Hausner ratio, Carr's index and flow function.

Characteristic	Zeolite
Particle absolute density (g/cm <sup>3</sup> )	2.41
Bulk poured density (g/cm <sup>3</sup> )	0.672
Tapped density (g/cm <sup>3</sup> )	0.695
Hausner ratio – HR	1.034 (excellent flow)
Carr's Index – CI %	3.301 (excellent flow)
Pore volume (%v/v)	36

The excellent flow properties for the zeolite sample was probably the result of the spherical morphology and narrow range of particle size distribution. To confirm the good flowability for this material the Schulze ring test was also conducted.

### 3.3.3 Definition of flow function (*ffc*): Schulze ring tester

A consolidated bulk material will start to flow (incipient flow) when sufficient stress is applied, and limit when the bulk material fails and starts to flow is represented by the *yield locus* (or yield limit) represented in Figure 3.7 [47]. Each point on the yield locus is determined as relationship between the measured shear force as a function of the applied normal loads.

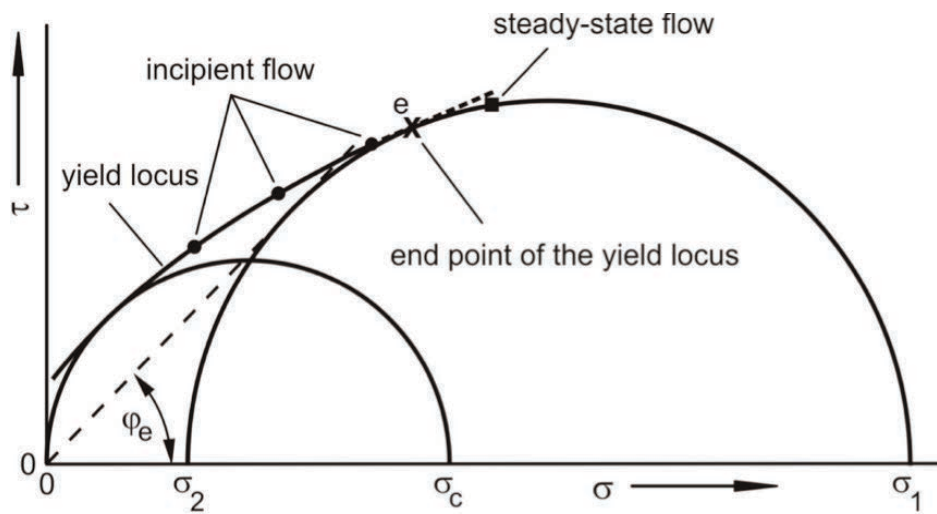


Figure 3.7: Yield locus and Mohr's circles.

The yield locus and corresponding Mohr's circles can be used to predict how easily a particulate material would flow under those conditions by using the definition of the flow function (*ffc*) which is defined from Eq.(3.6) [48,30]. Where  $\sigma_1$  and  $\sigma_c$  are defined as major

consolidation stress and unconfined yield strength. The classification for the  $ffc$  in Table 3.5 defines the flow behaviour according to Eq.(3.6).

$$ffc = \frac{\sigma_1}{\sigma_c} \quad (3.6)$$

The effective angle of internal friction (particle-particle) at steady-state flow,  $\varphi_e$ , and bulk density,  $\rho_b$ , can also be determined as demonstrated in Figure 3.7. Since the largest Mohr stress circle indicates a state of steady-state flow, the angle  $\varphi_e$  can be used as a measure of the internal friction,  $\eta$ , at steady-state flow. Which can be calculated as the *atan* of the angle  $\varphi_e$ .

Table 3.5: Classification of the flowability function  $ffc$  [49].

<b>Flowability</b>	<b><math>ffc</math></b>
Not flowing	<1
Very cohesive	1-2
Cohesive	2-4
Easy-flowing	4-10
Free-flowing	>10

The most common method to determine the yield locus and the Mohr's circle is to use a shear cell. To generate the yield locus the bulk solid specimen is repetitively loaded vertically by a normal stress (consolidation) and shear deformation is applied by a moving cell with a constant velocity which results in a horizontal shear stress (strength measurement) [25,26,27,28,29,30,31,32,50]. Here the Schulze ring tester is employed and the constitutive parts are shown in Figure 3.8. The shaped *bottom ring* of the shear cell contains the bulk solid

sample. The sample weight is recorded for the determination of the bulk density during the measurement. The *lid* placed on top of the bulk solid specimen and applies a normal force onto the specimen by the *computer controlled normal load system*. The bottom ring of the shear cell is rotated and the lid is held stationary by *two tie rods*, which are used to measure the shear stress applied on the sample. The wall coefficient of friction ( $\varphi_w$ ) can also be measured by using a different bottom ring with the desired material [47].

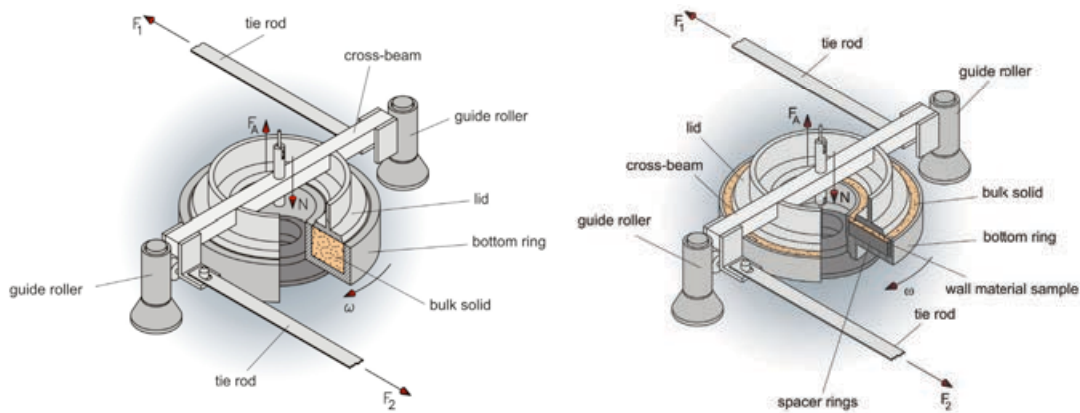


Figure 3.8: Set-up of the Schulze shear cell, for particle internal friction and wall friction [51].

Firstly the bulk solid specimen was consolidated. During consolidation the bulk solid specimen was loaded in the vertical direction by a well-defined normal stress  $\sigma = \sigma_{pre}$ , before the specimen was sheared. Initially, the shear stress increased with time before reaching a constant shear. The constant shear stress is called  $\tau_{pre}$ . At this point shear resistance and bulk density did not further increase. This type of shear is called steady-state flow and the state of the bulk solid after steady state is critically consolidated with respect to the normal stress  $\sigma_{pre}$ . After the bulk solid specimen had been consolidated by the preshear procedure the shear stress and the normal load reduced to zero. Then, the bulk solid specimen was loaded vertically by a normal stress  $\sigma$  and the shear deformation was applied by moving the bottom

ring with a constant velocity, resulting in a horizontal shear stress  $\tau$ . The bulk started to flow when a sufficiently large shear force was attained, at which point the particles started to move over each other. The maximum shear stress characterised the incipient flow and the corresponding pair of values  $\sigma$ - $\tau$  which is the point of the yield limit locus. A sufficient number of points of the yield locus were obtained by repeating the procedure for decreasing value of the normal load and measuring the corresponding shear force that characterised the incipient flow.

Differently from the Hausner ratio and Carr's index, which are based on an empirical method as function of bulk and tapped density, the flow properties obtained from the measured yield loci were defined physical figures.

#### **3.3.3.1 Flow function (ffc): ZSM5 zeolite sample**

The flowability of the ZSM5 zeolite sample was characterised under the following conditions by using a Schulze ring tester. The shear cell was filled with the powder sample and the excess of powder was scraped off with a spatula. The filled shear cell was then weighed to calculate the bulk density. The sample was loaded under three levels of normal load at pre-shear (6000, 4000 and 2000 Pa) and subsequently three other values of stress levels were measured with the lowest equal to the 12% of the normal load at pre-shear, the second and third were 46% and 80% of the normal load at pre-shear, respectively. From the measurements yield locus has been plotted for the different levels of normal load at pre-shear, Figure 3.9.

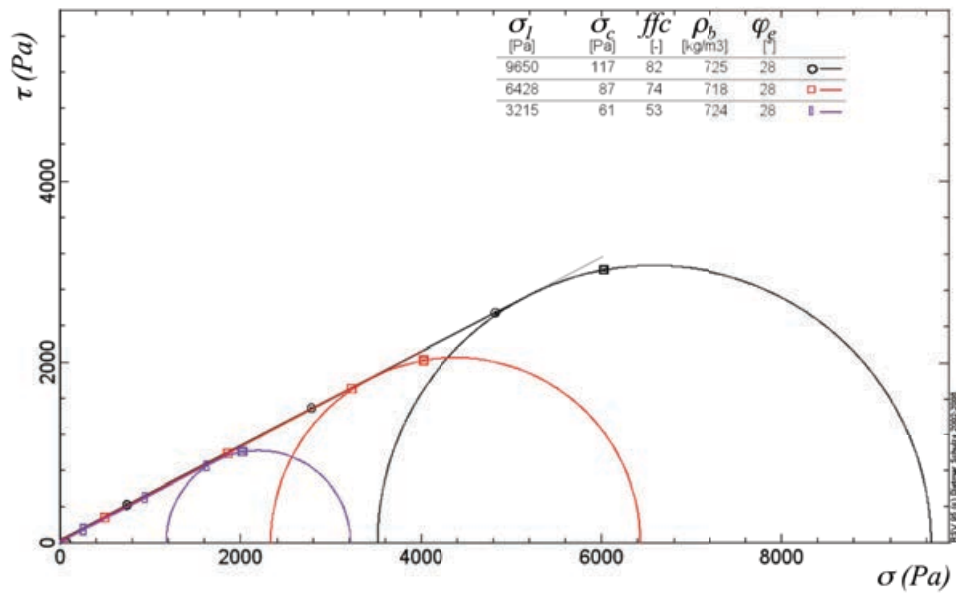


Figure 3.9: Zeolite yield locus for the normal load at pre-shear equals to 2000 (purple), 4000 (red), 6000 (black) Pa.

In Figure 3.10 the result regarding the flow function  $ffc$  for the zeolite is reported. The values for the  $\sigma_1$ ,  $\sigma_c$  and the flow function  $ffc$  are reported in Table 3.6. For all the cases the specimen was free flowing and the flowability increased with the consolidation stress which was opposite of what was expected.

Table 3.6: Results of the measurements at different values of normal load at pre-shear.

Normal load at pre-shear force (Pa)	$\sigma_1$ (Pa)	$\sigma_c$ (Pa)	$ffc$	$\tau_c$ (Pa)	$\rho_b$ (kg/m <sup>3</sup> )	$\varphi_e$ (°)	$\eta$
6000	9650	117	82.27	36	725	27.8	0.452
4000	6428	87	73.75	26	718	27.9	0.453
2000	3215	61	52.5	19	724	27.7	0.450
Average						27.8	0.452

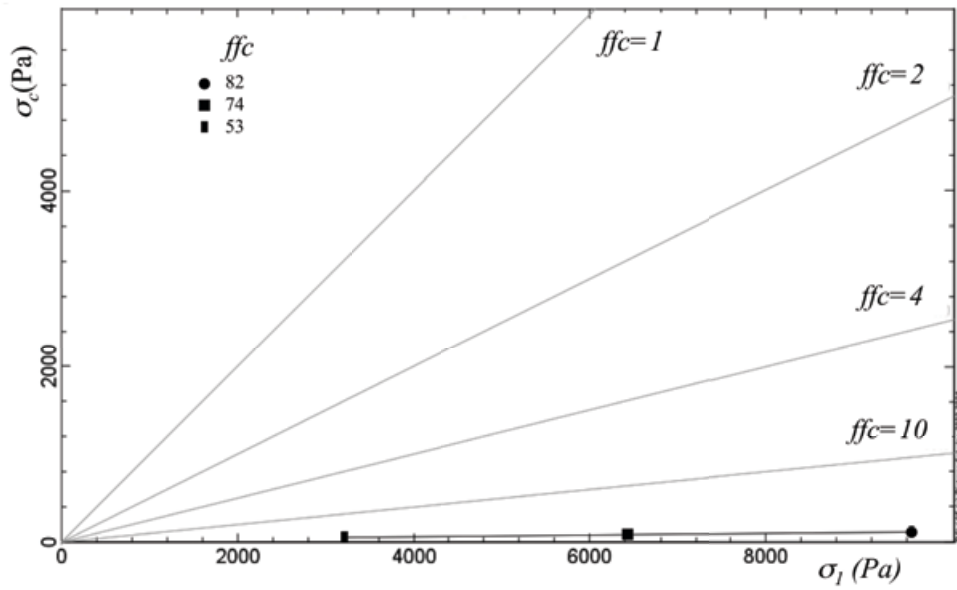


Figure 3.10: Zeolite unconfined yield strength  $\sigma_c$  versus consolidation stress  $\sigma_1$  and flow function  $ffc$ .

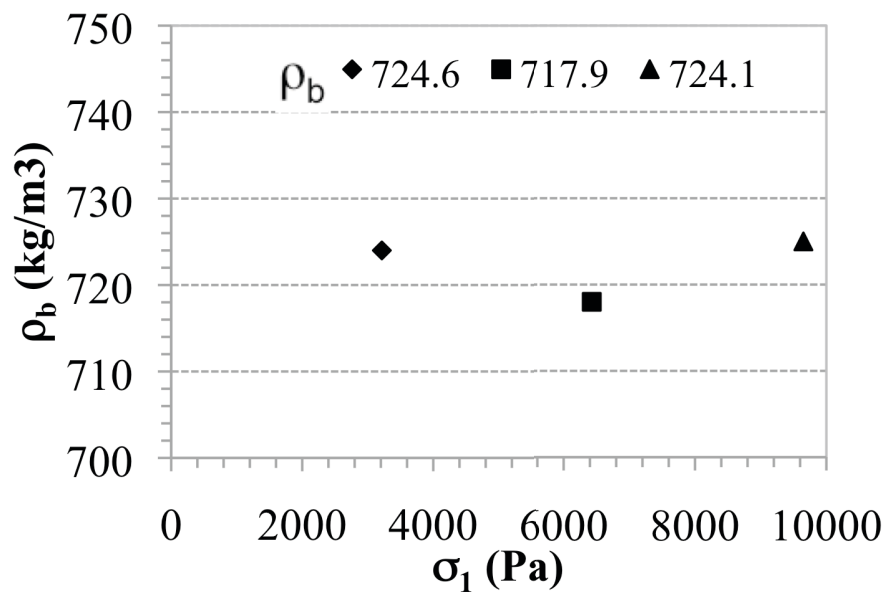


Figure 3.11: Zeolite bulk density  $\rho_b$  versus consolidation stress  $\sigma_1$ .

Figure 3.11 shows a constant value of bulk density,  $\rho_b$ , at incipient flow for different consolidation stresses. The increase in flowability was observed because applied stresses were

not high enough to consolidate the particles since the density did not change and, therefore, the unconfined yield strength  $\sigma_c$  did not increase as much as the consolidation stress  $\sigma_l$ . Thus, from the definition of the flow function  $ffc$  this leads to an increase of the flowability with the increase of the normal load at pre-shear force.

It is interesting to note in Table 3.7 that all the three measurements for the bulk density (poured), tapped density and average bulk density from the Schulze ring tester were very similar. This shows the poor compressibility of the powder bed, which is also demonstrated later by using bulk powder compression.

Table 3.7: Comparison between bulk density, tapped, density and bulk density from the Schulze ring test.

<b>Bulk density (kg/m<sup>3</sup>)</b>	<b>Tapped density (kg/m<sup>3</sup>)</b>	<b>Average bulk density Schulze test (kg/m<sup>3</sup>)</b>
0.672	0.695	0.722

Measurement of the kinematic angle of wall friction,  $\varphi_w$ , were taken by replacing the base of the shear cell with a ring of wall material (stainless steel). The wall shear stress was measured at decreasing normal wall stresses. Values of steady-state wall friction at several normal wall stresses were measured and depicted in Figure 3.12 where wall shear stress,  $\tau_w$ , is plotted against applied wall normal stress,  $\sigma_w$ . The coefficient of wall friction,  $\mu_w$ , is the ratio of wall shear stress,  $\tau_w$ , to wall normal stress,  $\sigma_w$ . The wall friction angle,  $\varphi_w$ , is the slope of a line running through the origin of the  $\sigma_w, \tau_w$  diagram and a point of the wall yield locus. For each value of wall normal stress  $\sigma_w$ , two measurements were taken. The minimum, maximum and

average values for the *wall angle coefficient of friction*  $\varphi_w$  deduced from yield locus are reported in Table 3.8. The *wall coefficient of friction* for the zeolite sample decreased with increasing applied normal wall stress  $\sigma_w$ .

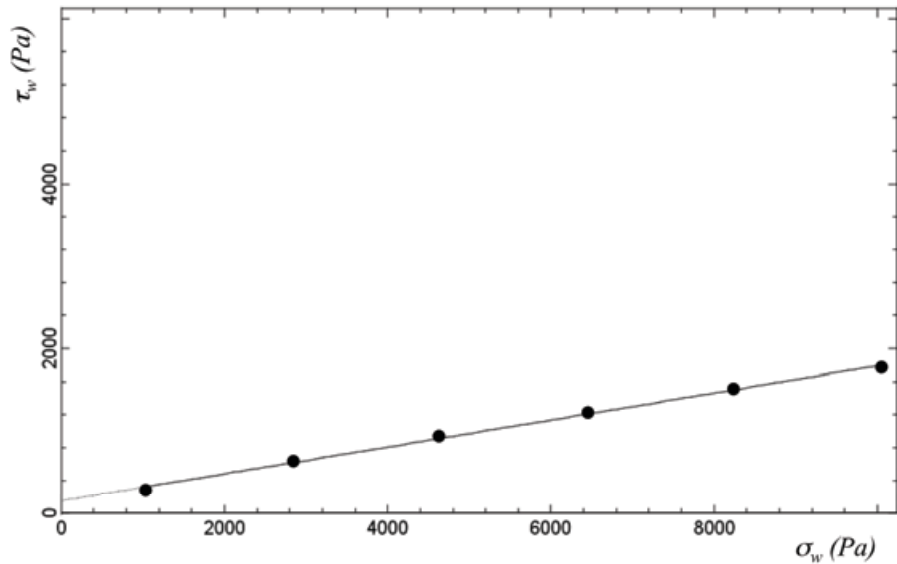


Figure 3.12: Zeolite wall shear stress in a wall friction test.

Table 3.8: Values of the kinematics angle of wall friction.

$\sigma_w$ (Pa)	$\varphi_{w,min}$ (°)	$\varphi_{w,max}$ (°)	$\varphi_{w,ave}$ (°)	$\eta_{w,ave}$
1039	14.9	15.3	15.1	0.270
2839	12.5	12.7	12.6	0.224
4639	11.6	11.6	11.6	0.205
6438	10.8	10.9	10.8	0.191
8238	10.3	10.4	10.4	0.184
10038	9.9	10	10	0.176
Average	11.7	11.8	11.75	0.208

For zeolite particles the Schulze ring tester provided bulk quantitative experimental values at consolidated state for the flowability function  $ffc$ , the coefficient of particle-particle internal friction  $\varphi_e$  and coefficient of wall friction  $\varphi_w$ . These values could be used to explore the particle-scale mechanics using a parametric approach to calibrate the DEM input parameters by modelling all or part of the shear cell under the same experimental conditions.

### 3.4 Single particle compression: reduced Young's modulus and strength of single particle

Single particle compression can give measurements of mechanical input parameters for single particles such as elastic modulus  $E$ . The elastic contact for spherical regular particle compressed between two flat rigid surfaces can be described by Hertz theory [52]. During compression of a single granule with a flat punch the contact area between them deforms as a circle as shown in Figure 3.13.

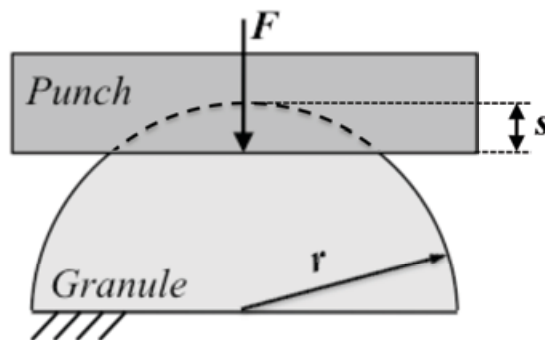


Figure 3.13: Characteristic plate-particle contact during single particle compression.

The relationship between the force,  $F$ , and the relative local displacement of the plates at each contact point,  $s$ , is as follows [52]:

$$F = \frac{4}{3} r^{1/2} E^* s^{3/2} \quad (3.7)$$

where  $r$  and  $E^*$  are the radius and equivalent (or reduced) Young's modulus of the particle.  $s$  is the probe height. The force is recorded when the tip touches the particle surface, and in principle, the Hertz equation applies to relatively small values of the nominal strain, usually in the order of <5%. The effective modulus of elasticity  $E^*$  of both particle (index 1) and punch, made in stainless steel, (index 2) is given (usually  $E_2 \gg E_1$ ) as:

$$E^* = \left( \frac{1-\nu_1^2}{E_1} + \frac{1-\nu_2^2}{E_2} \right)^{-1} \approx \left( \frac{1-\nu_1^2}{E_1} \right)^{-1} \quad (3.8)$$

The peak critical compression force  $F_{cr}$  recorded just before particle failure can be used to calculate the particle crushing strength  $\sigma_{cr}$ . Eq.(3.9) is used to calculate the particle crushing strength or nominal rupture stress for spherical particles [53].

$$\sigma_{cr} = \frac{F_{cr}}{\pi r^2} \quad (3.9)$$

The strength of particles depends on a variety of factors such as, size, shape and external surface conditions, porosity and pore network [54]. Particles are classified according to the failure mechanism, e.g. brittle, semi-brittle or ductile.

### 3.4.1 Diametrical compression of single zeolite particles

The breakage behaviour of the zeolite particles was investigated by the compression of a single particle. The Stable Micro Systems analyser mechanical testing machine, shown in Figure 3.14, was used with a stainless steel cylindrical tip probe of 2 mm diameter.

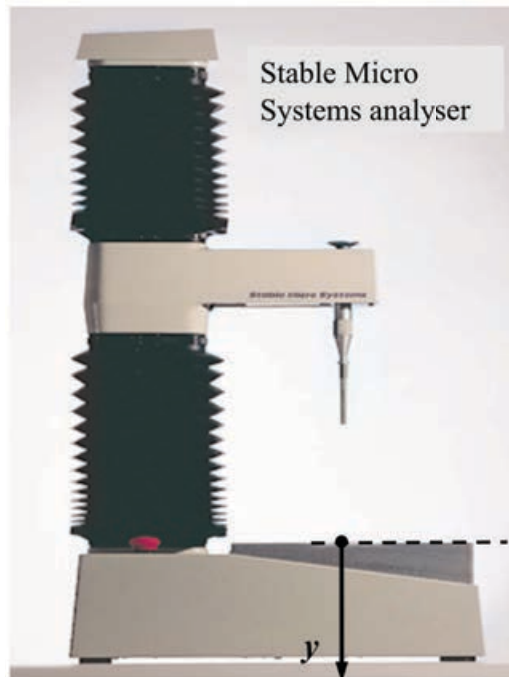


Figure 3.14: Stable Microsystems analyser [55].

During the movement of the punch towards the upper fixed plate, contact between the particle and the fixed plate is created. The tip zero position is recorded when the tip's flat surface touches the plate where the particles are located. The recorded punch displacement is considered negative since the vertical axis was considered positive as shown in Figure 3.14. During this period the displacement, force and time are measured. To obtain statistically significant results at least 45 particles were randomly chosen and compressed at velocity of  $0.01 \text{ mm s}^{-1}$  until the rupture point. Loading, holding and unloading tests were performed with a loading and unloading punch velocity of  $0.01 \text{ mm s}^{-1}$  in order to assess the elastic-plastic transition.

Load displacement data were recorded and used for drawing the load displacement curves as shown in Figure 3.15, where the particle diameter can be inferred from the sudden increase of the measured force (tip touches the particle surface) and the breakage (failure) point

corresponding to the sudden decrease in the load. The material appeared to be semi-brittle since the rate of drop in the force was dramatic.

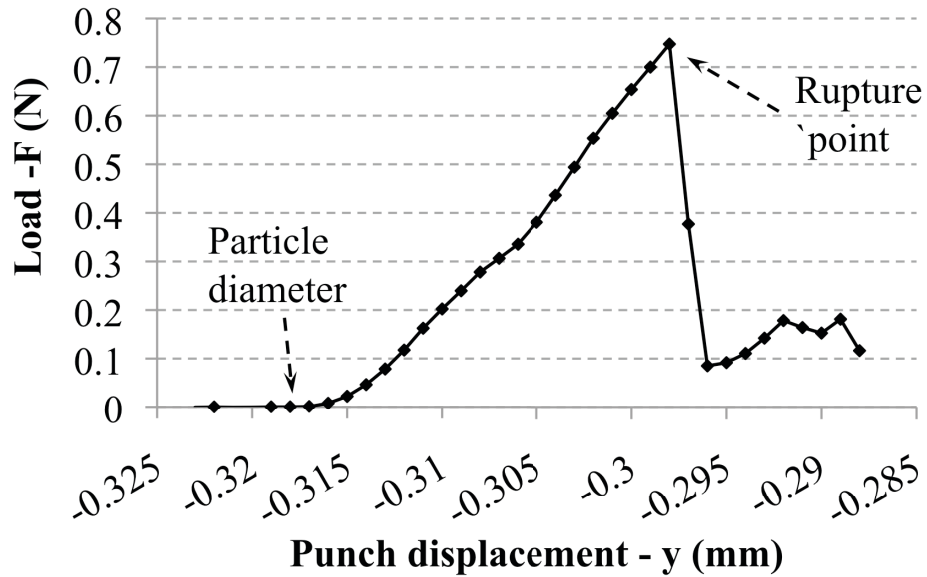
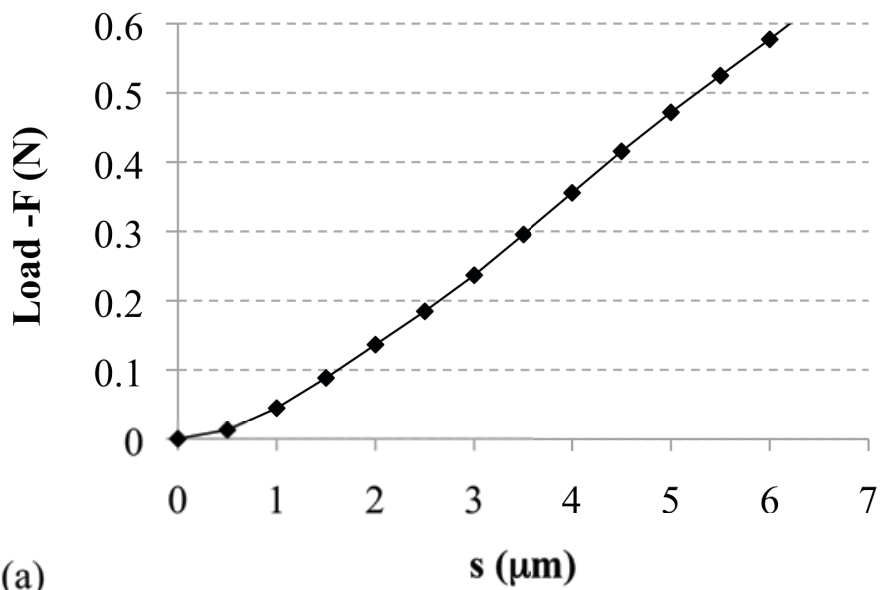
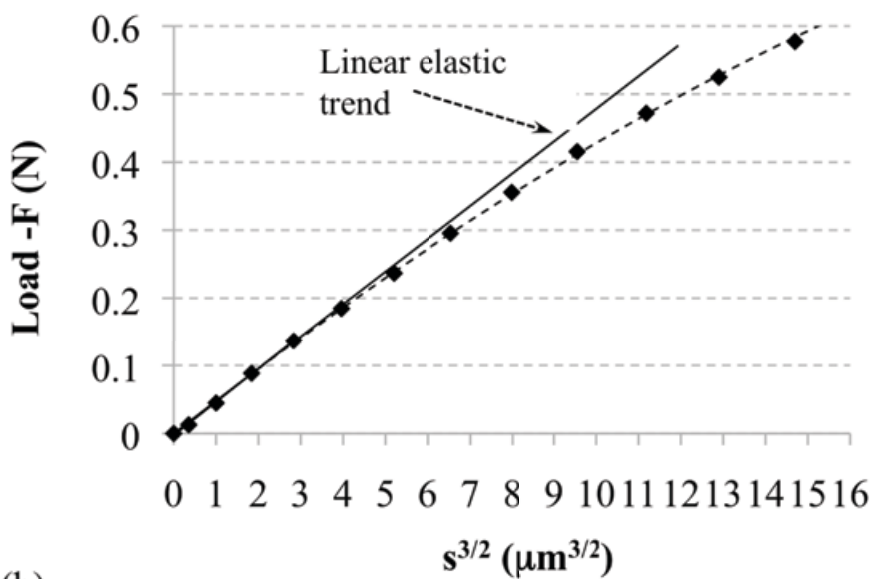


Figure 3.15: Typical force displacement curve for the zeolite sample. Crushing measurement on particles by the Stable Microsystems analyser.

In Figure 16.a, the compression force against the local displacement is shown for a single particle. The reduced elastic modulus  $E^*$  was determined by plotting the load force  $F$  versus the local displacement  $s^{3/2}$  according to Eq.(3.7), Figure 3.16. The reduced elastic modulus, Figure 3.17, was therefore inferred from the gradient of the linear fitting. The average value for the reduced elastic modulus  $E^*$  was equal to  $2.93 \pm 0.63$  GPa.



(a)



(b)

Figure 3.16: Data for single particle compression (a) local displacement (b) data plotted according the Hertz contact theory and linear fitting.

The elastic modulus, defined in Eq.(3.8), is commonly employed in micromanipulation studies and assumes an isotropic material behaviour. Spray dried zeolite particles, however, are microporous inorganic composites which contain small pores and therefore they can

exhibit anisotropic behaviour. Therefore the elastic modulus value determined here should be considered as an effective particle value, rather than the absolute material property of the zeolite particles. The variation of crushing force and reduced elastic modulus with particle size are shown in Figure 3.17.

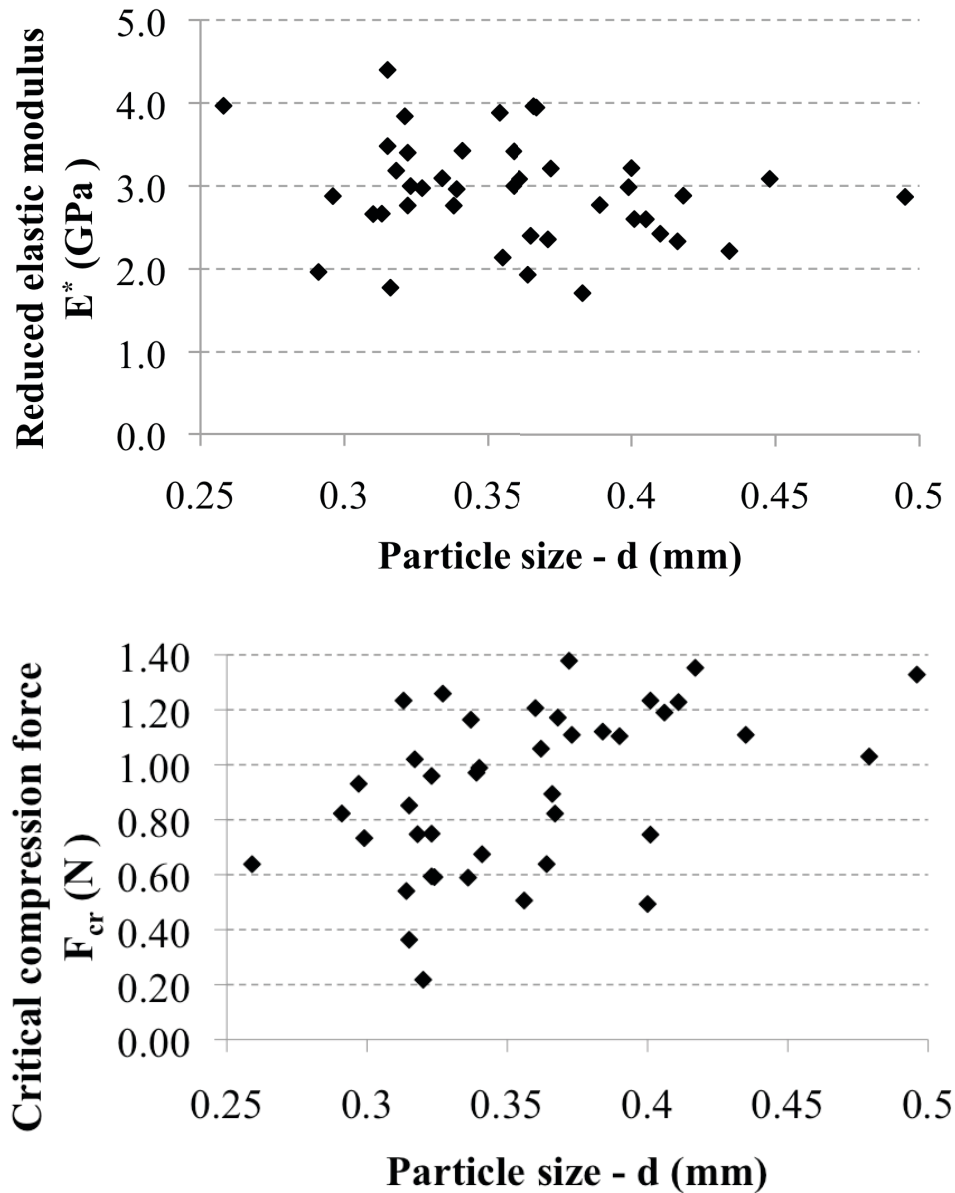


Figure 3.17: Reduced elastic modulus and critical force for individual zeolite particle.

The peak compression force called the breakage point is used to calculate the nominal rupture stress using Eq.(3.9). The values of the nominal rupture stress and corresponding diameter of individual zeolite particles are plotted in Figure 3.18.

This type of material can have a wide strength distribution due to the presence of defects, pores and binders, causing early breakage of the weakest particles. Moreover, the distribution of flaws size, shape, and orientation can differ from sample to sample. Zeolite particles are highly brittle materials and if subjected to compressive stress microcracks can form, that can reduce the strength of the particles, which consequently leads to particle fracture at a lower load.

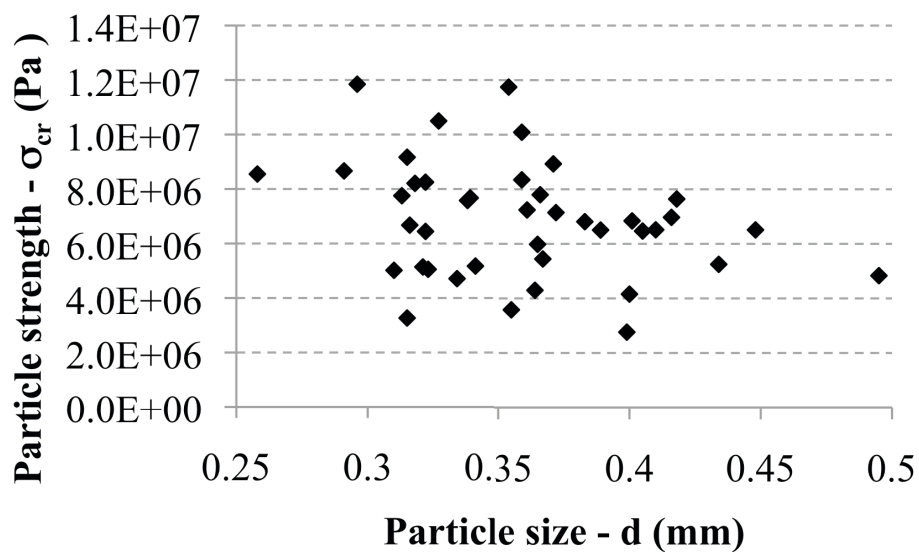


Figure 3.18: Nominal rupture stress of single zeolite particle.

The mean nominal rupture stress calculated according to Eq.(3.9) for the zeolite sample studied is reported in Table 3.9 together with the corresponding values of the force and nominal deformation at the rupture point (defined as the ratio between strain and the particle diameter). The values of standard deviation are high, showing large variation on mechanical

properties within the sample. The statistical distribution of such variability should also be considered.

Table 3.9: Mean rupture force, stress and strain, with standard deviation.

<b>Mean rupture force of single particles (mN)</b>	<b>Mean nominal rupture stress <math>\sigma_{cr}</math> (MPa)</b>	<b>Mean nominal deformation at rupture %</b>
981±321	9.8±3	5.2±2.6

Data from the compression test can be fitted to a statistical model to quantify the spread of the sample of particles. The Weibull statistical strength distribution has been shown to be an appropriate model to describe failure of brittle materials [56]. This is a two parameters distribution function and the relationship between the cumulative probability of failure,  $P_f$ , at or below a stress,  $\sigma$ , is represented in Figure 3.19 and calculated as follows:

$$P_f = F(\sigma_{cr}) = 1 - e^{-\left[\left(\frac{\sigma_{cr}}{\sigma_0}\right)^m\right]} \quad (3.10)$$

Where  $\sigma_{cr}$  is the failure stress (particle strength) and  $m$  is the characteristic strength distribution parameter (Weibull modulus).  $\sigma_0$  corresponds to the crushing stress with a fracture probability of 63.2%.

The parameter  $m$  represents the nature, spread and dispersion of flaws and defects. In particular, a low value for  $m$  indicates a non-uniform broad distribution of flaws that leads to a broad distribution in strength. A high value for  $m$  indicates a narrow and uniform distribution of defects and therefore smaller strength distribution.

Hence the two parameter modulus  $m$  and  $\sigma_o$  from the Weibull can be extrapolated by linear regression of the strength data; thus Eq.(3.10) can be written as follows:

$$\ln \left[ \ln \left( \frac{1}{1-P} \right) \right] = m \ln \sigma_{cr} - m \ln \sigma_o \quad (3.11)$$

For the determination of the Weibull distribution parameters from a set of experimentally measured the fracture stresses it is necessary to assign a probability of failure. This is done by ranking the experimental strength data  $\sigma_{cr}$  (points in the graph Figure 3.18 from Eq.(3.9)) and assigning a probability of failure  $P_i$  to each stress  $\sigma_i$  ( $=\sigma_{cr}$  for the particle  $i$ ).

Since the true value of  $P_i$  is unknown, a prescribed estimator has to be defined. In this work the estimator described by Eq.(3.12) [57] has been employed.

$$P_i \approx \frac{i - 0.3}{n + 0.4} \quad (3.12)$$

where  $P_i$  is the probability of failure for the  $i$  ranked strength data, and  $n$  is the total number of particle crushing test observations.

The parameters  $m$  and  $\sigma_o$  ( $m=3.2$  and  $\sigma_o=10.8$  MPa) are determined from the slope and intercept of the trend line as shown in Figure 3.19 plot of  $\ln[\ln(1/(1-P_i))]$  versus  $\ln \sigma_{cr}$ .

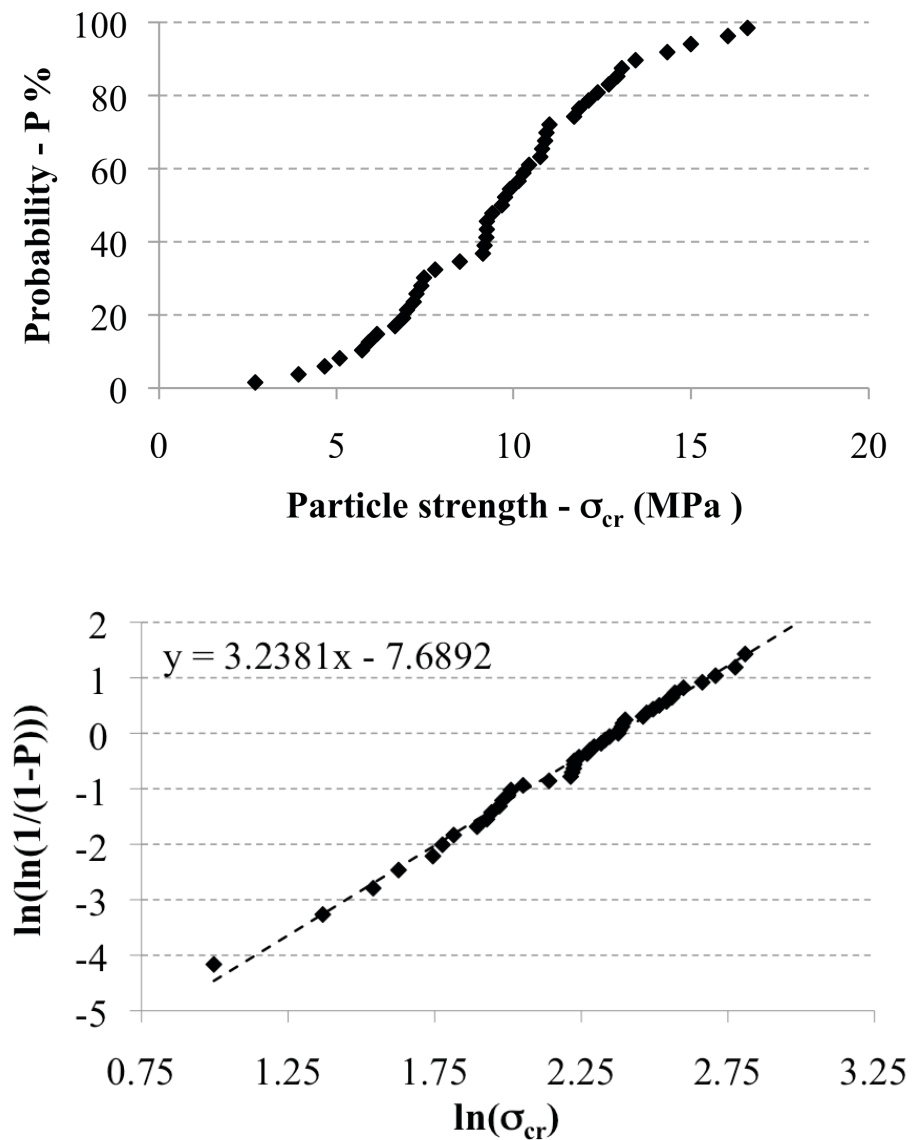


Figure 3.19: Cumulative distribution function for the zeolite sample, determination of the Weibull modulus  $m$  (dashed line).

For future work it would be useful to correlate the parameter  $m$  with tablet strength. This would allow characterisation of the influence of a broad distribution of flaws and defects, if the value of  $m$  is small, on the final strength of the tablet.

### 3.5 Nanoindentation: hardness and reduced Young's modulus

Nanoindentation is a measurement technique that allows the determination of mechanical properties such as hardness  $H$  or reduced elastic Young's modulus  $E^*$  for a material which can be used as input parameter for the DEM modelling. This technique has been widely used to characterize mechanical properties of powders, especially in the case of pharmaceutical materials [58,59].

It consists of the loading and unloading of an indent tip against the surface of the material. A typical loading-unloading hysteresis curve is shown in Figure 3.20 and the three parameters obtained during the measurement are  $P_{\max}$ , the load measured at a maximum depth of penetration  $h$  and  $A$  the projected area of contact between the indenter and sample at  $P_{\max}$ .

The material properties hardness  $H$  and the combined modulus of the system, or reduced indentation modulus  $E^*$  can be obtained from indentation load-displacement data.

The Berkovich indenter is a three-sided diamond pyramid-shape with a half-angle of  $65.3^\circ$  from vertical axis [60]. It is easier to manufacture a sharp tip for the Berkovich indenter than for a (four-sided) Vickers indenter and consequently more accurate results can be obtained especially at lower loads [61].

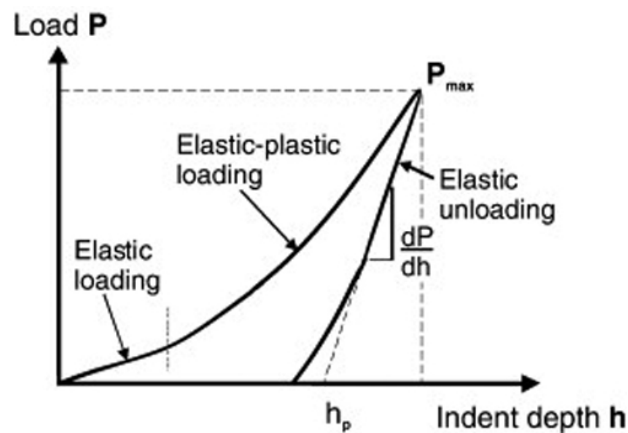


Figure 3.20: Schematic of a typical load–displacement curve during indentation test [59].

The combined modulus of the system, or reduced indentation modulus  $E^*$  is determined from the following expression [59]:

$$E^* = \frac{1}{2} \sqrt{\frac{\pi}{A}} \frac{1}{\beta} \frac{dP}{dh} \quad (3.13)$$

where  $\frac{dP}{dh}$  is the gradient of the tangent on the initial unloading curve on the load–displacement plot, Figure 3.20.  $\beta$  is a geometric correction factor ( $\beta = 1.034$  for a Berkovich indenter).

For a Berkovich indenter the nominal contact area,  $A$ , variation is related to the plastic depth  $h_p$ , which can be obtained from the load–displacement curve, shown in Figure 3.20, according to Eq.(3.14) [59]:

$$A = 24.5 h_p^2 \quad (3.14)$$

The reduced indentation modulus takes into account the compliance of the indenter tip as follows:

$$E^* = \left( \frac{1-\nu^2}{E} + \frac{1-\nu_i^2}{E_i} \right)^{-1} \quad (3.15)$$

where  $E$  and  $\nu$  are Young's modulus and Poisson's ratio for the specimen and  $E_i$  and  $\nu_i$  are modulus and Poisson's ratio for the indenter. Since the indenter is made of diamond it can be assumed that:

$$E^* \approx \left( \frac{1-\nu^2}{E} \right)^{-1} \quad (3.16)$$

The hardness can be calculated from Eq.(3.17):

$$H = \frac{P_{\max}}{A} \quad (3.17)$$

### 3.5.1 Nanoindentation of zeolite particles

Nanoindentation tests were performed using an MML NanoTest™ nanoindenter (MicroMaterials) with a diamond three-sided pyramid-shaped Berkovich-type indenter tip. The ZSM5 zeolite particles were held on the sample holder by adhesive glue (Loctite® 496™, methyl cyanoacrylate, Henkel, UK).

The diamond tip was pressed against the particle surface to create the indent and the load and displacement were monitored continuously. Four levels of indentation depth, 1, 4, 5 and 6 μm, were considered. From the unloading Young's modulus and hardness can be determined using Eq.(3.13), Eq.(3.14) and Eq.(3.17).

Each indentation experiment consisted of six segments as shown in Figure 3.21 and Figure 3.22. Initially the tip approaches the surface of the particle. Once the indenter touches the surface the loading is applied until the desired indentation depth (A). The load is held constant (B) for the desired time (30 seconds for 1 μm and 20 seconds for 4,5,6 μm) to assess possible creep or mechanical stabilization (relaxation). In the segment (C) 90% of the maximum load was removed then held for 30 seconds, segment D. This hold segment, inserted after a partial unloading segment, can be used to correct for the thermal drift of the apparatus during the indentation process [60]. During segment (E) the indent is totally unloaded from the particle surface.

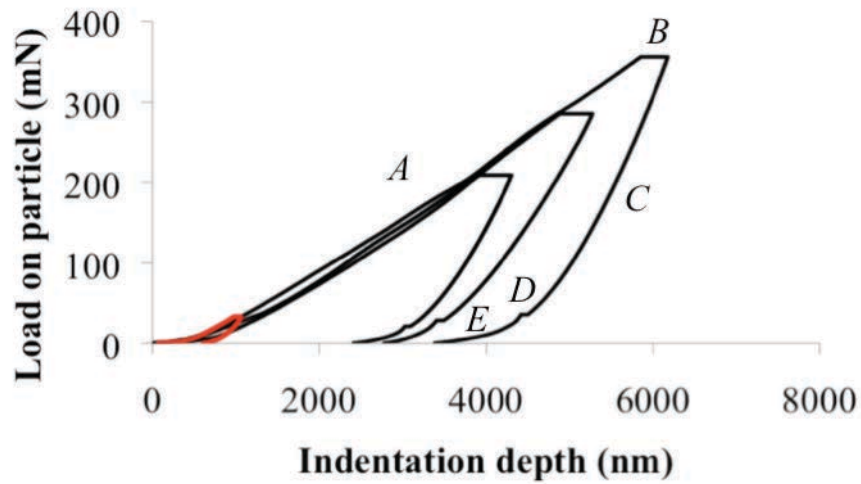


Figure 3.21: Typical load and unload curves for a zeolite particles with different levels of indentation depth: 1, 4, 5 and 6  $\mu\text{m}$ . A loading, B hold, C unloading, D hold, E no load.

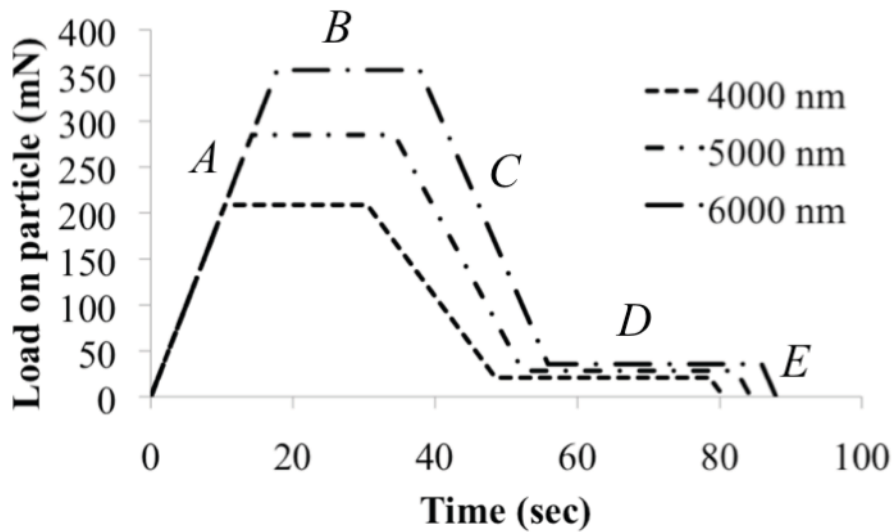


Figure 3.22: Typical load versus time for a zeolite particles with different levels of indentation depth: 4, 5 and 6  $\mu\text{m}$ . A loading, B hold, C unloading, D hold, E no load.

In Figure 3.23 Young's modulus and hardness are shown over the indentation depth for 13 different indentation experiments on zeolite particles. It can be seen, that there is a decrease in Young's modulus and hardness with indentation depth. This is called indentation size effect,

wherein the hardness is observed to increase with decreasing indentation size [62]. This is due to a lower number of dislocations necessary to create a permanent shape change with increasing indentation depth, which results in decreasing hardness and Young's modulus values.

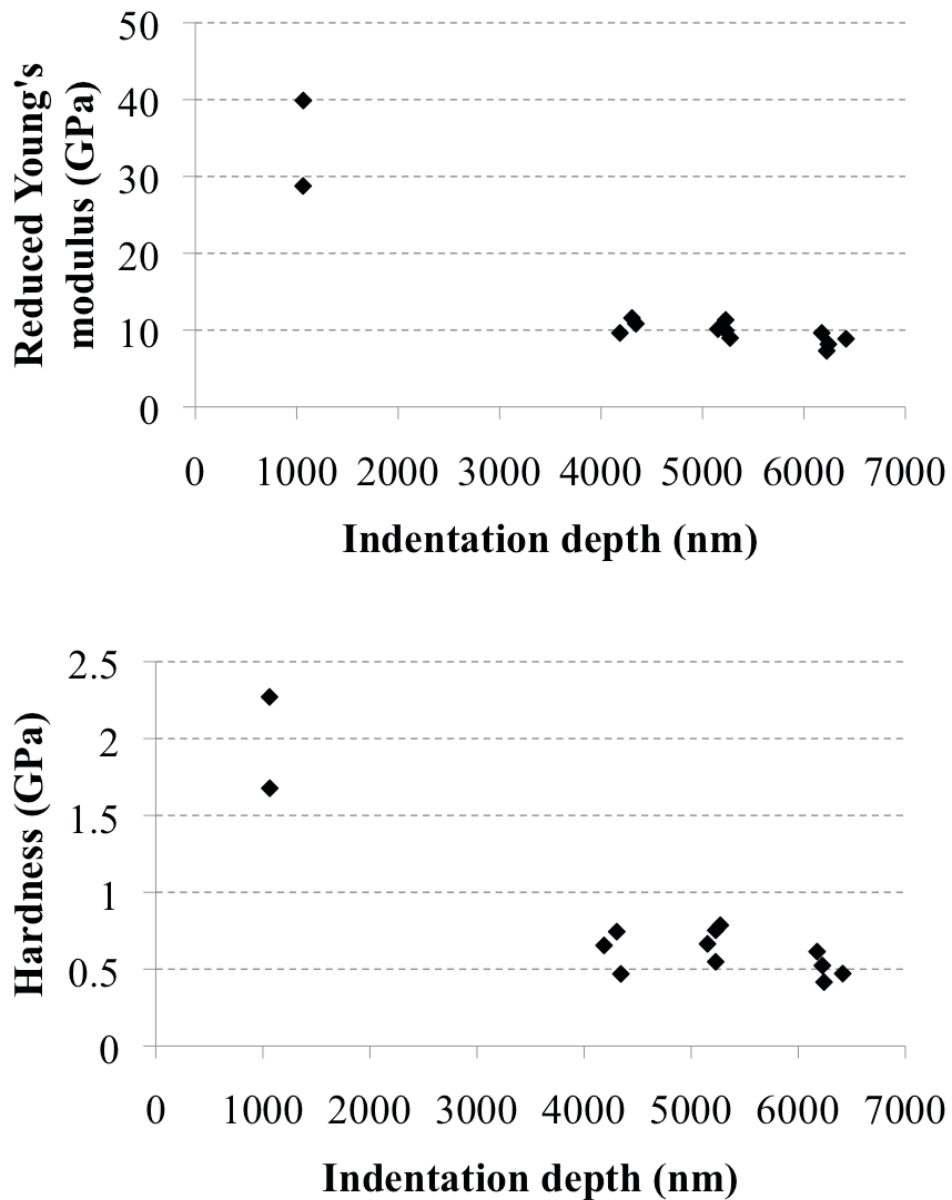


Figure 3.23: (a) Reduced Young's modulus and (b) hardness during indentation of ZSM5 particles.

The indentation size effect decreased with increased indentation depth. At higher indentation depths the Young's modulus and the hardness were less variable.

The previous graphs show that the elastic modulus and hardness had an indentation size effect. Therefore the value that is considered should be related with the indentation depth, for consistency. The average values of reduced Young's modulus  $E^*$  and hardness  $H$  for each indentation depth are given in Table 3.10. It remains unclear as to what constitutes the correct elastic modulus to be used as a DEM input parameter.

Table 3.10: Average values for the reduced Young's modulus  $E^*$  and hardness  $H$  for each indentation depth with standard deviation.

<b>Indentation depth considered (nm)</b>	<b>H (GPa)</b>	<b><math>E^*</math> (GPa)</b>
1000	1.97±0.42	34.32±7.86
4000	0.62±0.14	10.67±0.98
5000	0.68±0.10	10.09±0.96
6000	0.51±0.08	8.49±0.99

### 3.6 Powder bulk compression

Bulk powder compression consists of compacting materials in a die to produce a coherent structure, namely tablets. Compression behaviour of the powder is an important characteristic since it influences the final tablet properties. The powder compaction process depends on a number of different factors and particle properties such as: powder flowability, particle size distribution, particle shape, particle hardness, particle strength, particle strength distribution and particle friction. However, the relation between single particle properties and bulk compression behaviour is not yet well understood [53]. Powder compression studies are

widely reported in literature for compression of powders with very different physical properties such as metal powder [63,64], pharmaceutical [65,66,67,68,69,70] and ceramic materials [71,72,73,74]. Powder compression is another bulk experimental technique that has also been used to validate and calibrate the DEM input parameters. For example, it was used as bulk physical test for the calibration of the DEM model [75]. An optimisation procedure was used, based on the comparison of bulk experimental results with the numerical model of the same bulk compression experiment in case of large size particles (single and paired glass beads, polyethylene terephthalate pellets, black eyed beans and black kidney beans).

In Figure 3.24 a general schematic of the micromechanics and deformation mechanisms that occurs during bulk compression are illustrated [76].

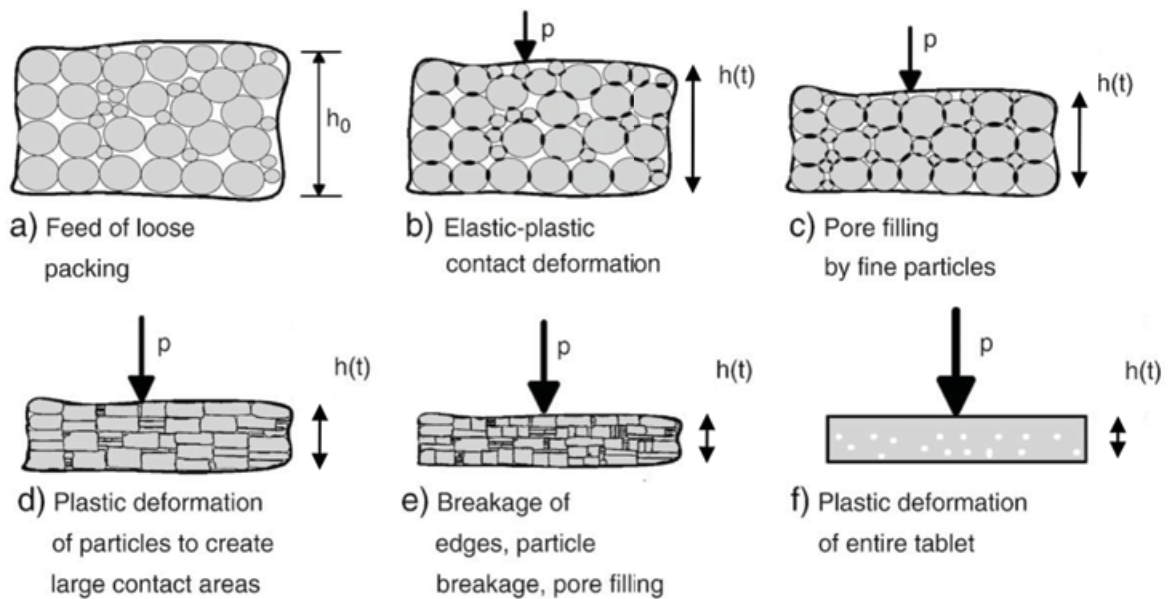


Figure 3.24: Typical sequences of mechanisms during powder compression [76].

$h_0$  is the initial bed height and  $h(t)$  is the value at the current applied pressure  $P$ . Initially during compression, loosely packed particles translate and rotate, at relatively small contact deformations. Subsequently particles deform and break as result of the increase in the elastic-

plastic contact stresses. Finally, the entire tablet would plastically deform. The influence and the extent of the described steps depend on the physical and mechanical properties for the particulate material that is undergoing compression.

Different porosity-pressure models such as: Heckel, Kawakita and Lüdde and Adams, can be employed to correlate the amount of volume reduction to the applied pressure during compression for a single powder component or a compound of powders [77,78,79,80].

### 3.6.1 Bulk powder compaction: tests results for zeolite ZSM5

Confined compression of the powders was performed using a materials testing machine Instron 5500 equipped with a cylindrical die with an internal diameter of 27.56 mm and flat-faced punches. The compression force was measured using a 15 kN load cell transducer. The schematic diagram of the axial machine is shown in Figure 3.25. The movable top punch was made to descend in order to compress the powder samples until the maximum compaction force 12 kN was reached.

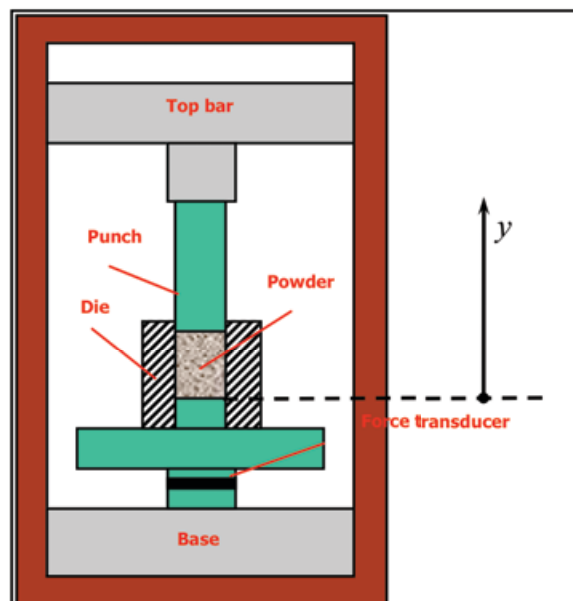


Figure 3.25: Schematic representation set-up of the bulk compression machine Instron 5500.

The amount of powder introduced into the die for each test was pre-weighed. The displacement-force data were collected and transferred to a computer. The initial powder bed height was recorded when contact was first made between the punch surface and the bed. The aspect ratio was calculated from the recorded bed height. Tablets were compressed at different punch speeds as reported in Table 3.11. The stress transmission and stress distribution during the compression process could be affected by the aspect ratio A.R., ratio of the initial bed height to powder bed diameter. Therefore in order to evaluate the potential influence of this ratio on the derived bulk compression parameters, different bed aspect ratios were considered, by pouring different quantity of material into the die.

Table 3.11: Bulk compaction conditions.

<b>Tablet</b>	<b>A.R.</b>	<b>Velocity punch (mm s<sup>-1</sup>)</b>
T1	0.98	0.01
T2	0.83	0.01
T3	0.91	0.01
T4	1.14	0.05
T5	0.78	0.05
T6	0.89	0.1
T7	1.56	0.1
T8	0.66	0.1
T9	0.84	0.2
T10	1.56	0.8

In Figure 3.26 typical compression pressure–engineering strain curves are reported for bulk compression of zeolite particles at different punch speeds for the Instron machine. The data were used to plot the Heckel, Kawakita and Adams models. It can be observed that there is no variation in the compaction behaviour with punch speed. All the curves show a similar trend.

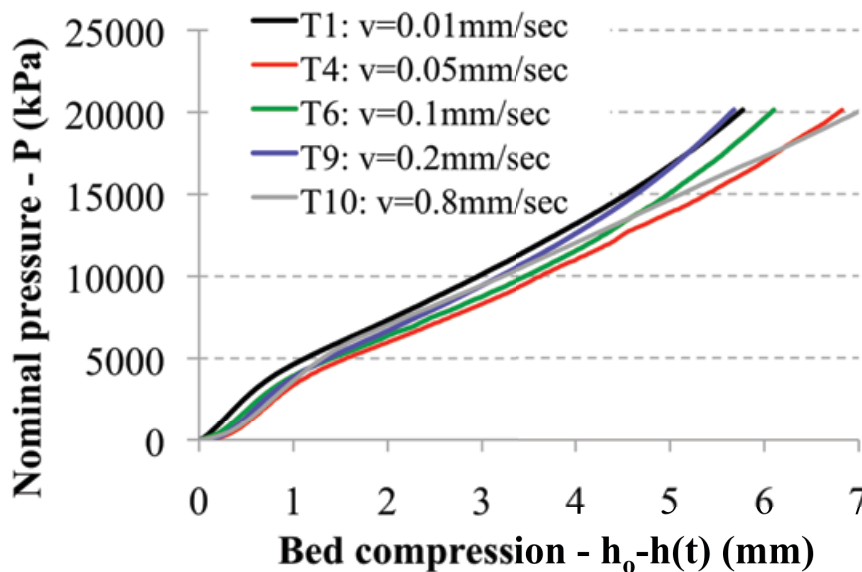


Figure 3.26: Nominal pressure  $P$  against punch displacement curves for the bulk compression for different punch speed.

Considering the bulk compression curve for the tablet T1 reported in Figure 3.27, three different changes in slope can be observed. These represent to different densification behaviour of the powder bed during the compression. During the *first stage*: the powder densification is low (steeper slope) probably due to that the particles are very hard and probably only deform elastically, bulk bed density slightly increases due to particle rearrangement (see also Figure 3.28). During the *second stage* the bulk of bed is probably deforming plastically, particle breakage is occurring with a decrease in bed voidage (higher bed densification). During the *third stage* the voidage has reduced and bulk and the bed

densification decreases. During this stage the entire bulk of material is probably deforming elasto-plastically (see also Figure 3.28.a).

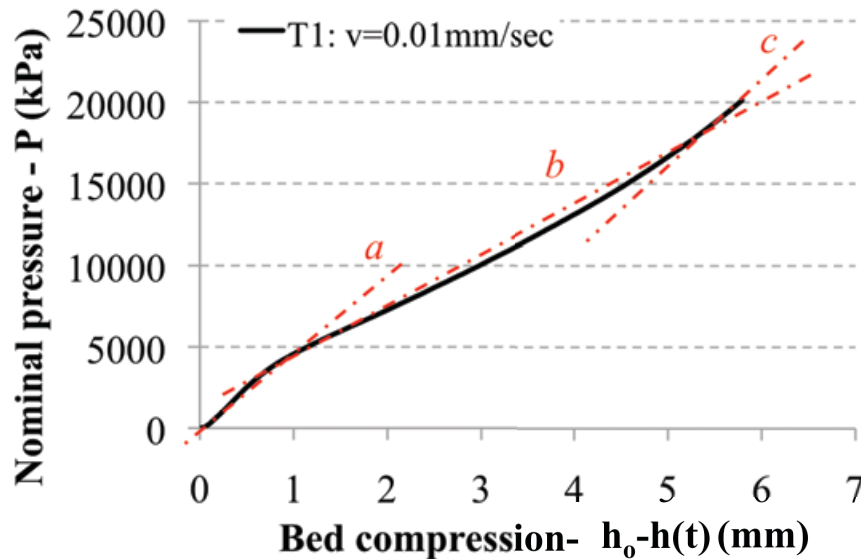


Figure 3.27: Bulk compression for zeolite particles for different punch speed.

To study the bulk behaviour of the bed during compression, one single tablet has been compressed in multiple stages as follows. These measurements have been performed at low punch speed of  $0.01 \text{ mm s}^{-1}$ . The nominal pressure versus displacement is reported in Figure 3.28 for the multiple stages compressions.  $h_o$  is the initial bed height and  $h$  is the actual bed height during compression. The unloading cycle is not shown on the graph for clarity.

- 1<sup>st</sup> compression from 0 up to 1000 N (1677 Pa) then load released to 0;
- 2<sup>nd</sup> compression from 0 up to 2000 N (3354 Pa) then load released to 0;
- 3<sup>rd</sup> compression from 0 up to 3000 N (5031 Pa) then load released to 0;
- 4<sup>th</sup> compression from 0 up to 4000 N (6709 Pa) then load released to 0;
- 5<sup>th</sup> compression from 0 up to 8000 N (13417Pa) then load released to 0;
- 6<sup>th</sup> compression from 0 up to 12000 N (20126 Pa) then load released.

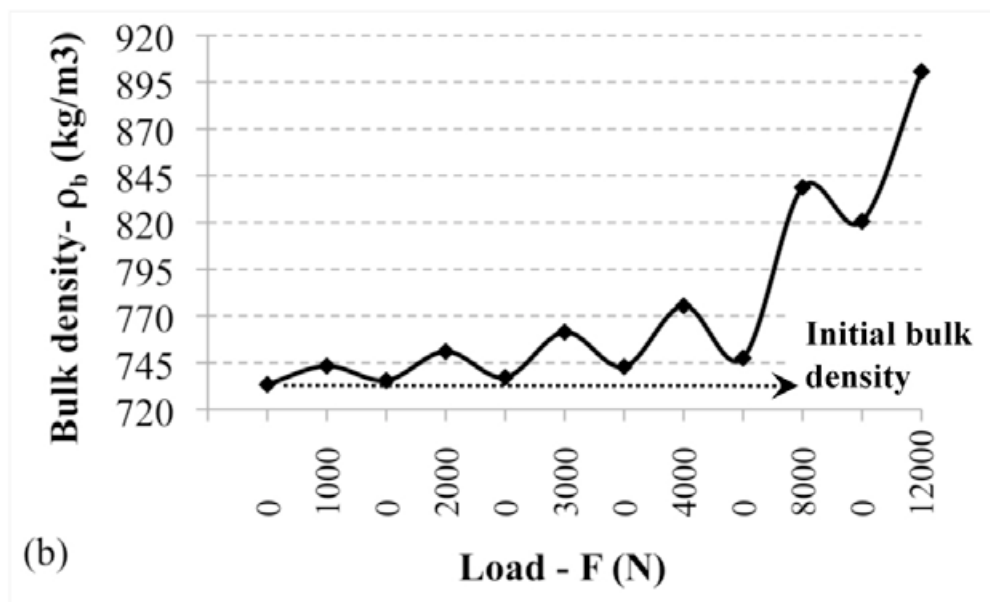
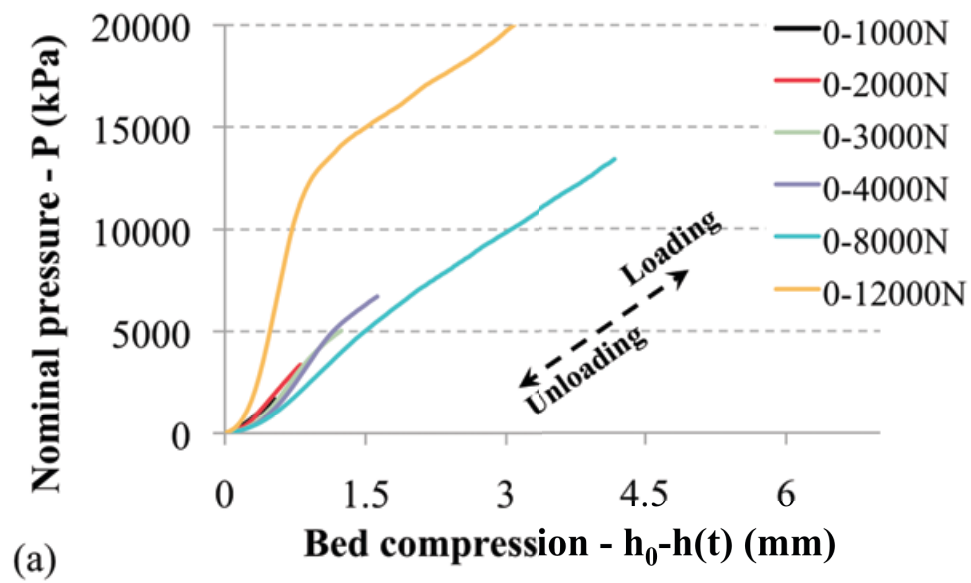


Figure 3.28: Single tablet multiple compression loading and unloading cycles. Powder bed is subsequently loaded and unloaded for different cycles. (a) only the loading curves are shown for clarity. (b) the change in bulk density is shown.

It can be observed from Figure 3.28 that up to 2000 N the bed is deforming almost elastically. When the load is released the bulk density returns close to the same initial value of the poured density. In the normal pressure versus normal displacement plot it is a straight line. When the

tablet is compressed again up to 3000 and 4000 N some changes in bulk density occur and after releasing the load the bulk density is increased. In the normal pressure against normal displacement plot the data is not linear. The bed starts to deform plastically as can also be observed in Figure 3.28.b, when the slope of the compression curve starts to change, approximately during the 8000 N compression cycle. It can be observed that the bulk density changes dramatically corresponding probably with plastic deformation of bed.

### 3.6.2 The Heckel model

The Heckel model is widely used in literature and it can be used to describe the change in bed density as function of the applied stress. Initially it was developed for metal powders and therefore it was only meant to apply to materials when plastic deformation is the predominant mechanism, however it has been used in pharmaceutical and ceramic applications as well [69,70,71,72].

The Heckel model was derived from the first order differential equation, Eq.(3.18), first presented in which relates the bed porosity  $e_b$  to the applied pressure  $P$  and the parameter  $K$ .

$$\frac{-de_b}{dP} = K e_b \quad (3.18)$$

By integrating and applying the initial boundary condition,  $e_i$  the initial bed porosity at zero pressure, Eq.(3.18) becomes:

$$\ln \frac{1}{e} = \ln \frac{1}{e_i} + K P \quad (3.19)$$

Heckel modified the previous equation by replacing the parameter bed porosity  $e$  with the  $(1-D)$ , where  $D$  is the relative density and assumed that the term  $\ln(1/e_i)$  is a constant parameter  $A$ , therefore:

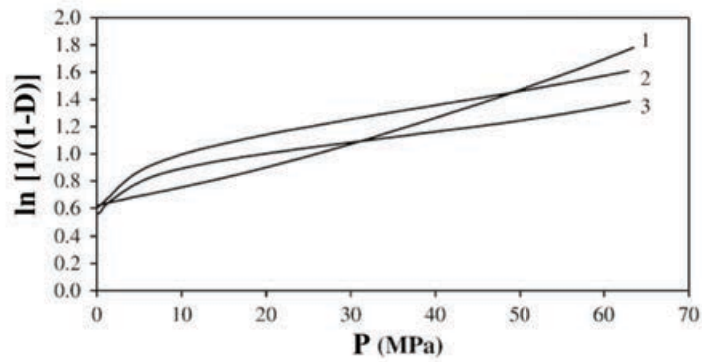
$$\ln \frac{1}{1-D} = A + K P \quad (3.20)$$

The relative density  $D$  is the ratio of the bed bulk density to the true particle density. The slope and intercept of the linear relationship involving  $\ln[1/(1-D)]$  as a function of applied pressure  $P$  can be used to determine the Heckel parameters  $A$  and  $K$  by fitting the compression data using Eq.(3.20). Usually the plots show deviation from linearity especially in the initial stage when particles undergo some rearrangement without any deformation or breakage and at high pressure. Linearity is usually observed in the middle pressure range. It has been shown that harder materials are then more difficult are to densify. A linear Heckel plot should indicate ductile behaviour of particles during compaction, whereas a curvilinear plot usually indicates brittle behaviour [81]. The effect of several parameters can change the Heckel plot, in particular the particle size, lubrication, compression rate, technique of die filling [53].

The Heckel parameter  $K$  is inversely related to the yield stress  $\sigma_y$  (yield strength of unconfined single particle) of individual particles as given by Eq.(3.21) and is related with the ability of the material to deform plastically [67,82]. Hence the Heckel model can be employed mainly for materials that consolidate by plastic deformation [67].

$$K = \frac{1}{H} \quad (3.21)$$

An example for Heckel plot is given in Figure 3.29, the data sets reported are for Eudragit® polymer particles. In case of the Heckel plot the initial curvature is attributed to initial particle



Heckel plots for Eudragit® particles:  
(1) L100-55, (2) L100, (3) S100.

Figure 3.29: Typical Heckel plot for Eudragit® polymer particles [67].

### 3.6.3 The Kawakita model

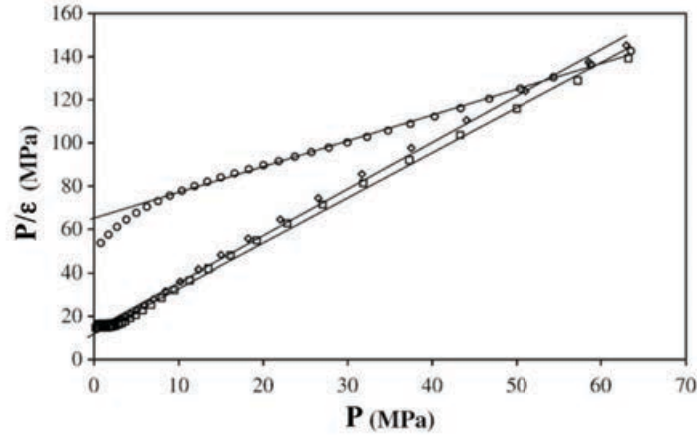
Another model extensively employed in pharmaceutical industry, [66,67,68,69], was proposed by *Kawakita and Lüdde* for fluffy and soft materials by the following linear empirical equation:

$$\frac{P}{\varepsilon} = \frac{1}{ab} + \frac{P}{a} \quad (3.22)$$

where  $\varepsilon$  is defined as the extent of volume reduction or uniaxial strain as follows:

$$\varepsilon = \frac{h_o - h}{h_o} = \frac{V_o - V}{V_o} \quad (3.23)$$

$h_o$  is the initial bed height and  $h$  is the value at the current applied pressure  $P$ . The constant  $a$  is related to the initial bed porosity and constant  $b$  is related to the resistance force. The term  $b$ , called Kawakita parameter, has been shown to be proportional to the reciprocal of the single particle failure stress forming the tablet feed [66]. An example for Kawakita plot is given in Figure 3.30, the data sets reported are for Eudragit® polymer particles.



Kawakita plot for Eudragit® particles:  
 (○) L100-55, (◇) L100 and (□) S100.

Figure 3.30: Typical Kawakita plot for Eudragit® polymer particles [67].

### 3.6.4 The Adams model

The Adams model consists of a theoretical model for the confined uniaxial compression of agglomerates based on a first-order lumped-parameter analysis for the compression process. The failure of single particles within a column of particles is due to the uniaxial compression stress  $P$ , constrained by the radial stress  $P_l$  that acts laterally on the neighbouring particles. The relationship between the bed pressure  $P$  and the bed height  $h$  is:

$$dP = -k_2 \tau \frac{dh}{h} \quad (3.24)$$

where  $k_2$  is a constant. The Adams model was developed to estimate the fracture strength of single granules from the Mohr-Coulomb failure criterion, which was employed to explain the macroscopic failure stress. In this criteria the shear failure stress,  $\tau$  is related to the sum of the cohesive strength,  $\tau_0$  and the frictional stress,  $\alpha P_l$ , acting at the failure plane as follows:

$$\tau = \tau_0 + \alpha P_l \quad (3.25)$$

$\alpha$  is defined as the lateral pressure coefficient. It was also assumed that the force  $F$ , the failure force of the weakest granule in axial direction, is proportional to the product of the failure stress  $\tau$  and the cross-sectional area of the fracture plane,  $A$ , as follows

$$F = k_1 \tau A \quad (3.26)$$

where  $k_1$  is a proportional constant. By including Eq.(3.25) into Eq.(3.24) and considering that lateral pressure  $P_l$  is related to the axial pressure by the constant  $k_3$ , ( $P_l = k_3 P$ ) the following equation is derived:

$$\ln P = \ln\left(\frac{\tau'_o}{\alpha'}\right) + \alpha' \varepsilon_n + \ln\left(1 - e^{(-\alpha' \varepsilon_n)}\right) \quad (3.27)$$

where  $\tau'_o$  is the apparent strength of the single particles and  $\alpha'$  is the apparent coefficient of friction and  $\varepsilon_n = \ln\left(\frac{h_o}{h}\right)$  is the natural bed strain. At high stress the last term of Eq.(3.27) becomes negligible and can be eliminated, leaving a linear function. The slope and intercept of the linear part of the graph can be used to calculate the Adams parameters  $\tau'_o$  and  $\alpha'$ . The previous parameters are related to  $\tau_o$  and  $\alpha$ :

$$\tau'_o = k_2 \tau_o \quad (3.28)$$

$$\alpha' = k_2 k_3 \alpha \quad (3.29)$$

An example for Adams plot is given in Figure 3.31, the data sets reported are for Eudragit<sup>®</sup> polymer particles.

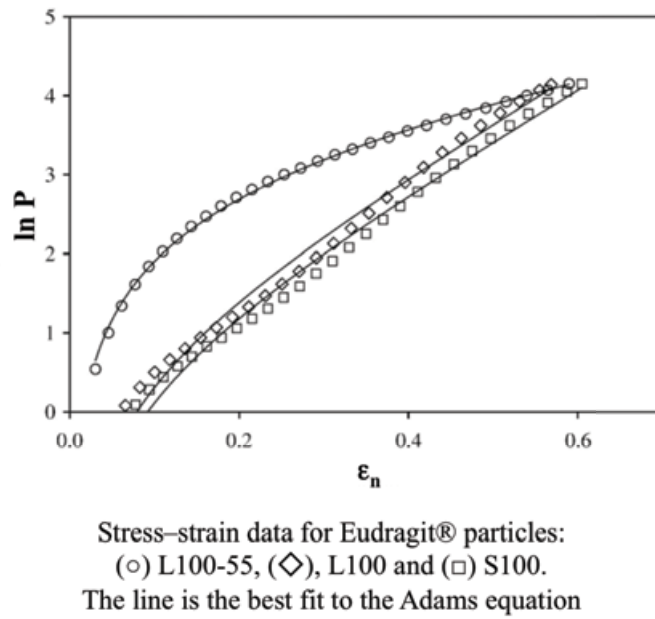


Figure 3.31: Typical Adams plot for Eudragit® polymer particles [67].

### 3.6.5 Heckel, Kawakita and Adams plots for zeolite ZSM5

In Figure 3.32, Figure 3.33 and Figure 3.34 the Heckel, Kawakita and Adams plots over full the compression load (12 kN) are showed for the tablet T1.

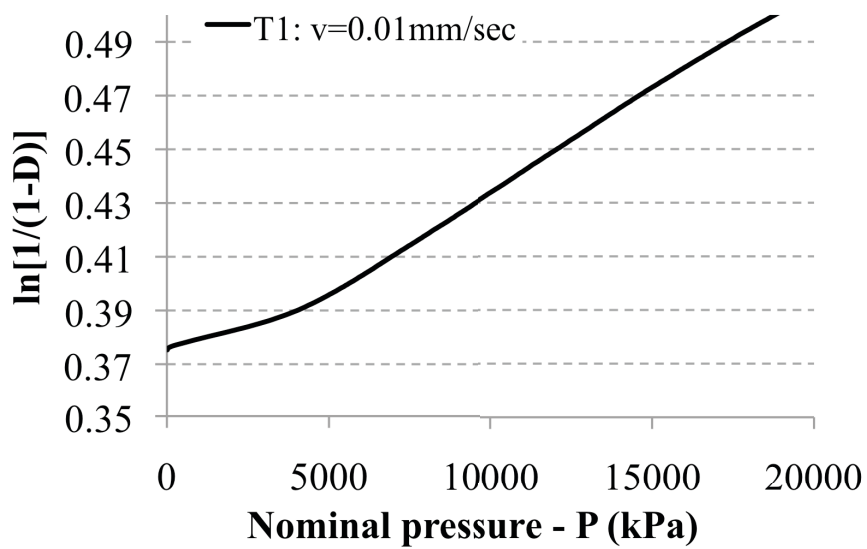


Figure 3.32: Heckel compression curve for tablet T1.

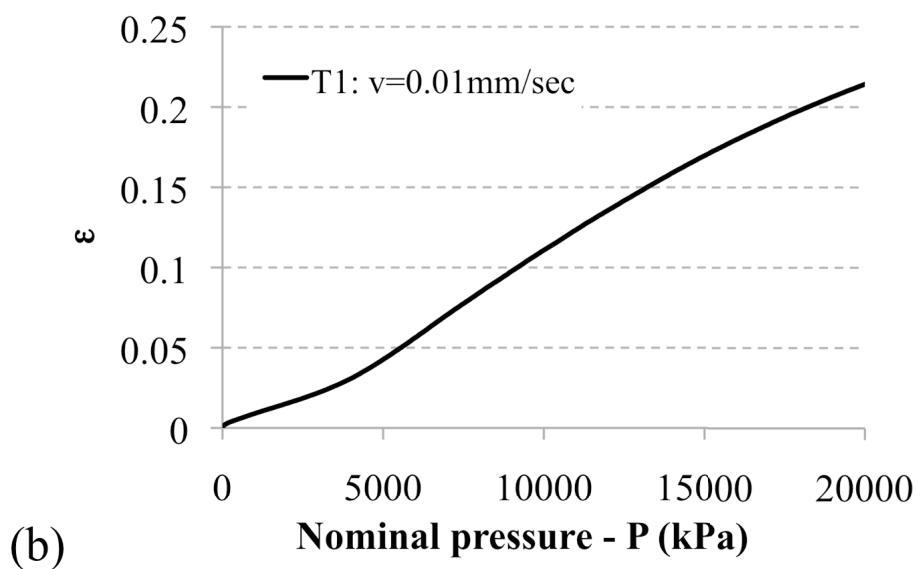
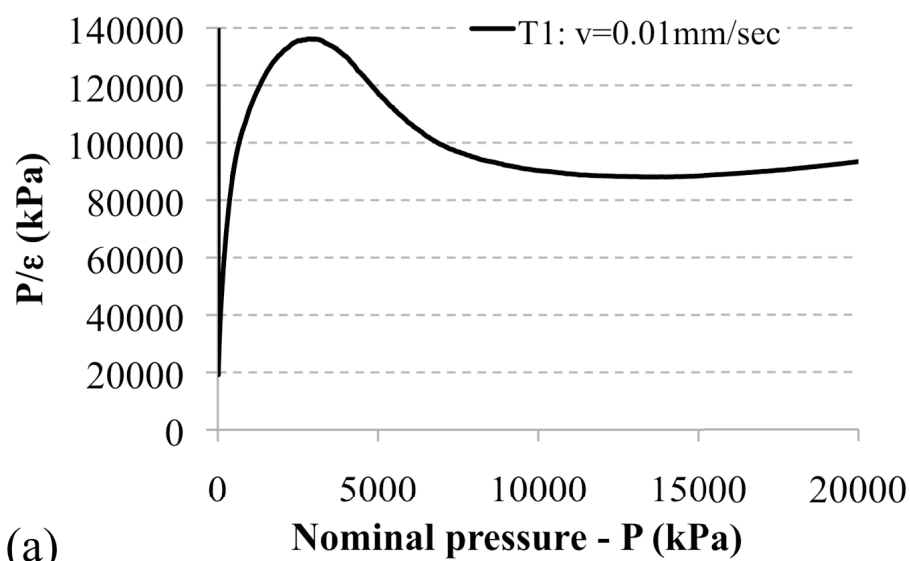


Figure 3.33: (a) Kawakita compression curve for tablet T1 (b) degree of compression as function of the applied pressure.

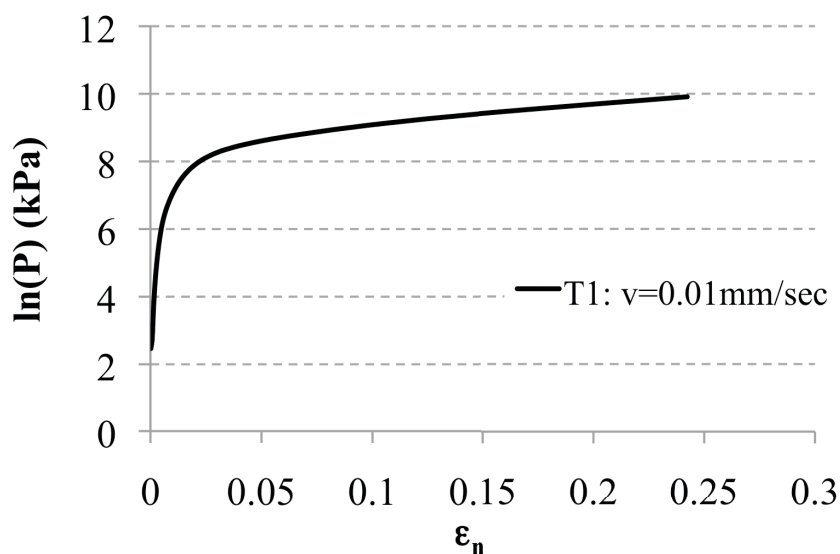


Figure 3.34: Adams compression curve for tablet T1.

It can be observed that the Heckel and Kawakita models are not linear over the full compression range up to 12 kN. Therefore the Heckel and Kawakita models, Eq.(3.20) and Eq.(3.22), do not fit the experimental data for the entire compression range.

The Heckel and Kawakita data are also presented for the initial stages of compression (up to 2000 kPa) as shown in Figure 3.35. Therefore, parameters  $K$ ,  $a$ ,  $b$ , were determined by linear regression in the pressure range 0 to 2000 kPa, using the expression of the Heckel and Kawakita equations Eq.(3.20) and Eq.(3.22). The parameters  $\tau'_o$  and  $\alpha'$  were thus determined over the full compression range by linear regression in the linear interval as depicted in Figure 3.36 according to the Adams relationship, Eq.(3.27).

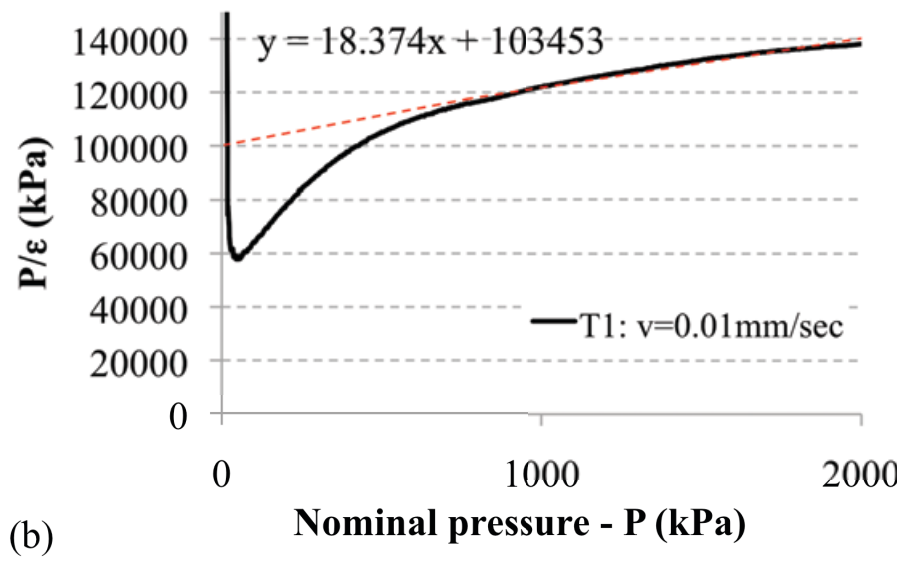
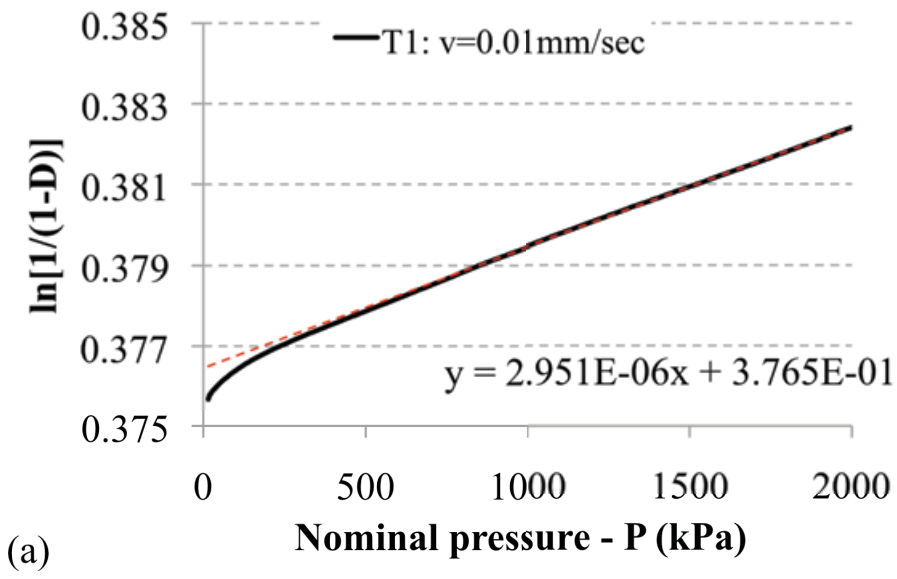


Figure 3.35: Linear fitting compression curves for table T1 up to 2000 N normal load.

(a) Heckel relationship. (b) Kawakita relationship.

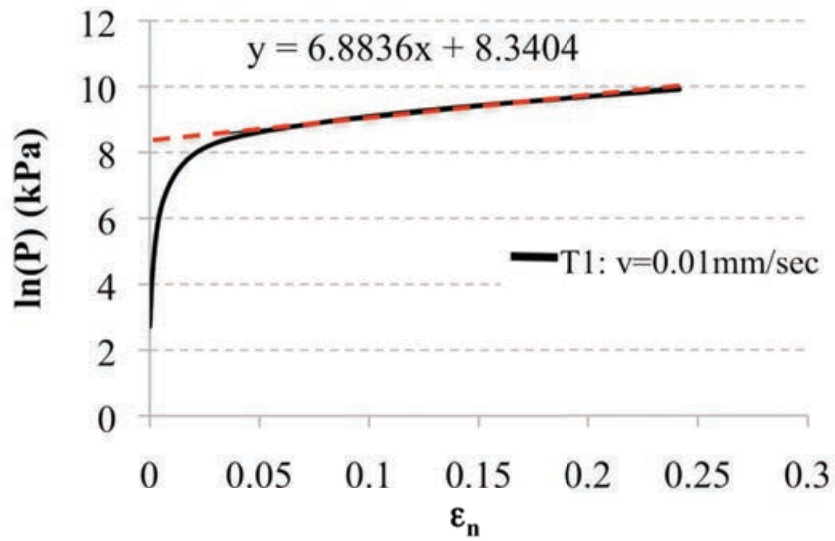


Figure 3.36: Linear fitting compression curves for table T1 up to 12000 N normal load, Adams relationship.

Figure 3.37 shows the parameters (apparent strength of the single particles  $\tau'_o$  and the apparent coefficient of friction  $\alpha'$ ) from the Adams model as function of the initial aspect ratio A.R. From the plots it can be commented that the aspect ratio has an effect on the bed compressibility, as probably function of wall friction [53]. Therefore the apparent strength of the single particles  $\tau'_o$  and the apparent coefficient of friction  $\alpha'$  have been extrapolated by linear fitting at zero aspect ratio A.R. and reported in Table 3.12.

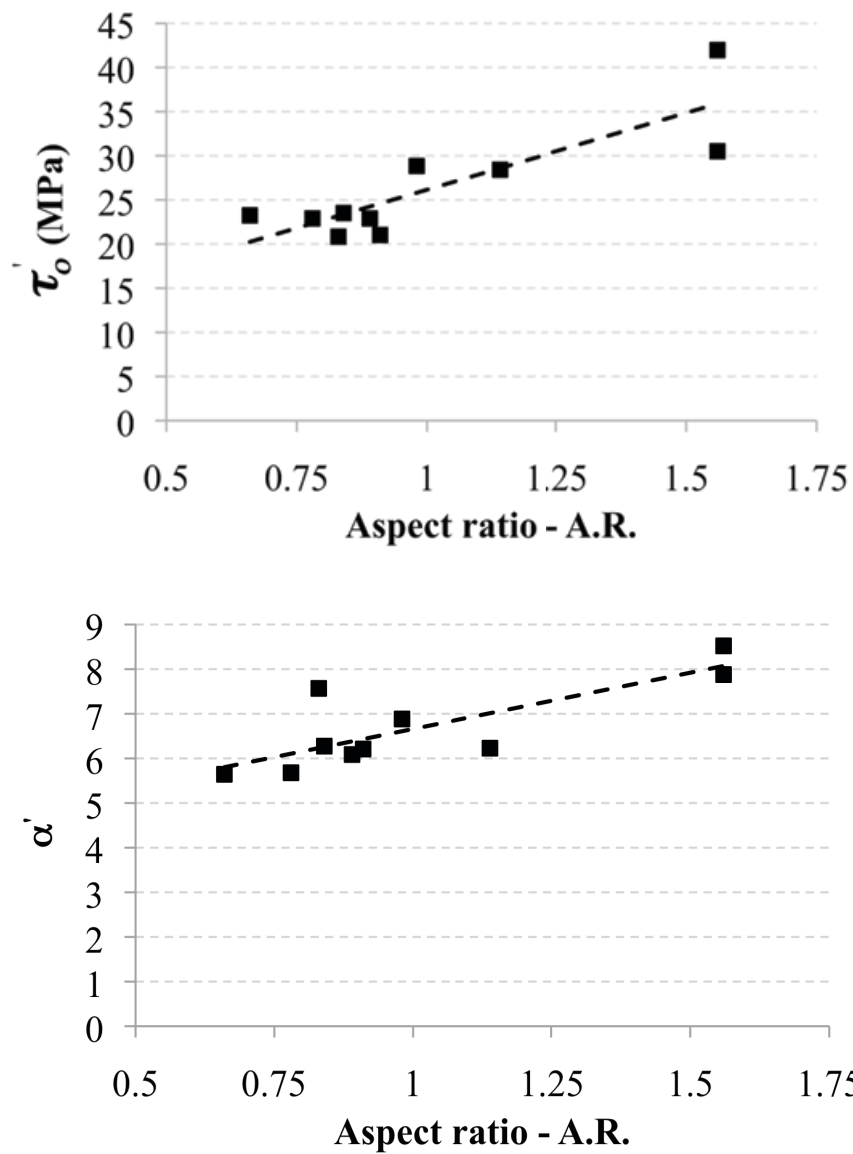


Figure 3.37: Effect of aspect ratio A.R. on  $\tau_o'$  and  $\alpha'$  parameters from the Adams model.

A comparison between the parameters obtained by bulk compression models (*Heckel*, *Kawakita* and *Adams*) and the results from the single particle compression is reported in Table 3.12.

Table 3.12: Average values of bulk compression parameters from Heckel, Kawakita and Adams models compared with single particles compression test and Nanoindentation. Only the apparent strength from the Adams model is comparable with single particle strength data.

Heckel	Kawakita		Adams (A.R.=0)		Single particle compression		Nanoindentation
	a	1/b (kPa)	$\alpha'$	$\tau'_o$ (MPa)	$\sigma_{cr}$ (MPa)	$\sigma_0$ (MPa)	
0.31	0.04	1.93	4.14	8.76	9.8	10.8	0.604 - 1.973

From Table 3.12 it can be observed that the Heckel parameter,  $1/K$ , is not comparable with the particles hardness  $H$  as defined in Eq.(3.21). This probably remarks that the Heckel model is not suitable to represent the bulk compression of ZSM5 zeolite particles. Also the Kawakita model seems to be not suitable, as the Kawakita parameter,  $1/b$ , should be proportional to the single particle strength. The Adams models which was developed for granules seems to fit the bulk compression data according as the predicted apparent strength of the single particles  $\tau'_o$  is in good agreement with the particle strengths  $\sigma_{cr}$  and  $\sigma_0$  determined by single particle compression test ( $\sigma_{cr}$  particle crushing strength and  $\sigma_0$  crushing strength with a fracture probability of 63.2%).

### 3.7 Conclusions

The mechanical properties for ZSM5 zeolite particles have been characterized by using different powder characterisation techniques. Mechanical properties such as reduced elastic Young's modulus, yield stress and particle strength was characterized by single particle compression test. Hardness and reduced elastic Young's modulus was also measured by Berkovich nanoindentation and they were found to be proportional to the indentation depth. The elastic modulus measured by nanoindentation (between 9.6 and 34.3 GPa) was found to

be different from the value obtained by single particle compression (2.93 GPa). Differences in value between the two techniques indicates the heterogeneity of the porous particles in terms of mechanical properties. Flowability of material can be described by using methods such as Carr's index and Hausner ratio, which show exceptional flowability for the zeolite particles. Internal friction coefficients, particle-particle and particle-wall material, were measured as bulk measurement at consolidated state by using a Schulze shear cell. Again it was observed that zeolite spray dried particles have exceptional flowability. Although these techniques give an indication of flowability of a powder and specifically the Schulze ring tester gives a numerical value for an internal coefficient of particle-particle and particle-wall friction it is difficult to obtain the DEM input parameter for friction (static and rolling) as conventionally defined in Chapter 2. The bulk compression test showed that, at low pressure the densification is low and this is probably due to the high particle strength and particle hardness. It was also found that for the material under exam the usual bulk compression models, Heckel and Kawakita, do not fit the experimental data. The Adams model seems to describe the experimental bulk compression data and the predicted Adams parameter, apparent strength for the single particles  $\tau'_o$  was in good agreement with the particle strength determined by single particle compression test,  $\sigma_{cr}$ . These latter bulk measurements techniques can not be used to determine directly the DEM single particle input parameters, however they can be employed for DEM model calibration by fitting the numerical simulations to the bulk experiment results and optimization of the simulation parameters. However, this procedure can be time consuming and difficulties arise in case of small particles since the computational effort can be unachievable with the current state of the art. An example of the unachievable long predicted simulation time is given in Chapter 5, in the case of mixing of zeolite particles in a Turbula blender.

### 3.8 References

- [1] J.C. Bailly, R. Hagege, Use of image analysis for the knowledge and control of polymer and Ziegler-Natta catalyst granulometry, *Polymer* **32** (1991), pp. 181-190.
- [2] F. Mahmud, M. Atiqullah, N. Jarrah, I. Hussain, Measurement of shape and size distributions of PVC resin particles by scanning electron microscopy and image analysis, *European Polymer Journal* **28** (1992), pp. 1039-1043.
- [3] M.M. Haridas, J.R. Bellare, Differences in particle sizes measured by cryo-sem and quasi-elastic light scattering in latex particles, *Colloids and Surfaces A: Physicochemical and Engineering Aspects* **133** (1998), pp. 165-171.
- [4] U. Foerter-Barth, U. Teipel, Characterization of particles by means of laser light diffraction and dynamic light scattering, *Developments in Mineral Processing* **13** (2000), pp. C1-1-C1-8.
- [5] Z. Ma, H.G. Merkus, J.G.A.E. de Smet, C. Heffels, B. Scarlett, New developments in particle characterization by laser diffraction: size and shape, *Powder Technology* **111** (2000), pp. 66-78.
- [6] C. Marriott, H.B. MacRitchie, X.-M. Zeng, G.P. Ma, Development of a laser diffraction method for the determination of the particle size of aerosolised powder formulations, *International Journal of Pharmaceutics* **326** (2006), pp. 39-49.
- [7] L.-S. H. Lum, S.G. Malghan, S.B. Schille, Standard reference materials for particle size analysis of ceramic powders by gravity sedimentation, *Powder Technology* **87** (1996), pp. 233-238.
- [8] R. Beckett, D. Murphy, S. Tadjiki, D.J. Chittleborough, J.C. Giddings, Determination of thickness, aspect ratio and size distributions for platey particles using sedimentation field-flow fractionation and electron microscopy, *Colloids and Surfaces A:*

- Physicochemical and Engineering Aspects* **120** (1997), pp. 17-26.
- [9] H. Yoshida, H. Masuda, K. Fukui, Y. Tokunaga, Particle size measurement with an improved sedimentation balance method and microscopic method together with computer simulation of necessary sample size, *Advanced Powder Technology* **12** (2001), pp. 79-94.
- [10] L. Pieri, M. Bittelli, P.R. Pisa, Laser diffraction, transmission electron microscopy and image analysis to evaluate a bimodal Gaussian model for particle size distribution in soils, *Geoderma* **135** (2006), pp. 118-132.
- [11] S.J. Andersen, B. Holme, C.D. Marioara, Quantification of small, convex particles by TEM, *Ultramicroscopy* **108**, pp. 750-762.
- [12] C.M.P. Vaz, P.S. P. Herrmann, S. Crestana, Thickness and size distribution of clay-sized soil particles measured through atomic force microscopy, *Powder Technology* **126**, pp. 51-58.
- [13] L.G. Gladkis, R.W. Li, J.M. Scarvell, P.N. Smith, H. Timmers, Exploration of the size, shape and abundance of UHMWPE wear particles using atomic force microscopy *Wear* **267** (2009), pp. 632-638.
- [14] V. Gélinas, D. Vidal, Determination of particle shape distribution of clay using an automated AFM image analysis method, *Powder Technology* **203** (2010), pp. 254-264.
- [15] D.C. Joy, Scanning electron microscopy for materials characterization, *Current Opinion in Solid State and Materials Science* **2** (1997), pp. 465-468.
- [16] A. Markowicz, B. Raeymaekers, R. Van Grieken, F. Adams, Analytical electron microscopy of single particles, In: *Physical and Chemical Characterization of Individual Airborne Particles K.R. Spurny (Ed.)*, Ellis Horwood, Chichester UK, (1986), pp. 173–197.

- [17] B. Raeymaekers, P. Van Espen, F. Adams, The morphological characterization of particles by automated scanning electron microscopy, *Mikrochimica Acta* **83** (1984), pp. 437–454.
- [18] F. Mahmud, M. Atiqullah, N. Jarrah, I. Hussain, Measurement of shape and size distributions of PVC resin particles by scanning electron microscopy and image analysis, *European Polymer Journal* **28** (1992), pp. 1039-1043.
- [19] E.M. Ålander, M.S. Uusi-Penttilä, Å.C. Rasmuson, Characterization of paracetamol agglomerates by image analysis and strength measurement, *Powder Technology* **130** (2003), pp. 298-306.
- [20] E.T. Bowman, K. Soga, T.W. Drummond, Particle shape characterisation using Fourier descriptor analysis. *Géotechnique*, **51** (2001), pp. 545-554.
- [21] H. Abou-Chakra, J. Baxter, U. Tüzün, Three-dimensional particle shape descriptors for computer simulation of non-spherical particulate assemblies, *Advanced Powder technology* **15** (2004), pp. 63-77.
- [22] Britannica Online Encyclopedia, (2010). Scanning Electron Microscope [online]. Available: <http://www.britannica.com/EBchecked/topic/526571/scanning-electron-microscope>, [accessed June 2010].
- [23] Z. Ma, H.G. Merkus, J. G.A.E. de Smet, C. Heffels, B. Scarlett, New developments in particle characterization by laser diffraction: size and shape, *Powder Technology* **111** (2000), pp. 66-78.
- [24] A. Santomaso, P. Lazzaro, P. Canu, Powder flowability and density ratios: the impact of granules packing, *Chemical Engineering Science* **58** (2003), pp. 2857-2874.
- [25] K. Thalberg, D. Lindholm, A. Axelsson, Comparison of different flowability tests for powders for inhalation, *Powder Technology* **146** (2004), pp. 206-213.

- [26] J.F. Carr, D.M. Walker, An annular shear cell for granular materials, *Powder Technology* **1** (1968), pp. 369-373.
- [27] K. Shinohara, B. Golman, Dynamic shear properties of particle mixture by rotational shear test, *Powder Technology* **122** (2002), pp. 255-258.
- [28] R. Freeman, Measuring the flow properties of consolidated, conditioned and aerated powders — A comparative study using a powder rheometer and a rotational shear cell, *Powder Technology* **174** (2007), pp. 25-33.
- [29] A.W. Jenike, Gravity flow of bulk solids, *Utah Eng Exp Stn Bull.* **108** (1961), pp. 1-294.
- [30] A.W. Jenike, Storage and flow of solids, *Utah Eng Exp Stn Bull.* **123** (1964), pp. 1-194.
- [31] S. Kamath, V.M. Puri, H.B. Manbeck, Flow property measurement using the Jenike cell for wheat flour at various moisture contents and consolidation times, *Powder Technology* **81** (1994), pp. 293–297.
- [32] H. Jaeda, The Use of a Ring Shear Tester to Evaluate the Flowability of Pharmaceutical Bulk Solids, PhD thesis, Fakultät der Heinrich-Heine-Universität Düsseldorf DE (2009).
- [33] J. Schwedes, Testers for measuring flow properties of particulate solids, *Powder Handling & Processing* **12** (2000), pp. 337-354.
- [34] J. Schwedes, Review on testers for measuring flow properties of bulk solids, *Granular Matter* **5** (2003), pp. 1-43.
- [35] R.J.M. Janssen, M.J. Verwijs, B. Scarlett Measuring flow functions with the Flexible Wall Biaxial Tester, *Powder Technology* **158** (2005), pp. 34-44.

- [36] N. Harnby, A.E. Hawkins, D. Vandame, Use of bulk density determination as a means of typifying the flow characteristics of loosely compacted powders under conditions of variable relative humidity, *Chemical Engineering Science* **42** (1987), pp. 879–888.
- [37] A.C.-Y. Wong, Characterisation of the flowability of glass beads by bulk densities ratio, *Chemical Engineering Science* **55** (2000), pp. 3855-3859.
- [38] D. Geldart, E.C. Abdullah, A. Hassanpour, L.C. Nwoke, I. Wouters, Characterization of powder flowability using measurement of angle of repose, *China Particuology* **4** (2006), pp. 104-107.
- [39] R. Hedge, J.L. Rheingold, S. Welch and C.T. Rhodes, Studies of powder flow using a recording powder flowmeter and measurement of the dynamic angle of repose, *Journal of Pharmaceutical Sciences* **74** (1985), pp. 11–15.
- [40] D.M. Walker, An approximate theory for pressures and arching in hoppers, *Chemical Engineering Science* **21** (1966), pp.975–997.
- [41] J.J. McCarthy, V. Jasti, M. Marinack, C.F. Higgs, Quantitative validation of the discrete element method using an annular shear cell, *Powder Technology* **203** (2010), pp. 70-77.
- [42] R.O. Greyand, J.K. Beddow, On the Hausner, Ratio and its relationship to some properties of metal powders, *Powder Technology* **2** (1969), pp. 323-326.
- [43] H.H. Hausner, Friction conditions in a mass of metal powder, *International Journal of Powder Metallurgy* **3** (1967), pp. 7-13.
- [44] X. Xu, S. Yao, N. Han B. Shao, Measurement and Influence Factors of the Flowability of Microcapsules with High-content  $\beta$ -Carotene, *Chinese Journal of Chemical Engineering* **15** (2007), pp. 579-585.

- [45] R. Carr, Evaluating flow properties of solids, *Chemical Engineering Journal* **72** (1965), pp. 163-168.
- [46] Copley Scientific website, (2009). Quality Solutions for the Testing of Pharmaceuticals [online]. Available: [http://www.copleyscientific.co.uk/documents/ww/Solid%20Dosage%20Brochure%202009%20\(Low%20Res\).pdf](http://www.copleyscientific.co.uk/documents/ww/Solid%20Dosage%20Brochure%202009%20(Low%20Res).pdf), [accessed July 2010].
- [47] D. Schulze, (2006). Flow properties of Powders and Bulk Solids [online]. Available: <http://www.dietmar-schulze.de/grdle1.pdf>, [accessed June 2010].
- [48] J.P.K. Seville, U. Tuzun, R. Cliff, Processing of particulate solids, first ed., *Blackie academic & professional*, London UK, (1997).
- [49] J. J. Fitzpatrick, S. A. Barringer, T. Iqbal, Flow property measurement of food powders and sensitivity of Jenike's hopper design methodology to the measured values, *Journal of Food Engineering* **61** (2004), pp. 399-405.
- [50] J. Tomas, Assessment of Mechanical Properties of Cohesive Particulate Solids. Part 2: Powder Flow Criteria *Particulate Science and Technology* **19** (2001), pp. 111-129.
- [51] D. Schulze, (2008). A test with the Ring Shear Tester RST-XS [online]. Available: <http://www.dietmar-schulze.de/leafxse.pdf>, [accessed June 2008].
- [52] H. Hertz, Über die Berührung fester elastischer Körper, *Journal für die Reine und Angewandte Mathematik* **92** (1882), pp. 156–171.
- [53] A. Samimi, A. Hassanpour, M. Ghadiri, Single and bulk compressions of soft granules: Experimental study and DEM evaluation, *Chemical Engineering Science*, **60** (2005), pp. 3993-4004.
- [54] R. Pitchumani, O. Zhupanska, G.M.H. Meesters, B. Scarlett, Measurements and characterization of particle strength using a new robotic compression tester, *Powder*

- Technology* **143-144** (2004), pp. 56-64.
- [55] Stable Micro System LTD, (2010). Catalysts seeking the next big thing, *Chemical Week* [online]. Available: <http://www.stablemicrosystems.com>, [accessed December 2010].
- [56] W. Weibull, A statistical distribution function of wide applicability, *Journal of Applied Mechanics* **18** (1951), pp. 293–297.
- [57] J.D. Sullivan, P.H. Lauzon, Experimental probability estimators for Weibull plots, *Journal of Materials Science Letters* **5** (1986), pp. 1245–1247.
- [58] J. Lin, X.F. Shu, J.X. Dong, The experimental determination of mechanical properties of zeolite ferrierite crystal, *Materials Letters* **59** (2005), pp. 1595-1597.
- [59] M. Meier, E. John, D. Wieckhusen, W. Wirth, W. Peukert, Influence of mechanical properties on impact fracture: Prediction of the milling behaviour of pharmaceutical powders by Nanoindentation, *Powder Technology* **188** (2009), pp. 301-313.
- [60] R. Wimmer, B.N. Lucas, T.Y. Tsui, W.C. Oliver, Longitudinal hardness and Young's modulus of spruce tracheid secondary walls using nanoindentation technique, *Wood Science and Technology* **31** (1997), pp. 131–141.
- [61] R.D. Dukino, M.V. Swain, Comparative measurement of indentation fracture toughness with Berkovich and Vickers indenters, *Journal of American Ceramic Society*, **75** (1992), pp. 3299-3304.
- [62] W.D. Nix, H. Gao, Indentation size effects in crystalline materials: a law for strain gradient plasticity, *Journal of Mechanics and Physics of Solids* **46** (1998), pp. 411–425.
- [63] K. Gan, M. Gu, The compressibility of Cu/SiC<sub>p</sub> powder prepared by high-energy ball milling, *Journal of Materials Processing Technology* **199** (2008), pp. 173-177.

- [64] S. Sivasankaran, K. Sivaprasad, R. Narayanasamy, Vijay Kumar Iyer, An investigation on flowability and compressibility of AA 6061100 -x-x wt.% TiO<sub>2</sub> micro and nanocomposite powder prepared by blending and mechanical, alloying *Powder Technology* **201** (2010), pp. 70-82.
- [65] A. Michrafy, D. Ringenbacher, P. Tchoreloff, Modelling the compaction behaviour of powders: application to pharmaceutical powders, *Powder Technology* **127** (2002), pp. 257-266.
- [66] Z. Zhang, J.P.K. Seville, M. Adams, S.F. Yap, Understanding the mechanical properties of single micro-particles and their compaction behaviour, *China Particuology*, **4** (2006), pp. 35-40.
- [67] S.F. Yap, M.J. Adams, J.P.K. Seville, Z. Zhang, Single and bulk compression of pharmaceutical excipients: Evaluation of mechanical properties, *Powder Technology* **185** (2008), pp. 1-10.
- [68] G. Frenning, J. Nordström, G. Alderborn, Effective Kawakita parameters for binary mixtures, *Powder Technology* **189** (2009), pp. 270-275.
- [69] I. Klevan, J. Nordström, A. Bauer-Brandl, G. Alderborn, On the physical interpretation of the initial bending of a Shapiro–Konopicky–Heckel compression profile, *European Journal of Pharmaceutics and Biopharmaceutics* **71** (2009), pp. 395-401.
- [70] I. Klevan, J. Nordström, I. Tho, G. Alderborn, A statistical approach to evaluate the potential use of compression parameters for classification of pharmaceutical powder materials, *European Journal of Pharmaceutics and Biopharmaceutics* **75** (2010), pp. 425-435.
- [71] R.E. Caligaris, R. Topolevsky, P. Maggi, F. Brog, Compaction behaviour of ceramic

- powders, *Powder Technology* 42 (1985), pp. 263-267.
- [72] M. Djuri, R. Marinkovi-Neduin, J. Ranogajec, M. Radeka, Particle size range as a factor influencing compressibility of ceramic powder, *Ceramics International* 21 (1995), pp. 227-230.
- [73] K.N. Ramakrishnan, R. Nagarajan, G.V. RamaRao, S. Venkadesan, A compaction study on ceramic powders, *Materials Letters* 33 (1997), pp. 191-194.
- [74] T.J. Vogler, M.Y. Lee, D.E. Grady, Static and dynamic compaction of ceramic powders, *International Journal of Solids and Structures* 44 (2007), pp. 636-658.
- [75] M.W. Johnstone, Calibration of DEM models for granular materials sing bulk physical tests, PhD thesis, The University of Edinburgh UK (2010).
- [76] M. Stasiak, J. Tomas, M. Molenda, R. Rusinek, P. Mueller, Uniaxial compaction behaviour and elasticity of cohesive powders, *Powder Technology* 203 (2010), pp. 482-488.
- [77] R.W. Heckel, Density–pressure relationships in powder compaction, *Trans. Metall. Soc. AIME* 221 (1961), pp. 671–675.
- [78] K. Kawakita, K.-H. Lüdde, Some considerations on powder compression equations, *Powder Technology* 4 (1971), pp. 61-68.
- [79] M.J. Adams, M.A. Mullier, J.P.K. Seville, Agglomerate strength measurement using a uniaxial confined compression test, *Powder Technology* 78 (1994), pp. 5–13.
- [80] P.J. Denny, Compaction equations: a comparison of the Heckel and Kawakita equations, *Powder Technology* 127 (2002), pp. 162-172.
- [81] G. Alderborn, C. Nyström, Pharmaceutical Powder Compaction Drugs and the pharmaceutical sciences, *Marcel Dekker Editor*, New York (1996).
- [82] R.J. Roberts, R.C. Rowe, The compaction of pharmaceutical and other model

materials - a pragmatic approach, *Chemical Engineering Science* **42** (1987), pp. 903-911.

## Chapter 4

### **Turbula mixer motion measurement and reconstruction using Positron Emission Particle Tracking (PEPT)**

*The complex motion of the Turbula mixer has been measured using Multiple-Positron Emission Particle Tracking (Multiple PEPT). A description of PEPT and the development of the Multiple-PEPT technique is given in the present chapter. Positron emitting radioactive tracers were attached to three points of the pivot bearings on the shaft of the mixer enabling the rotation and translation of the mixer chamber to be tracked in the PEPT camera. The measured movement was mathematically reconstructed and the dynamic imported into the DEM numerical model.*

#### **4.1 Introduction: Positron Emission Particle Tracking technique (PEPT)**

In order to determine the Turbula motion the Multiple-PEPT technique was employed. It has been shown that that Multiple-PEPT can track three particles at the same time with good accuracy [1]. It was shown that both the rotational and the translational motions of a solid body can be reconstructed by tracking three radioactively labelled tracers mounted to corners of the solid. The accuracy of the method relies on the fact that the tracers must be fixed and known distance apart.

##### **4.1.1 Positron Emission Particle Tracking**

PEPT is a non-invasive technique for following the motion of a radioactive tracer particle. It was developed at the University of Birmingham [2,3,4,5] from the established medical imaging technique Positron Emission Tomography (PET). The main advantages are that this technique allows us to see through and into opaque system and it does not need to be calibrated for attenuation such as Computer Automated Radioactive Particle Tracking (CARPT) [6]. This technique produces the trajectory of the particle moving in three dimensions. The path of the particle is given in Cartesian co-ordinates  $(x,y,z)$  versus time. By tracking the particle position with time it is also possible to calculate the particle speed and kinetic energy.

The camera used in the present work is the ADAC Forte dual-headed gamma camera located at the University of Birmingham, Figure 4.1. It consists of two heads on a motorised system, which permits rotation about a horizontal axis and adjustment of the face-to-face separation of the detectors from 250 to 800 mm. Each detector has an active area of  $500 \times 400 \text{ mm}^2$  and is mounted on either side of the field of view.

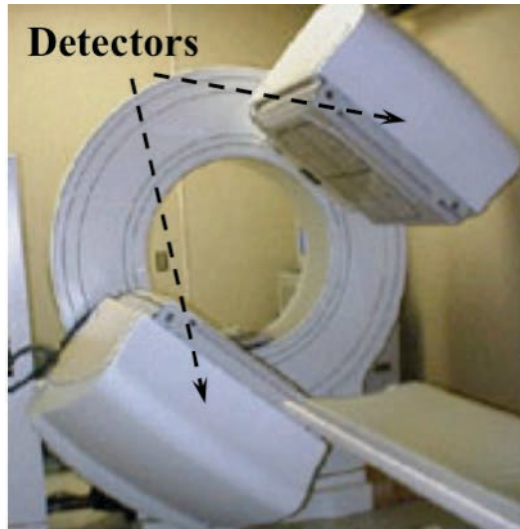


Figure 4.1: Positron ADAC Forte camera.

This camera is able to operate at useful count rates up to  $1 \times 10^5 \text{ s}^{-1}$ . The scintillator is optically coupled to an array of 55 photomultiplier tubes with each photomultiplier tube connected to a separate Analogue Digital Converter (ADC). Data is recorded event by event then processed. The accuracy of the technique depends on the measurement conditions, in particular the mass of material between the tracer particle and the camera detectors. In the setup employed to measure the Turbula mixer motion the tracer particles were not contained by any metallic part, since attached on the external chamber geometry as reported later. The only material between the tracers and the detectors was the 5 mm thickness polycarbonate guard. This should guarantee a good accuracy on the collected data.

The schematic set-up for the PEPT camera is shown in Figure 4.2. It consists of the pair of parallel detectors and the radioactive tracer. The tracer particle is labelled with a radionuclide, which decays by  $\beta^+$  decay resulting in the emission of a positron. Each positron rapidly annihilates with an electron, producing a pair of back-to-back  $\gamma$ -rays with an energy of 511 keV, which are then captured by the two position-sensitive detectors.

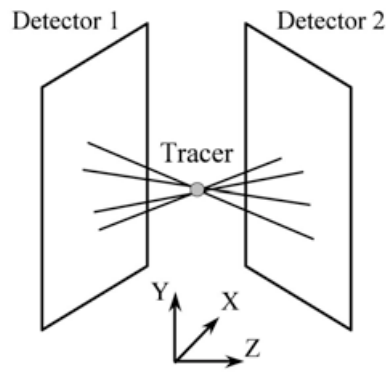


Figure 4.2: Schematic representation of PEPT (Positron Emission Particle Tracking) camera.

The position of the labelled tracer is determined by triangulation from a small number of detected  $\gamma$ -ray pairs. In practice many of the detected events are corrupted, therefore the calculation of an accurate location requires the acquisition of a sufficient number of events so that the valid ones, whose reconstructed lines essentially meet a point, can be distinguished from the corrupted ones. Corruption of the data due to photo scattering and incorrect pairings, Figure 4.3, are disregarded by a statistical algorithm.

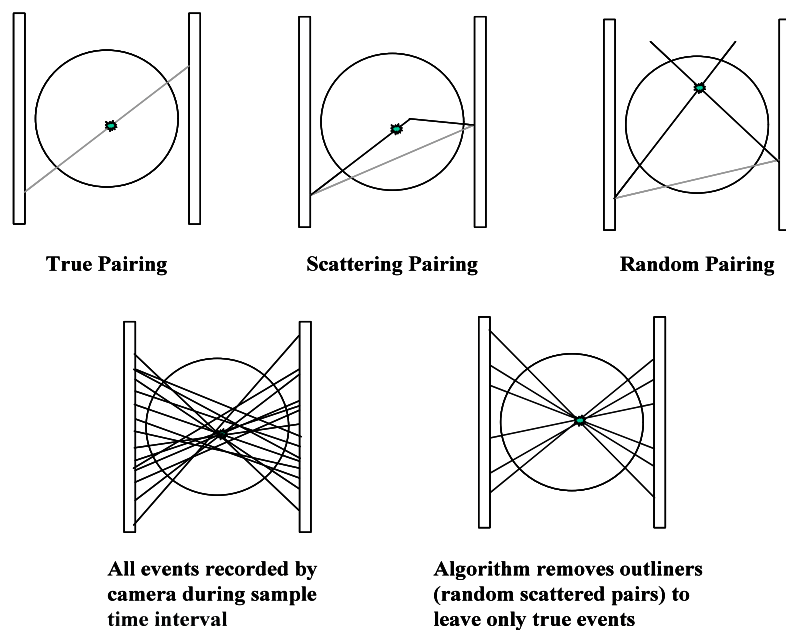


Figure 4.3: Categories of valid and invalid gamma pairs.

The algorithm homes in on the centre of crossing  $\gamma$ -ray pairs, eliminating outliers and recalculating the location until a tight cluster remain. The true pairings are kept and the pairings due to scattering and random effects eliminated.

The algorithm converts the data to an ASCII file containing a list of tracer co-ordinates  $(x,y,z)$  each with its time  $t$ . From the difference between successive locations, an estimate of instantaneous vector velocity of the tracer can be obtained.

The technique has been employed in numerous applications as extensively reported in the literature [7,8,9,10,11,12]. PEPT can be applied to batch, continuous or non-steady state processes. It was used, for example, to understand the behaviour of dry granular materials or particles in fluids [13]. For a rotating drum operating at low and medium speed the characteristic rolling mode and the solid motion in the active and passive regions were characterised by PEPT [14]. The movement of particle between inter-plough regions within a ploughshare mixer was also studied [15]. The latest studies reported have involved the development of a portable modular version of the camera, which can be applied to a number of applications in industry. For example, the modular camera was used to understand particle motion in a 750 mm diameter pressurised fluidised bed pilot plant reactor on an industrial plant [16]. By using PEPT and a tracer the plug flow of the paste inside the barrel and die land region during ceramic paste extrusion was demonstrated by analysis of particle speed [17]. Previous examples of PEPT refer to the use of only one single tracer since during the early development of the technique it was only capable of following a single tracer at any one time. In some situations, such as for mixing of multiple component particle systems, it would be beneficial to track more than one particle in order to have a better understanding of the mixing mechanisms. For this reason the Multiple-PEPT technique was developed so that up to 3 particles at the same time could be traced.

To ensure the PEPT data reflects the dynamic behaviour of the system under study, tracer materials are required to have the same characteristic of the bulk of material in the system. In addition, the radioactivity of the single tracer must be sufficiently high to achieve an acceptable accuracy. The radioactive tracer can be prepared by direct irradiation and ion-exchange methods. The radioactivity suitable for PEPT is typically within a range from 300 to 1000  $\mu\text{Ci}$  [5]. Typical tracers used are sand, glass, Balottini beads, ion exchange resin, coal, apatite, microcrystalline cellulose and polyethylene. Direct activation is used to label a particle with a size range from 1 to 10 mm. The particle to be labelled is directly bombarded using a 33 MeV  $^3\text{He}$  beam, resulting in a small proportion of the oxygen atoms in the particle being converted into a series of radioisotopes. Only the  $^{18}\text{F}$  radioisotope is used in PEPT since it has longer half-life compared with potential alternative isotopes. In addition to containing bound oxygen, the material must be able to withstand high temperature produced during the bombardment process. The ion-exchange technique was developed to produce smaller tracers with a size less than 1 mm. Firstly the radioisotope  $^{18}\text{F}$  is created as a very dilute solution of fluoride ions in deionised water, the  $^{18}\text{F}$  is then impregnated into the tracer particle. In an ion-exchange particle the degree of activity in a single particle is controlled by the ion-exchange properties of the resin material, the anions present in the  $^{18}\text{F}$  solution and the impregnation time [18].

At present new tracers, materials and isotopes for new applications, in particular to extend the lifetime of the modular portable PEPT for direct industrial application, are being studied.

#### **4.1.2 Improvements: Multiple Positron Emission Particle Tracking**

Multiple Positron Emission Particle Tracking (Multiple-PEPT) is a technique that was developed from the single particle tracking PEPT. This technique makes possible to follow up

to three multiple particles simultaneously through a considerable thickness of surrounding material with reasonable accuracy. Since each tracer emits the same gamma photons, in order to distinguish the tracers they are labelled with three different levels of radioactivity and a statistical approach is used to determine the centres of emission. However, in general using more tracers leads to errors since the gamma photons from each particle are identical and it is difficult to discriminate the signal when the tracers are in close proximity. This leads to less reliable trajectories than single particle tracking. An improved technique for particle identification and calculation of the locations has been described [19,20]. The radioactive concentration of each tracer is determined and the corrupted  $\gamma$ -ray trajectories discarded. By tracking multiple particles it is also possible to study the dynamic interaction of particles, segregation of particles or rotation and translation of large particles or objects. In the present work the tracer particles are attached to the surface of a larger object.

#### **4.2 Experimental set-up: Turbula mixer motion measurement**

In order to determine the motion the Multiple-PEPT technique was employed. Yang *et. al* [21] showed that the Multiple-PEPT technique can be used to track, with good accuracy, three particles at the same time. In one application it was shown that the rotational and translational motion of a solid body can be reconstructed from three positron emitting tracers mounted at fixed and known locations on the surface of the solid.

##### **4.2.1 Experimental set-up for the motion measurement**

Figure 4.4 shows the schematic experimental set-up for the Turbula motion measurements. Three tracers were precisely fixed on the Turbula shaft at location points  $\mathbf{P}_A$ ,  $\mathbf{P}_C$  and  $\mathbf{P}_D$ . These points were chosen to allow the largest reciprocal distances between the tracers

mounted on the cage. The choice of these locations and the non-metallic containment should guarantee good accuracy for the measurement.

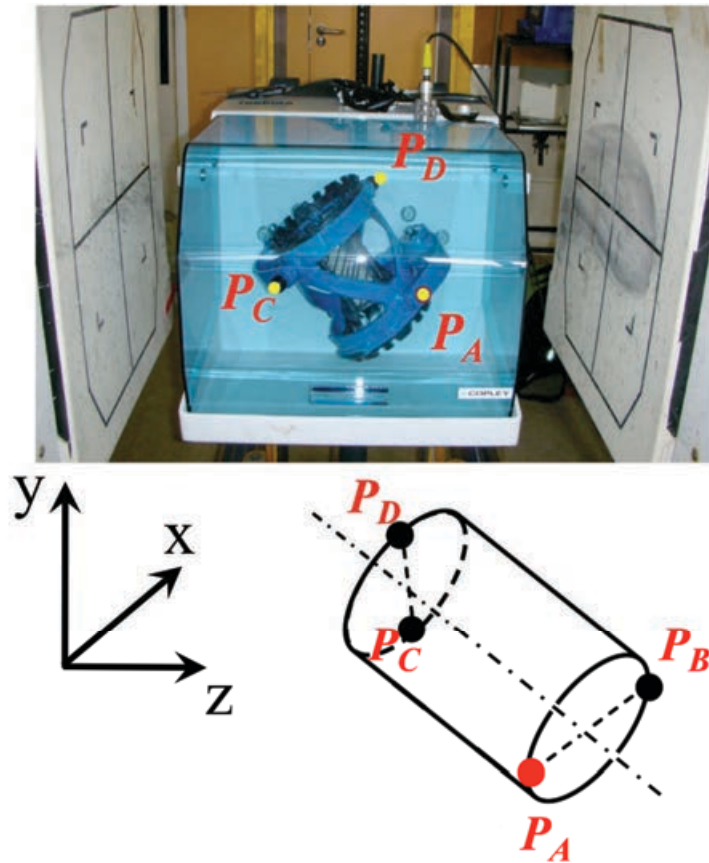


Figure 4.4: Schematic representation of the experimental measurement of the Turbula motion by PEPT.

Zeolite particles from a sample with a  $d_{50}$  of  $338 \mu\text{m}$  were labeled by ion-exchange. Zeolite particles are ideal tracer particles for PEPT since they are porous and have very large surface area. In addition the small size would guarantee higher confidence for the centre particle location. Particles were prepared with different levels of initial radioactivity: tracer 1 (point  $P_A$ ):  $880 \mu\text{Ci}$ ; tracer 2 (point  $P_C$ ):  $596 \mu\text{Ci}$ ; tracer 3 (point  $P_D$ ):  $395 \mu\text{Ci}$ . With three tracers, it is important to have a range of activity so the strongest tracer always has the highest data

logging rate and is found first by using the single-particle tracking technique, while the trajectories from the remaining tracers are regarded as corrupt trajectories. After the strongest tracer is located, trajectories passing close to the located tracer are then removed from the dataset. The locations of the second and the third tracers are calculated in a similar way.

During measurements the three tracers were tracked over several periods of the Turbula rotation to obtain an accurate trajectory for each of the three points from which the complete motion of the Turbula would be determined.

#### **4.3 Data processing: solid body translational and rotational motion reconstruction**

The translational and rotational motion of the Turbula can be reconstructed by knowing the position over time of the three points that are rigidly attached to the moving shaft of the mixer.

The positions of points  $\mathbf{P}_A$ ,  $\mathbf{P}_C$  and  $\mathbf{P}_D$ , for one shaft rotation, are shown in Figure 4.5 in Cartesian coordinates with respect to the camera coordinate versus the shaft angle at 23 rpm (rotation period 2.613 s). The motion was measured over a period of three minutes. The averaged cycle, determined by averaging the values over three minutes for points  $\mathbf{P}_A$ ,  $\mathbf{P}_C$  and  $\mathbf{P}_D$ , was used for the motion reconstruction.

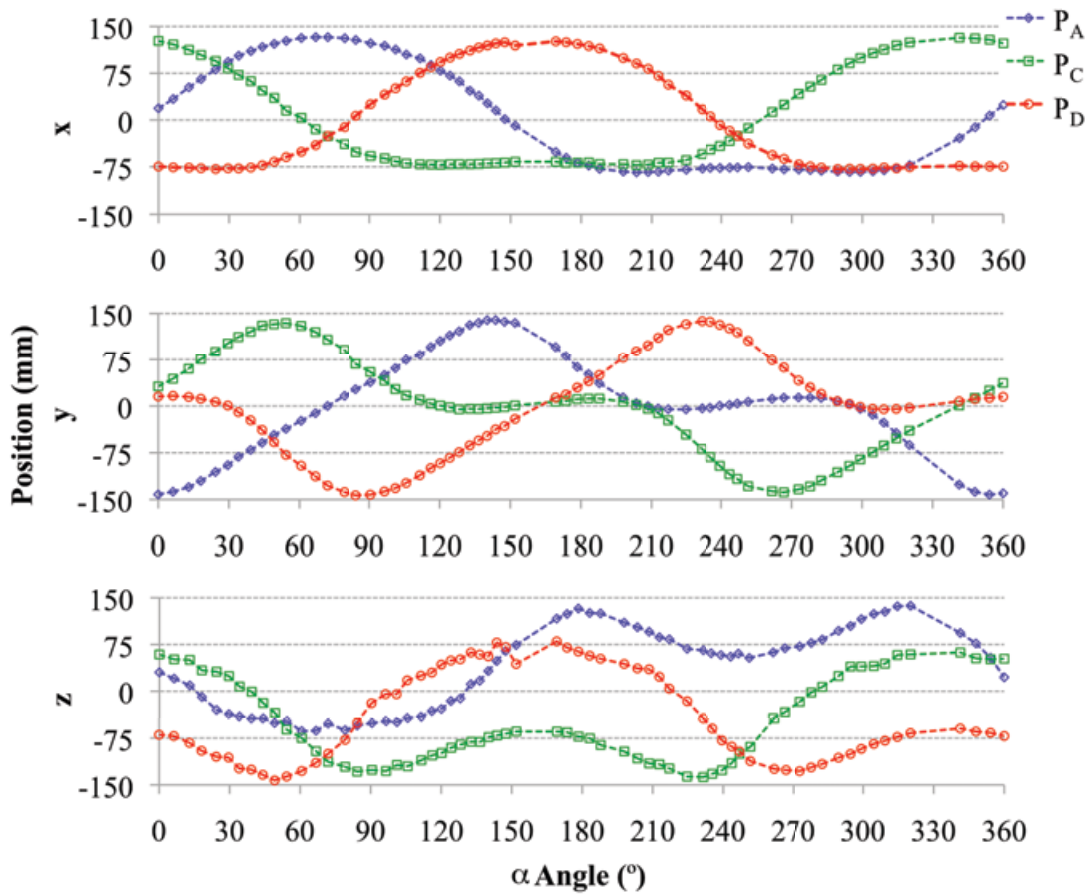


Figure 4.5: Measured position  $x,y,z$  for the tracers fixed at position  $\mathbf{P}_A$ ,  $\mathbf{P}_C$  and  $\mathbf{P}_D$  by Multiple-PEPT at 23 rpm for one shaft rotation.

The time interval between PEPT locations is variable as can be seen in Figure 4.5. This can be attributed to the PEPT algorithm and the way that the data is used to compute tracer location. The algorithm uses a fixed number of photon pairs to compute each location – the frequency of these can be variable depending on where the particles are in the field of view. Furthermore, the algorithm rejects computed locations that have high uncertainty and this can give apparent gaps in the data. The latter is more of an issue with multiple particles tracking due to the inherent corrupting effect of multiple sources of identical gamma photons. In order to reconstruct a more useable motion for DEM the data is linearly interpolated and filtered at a constant time step.

Considering Figure 4.5, where the tracked locations are fixed relative to each other and correspond to the pivoting points of the vessel holder, some symmetry in the trajectories is apparent. Since the central axis of the machine is horizontal, each tracked point follows the same trajectory in the transverse (x,y) plane out of phase by a multiple of  $90^\circ$  from the other points. Motion in the horizontal (z) direction is slightly more complex. Points at the same end of the vessel holder follow the same path, but out of phase by  $180^\circ$ . The trajectories of points at opposite ends are also out of phase with each other (by  $90^\circ$ ). In addition, there is an horizontal displacement and an inversion (mirror image). These transformations, where  $\mathbf{P}_C$  and  $\mathbf{P}_D$  have been transformed applying the rule above, as shown in Figure 4.6.

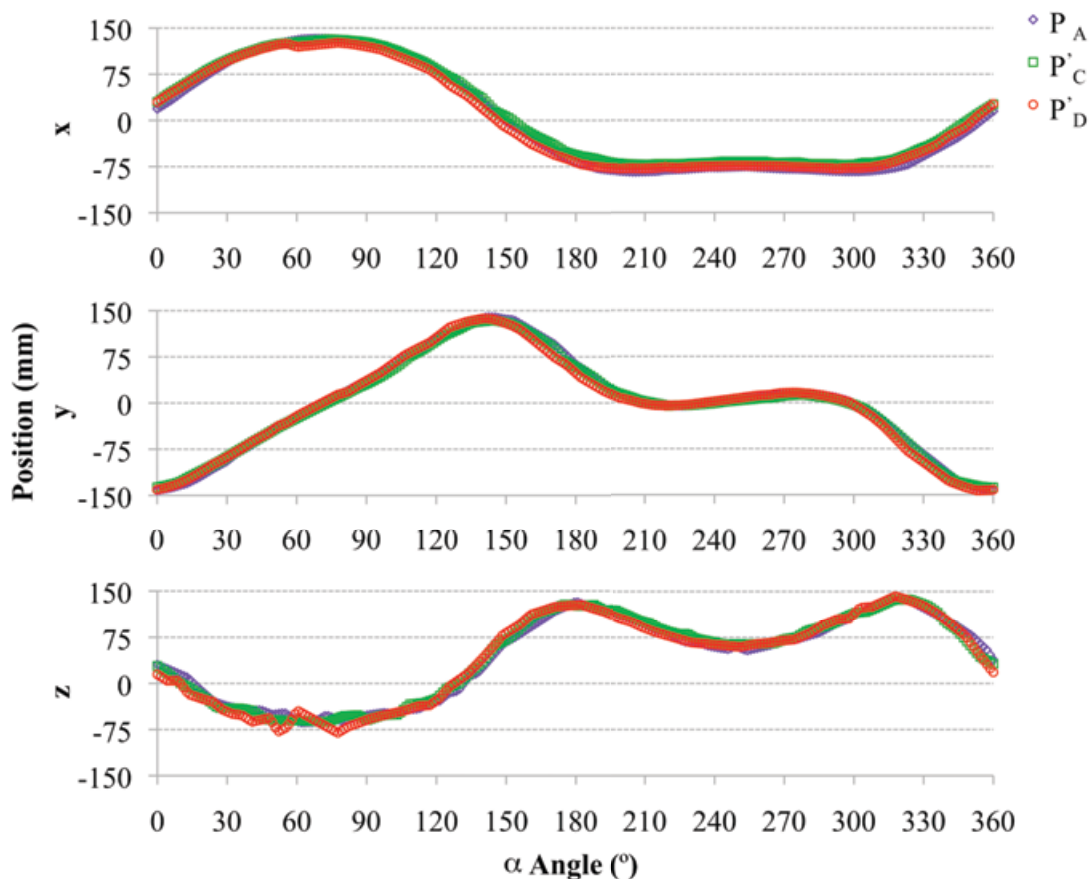


Figure 4.6:  $x, y, z$  positions for point  $\mathbf{P}_A$ ,  $\mathbf{P}'_C$  and  $\mathbf{P}'_D$  from Multiple-PEPT at 23 rpm for one shaft rotation.

From Figure 4.6 it can be seen that the three measured points follow the same trajectories. There are some small differences due to the location error for the tracers' location in the measurement. It can be concluded though that to minimize the error, and obtain a better motion reconstruction into DEM, only the trajectory of a single point  $P_A$  need be used as this is the most intense source. Subsequent calculation and experiments used a single particle on point  $P_A$  in order to yield a more accurate trajectory. Hence, the trajectories for the other  $P_B$ ,  $P_C$  and  $P_D$  points were inferred from point  $P_A$  using the symmetry described above. Note that the point  $P_B$  is on the opposite knob with reference to the point  $P_A$  in Figure 4.4.

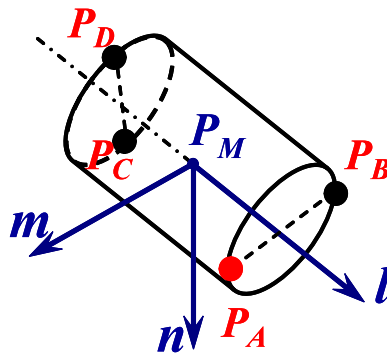


Figure 4.7: Definition of the vessel fixed unit vector coordinate system ( $\mathbf{l}, \mathbf{m}, \mathbf{n}$ ) Schematic representation of the experimental measurement of the Turbula motion by PEPT.

The position and orientation of the Turbula can be defined uniquely by the position vector of its centroid,  $P_M$ , a vector along its axis  $\mathbf{l}$  ( $\hat{\mathbf{l}}$  unit vector), and a radial vector  $\mathbf{m}$  ( $\hat{\mathbf{m}}$  unit vector) as shown in Figure 4.7 above. The vector  $\mathbf{n}$  is always normal to  $\mathbf{m}$  and  $\mathbf{l}$ .  $P_M$ ,  $\mathbf{l}$  and  $\mathbf{m}$  are related to  $P_A$ ,  $P_B$ ,  $P_C$  and  $P_D$  by:

$$P_M = \left( \frac{P_A + P_B + P_C + P_D}{4} \right) \quad (4.1)$$

$$\hat{\mathbf{i}} = \frac{\left[ \left( \frac{\mathbf{P}_A + \mathbf{P}_B}{2} \right) - \left( \frac{\mathbf{P}_C + \mathbf{P}_D}{2} \right) \right]}{\left\| \left( \frac{\mathbf{P}_A + \mathbf{P}_B}{2} \right) - \left( \frac{\mathbf{P}_C + \mathbf{P}_D}{2} \right) \right\|} = (\hat{l}_1, \hat{l}_2, \hat{l}_3) \quad (4.2)$$

$$\hat{\mathbf{m}} = \frac{\left[ \mathbf{P}_A - \left( \frac{\mathbf{P}_A + \mathbf{P}_B}{2} \right) \right]}{\left\| \mathbf{P}_A - \left( \frac{\mathbf{P}_A + \mathbf{P}_B}{2} \right) \right\|} = (\hat{m}_1, \hat{m}_2, \hat{m}_3) \quad (4.3)$$

The components of  $\mathbf{P}_M$ ,  $\hat{\mathbf{I}}$  and  $\hat{\mathbf{m}}$  are periodic and can therefore be expressed as Fourier series of the form:

$$f(t) = \frac{1}{2}a_0 + \sum_{n=1}^{\infty} [a_n \cos(2\pi n t / T) + b_n \sin(2\pi n t / T)] \quad (4.4)$$

where  $a_0$ ,  $a_n$  and  $b_n$  are Fourier coefficients and  $T$  is the rotational period, 2.613 s at 23 rpm. Satisfactory approximations can be obtained by using only a few terms in the Fourier series; the original and reconstructed values of the components of  $\mathbf{l}$  and  $\mathbf{m}$  are compared in Figure 4.8 and Figure 4.9.

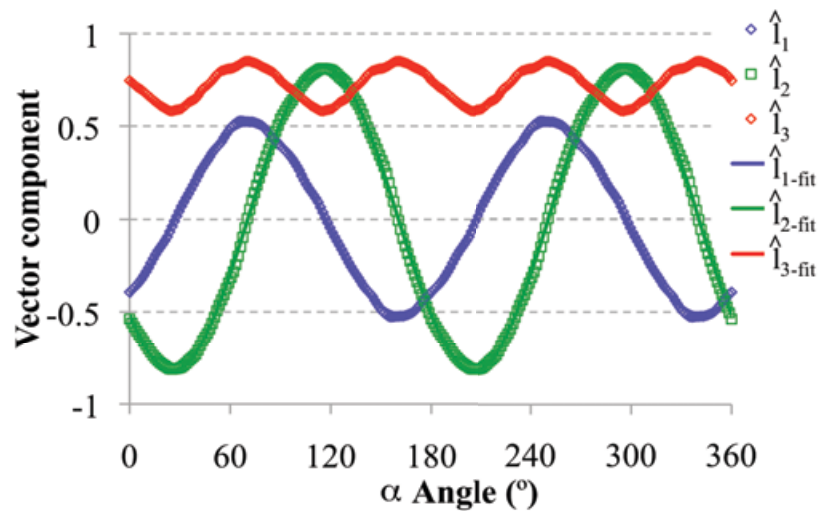


Figure 4.8: Components for the unit vector  $\hat{\mathbf{I}}$ .

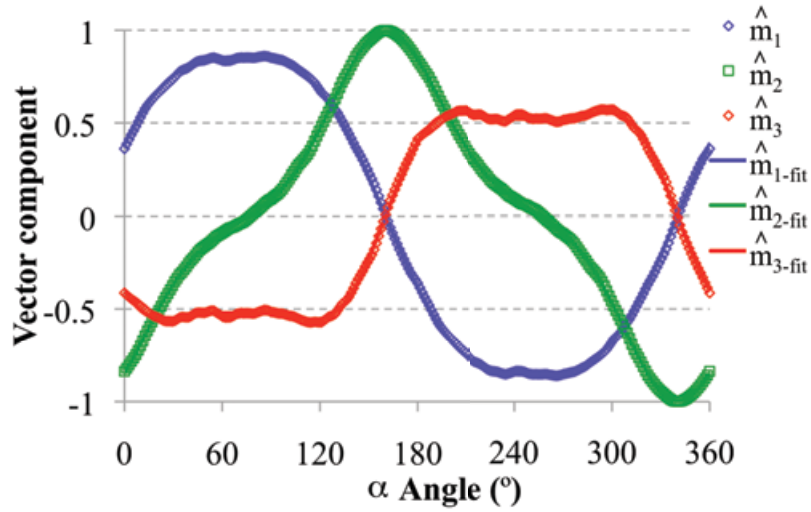


Figure 4.9: Components for the unit vector  $\hat{\mathbf{m}}$ .

#### 4.4 Results and discussion

The Gibbs-Rodrigues representation [22] provides a convenient way to calculate  $\boldsymbol{\omega}_i$ . A rotation by an angle  $\theta$  about an axis defined by a unit vector  $\mathbf{n}$  is represented by a vector  $\mathbf{r} = \mathbf{n} \tan(\theta/2)$ .

The rotation from orientation  $\mathbf{l}, \mathbf{m}$  at time  $t$  to new orientation  $\mathbf{l}', \mathbf{m}'$  at time  $t' = t + t_{\text{step}}$  is given by:

$$r_i = \frac{\sum_{j=1}^3 \sum_{k=1}^3 \varepsilon_{ijk} l_j l'_k + \gamma (l_i + l'_i)}{\sum_{k=1}^3 l_k (l_k + l'_k)} \quad (4.5)$$

where  $\varepsilon_{ijk}$  is the unit anti-symmetric tensor and  $\gamma$  is calculated as follows:

$$\gamma = - \frac{\sum_{i=1}^3 \sum_{j=1}^3 \sum_{k=1}^3 \varepsilon_{ijk} l_j l'_k (m_i - m'_i)}{\sum_{i=1}^3 (l_i + l'_i) (m_i - m'_i)} \quad (4.6)$$

The average angular velocity over this time step is therefore given by:

$$\boldsymbol{\omega} = \frac{\theta}{t'-t} \cdot \frac{\mathbf{r}}{\|\mathbf{r}\|} = (\omega_1, \omega_2, \omega_3) \quad (4.7)$$

Figure 4.10 shows the calculated components of the angular velocity as a function of time.

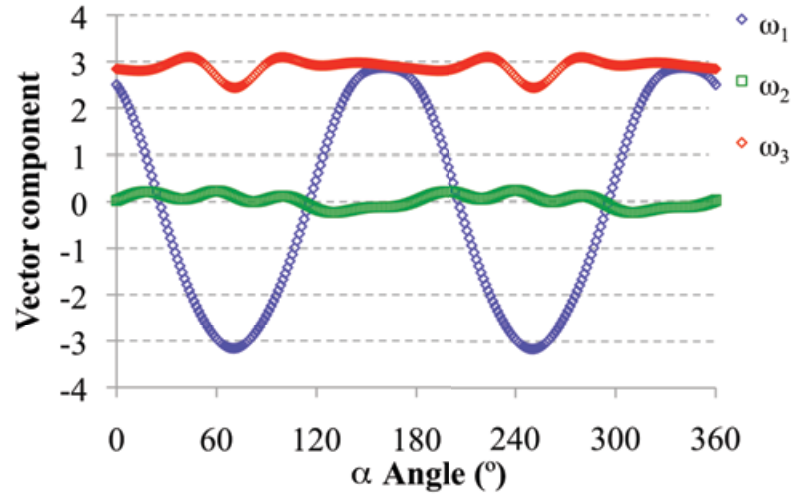


Figure 4.10: Components of the angular velocity  $\boldsymbol{\omega}$ .

EDEM imposes  $\boldsymbol{\omega}$  about the origin of the coordinate system rather than the centroid of the Turbula, so the translational velocity necessary to match the movement of the centroid is given by:

$$\mathbf{v} = \dot{\mathbf{P}}_{\mathbf{M}} - \boldsymbol{\omega} \wedge \mathbf{P}_{\mathbf{M}} = (v_1, v_2, v_3) \quad (4.8)$$

Again, the components are reported in Figure 4.11.

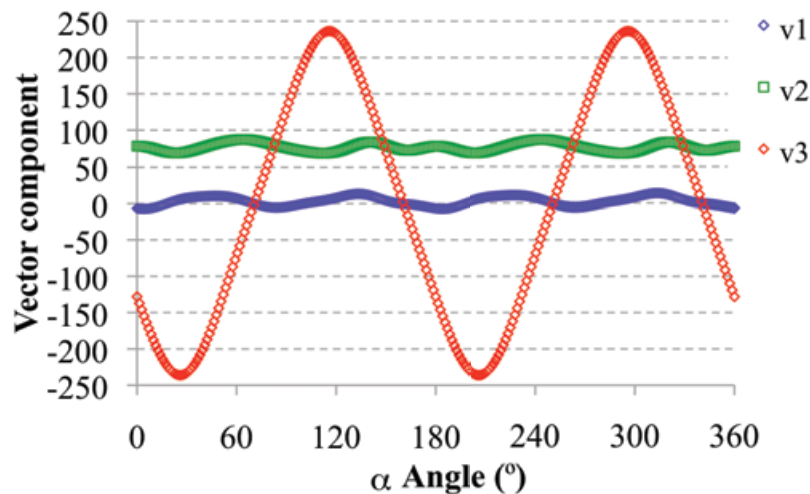


Figure 4.11: Components of the linear velocity  $\mathbf{v}$ .

The tabulated values of  $\mathbf{v}$  and  $\boldsymbol{\omega}$  at each timestep are used for importing the motion into DEM. The experimental measurement of the motion tracking has been conducted at 23 rpm, but can easily be scaled to other speeds by modifying  $\mathbf{v}$  and  $\boldsymbol{\omega}$ , this allowed the selection of different operational speeds.

The EDEM software allows the motion of a rigid solid body to be defined as a superposition of translational and rotational movements by definition of the velocities, translational and rotational at every specific timestep as reported in Figure 4.12. It does this by approximating the smooth motion of the Turbula as a succession of discrete timesteps during which the translational and angular velocities are constant. The procedure to import the measured motion into EDEM is extensively explained in Chapter 5. In this first attempt of modelling the Turbula mixer, a motion timestep of  $t_{step}=0.01$  s has been chosen since the EDEM software is limited in how many total superimposed translations and rotations can be defined due to computational limitations. However, this time step should be chosen sufficiently small to have negligible effect on the solution. In the DEM simulations the translations and rotations values here defined for one cycle are repeated for the total number of desired motion periods. These

methodology guarantees the modelled vessel always repeat the same motion over time and return to the initial position after each cycle (ref. Chapter 5).

Translational velocity:

```
<linear_translation name="ti" t_start="tI+(i-1)·tstep" t_end="tI+i·tstep"
start_vel_x="v1i" start_vel_y="v2i" start_vel_z="v3i"
```

.....

Rotational velocity:

```
<linear_rotation name="ri" t_start="tI+(i-1)·tstep" t_end="tI+i·tstep"
start_angvel_x="ω1i" start_angvel_y="ω2i" start_angvel_z="ω3i"
```

Figure 4.12: Coding for translations and rotations into EDEM.

with  $i=1:n$ , where  $n$  is the desired number of translation and rotations that will give the total motion duration.  $t_i$  is the actual time at which the linear translational velocity ( $v_{1i}, v_{2i}, v_{3i}$ ) and rotational velocity ( $\omega_{1i}, \omega_{2i}, \omega_{3i}$ ) are applied.

#### 4.5 Conclusions

Multiple Positron Emission Particle Tracking has been used to measure the Turbula motion. It has been shown that the Multiple-PEPT technique can track three particles and it has been used to understand the Turbula motion showing that only one tracked point is sufficient to describe the dynamic due to the symmetry in the Turbula motion. Both the translational and rotational motions of the solid body (mixer chamber) are calculated to recreate the motion into the DEM software.

#### 4.6 References

- [1] Z. Yan, X. Fan, S. Bakalis, D.J. Parker, P.J. Fryer, A method for characterising solids translational and rotational motions using Multiple-Positron Emission Particle Tracking (Multiple-PEPT), *International Journal of Multiphase Flow* **34** (2008), pp. 1152-1160.
- [2] M.R. Hawkesworth, D.J. Parker, P. Fowles, J.F. Crilly, N.L. Jefferies, G. Jonkers, Nonmedical applications of a positron camera, *Nuclear Instruments and Methods in Physics Research Section A: Accelerators, Spectrometers, Detectors and Associated Equipment* **310** (1991), pp. 423-434.
- [3] D.J. Parker, D.A. Allen, D.M. Benton, P. Fowles, P.A. McNeil, T. Min, T.D. Beynon, Developments in particle tracking using the Birmingham Positron Camera, *Nuclear Instruments and Methods in Physics Research Section A: Accelerators, Spectrometers, Detectors and Associated Equipment* **392** (1997), pp. 421-426.
- [4] D.J. Parker, R.N. Forster, P. Fowles, P.S. Takhar, Positron emission particle tracking using the new Birmingham positron camera, *Nuclear Instruments and Methods in Physics Research Section A: Accelerators, Spectrometers, Detectors and Associated Equipment* **477** (2002), pp. 540-545.
- [5] X. Fan, D.J. Parker, M.D. Smith, Labelling a single particle for positron emission particle tracking using direct activation and ion-exchange techniques, *Nuclear Instruments and Methods in Physics Research Section A: Accelerators, Spectrometers, Detectors and Associated Equipment* **562** (2006), no.1, pp. 345-350.
- [6] J.S. Lin, M.M. Chen, B.T. Chao, A novel radioactive particle tracking facility for measurement of solids motion in gas fluidized beds, *AIChE Journal* **31** (1985), pp. 465-473.

- [7] D.J. Parker, C.J. Broadbent, P. Fowles, M.R. Hawkesworth, P. McNeil Positron emission particle tracking - a technique for studying flow within engineering equipment, *Nuclear Instruments and Methods in Physics Research Section A: Accelerators, Spectrometers, Detectors and Associated Equipment* **326** (1993), pp. 592-607.
- [8] M. Stein, T.W. Martin, J.P.K. Seville, P.A. McNeil, D.J. Parker, Positron emission particle tracking: Particle velocities in gas fluidised beds, mixers and other applications, *Non-Invasive Monitoring of Multiphase Flows* (1997), pp. 309-333.
- [9] Y.S. Fangary, M. Barigou, J.P.K. Seville, D.J. Parker, Fluid trajectories in a stirred vessel of non-newtonian liquid using positron emission particle tracking, *Chemical Engineering Science* **55** (2000), pp. 5969-5979.
- [10] P.W. Cox, S. Bakalis, H. Ismail, R. Forster, D.J. Parker, P.J. Fryer, Visualisation of three-dimensional flows in rotating cans using positron emission particle tracking (PEPT), *Journal of Food Engineering* **60** (2003), pp. 229-240.
- [11] A. Guida, X. Fan, D.J. Parker, A.W. Nienow, M. Barigou, Positron emission particle tracking in a mechanically agitated solid–liquid suspension of coarse particles, *Chemical Engineering Research and Design* **87** (2009), pp. 421-429.
- [12] K.E. Cole, K.E. Waters, X. Fan, S.J. Neethling, J.J. Cilliers, Combining Positron Emission Particle Tracking and image analysis to interpret particle motion in froths *Minerals Engineering In Press* (2010), Corrected Proof, Available online.
- [13] J.P.K. Seville, A. Ingram, X. Fan, D.J. Parker, Chapter 4 Positron Emission Imaging in Chemical Engineering, *Advances in Chemical Engineering* **37** (2009), pp. 149-178.

- [14] Y.L. Ding, J.P.K. Seville, R. Forster, D.J. Parker, Solids motion in rolling mode rotating drums operated at low to medium rotational speeds, *Chemical Engineering Science* **56** (2001), pp. 1769-1780.
- [15] J.R. Jones, J. Bridgwater, A case study of particle mixing in a ploughshare mixer using Positron Emission Particle Tracking, *International Journal of Mineral Processing* **53** (1998), pp. 29-38.
- [16] A. Ingram, M. Hausard, X. Fan, D.J. Parker, J.P.K. Seville, N. Finn, et al., 12th International Conference on Fluidization, *New Horizons in Fluidization Engineering, ECI Engineering Conference International Symposium Series paper 60* (2007).
- [17] R.D. Wildman, S. Blackburn, D.M. Benton, P.A. McNeil, D.J. Parker, Investigation of paste flow using positron emission particle tracking, *Powder Technology* **103** (1999), pp. 220-229.
- [18] X. Fan, D.J. Parker, M.D. Smith, Labelling a single particle for positron emission particle tracking using direct activation and ion-exchange techniques, *Nuclear Instruments and Methods in Physics Research Section A: Accelerators, Spectrometers, Detectors and Associated Equipment* **562** (2006), pp. 345-350.
- [19] Z. Yang, P.J. Fryer, S. Bakalis, X. Fan, D.J. Parker, J.P.K. Seville, An improved algorithm for tracking multiple, freely moving particles in a Positron Emission, *Particle Tracking system Nuclear Instruments & Methods in Physics Research Section A, Accelerators Spectrometers Detectors and Associated Equipment* **577** (2007), pp. 585-594.
- [20] Z. Yang, D.J. Parker, P.J. Fryer, S. Bakalis, X. Fan, Multiple-particle tracking—an improvement for positron particle tracking, *Nuclear Instruments and Methods in Physics Research Section A: Accelerators, Spectrometers, Detectors and Associated*

*Equipment* **564** (2006), pp. 332-338.

- [21] Z. Yang, X. Fan, S. Bakalis, D.J. Parker, P.J Fryer, A method for characterising solids translational and rotational motions using Multiple-Positron Emission Particle Tracking (Multiple-PEPT). *International Journal of Multiphase Flow* **34** (2008), pp. 1152-1160.
- [22] I.R. Peterson (2003). The Gibbs Representation of 3D Rotations. Available: <http://arxiv.org/pdf/cs/0104016>, [accessed July 2008].

## Chapter 5

### DEM modelling of particle motion in a Turbula mixer

*The overall aim of this work is to evaluate the usefulness of DEM to investigate flow and mixing mechanisms in systems difficult to study experimentally. The Turbula mixer was selected because it exhibits a regular yet complex motion.*

*In this chapter the three-dimensional motions of particles in a Turbula mixer were calculated using the 3D discrete element modelling commercial package EDEM provided by DEM-Solutions. This package is capable of managing complicated geometries and complicated dynamics. The Hertz Mindlin contact model implemented in EDEM was adopted for the interparticle force calculations. The mixer motion was measured and mathematically reconstructed, as described in Chapter 4, and then imported into EDEM so that the same movement could be applied to the modelled vessel. This chapter describes the output of the model and discusses the new challenges of interpreting the large quantity of complex numerical data. The vessel located in the mixer chamber is subjected to intensive, periodically pulsating movements. In particular, initial studies on the mixing mechanisms and description of macroscopic particle movement have been carried out. The dispersion coefficients in axial and radial directions were defined and related with the mixing effectiveness at different rotational speeds. The mixer displayed a very interesting relationship with speed. At low speed, its transverse and axial mixing performance decreased significantly with increasing speed, going through a minimum at medium speed before*

*recovering completely at high speed. It appears that the motion of the Turbula mixer goes through a transition that has a profound effect on mixing performance. The implication is that unless this is understood, it will be difficult a priori to identify optimum operating conditions.*

### 5.1 Introduction: uni-axis and multiple-axes blender motion

Granular mixing in rotating blenders has been extensively studied [1,2,3,4,5]. Most of the DEM numerical models of rotating blenders from the literature involve relatively simple rotating systems in which motion is characterised by one-dimensional motion for the vessel about one-fixed axis due most probably to the geometric limitations of codes used. This has been addressed to a large extent by the developers of commercial DEM packages, such as EDEM, who have placed emphasis on integration with CAD. Thus it is now possible to model complex geometries [6] and also complex movement of these geometries. The Turbula mixer is a laboratory scale mixer, which is widely used in industry for the development or testing of new granular products. It comprises a simple vessel geometry (cylinder) that moves with a complex, yet regular 3D motion giving rise to rapid and thorough mixing of the contents. The container motion consists of two rotations of the container around its longitudinal axis and a horizontal translation. The operation of the Turbula is as follows: the mixing vessel is held within a cage that undergoes regular periodic motion driven by drive shafts through universal couplings at each end of the cage, as depicted in Figure 5.1.

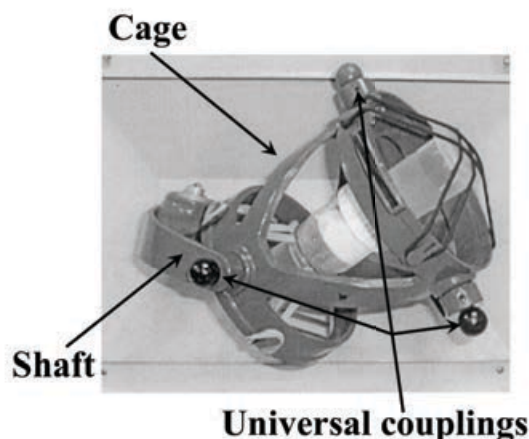


Figure 5.1: The container, located in the centre of the cage in the Turbula mixer.

The mixer presents an ideal system for evaluation of the power of DEM to simulate complex simulations. In the present work the first DEM numerical modelling of the Turbula mixer has been developed.

The application of Magnetic Resonance Imaging (MRI) [7] is the only study in the literature where the mixing process, for free flowing non-cohesive material, has been characterised under different conditions. In this work the rate of mixing of particles with monomodal and bimodal size distributions was quantified using a segregation index. Experiments revealed that segregation appeared as soon as different sized particle were present. Moreover, the lower the rotation speed, the more segregated the final state was.

## **5.2 Simulation conditions and DEM input parameters**

EDEM is based on the algorithm developed by Cundall and Strack [8]. The Hertz Mindlin no slip contact model is employed. Mixing experiments by PEPT were used to validate the simulation, and results will be presented in Chapter 7.

This chapter has focussed on simulation of granular mixing of simple particles (spheres) in a simple cylindrical geometry that is subject to a highly complex, but regular motion measured, as mathematically described in Chapter 4. The cylindrical vessel is driven by the Turbula chamber, which is moved by a shaft connected with the motor. In Chapter 4 the method of physically recording the 3D motion of the Turbula mixer, converting this to time dependent (periodic) rotational and translational velocity vectors and importing this motion into EDEM was described. EDEM is capable of simulating granular flow in complex geometries, imported from CAD software, subject to complex motion.

Here that motion has been applied to a 45 mm diameter and 80 mm long cylindrical vessel 50% filled with spheres (assuming packing of about 60%), monomodal and bimodal particle

size, as defined from particle bed size ratio  $R=d_{particle\_type\_A}/d_{particle\_type\_B}$ . The volume was the same for particle type  $A$  and type  $B$ . A range of Turbula shaft rotating speeds, from 23 rpm up to 69 rpm, were studied, corresponding to the physical range of the T2F commercial machine already described in Chapter 4. The different simulations conditions are reported in Table 5.1.

Table 5.1: Turbula mixer EDEM simulation conditions.

Particle diameter (mm) (Number of particles)	Fill %	Particle diameter ratio R	Turbula speed (rpm)	Loading pattern	Baffle
2 (9000)	≈50	1	23-34-46-57-69	Axial	No
2 (9000)	≈50	1	23-34-46-57-69	Transverse	No
2 (4500) 1.4 (13100)	≈50	1.4	23-34-46-57-69	Axial	No
2 (4500) 1.4 (13100)	≈50	1.4	23-34-46-57-69	Axial	Yes

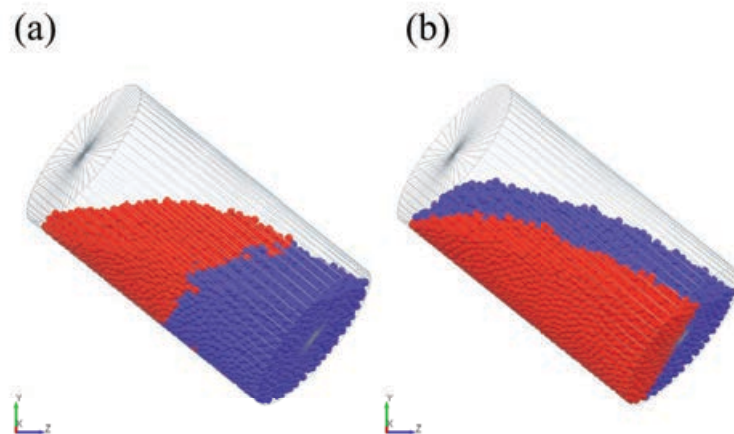


Figure 5.2: Initial loading patterns: (a) Axial. (b) Transverse.

For the monomodal particle size ( $R=I$ ) the two different initial distributions, axial and transverse, were investigated in an attempt to elucidate axial and radial mixing respectively. In the axial distribution pattern the spheres were initially completely segregated in the axial direction while the transverse loading the segregation was in the radial direction.

The properties of the spheres used in the DEM simulations are listed in Table 5.2. These have the same properties to spheres which have previously been employed for glass beads in [9]. The shear modulus was chosen at an artificially low value of  $2 \times 10^6$  Pa in order to reduce the simulation time, as has been extensively done in the literature. The particle size used in this work was chosen in order to obtain a reasonable simulation time. The effect of air was not considered in the simulations.

Table 5.2: Physical parameters and their values used in the EDEM simulations.

<b>Parameter</b>	<b>Value</b>
Particle density, $\rho$ (kg/m <sup>3</sup> )	2500
Particle shear modulus, $G$ (Pa)	$2 \times 10^6$
Particle Poisson's ratio, $\nu$	0.3
Vessel density, $\rho$ (kg/m <sup>3</sup> )	1200
Vessel shear modulus, $G$ (Pa)	$3 \times 10^9$
Vessel Poisson's ratio, $\nu$	0.3
Particle-particle static friction coefficient, $\mu_s$	0.5
Particle-particle rolling friction coefficient, $\mu_r$	0.01
Particle-vessel static friction coefficient, $\mu_s$	0.35
Particle-vessel rolling friction coefficient, $\mu_r$	0.005
Particle-particle restitution coefficient, $\varepsilon$	0.75
Particle-vessel restitution coefficient, $\varepsilon$	0.75

Table 5.3: Summary for the predicted EDEM (version 2.3, 2 processors) simulation time for 45 s total simulation time (23 rpm) if input parameters were chosen were same as those measured for zeolite particles in Chapter 3.

Parameter	Value
Number of particles ( $\approx 50\%$ fill) (assuming 60% packing)	2,143,347
Particle diameter, $d_{50}$ (mm)	0.338 (measured)
Particle density, $\rho$ ( $\text{kg/m}^3$ )	2410 (measured)
Reduces Elastic modulus $E^*$ (Pa)	$2.93 \times 10^9$ (single particle compression) $9.7 \times 10^9 - 34.3 \times 10^9$ (nanoindentation)
Particle Poisson's ratio, $\nu$	0.3 (assumed)
Particle shear modulus $G$ (Pa)	$1.2 \times 10^9 - 14.5 \times 10^9$
Vessel density, $\rho$ ( $\text{kg/m}^3$ )	1200
Vessel shear modulus, $G$ (Pa)	$3 \times 10^9$
Vessel Poisson's ratio, $\nu$	0.3
Particle-particle static friction coefficient, $\mu_s$	0.53 ( $\tan \varphi_e$ ref. Chapter 3)
Particle-particle rolling friction coefficient, $\mu_r$	0.01 (assumed)
Particle-vessel static friction coefficient, $\mu_s$	0.21 ( $\tan \varphi_w$ ref. Chapter 3)
Particle-vessel rolling friction coefficient, $\mu_r$	0.005 (assumed)
Particle-particle, particle-vessel restitution coefficient, $\varepsilon$	0.75 (assumed)
<b>Predicted total simulation time after 0.00534 s (total desired simulation time 45 s)</b>	<b>450 hours with only 5343 particles created</b> (Particle shear modulus $G$ $1.2 \times 10^9$ Pa)

The initial idea was to model particles with the properties measured in Chapter 3. The true material properties of this material, such as shear modulus and particle size, however, meant

that simulations would have been unfeasibly long for the available software version and the purpose of this study. An example of the very long predicted time for the zeolite catalyst material is reported in Table 5.3. The prediction was done by setting up the model and running it, the EDEM software calculated the simulation time as it progressed. The predicted total computational time after just 0.00534 s of simulation, was 450 hours with only 5343 particles created.

### **5.2.1 Definition of vessel motion in EDEM package**

The EDEM software allows the motion of a rigid solid body to be defined as a superposition list of translational and rotational movements as schematically reported in Figure 5.3. It does this by approximating the smooth motion of the Turbula as a succession of discrete timesteps during which the translational and angular velocities are constant. These values for the translation and rotational speeds imported into the model were directly measured as reported in Chapter 4. In this first attempt of modelling the Turbula mixer, a motion timestep of  $t_{step\_motion} = 0.01$  s ( $i=1:n$ ) was chosen since the EDEM software is limited in how many total superimposed translations and rotations can be defined due to computational limitations.  $n$  is the desired number of translation and rotations that will give the total motion duration.  $t_i$  is the actual time at which the linear translational velocity  $(v_{1i}, v_{2i}, v_{3i})$  and rotational velocity  $(w_{1i}, w_{2i}, w_{3i})$  are applied. Physically, this corresponds to subjecting the contents of the Turbula mixer to a succession of small impulsive blows, but the time step has been chosen sufficiently small that this should have a negligible effect on the solution.

Translational velocity:

```
<linear_translation name="ti" t_start="tI+(i-1)·tstep" t_end="tI+i·tstep"  
start_vel_x="v1i" start_vel_y="v2i" start_vel_z="v3i"
```

.....

Rotational velocity:

```
<linear_rotation name="ri" t_start="tI+(i-1)·tstep" t_end="tI+i·tstep"  
start_angvel_x="w1i" start_angvel_y="w2i" start_angvel_z="w3i"
```

Figure 5.3: Definition of list of translations and rotations into EDEM at each motion timestep.

The procedure to import and superimpose the list translational and rotational movements to the cylindrical vessel is represented in Figure 5.4. This consists of various steps in the two different EDEM environments: the EDEM Creator and the EDEM Analyst. Firstly the cylindrical geometry was created in the EDEM Creator. Secondly, the input deck file (extension \*.xml) was exported from the EDEM Analyst and modified by substitution of the PEPT measured list of translational and rotational velocities at each motion timestep in the section corresponding to the definition of the dynamic. Finally the \*.xml input deck was re-imported from EDEM and hence the dynamic was superimposed to the cylindrical geometry.

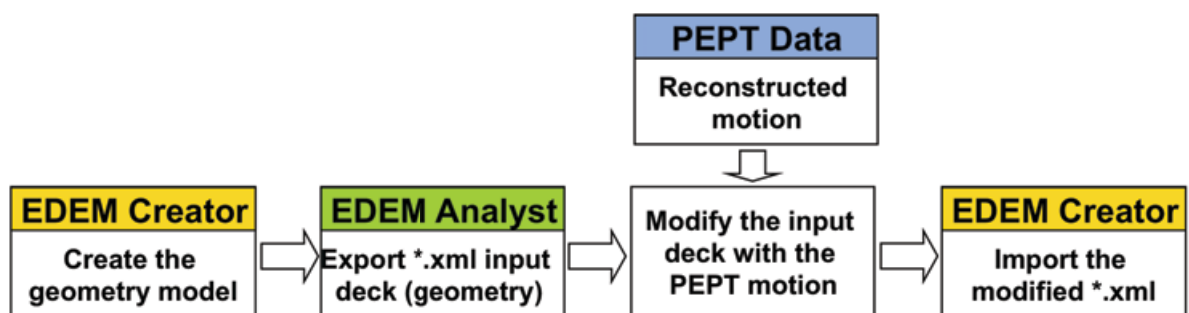


Figure 5.4: Steps in EDEM software to define the translational and rotational movements for the cylindrical geometry.

Driven by the vessel movement, the particle bed moves within the vessel with a periodic behaviour (see movie files in the attached DVD, the list of simulation is contained in the simulation\_list.txt files). Figure 5.5 shows the vessel movement during one complete shaft rotation. One rotation of the shaft imparts one rotation of the vessel around its longitudinal axis and two backward-forward horizontal translational motions. In order to help the reader to visualize the rotation of the vessel, three fixed points ( $a,b,c$ ) have been highlighted at the sequential time-steps (from 1 to 21) and the horizontal translation is exaggerated for clarity. *Vessel translation*: the vessel moves backwards and forwards, changing its direction of motion at the end of each quarter turn of the shaft. At the same time the inclination of the vessel to the horizontal reverses. *Inversion*: the sharp reversal in direction of translation and the rapid change in orientation of the vessel at the end of each quarter revolution give a “kick” to the contents of vessel.

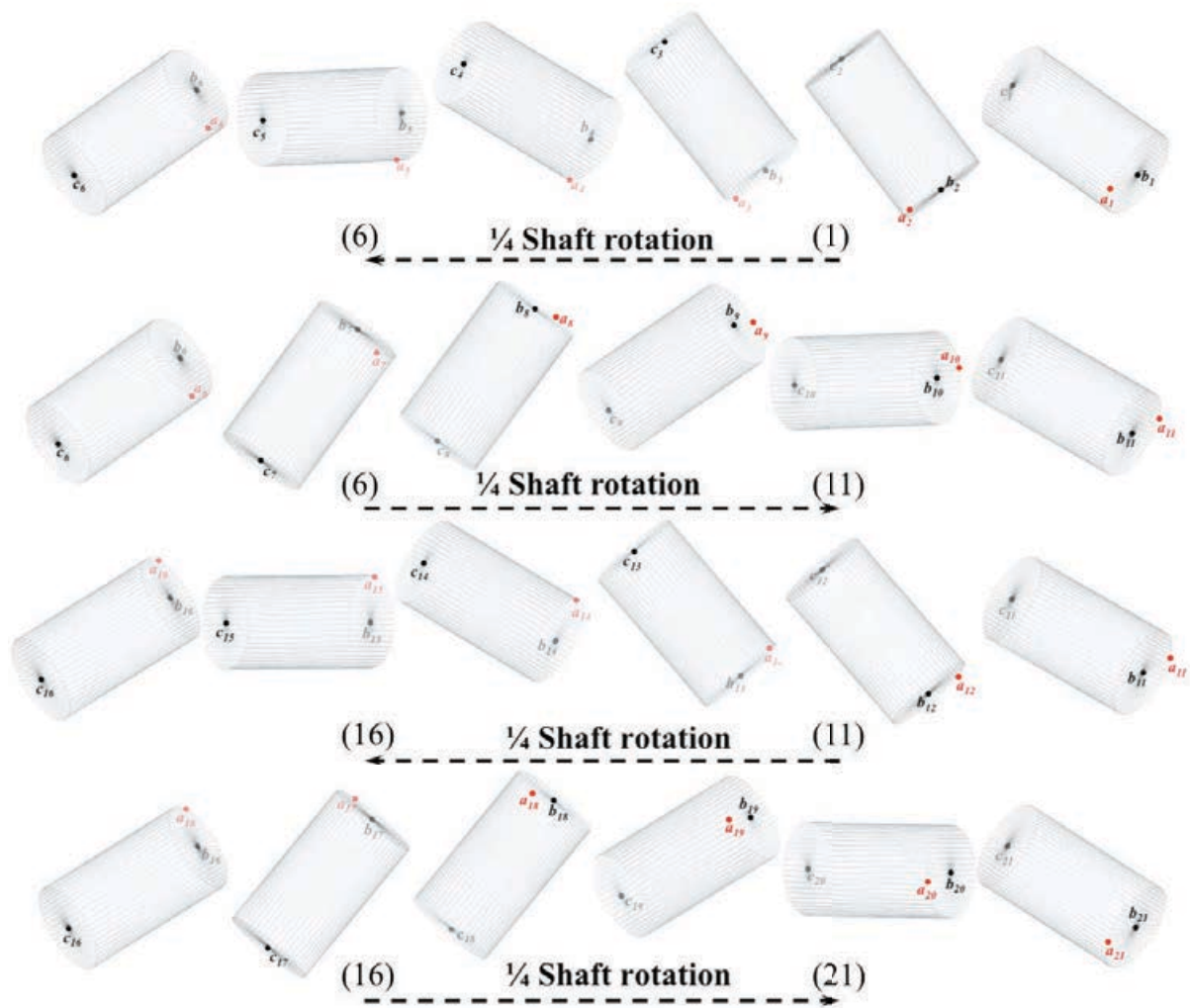


Figure 5.5: Schematic explanation of vessel motion and idea of inversion.

A range of Turbula shaft rotating speeds, from 23 rpm up to 69 rpm, were studied. Figure 5.6 shows the origin  $O'$  of the vessel co-ordinate system  $(x,y,z)$  defined at the midpoint of the vessel axis and by the three components of the unit vectors  $(\hat{l}, \hat{m}, \hat{n})$  from the EDEM model. These describe the orientation of the vessel at every motion timestep.  $P_1, P_2, P_3, P_4$  are four points fixed on the cylindrical vessel and  $(X,Y,Z)$  is the absolute EDEM fixed coordinate system and the cylinder moves with respect to such system. Particles inside the vessel (only a

blue one is represented) move with respect to the absolute coordinate system  $(X,Y,Z)$ , vector  $r'$ , but also relative to the  $(x,y,z)$  coordinate system.

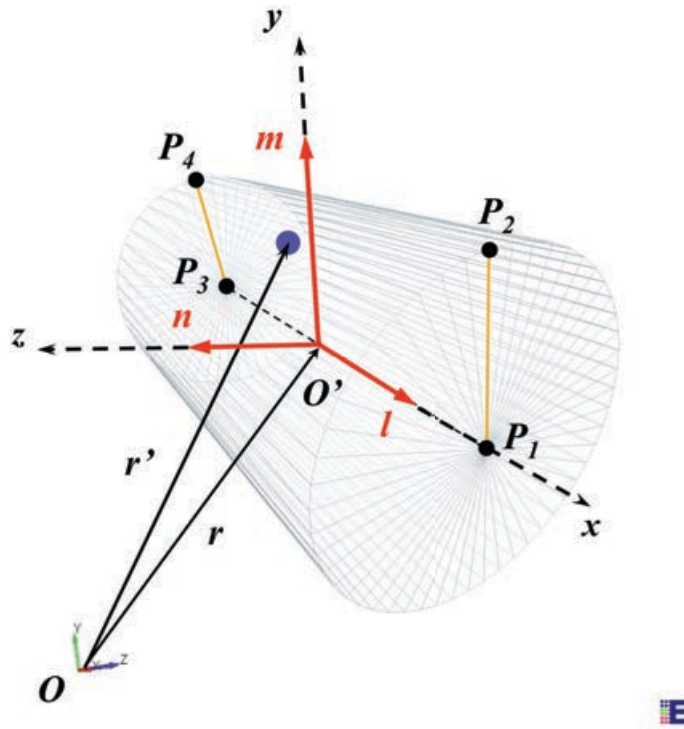


Figure 5.6: Definition of the coordinate system  $x,y,z$  fixed with the vessel geometry from the  $X,Y,Z$  coordinate system from DEM.

To demonstrate that the actual motion reproduced in EDEM was correct, the components for unit vectors  $\hat{l}, \hat{m}$  from the EDEM model were plotted at different rotational speeds for the first complete period of motion, Figure 5.7. The component  $\hat{n}$  was always normal to the component  $\hat{l}, \hat{m}$ . The periods of motion respectively at 23, 34, 46, 57 and 69 rpm corresponded to about 2.61, 1.76, 1.30, 1.05 and 0.87 s. The plot shows how the motion was uniformly and correctly scaled with the speed. For each period of motion related to the desired speed, the vessel always assumed the same orientation and position.

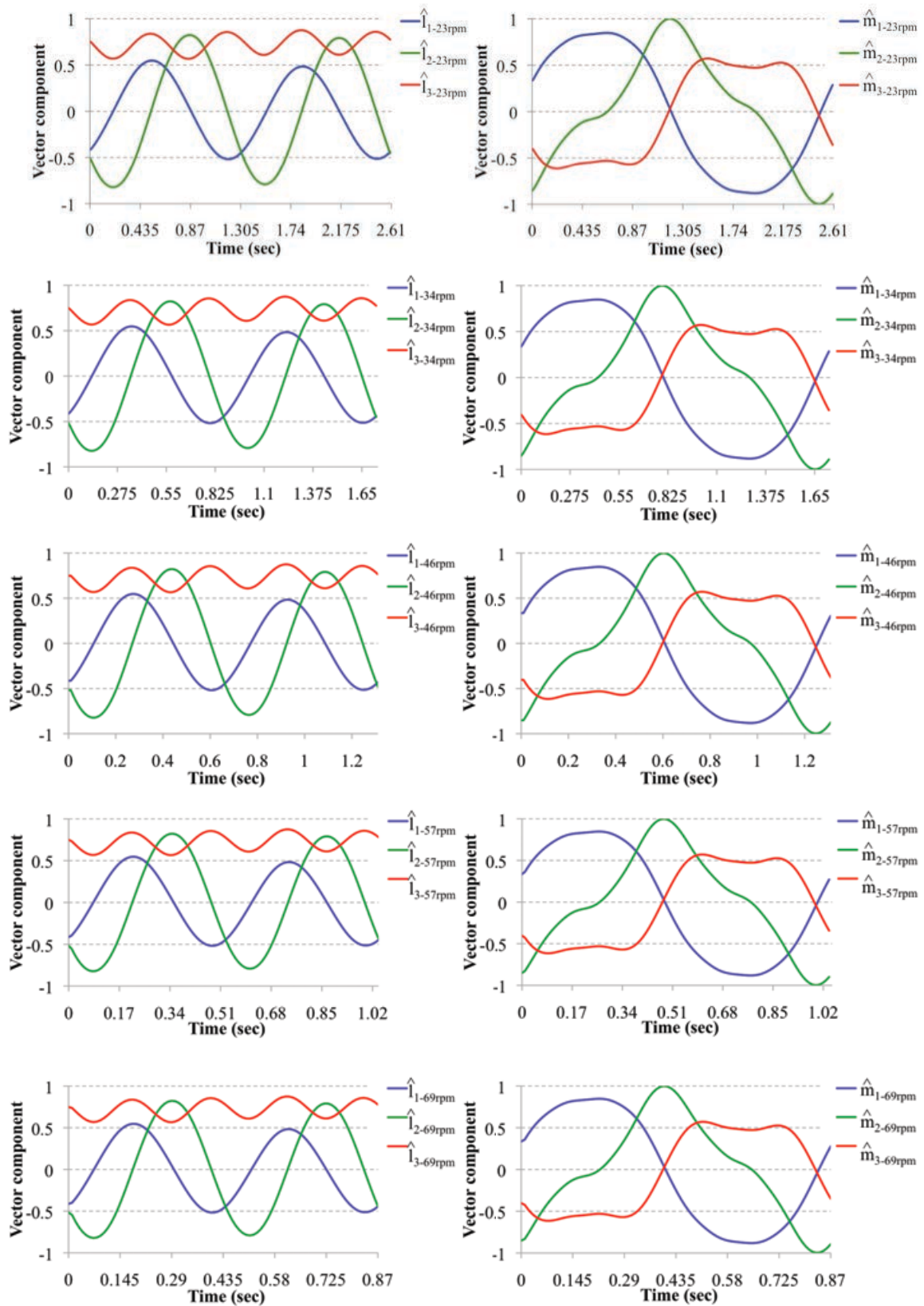


Figure 5.7: Comparison between unit vectors  $\hat{l}, \hat{m}$  at different rotational speeds.

From Figure 5.7, it can be seen that over just one period of motion the components for the unit vector  $\hat{l}, \hat{m}$  from the simulations assumed the same values (cylinder occupied the same position in the space) during the application of the motion but with different period of motion and hence different operating speeds. It is important to note that the total motion was nevertheless equal to the application of such motion over the total number of motion periods desired (total simulation time).

### 5.2.2 Data processing

The DEM software can provide micro-dynamic information at the particle scale level. For each particle the positions  $(X, Y, Z)$  relative to the DEM origin fixed coordinate system are obtained. The vessel translates and rotates relative to this coordinate system and, therefore, the position of each particle must be transformed from the fixed coordinate  $(X, Y, Z)$  system to a Lagrangian coordinate system  $(x, y, z)$  fixed with the vessel geometry as described in Figure 5.6.

The transformation represented by Eq.(5.1) was used to obtain the particle position  $(x, y, z)$  in cylinder coordinates from the particle position  $(X, Y, Z)$  in EDEM coordinates at each time step.

$$\bar{r} = \begin{pmatrix} X \\ Y \\ Z \end{pmatrix} = \begin{pmatrix} X_{O'} \\ Y_{O'} \\ Z_{O'} \end{pmatrix} + \begin{bmatrix} \hat{l}_x & \hat{m}_x & \hat{n}_x \\ \hat{l}_y & \hat{m}_y & \hat{n}_y \\ \hat{l}_z & \hat{m}_z & \hat{n}_z \end{bmatrix} \cdot \begin{pmatrix} x \\ y \\ z \end{pmatrix} \quad (5.1)$$

Where  $(X, Y, Z)$  are the coordinates of the particle  $P$  (blue particle in Figure 5.6) with respect to fixed DEM coordinate system.  $(X_{O'}, Y_{O'}, Z_{O'})$  and  $(\hat{l}_{xyz}, \hat{m}_{xyz}, \hat{n}_{xyz})$  are origin position and the

unit vector components that define the orientation of the  $(x,y,z)$  vessel coordinate system at any moment in time.

Figure 5.8 shows the movement of a randomly selected particle in terms of its coordinates  $(x,y,z)$  for different Turbula shaft operational speeds (23, 46, 69 rpm).

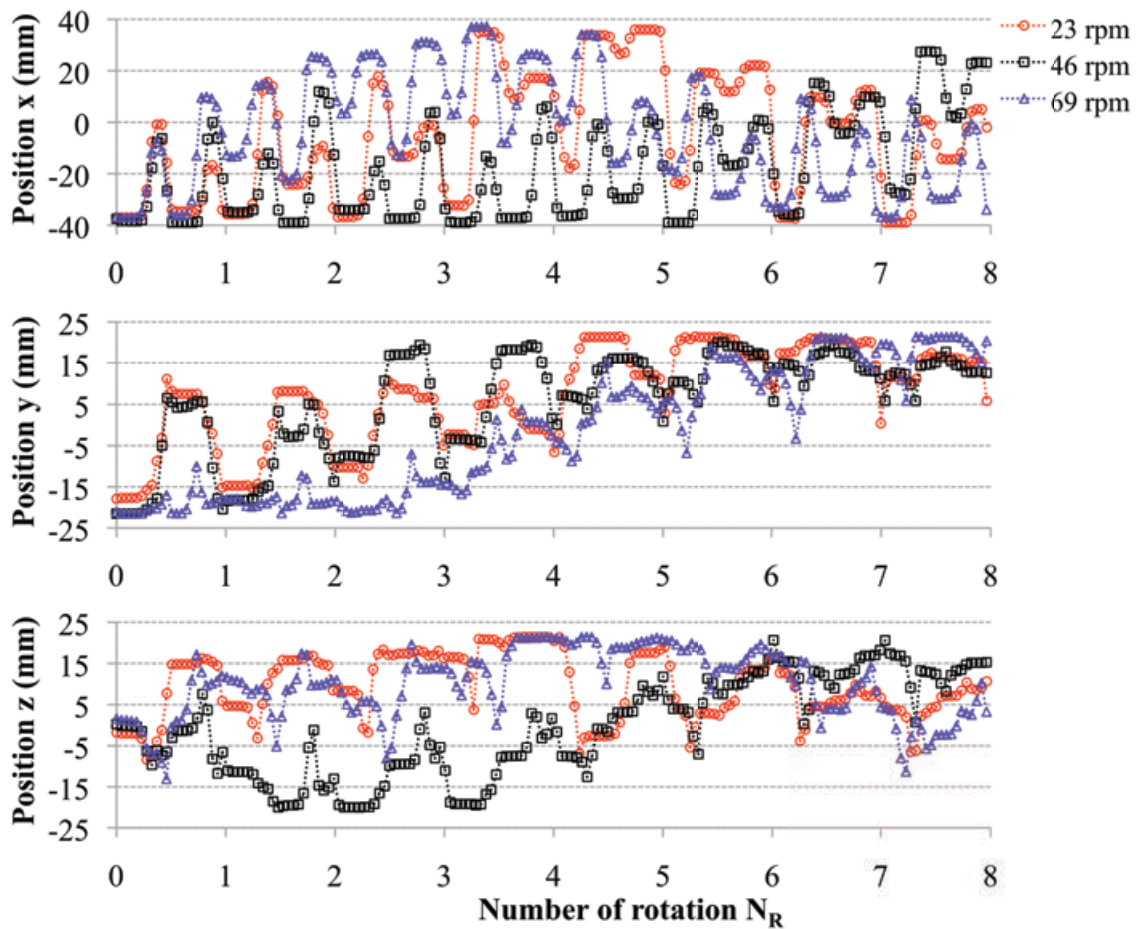


Figure 5.8: Typical particle position  $(x,y,z)$  with respect to the vessel coordinate system.

Movement was rhythmic and pulsating. The particle spent a relatively long period stationary (relative to the vessel) followed by rapid movement, repeated twice during each shaft rotation. It is interesting to note that, despite large displacement of the particle during the rapid movements, the net displacement over the course of a shaft rotation was relatively small. The

particle moved and then returned almost to the same position. In axial movement the forward and reverse movement comprised a single rapid swing, occurring twice within each shaft rotation. Conversely, in the cross-section, the forward and reverse motions were separated by the quiescent periods, and so occurred just once per shaft rotation. It would appear that these large rapid movements were bulk, with little movement of particles relative to each other.

### 5.2.3 Definition of the segregation (mixing) index

The degree of mixing and the time needed to achieve acceptable mixing can be predicted by simulations. There are two main approaches that can be used to quantify mixing in DEM simulations. The first is analogous to experimental approaches in which the coefficient of variation of the composition of “samples” is computed [10]. This approaches an asymptotic value as complete mixing is reached [11]. The alternative, adopted here, is to use the distribution of contacts between particles, as previously described [12,13]. A bed of particles was assumed to be uniformly mixed when the number of contacts between the particles of opposite fractions started to randomly fluctuate around a constant value. In this work a segregation parameter based on contact between particles of different species type *A* and type *B* was employed as previously proposed [14]. Here the segregation index *S* is defined as:

$$S = \frac{C_{AA}}{C_{AA} + C_{AB}} + \frac{C_{BB}}{C_{BB} + C_{AB}} \quad (5.2)$$

where  $C_{AA}$ ,  $C_{BB}$  and  $C_{AB}$  is the total number of contact between particles of different species A and B as schematically described in Figure 5.9.

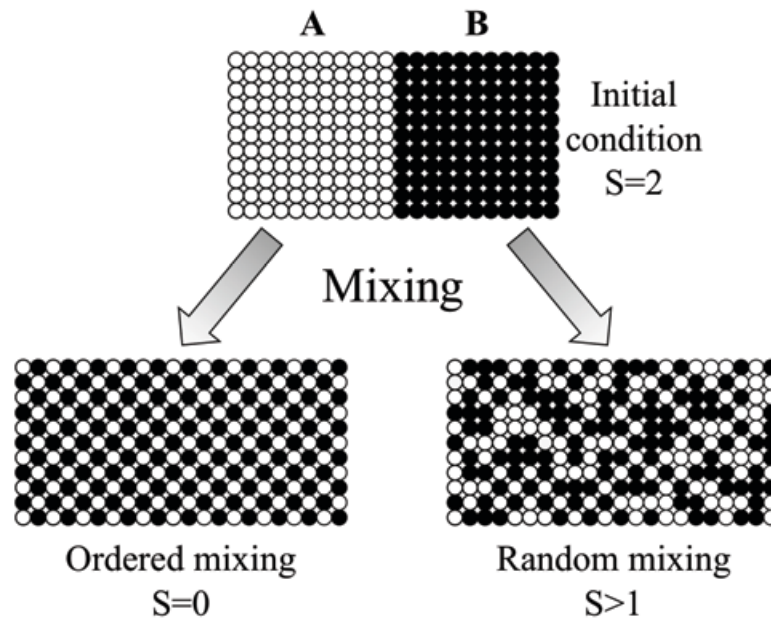


Figure 5.9: Schematic representation of contacts between particles for the definition of the segregation index based on contacts between particles of different species.

The segregation index can range between  $0 \leq S \leq 2$  according to Table 5.4, and for random mixtures it assumes the value of  $S=1$ . Either side of  $S=1$  are unstable states of segregation ( $S > 1$ ) and an ordered mixed system ( $S < 1$ ).  $S=0$  corresponds to a special ordered system in which there are no  $C_{AA}$  or  $C_{BB}$  contacts.

Table 5.4: Values for the segregation index  $S$ .

$C_{AA}$	$C_{BB}$	$C_{AB}$	<i>Segregation index</i>
$\neq 0$	$\neq 0$	$= 0$	Completely segregated system $S=2$
$\neq 0$	$\neq 0$	$\neq 0$	$2 > S > 0$
$= 0$	$= 0$	$\neq 0$	Perfect ordered system $S=0$

The definition of such index can be statistically described as follow. In a truly random mixture, the fraction,  $F$ , of the total contacts associated with each type is determined from the number fractions,  $N_A$  and  $N_B$ :

$$F_{AA} = N_A N_A \quad (5.3)$$

$$F_{BB} = N_B N_B \quad (5.4)$$

$$F_{AB} = N_A N_B \quad (5.5)$$

$$F_{BA} = N_B N_A \quad (5.6)$$

By definition  $F_{AB} = F_{BA}$  = half the total number of  $A$ - $B$  contacts counted and  $F_{AA} + F_{BB} + F_{AB} + F_{BA} = 1$ . So for a truly random mixture:

$$\begin{aligned} S &= \frac{C_{AA}}{C_{AA} + C_{AB}} + \frac{C_{BB}}{C_{BB} + C_{BA}} \\ &= \frac{F_{AA}}{F_{AA} + F_{AB}} + \frac{F_{BB}}{F_{BB} + F_{BA}} \\ &= \frac{N_A N_A}{N_A N_A + N_A N_B} + \frac{N_B N_B}{N_B N_B + N_B N_A} \\ &= 1 \end{aligned} \quad (5.7)$$

#### 5.2.4 Definition of coefficients of dispersion: particle dynamic analysis

The effect of the rotational speed on the mixing efficiency can be quantitatively estimated by studying the particle motion in the axial and radial directions, and by defining axial and radial dispersion coefficients,  $D_x$  and  $D_r$  in  $\text{mm}^2\text{s}^{-1}$ . The axial position was here considered along the  $x$ -direction, the cylinder axis in Figure 5.6, while the radial position was given by

$r = \sqrt{y^2 + z^2}$ . The axial dispersion coefficient has been used to measure the rate of mixing in the V-blender where side-to-side mixing happens in the axial direction [15].

In this work axial and radial dispersion coefficients have been defined as the square of the axial and radial displacements for all the particles within the vessel in one shaft rotation period:

$$D_x = \frac{1}{N-1} \sum_{k=1}^{k=N-1} \frac{\sum_{i=1}^{i=n} (x_i^{k+1} - x_i^k)^2}{(t^{k+1} - t^k)n} \quad (5.8)$$

$$D_r = \frac{1}{N-1} \sum_{k=1}^{k=N-1} \frac{\sum_{i=1}^{i=n} (r_i^{k+1} - r_i^k)^2}{(t^{k+1} - t^k)n} \quad (5.9)$$

Where  $x_i^k$  and  $x_i^{k+1}$  are the axial positions of the particle  $i$  at time  $t^k$  and at time  $t^{k+1}$ ;  $n$  is the total number of particles and  $N$  is the total number of shaft rotation considered ( $N_R=15$ ). Similarly  $r_i^k$  and  $r_i^{k+1}$  are the radial positions of the particle  $i$  at time  $t^k$  and at time  $t^{k+1}$ .  $(t^{k+1}-t^k)$  corresponds to the shaft period of rotation. These two coefficients will be compared with the results obtained from mixing experiment in PEPT and presented in Chapter 7.

### 5.3 Results: DEM mixing studies bed size ratio R=1

In order to follow and quantify the mixing process, the particle population was divided into two equal sized fractions of identical 2 mm particles  $A$  and  $B$ . The vessel was filled sequentially to give initially segregated fill patterns shown in Figure 5.2. The particles were identical so it would be expected that the mixing process would eventually lead to a random distribution of the two fractions corresponding to a segregation index  $S$  equal to 1.

### 5.3.1 Axial loading patterns: influence of rotational speed on the mixing rate

Firstly, the system with the “axial” loading pattern was studied. The segregation index  $S$  for various rotational speeds is presented in Figure 5.10. It can be observed that all the lines tended towards the asymptotic value corresponding to random mixing  $S=1$ . At different rotational speeds, however, the number of rotations necessary to achieve this value changed, implying a change in mixing rate per revolution.

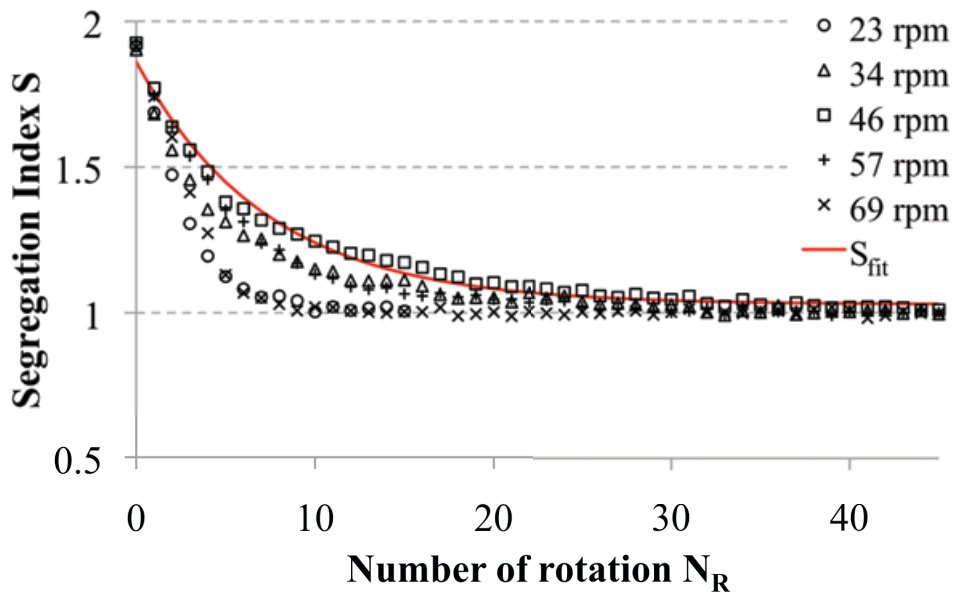


Figure 5.10: Segregation index as a function of rotational speed and blender revolutions  $N_R$ .

Example of fitted curve for 46 rpm.

It can be seen that the mixing process can be fitted with the exponential decay curve, Eq.(5.10). A representative fit (for 46 rpm) is shown in Figure 5.10.

$$S_{fit} = S_{\infty} + (S_0 - S_{\infty})e^{-N_R/N_{mix}} \quad (5.10)$$

where  $N_R$  is the actual number of rotations,  $N_{mix}$  is the characteristic number of shaft rotations required to achieve a 63.2% decrease in the segregation index (mixing),  $S_0$  the initial segregation index (approximately 2), and  $S_\infty$  the asymptotic value for the segregation index (equal to 1 in the case of random mixing). The values of  $S_\infty$  and  $N_{mix}$  were determined by minimization of the sum of squares of the difference between the segregation index determined from the simulation by using Eq.(5.2) and the exponential decay law, Eq.(5.10). The shape of these curves is typical of mixing curves seen in other systems [16]. In Figure 5.10 the initial steep part of the curve corresponded to a fast reduction in heterogeneity associated with macroscopic bulk movement of material (shearing or convection). These large movements of material had the major effect in terms of the initial mixing rate. This is followed by a much slower period where mixing was achieved by microscale diffusive mechanisms in which movement of single or small groups of particles were contributing to the improvement of mixing [17]. Although the particle movements associated with both mixing mechanisms occurred simultaneously throughout the mixing process, the importance of each depended on the magnitude of movement of particles relative to each other compared to the scale of segregation. In a segregated system (i.e. early in the mixing process described here) the average separation distance of the two populations is relatively high and small scale movements from dispersive mechanisms have a limited effect compared to the large bulk movements arising from convective flows. As mixing proceeds, the clusters of the like particles become smaller and the average separation distance of the two populations will reduce. Once this separation approaches the mean free movement due to dispersion, then dispersive mechanisms start to dominate. The characteristic mixing time,  $t_{mix}$ , can also be defined as the quotient of  $N_{mix}$  and the rotational speed of the mixer. These two numbers illustrate the effect of speed on mixing efficiency for the Turbula as shown in Figure 5.11.

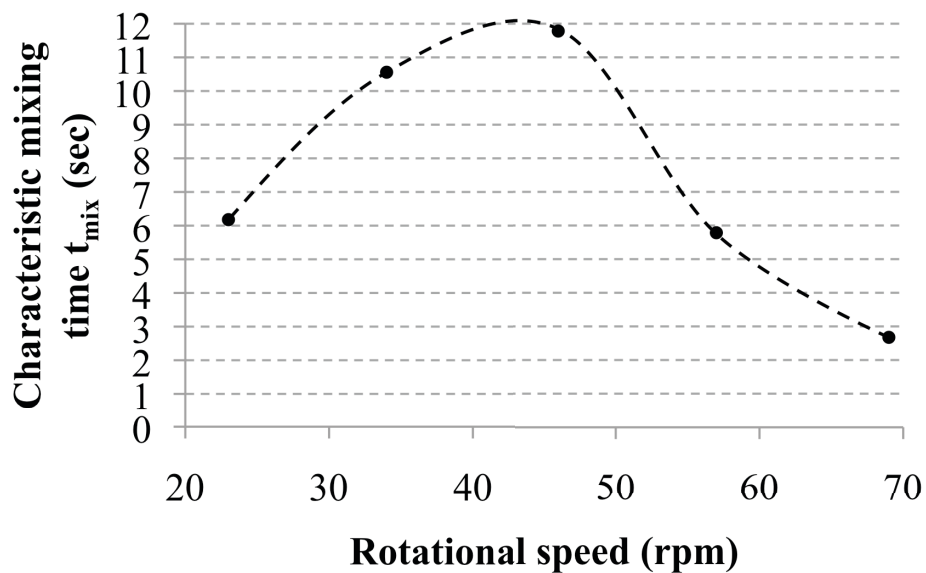
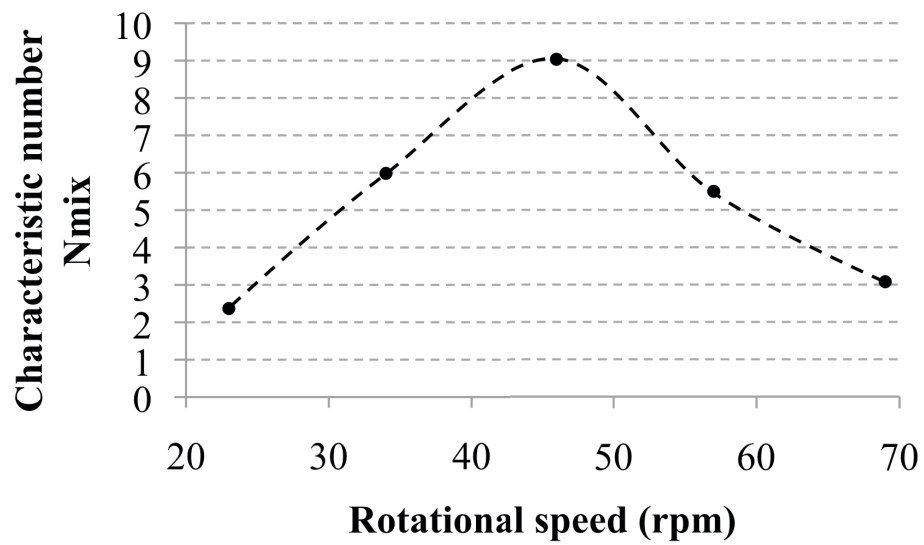


Figure 5.11: Characteristic number of rotations and characteristic mixing times (to achieve 63.2% mixing) as function of shaft rotation speed.

The non-monotonic relationship between characteristic number of rotations (rate of mixing) and operational speed is interesting. Figure 5.11 shows there was a steady and marked deterioration in mixing efficiency as shaft speed increased from 23 to 46 rpm, followed by improvement as speed further increased to 69 rpm. In fact, in terms of the number of

revolutions required to achieve mixing, 23 rpm and 69 rpm were almost identical (the 23 and 69 rpm curves in Figure 5.10 overlap) hence the faster speed achieves the mixing three times faster. At 46 rpm, the mixing efficiency was so poor relative to 23 rpm that, despite operating at twice the speed, it still took double the time to achieve the same degree of mixedness. The use of the segregation index was demonstrated qualitatively by snapshots of the vessel contents in Figure 5.12. The difference in mixing as speed increased from 23 to 46 to 69 rpm is clear: after just five rotations the particles were almost completely dispersed at 23 and 69 rpm compared to 46 rpm where the particles appeared to have barely moved from the initial loading pattern. The mixing was clearly less effective in the axial direction at 46 rpm. In fact, according to Figure 5.11, it would take about 20 revolutions to achieve the same degree of mixing at this speed.

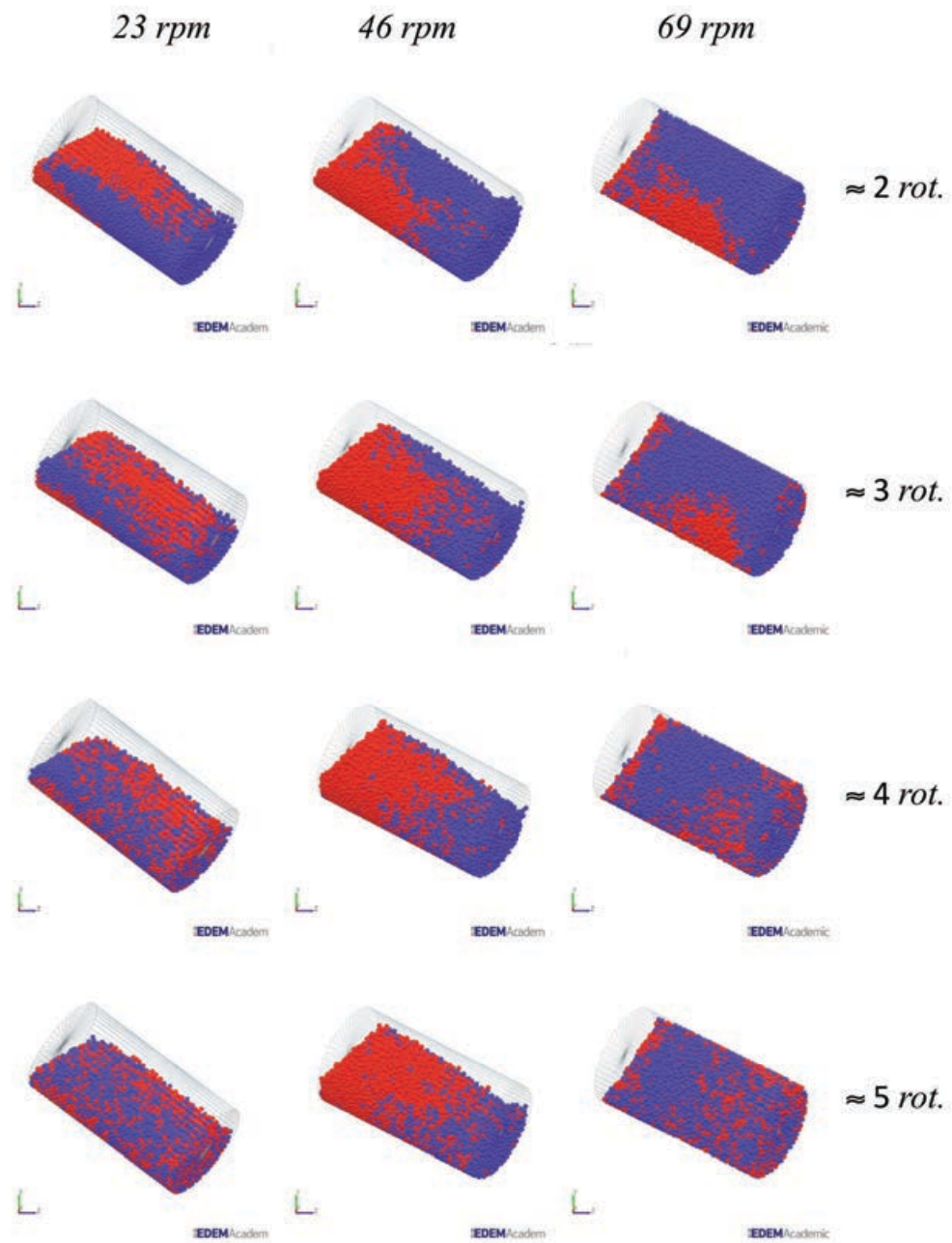


Figure 5.12: Snapshots of particles within the vessel as mixing proceeded from the 2<sup>nd</sup> to the 5<sup>th</sup> shaft rotation at 23, 46 and 69 rpm.

Snapshots at different rotational speeds of 23, 46 and 69 rpm are reported to show the vessel position and direction of motion to visualise the bed behaviour at different point in time (*a,b,c,d,e,f,g,h*).

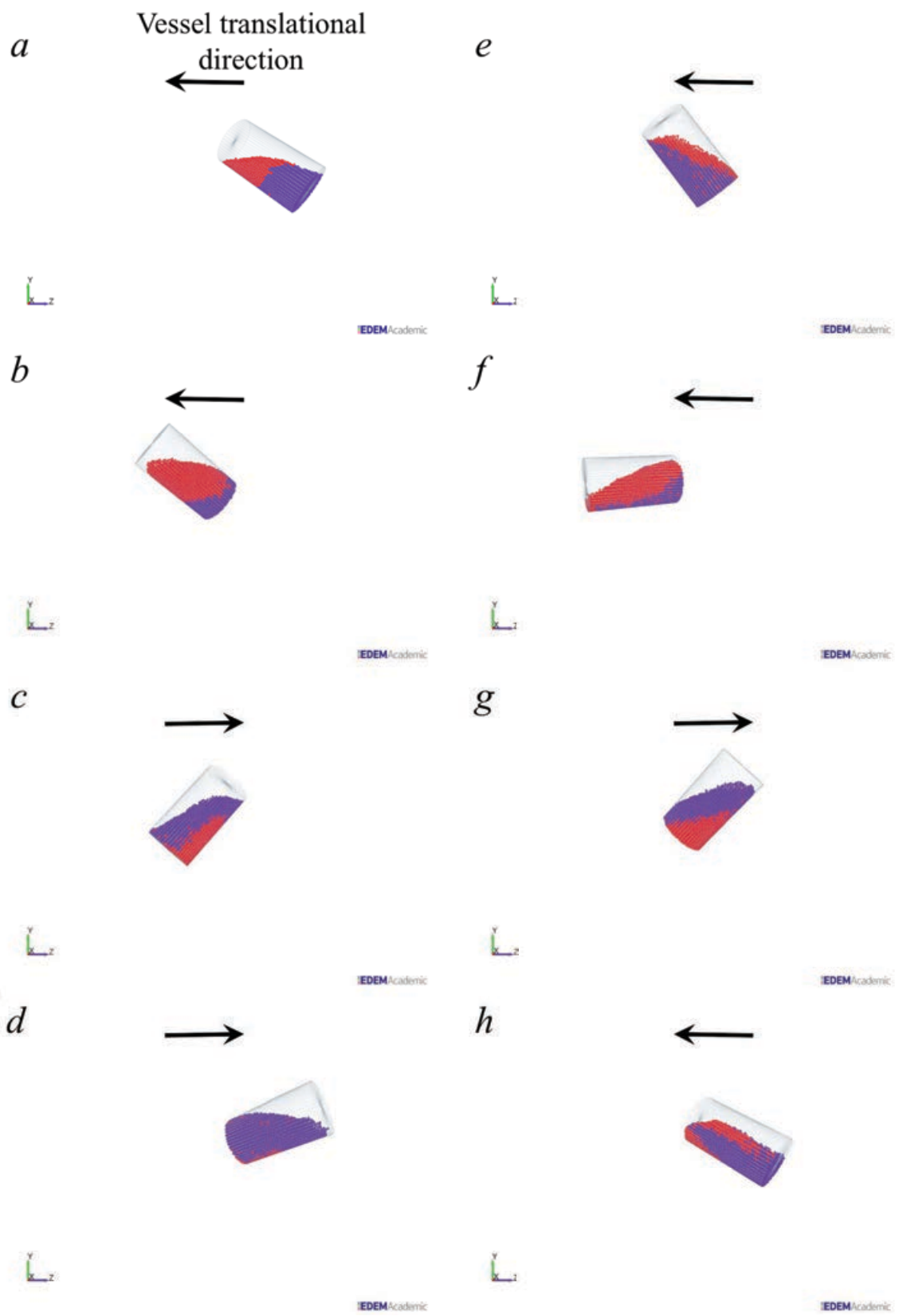


Figure 5.13: Snapshots of vessel position during the first complete rotation at 23 rpm.

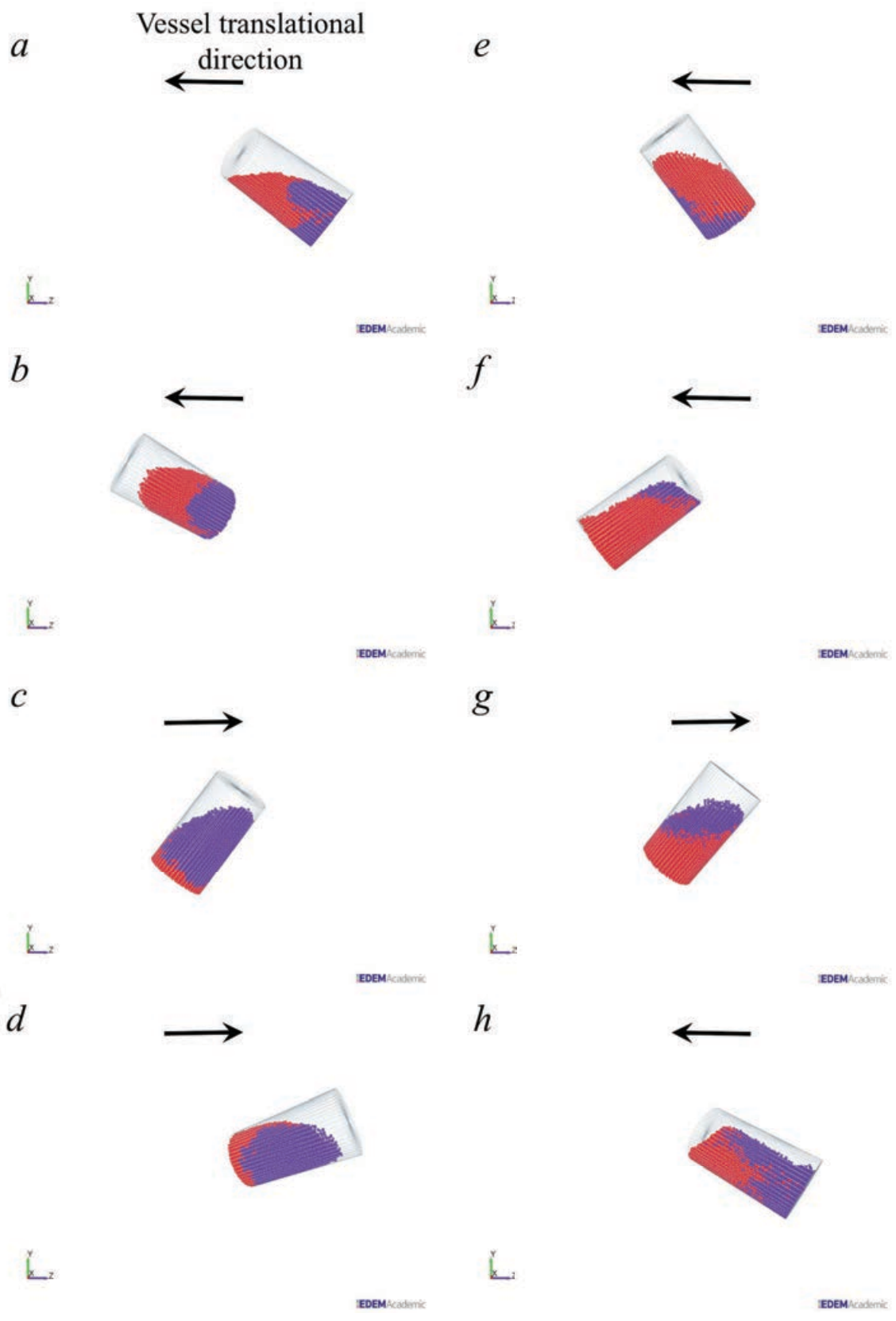


Figure 5.14: Snapshots of vessel position during the first complete rotation at 46 rpm.

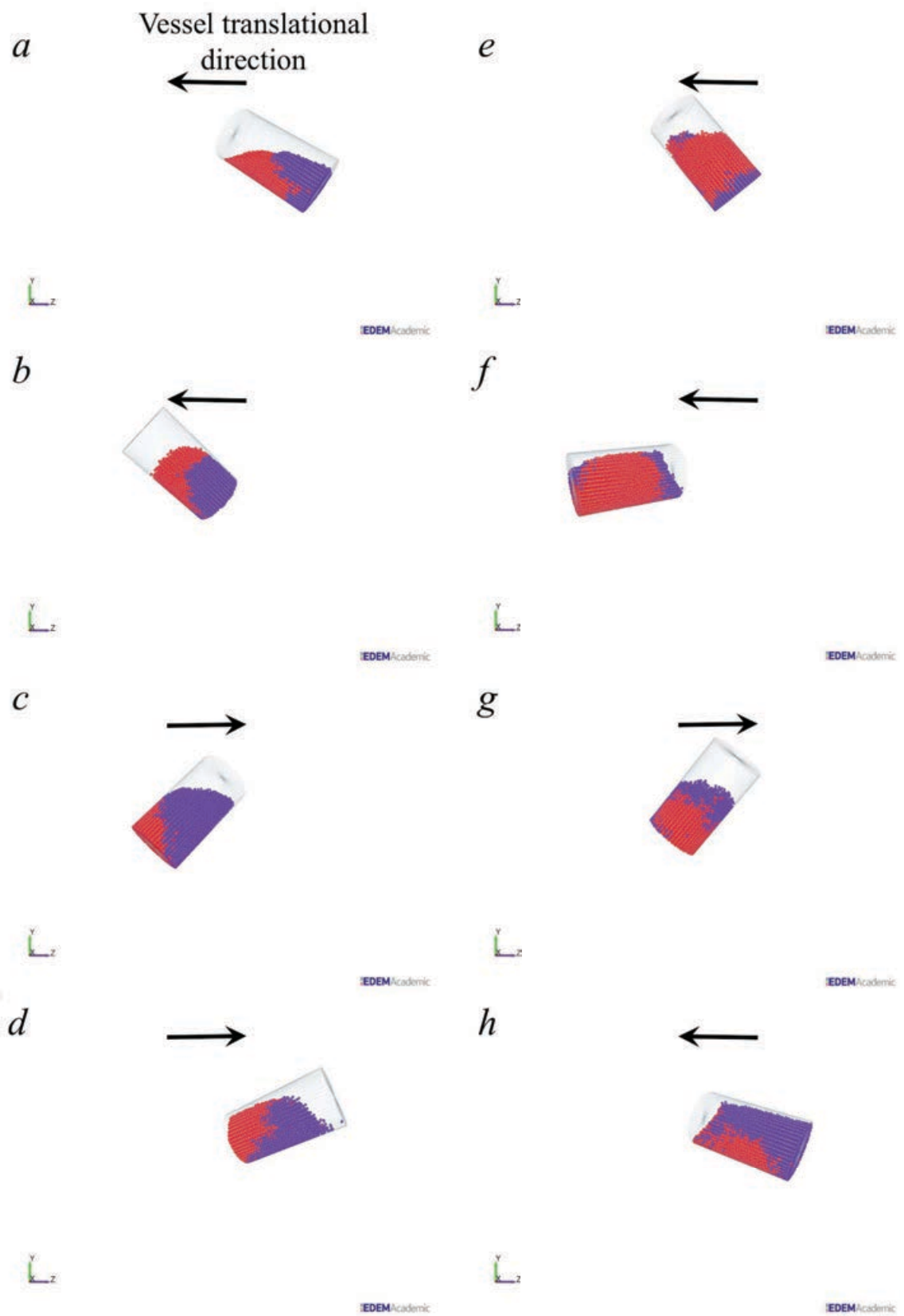


Figure 5.15: Snapshots of vessel position during the first complete rotation at 69 rpm.

As mixing progresses there is no reason to expect particles to return in their previous position after a shaft rotation of the mixer. The “dispersion coefficient”, therefore, should be related with the mixing time since it is a measure of the degree of disorder as a function of speed since it represents the change of particle positions after each rotational period. The effect of rotational speed on the mixing efficiency, qualitatively shown in Figure 5.12, has been estimated by using the definition of axial and radial dispersion coefficients,  $D_x$  and  $D_r$ , given by Eq.(5.8) and Eq.(5.9) which values are reported in Figure 5.16 as function of the mixer speed.

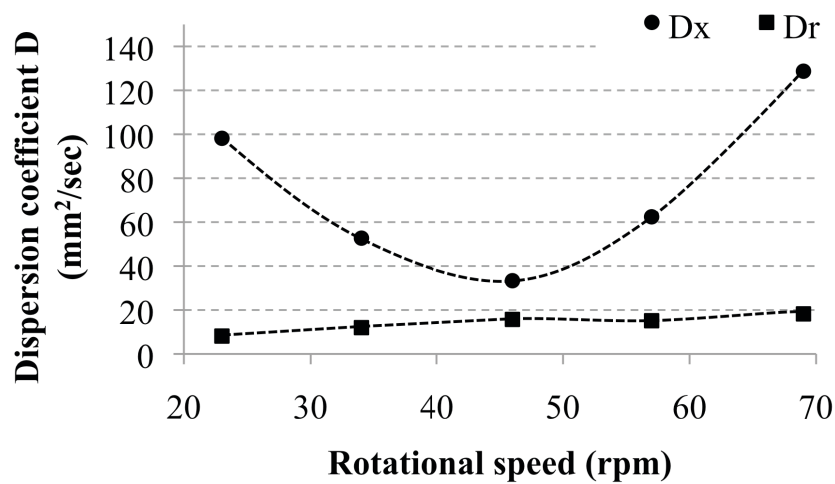


Figure 5.16: Axial and radial dispersion coefficients  $D_x$  and  $D_r$  as a function of the rotational speed.

It can be observed that the axial dispersion decreased initially until the rotational speed reached 46 rpm and above this value it increased again. The radial dispersion was considerably smaller than the axial coefficient and showed a very different dependence on speed. This and the similarity between the rate of mixing measured by contacts, Figure 5.10,

and the axial dispersion, Figure 5.16, suggests quite strongly that the dominant mixing mechanism was in the axial direction.

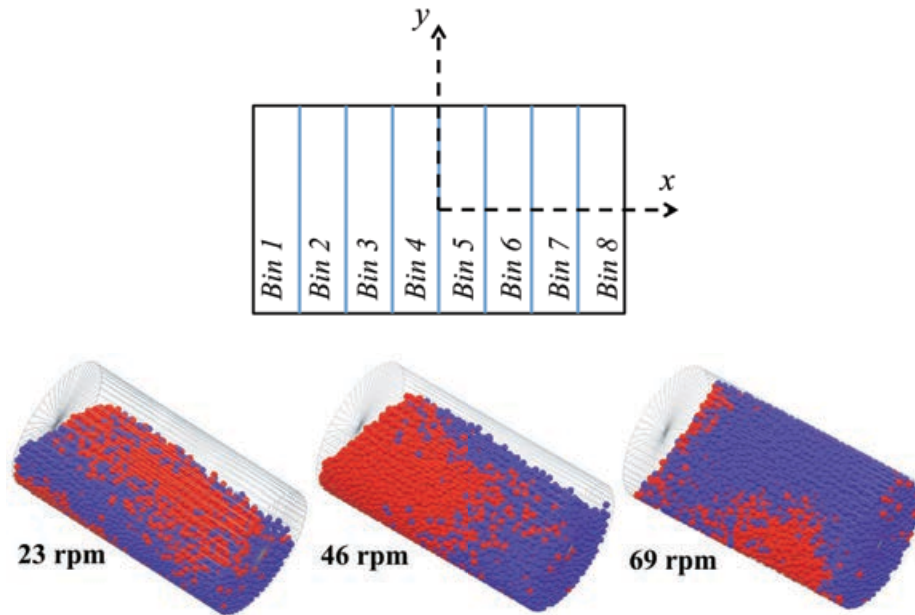


Figure 5.17: Cylindrical vessel binned in axial  $x$  direction every 10 mm and orientation of the vessel.

The cylindrical vessel was binned in the axial direction every 10 mm, Figure 5.17. For the cylinder orientated as shown in Figure 5.17 (this correspond to the position and orientation  $h$  in Figure 5.13, Figure 5.14 and Figure 5.15) the number of particles inside every bin was counted after each rotation for a total number of 15 rotations. Figure 5.18 shows the average number of particles inside each bin for the number of rotations considered. It can be seen that at high rotation speed the effect of inertial forces in the axial direction compressed the particles toward the end bin 8. Marked differences were seen between low speed and high speed with two apparent groups of curves. From 23 up to 46 rpm, the particles are uniformly distributed between bin 2 and 7. The medium speed seems to represent again some sort of

critical velocity with a step change beyond 46 rpm, which corresponded to an higher concentration of particles towards the right end of the vessel, from bin 5 until 8. This was probably another indication that the medium speed (46 rpm) corresponded to a critical speed for the change of the bed behaviour.

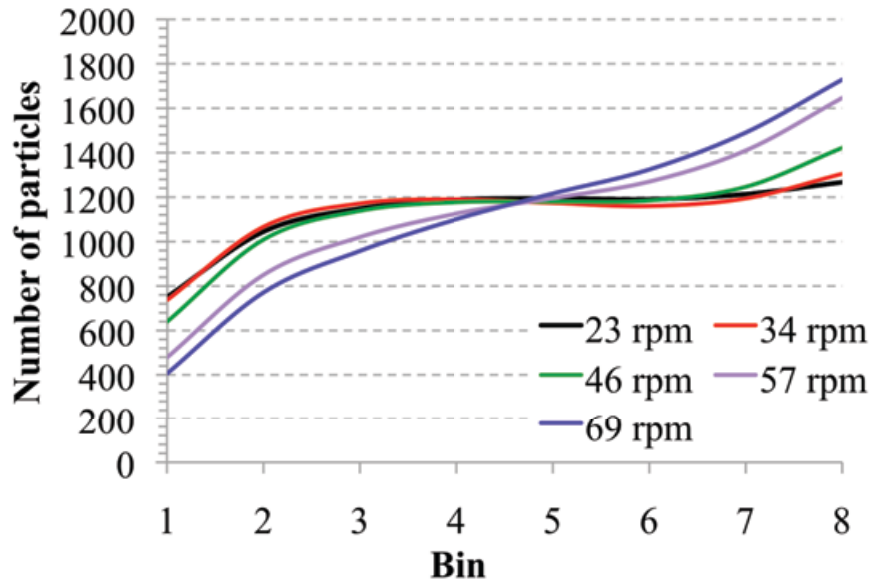


Figure 5.18: Average number of particles during the 15 rotations inside each bin.

The axial dispersion coefficient,  $D_x$ , has been calculated according to the particle positions in the axial direction (bin) at the beginning of each rotation. In Figure 5.19, it can be noted that the trend for the dispersion coefficient in the axial direction  $D_x$  was maintained and at medium speed the particles seemed to change their axial position less after each rotations. It can be noticed that the particles between bin 1 and bin 4 (particles in front of the bed) changed axial position more than the particles that were located between bin 5 and bin 8 (particles near the end wall and compressed with in the bed). These particles in the front of the bed had a greater degree of freedom and, therefore, more chance of changing their position after each rotation.

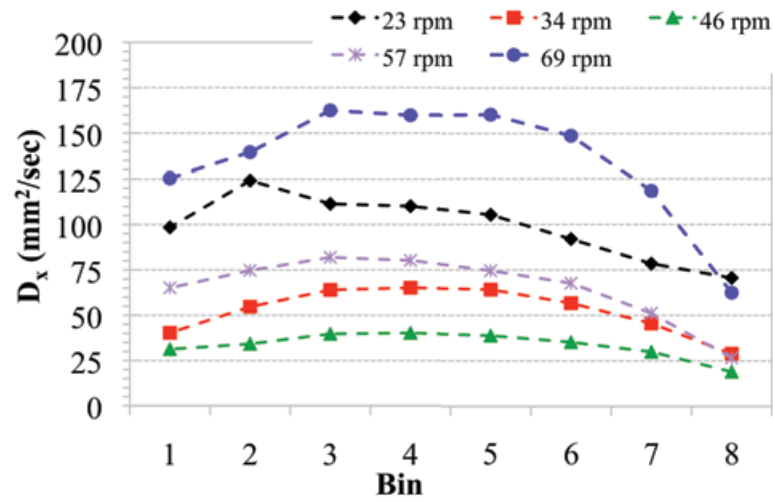


Figure 5.19: Axial dispersion coefficient  $D_x$  calculated considering particle binning.

### 5.3.2 Transverse loading patterns: influence of rotational speed on the mixing rate

From the previous discussion it seems that the mixing was less effective at 46 rpm due to the poor mixing in the axial direction. To investigate this, the vessel was filled with the transverse loading pattern shown in Figure 5.2, where the particles were initially uniformly distributed along the axial direction, but completely segregated in the transverse direction.

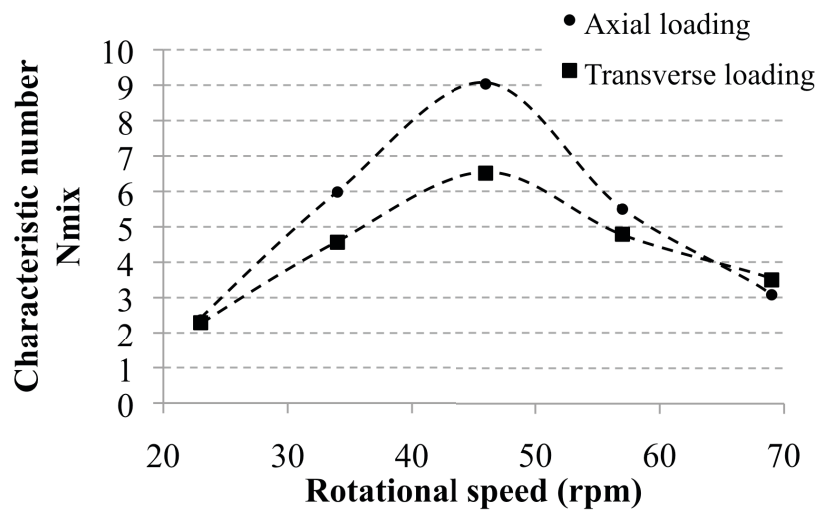


Figure 5.20: Characteristic number of rotations for the two loading patterns as a function of rotational speed.

As can be seen in Figure 5.20, the initial distribution had little effect at the extremes (23 and 69 rpm) where the mixing was efficient. At 46 rpm, where the efficiency was poor, the effect of distribution was quite marked: the effect of the initially uniform axial distribution was to reduce the number of revolutions required to achieve mixing – albeit only by about 25%. And at 46 rpm, mixing was still considerably less efficient than at 23 or 69 rpm. So, while important, it seems that axial dispersion was not the only reason for the change in efficiency.

### 5.3.3 Particle movement in axial direction

The  $x$  directional distance travelled at different speeds the movement of ten particles, as selected in Figure 5.21, was followed.

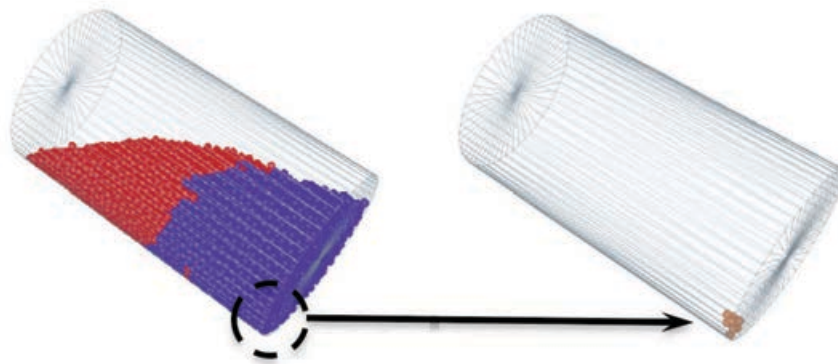


Figure 5.21: 10 particles selected for “bucket” analysis.

The periodic movement in axial direction is shown in Figure 5.22 for one of the selected particles. The axial position of the selected particle is depicted at 23, 46 and 69 rpm. Particle movement in the axial direction (from one peak to the following peak, distance travelled during horizontal translation of the vessel) was periodically alternated with a period of no

particle movement in the axial direction (plateau). These plateaus corresponded to the inversion of the vessel.

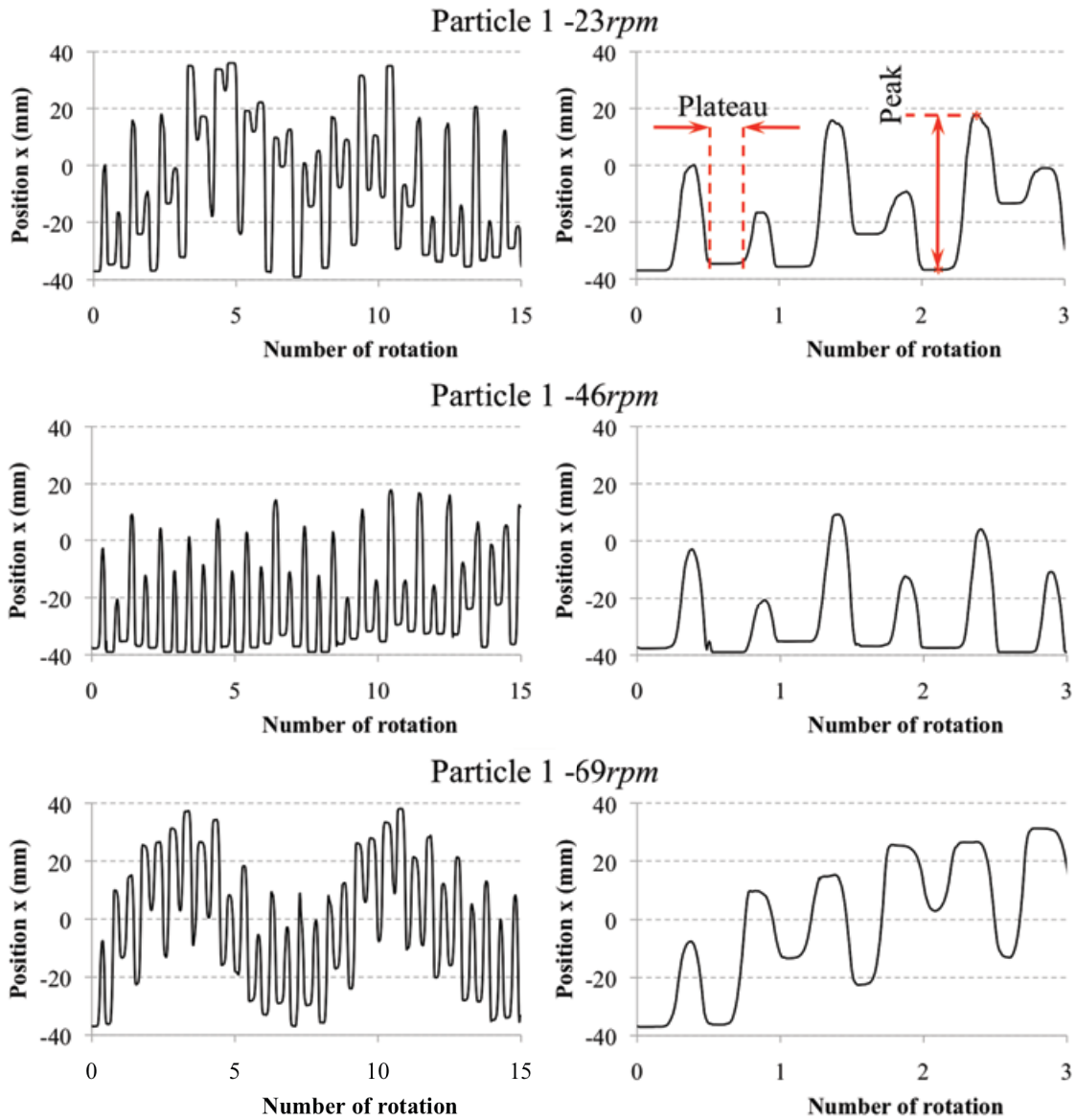
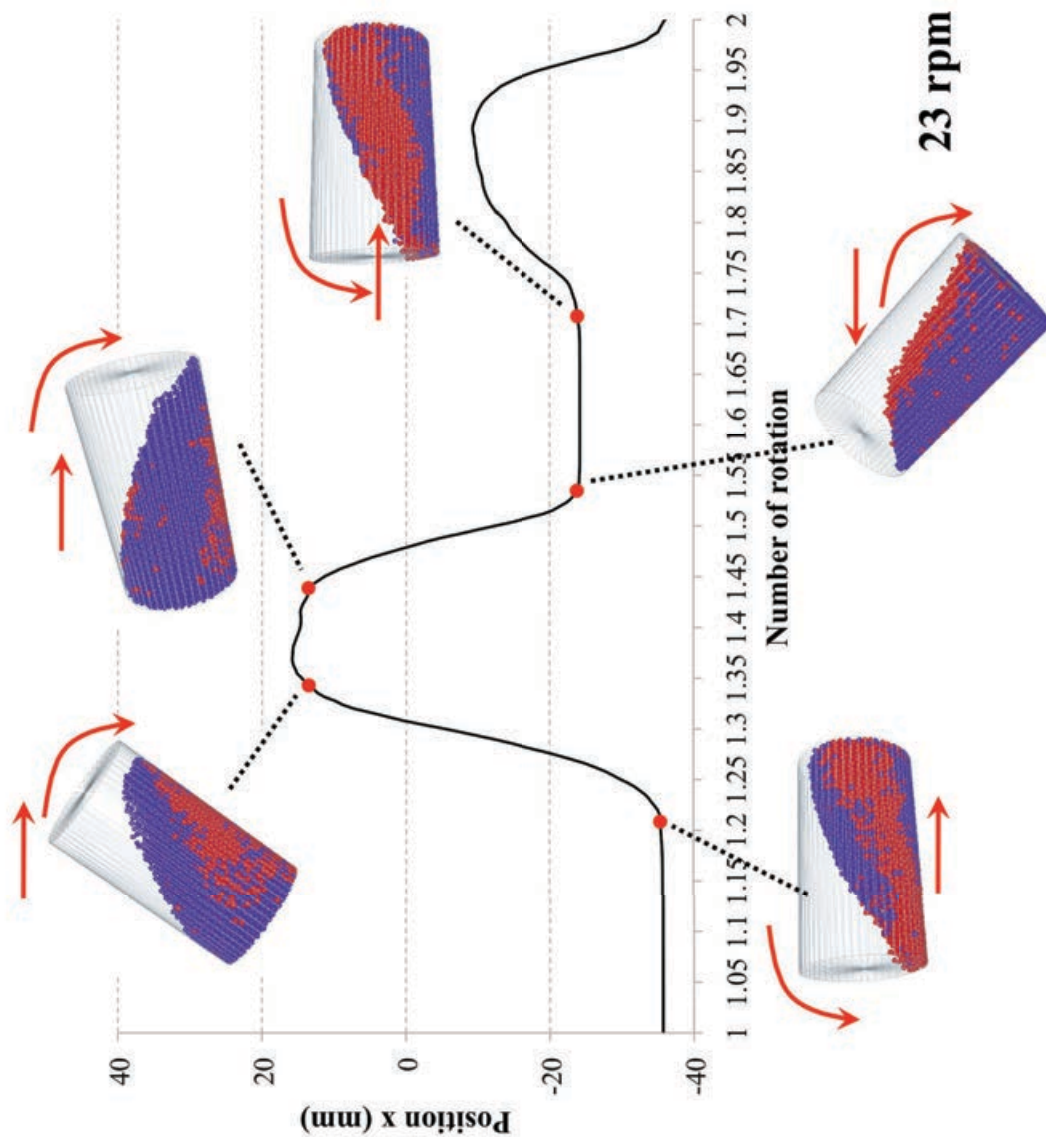
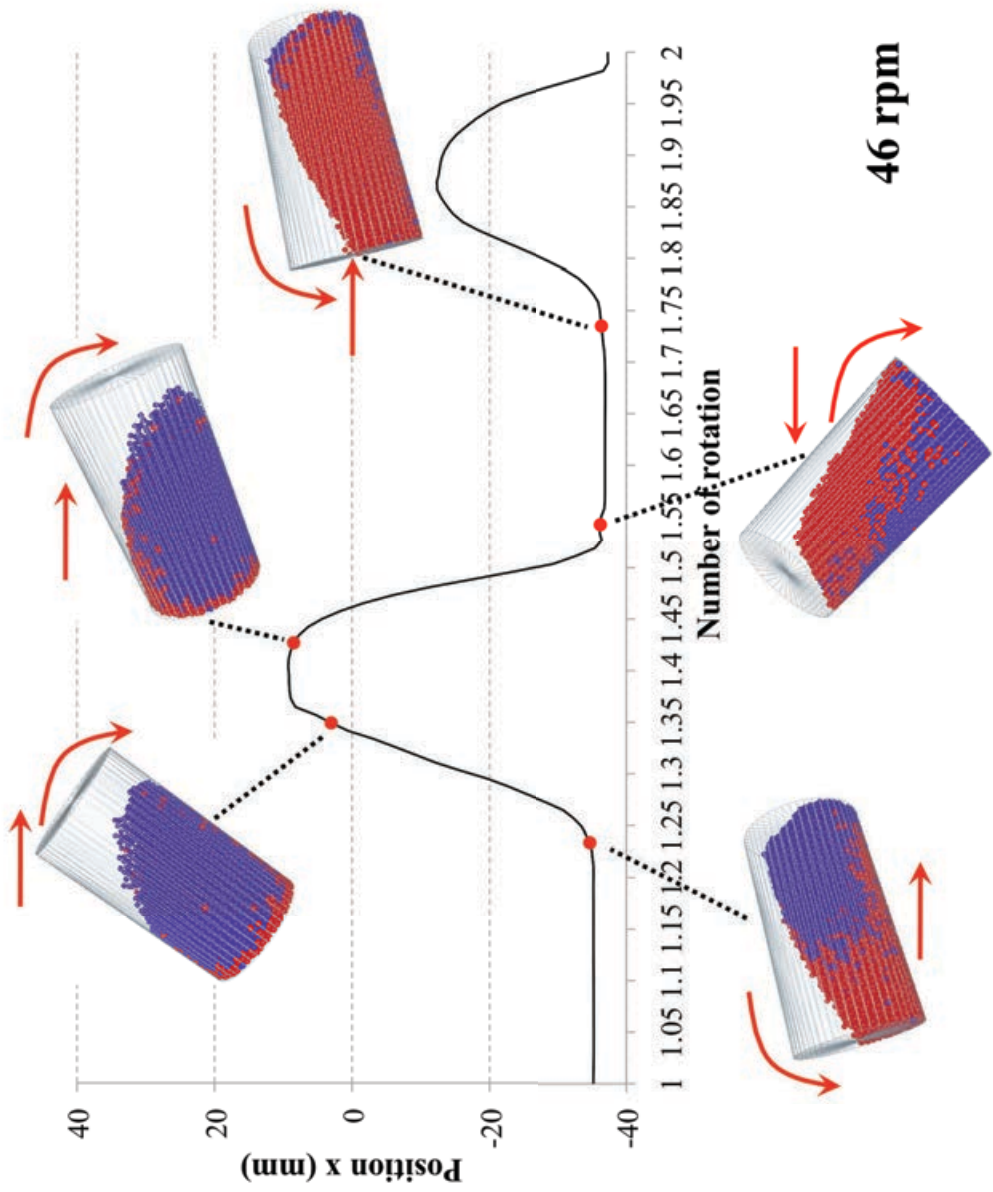


Figure 5.22: Plot of  $x$  position against number of rotation for one of the ten particles particle at 23, 46 and 69 rpm for 15 shaft rotations (left) and plot for the first 3 rotations (right), definition of peak.

During the motion of inversion for the vessel, there were periods during which the particles alternated between axial movement periods and static periods. For the three speeds (23, 46 and 69 rpm) the vessel orientation, between rotation 1 and 2, is shown in Figure 5.23 for the same fraction of rotation. This illustrates how the particle bed changed shape as a function of the operating speeds, indicating that inertial forces probably played an important role at the highest speed.





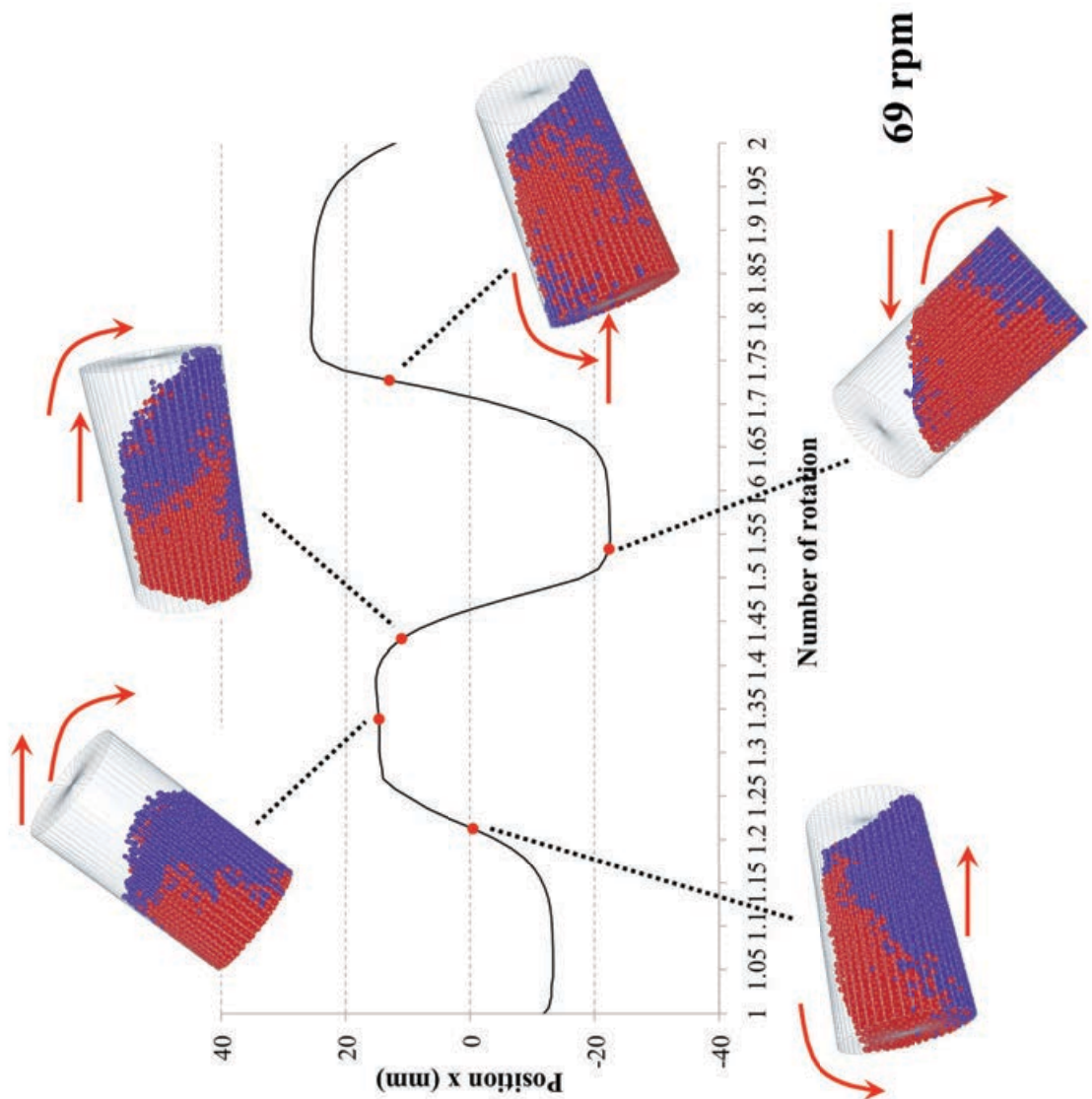


Figure 5.23: Plot of  $x$  position for one of the ten particles during the motion between rotation 1 and 2 with the corresponding orientation for the vessel at the same rotation fraction.

In the next plot, Figure 5.24, the average of the length of such static periods for the ten particles selected is plotted as a function of speed. The scatters for each data point were very small, hence no error bars are evident. It can be observed that by increasing the speed the bed movement in the axial direction showed shorter duration for the static periods during the vessel cycled movement.

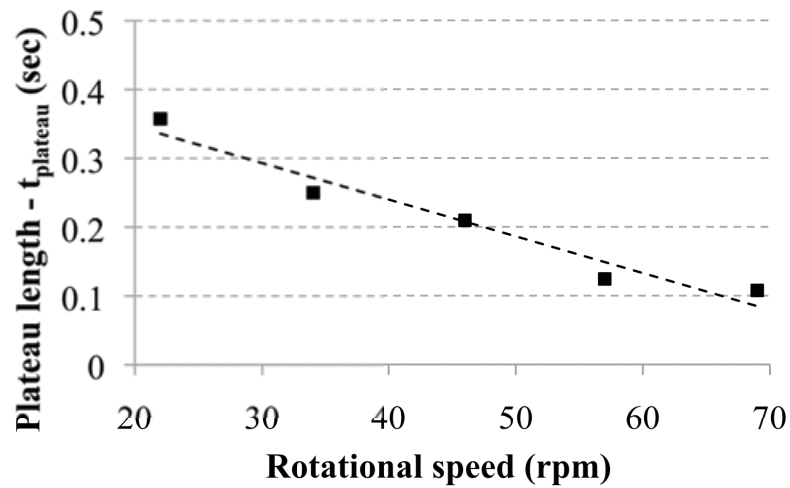
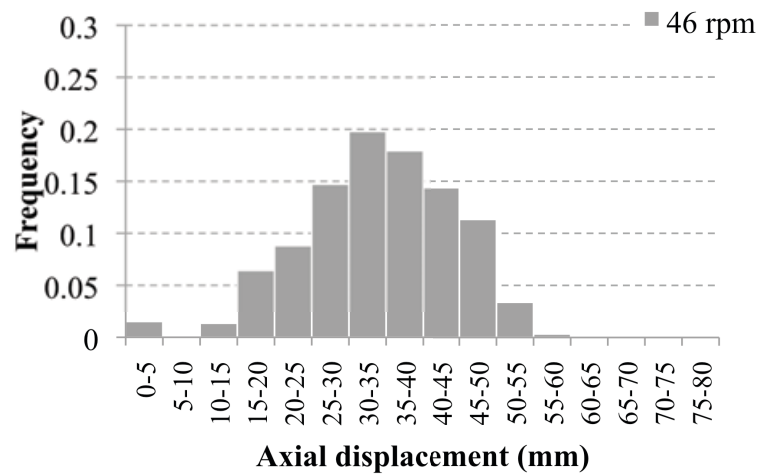
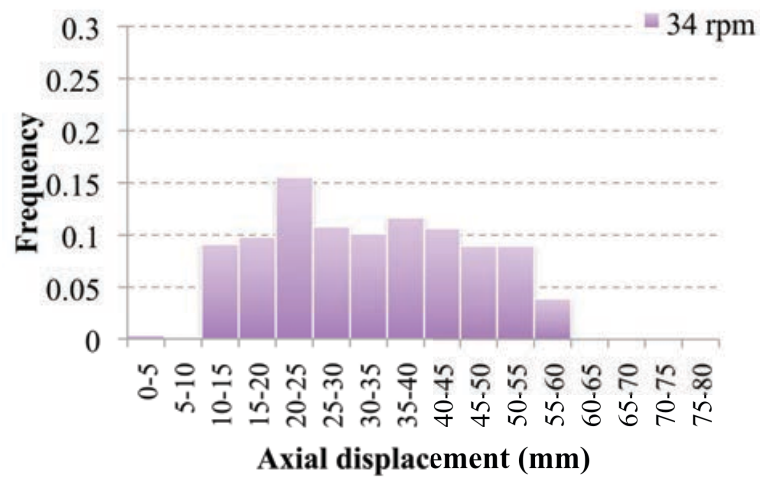
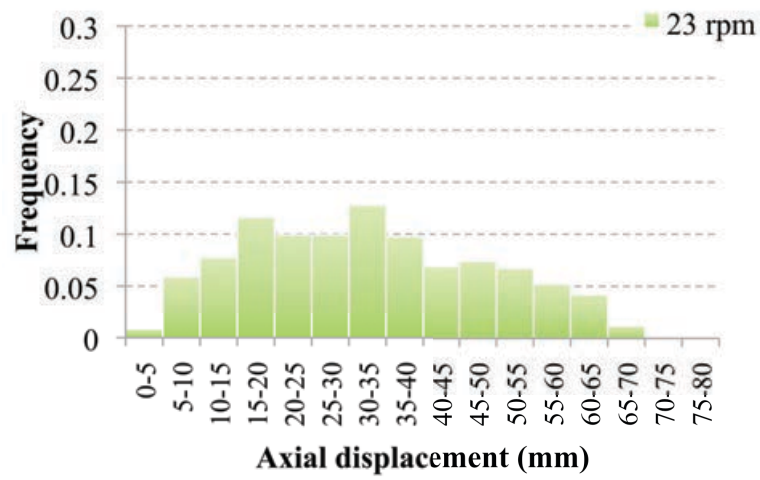


Figure 5.24: Length of average plateau periods in axial direction for the ten particles selected as a function of speeds.

For the 10 selected particles the frequency distribution peak axial displacement was calculated for all the 15 shaft rotations, Figure 5.25. By increasing the speed the distribution of peaks tended to reduce toward a narrower distribution (qualitatively same trends observed from PEPT, but not same absolute values, ref. Chapter 7).



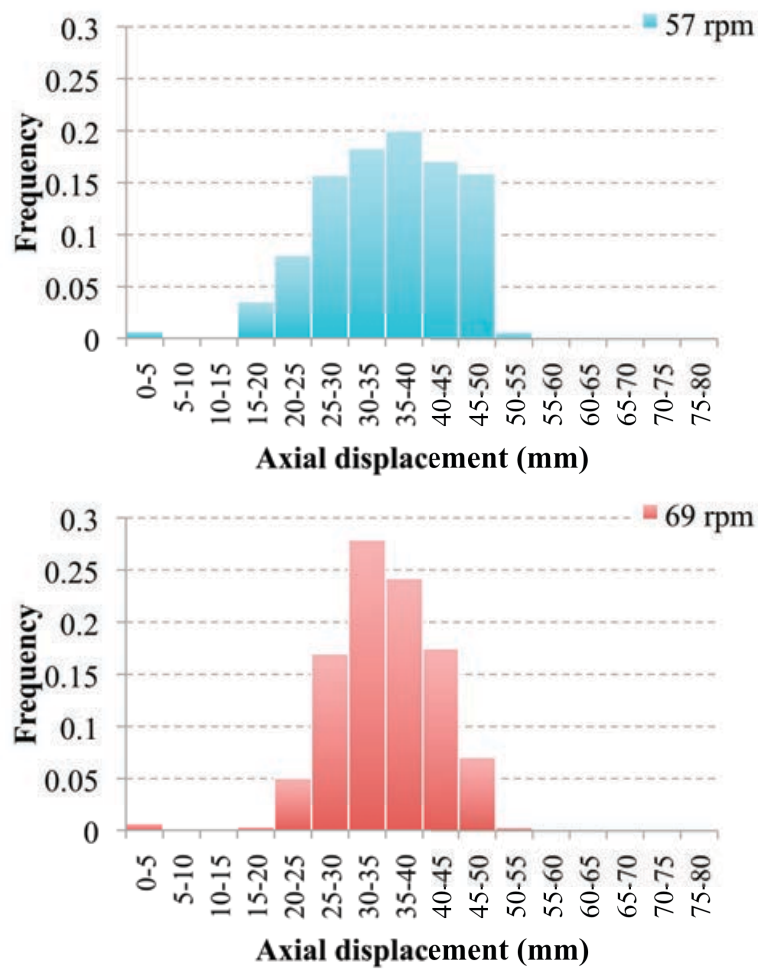


Figure 5.25: Number of peaks divided by total number of peaks during the 15 shaft rotations at different shaft rotational speeds.

It seems that different axial mixing mechanisms were competing as a function of the operating speeds. The more random distribution of axial movement in the axial direction at lower speed could explain why at such speed the dispersion coefficient in axial direction was high and therefore mixing rate assumed a high value. Particles at this lower speed probably also had more time for changing their reciprocal positions between two consecutive inversions of the vessel. By increasing the speed the distribution of axial movement for the ten particles became narrower. This indicated that during the motion between the vessel

inversions the particles travelled similar distances in the axial direction. This corresponded to the period where the particles are shunted from one end to the other end of the vessel. Similar qualitative trends have been observed in the experiments PEPT confirming the numerical predictions (ref. Chapter 7).

### 5.3.4 Particle speed analysis

In this section the scalar particle velocities with respect to the coordinate system  $(x,y,z)$  fixed to the vessel have been analysed during one rotation. The particles average speed in the axial direction  $v_{x\_particle}$ , the particles average transverse direction  $v_{t\_particle}$ , and the overall particle average speed  $v_{particle}$ , are defined as follows:

$$v_{x\_particle} = v_x \quad (5.11)$$

$$v_{t\_particle} = \sqrt{v_y^2 + v_z^2} \quad (5.12)$$

$$v_{particle} = \sqrt{v_x^2 + v_y^2 + v_z^2} \quad (5.13)$$

In Figure 5.26 the overall average particle speed,  $v_{particle}$ , during a vessel period motion is shown. As expected, the particle average speed increased with the increase of the operational speed. The period for the speed  $v_{particle}$  corresponded to the period of the shaft rotation since during each shaft rotation there were four inversions. The average particle speed being always higher than zero implies that the particles kept moving relative to each other even when the vessel was inverting the direction of motion.

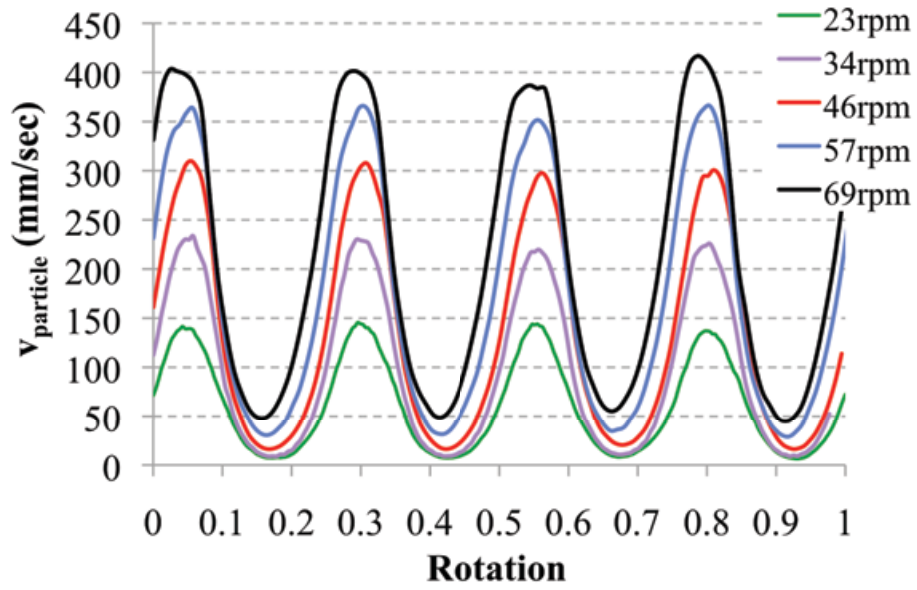


Figure 5.26: Particles average speed  $v_{particle}$  increases with the increase of the operating speed.

At each timestep the components for the vessel translational and rotational velocity components are known from the motion definition (ref. Paragraph 5.2.1). Axial and transverse particles speed  $v_{x\_particle}$ , and  $v_{t\_particle}$  have also been normalized with respect to the vessel translation and rotational velocity  $v_{vessel}$  and  $\omega_{vessel}$  as follows:

$$\frac{v_{x\_particle}}{v_{vessel}} = \frac{v_{x\_particle}}{\sqrt{v_1^2 + v_2^2 + v_3^2}} \quad (5.14)$$

$$\frac{v_{t\_particle}}{\omega_{vessel} D^*} = \frac{v_{t\_particle}}{D^* \sqrt{w_1^2 + w_2^2 + w_3^2}} \quad (5.15)$$

With  $D^*$  that is given as geometric parameter for the vessel considering the length and the radius:

$$D^* = \sqrt{\left(\frac{D_{vessel}}{2}\right)^2 + (L_{vessel})^2} = \sqrt{22.5^2 + 80^2} \quad (5.16)$$

For a given rotation Figure 5.27 and Figure 5.28 report the normalised particle speed, calculated by Eq.(5.14) and Eq.(5.15). It can be noted that the average axial velocity  $v_{x\_particle}$  had the same period of the vessel velocity  $v_{vessel}$ . Again it can be noted that the normalised velocity increased slightly with the operational speed.

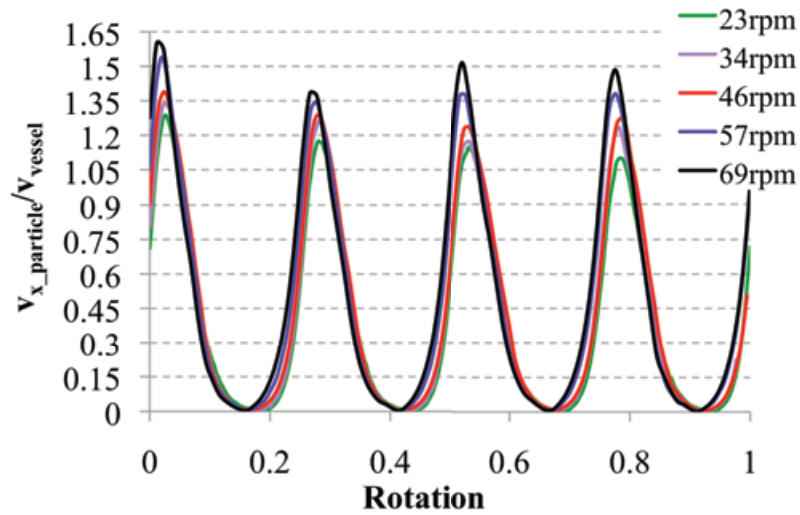


Figure 5.27: Normalised axial average particles velocity.

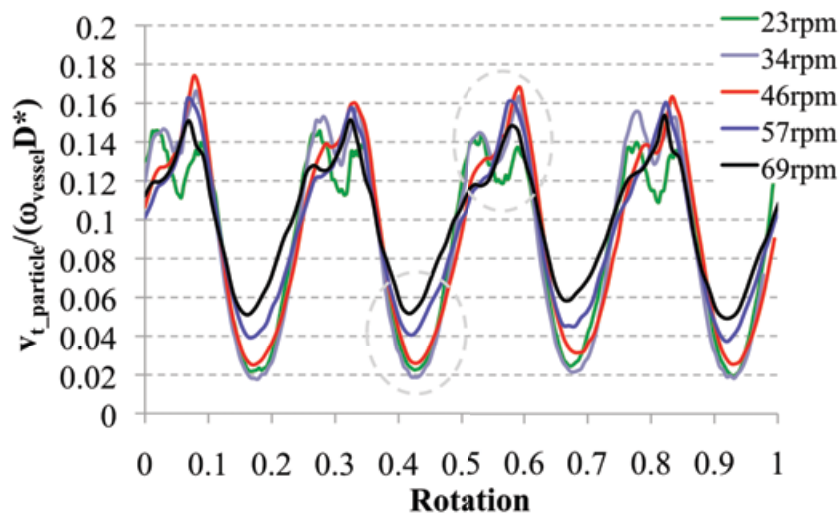


Figure 5.28: Normalised transverse average particle velocity.

The normalised transverse average particle velocity had an interesting behaviour as a function of operating speed. Two areas on the plot can be highlighted with apparent differences, firstly at low values and also at high values of the normalised transverse average particle velocities. From 23 up to 46 rpm there was not much difference at low values, with all three lines following a similar path. When the speed was increased to 57 rpm or 69 rpm, however, the path of the lines significantly deviated from the other three speeds and the minimum values obtained increased. At high values, for speeds of 23 and 34 rpm there were “double kicks” which became less evident at 46 rpm, and were almost absent at both 57 and 69 rpm.

From the previous plots it seems that different mechanisms occurred simultaneously and their importance probably changed as function of the operating speed. Mixing efficiency is likely a combination of their effect in the axial and transverse directions.

#### **5.4 Results: DEM mixing studies influence of rotational speed for a particle bed size ratio $R=1.4$ (bimodal particles)**

It is well known that during mixing particles of sufficiently different sizes may segregate [10], even in simple shear flows. Here we investigated segregation using a bi-disperse collection of particles with different sizes. The cylindrical vessel was partially filled (50% fill level including voidage) with spherical particles with a particle bed size ratio  $R=1.4$ ; the two particle fractions had equal volume. The movement of the vessel simulated at five speeds is summarised again in Table 5.5 for five different cases.

Table 5.5: EDEM simulations conditions for  $R=1.4$ .

Case	Particle diameter (mm) (Number of particles)	Fill %	R	Speed (rpm)
1	2 (4500) - 1.4 (13100)	≈50	1.4	23
2	2 (4500) - 1.4 (13100)	≈50	1.4	34
3	2 (4500) - 1.4 (13100)	≈50	1.4	46
4	2 (4500) - 1.4 (13100)	≈50	1.4	57
5	2 (4500) - 1.4 (13100)	≈50	1.4	69

In all simulations two different particle sizes with the same volume fraction were used. Figure 5.29.a shows the initial particle loading pattern, the colours represent the 2 types of particles (red for 1.4 mm diameter and blue for 2 mm diameter particles). In Figure 5.29.b and Figure 5.29.c the final particle pattern with a concentration of small particles in the middle of the particle bed can be observed for the 23 rpm operating speed. In this paragraph preliminary results and a qualitative comparison with data from MRI measurements are reported.

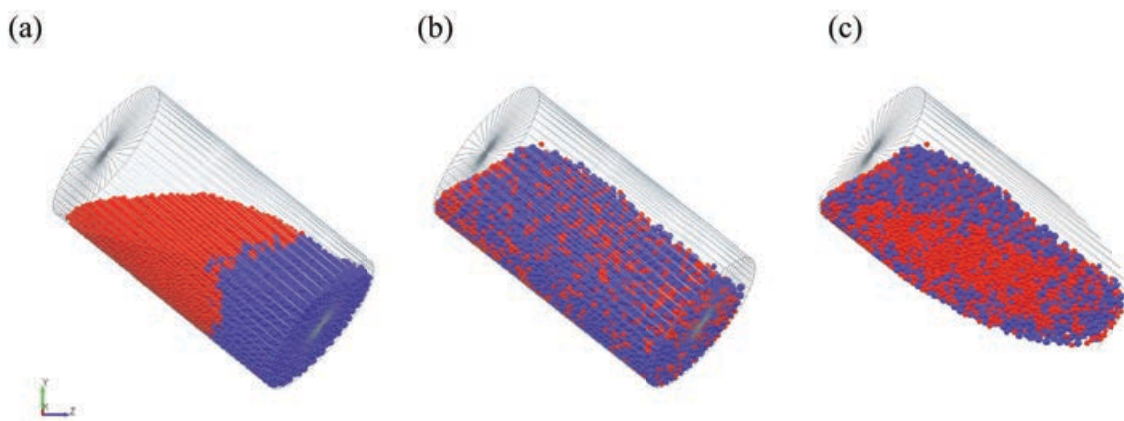


Figure 5.29: (a) Initial loading pattern, (b) final pattern and (c) section after 18 rotations for monodisperse and bidisperse simulations at 23 rpm and  $R=1.4$ .

For the Turbula mixer, experimental results have been presented in literature by Sommier *et al.* 2001 [7]. By using MRI imaging experiments using MRI doped and undoped sugar bead particles, it was observed that residual segregation occurred when particles with a diameter ratio were mixed. Large sugar bead particles became more concentrated along the inner wall of the container and on the free surface of the bed, whilst the smaller particles accumulated in the central area of the bulk of material, Figure 5.30.

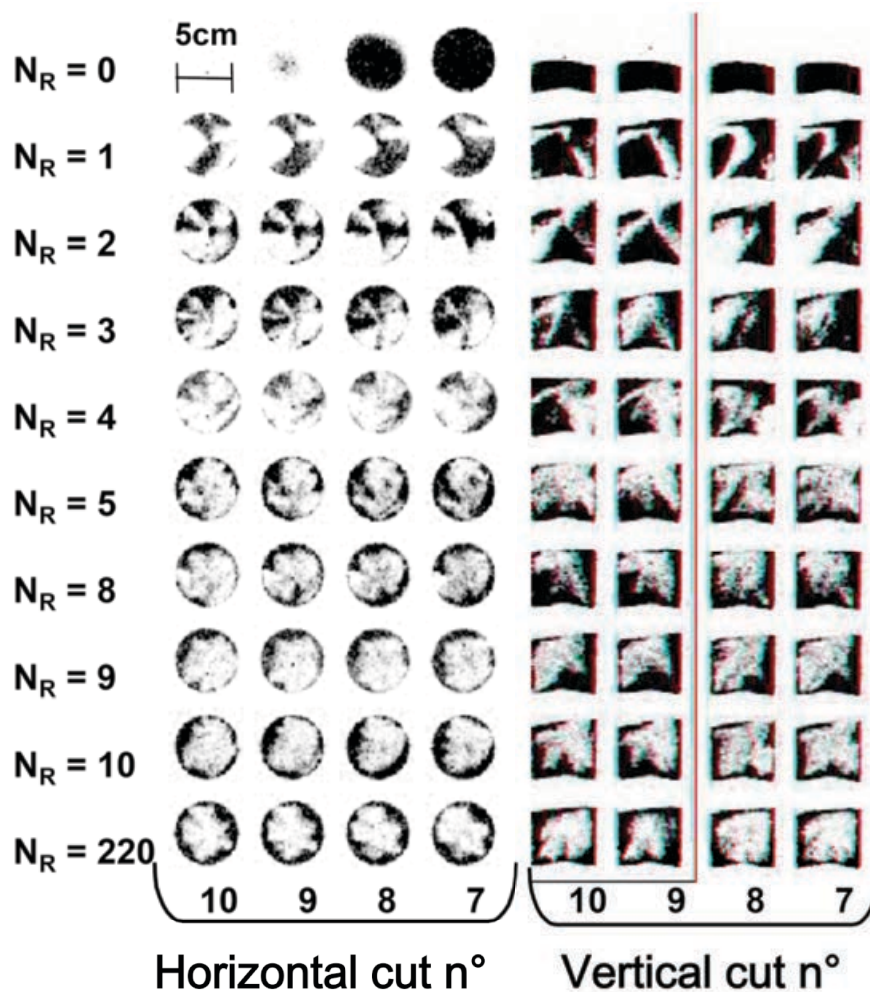


Figure 5.30: 1 mm doped beads with 0.35 mm undoped beads  $R=2.8$  at 23 rpm. Segregation of small particles in the centre of the bed (white area).

A similar effect was observed in the DEM simulations reported here as shown in Figure 5.29.c where high concentrations of large particles along the external surface of the bulk of material can be observed indicating a remarkable segregation effect.

The change of segregation index during mixing has been measured with voxel statistical analysis and the estimation of the variance for the concentration of particles  $S'$  [7]. This definition was different than the one used for the DEM simulation reported here and based on number of contacts between particles. However, similar comparable qualitatively trends should be expected regarding mixing behaviour.

Sommier *et al.* 2001 [7] observed that the number of rotations required to achieve a segregated system for  $R=2.8$  was much lower than the number of rotations to achieve mixing for  $R=1$ , Figure 5.31. Similar behaviour has been qualitatively observed by DEM simulation in case of bed size ratio of 1.4.

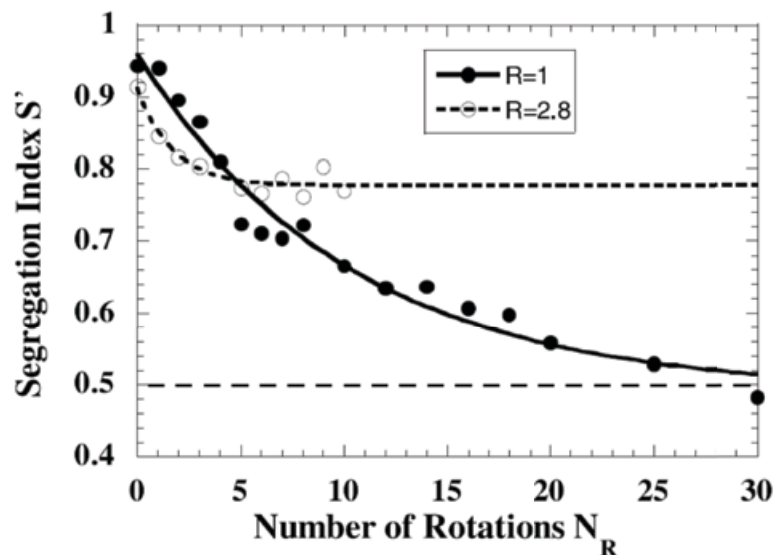


Figure 5.31: Trends for the segregation index for monodisperse ( $R=1$ ) and bidisperse particles ( $R=2.8$ ) at 22 rpm. Redrawn from [7].

Figure 5.32 shows from the DEM simulations that at steady state, the segregation index, when  $R=1.4$  (bidisperse particles), was greater than for  $R=1$  (monodisperse particles) showing the effect of segregation at low speed, 23 rpm. From the DEM simulation during the first few rotation the segregation index showed less differences between the monodisperse and bidisperse particles, if compared with MRI experimental results where more remarkable differences can be observed. This was probably due to the choice of particle bed size ratio  $R=1.4$  rather than 2.8. However, it can be observed that for  $R=1.4$  the point when mixing was not occurring anymore (residual segregation) was reached at a much smaller number of rotations than the number of rotation necessary to achieve random mixing ( $S=1$ ) for  $R=1$ .

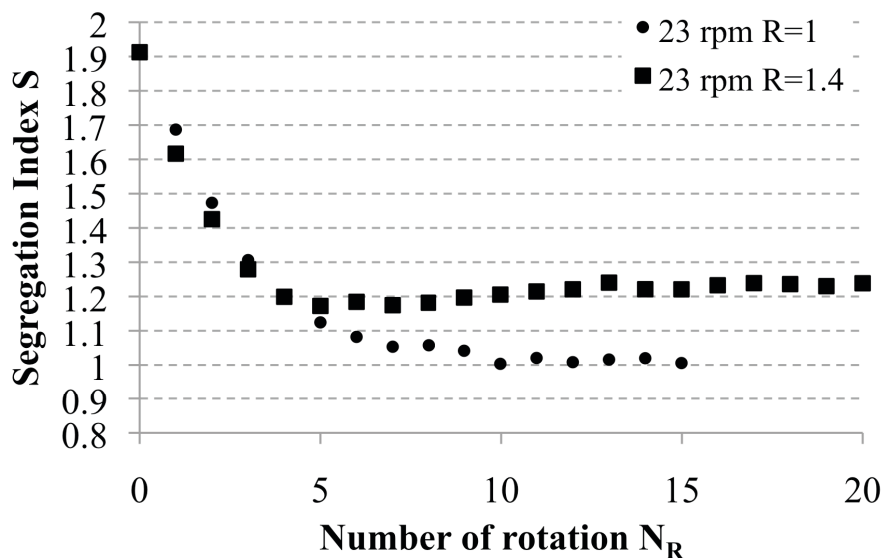


Figure 5.32: Trends for the segregation index from DEM simulations for monodisperse ( $R=1$ ) and for bidisperse particles ( $R=1.4$ ) at 23 rpm.

Figure 5.33 shows the segregation index from DEM simulations as a function of operational speed for a system comprising bidisperse particles ( $R=1.4$ ). It may be observed that by increasing the speed the system reached a better degree of mixing. Furthermore, it may be

noted that the initial rate of mixing decreased from 23 to 46 rpm and further increased up to 69 rpm. This is in agreement with what was already observed in the monodisperse system.

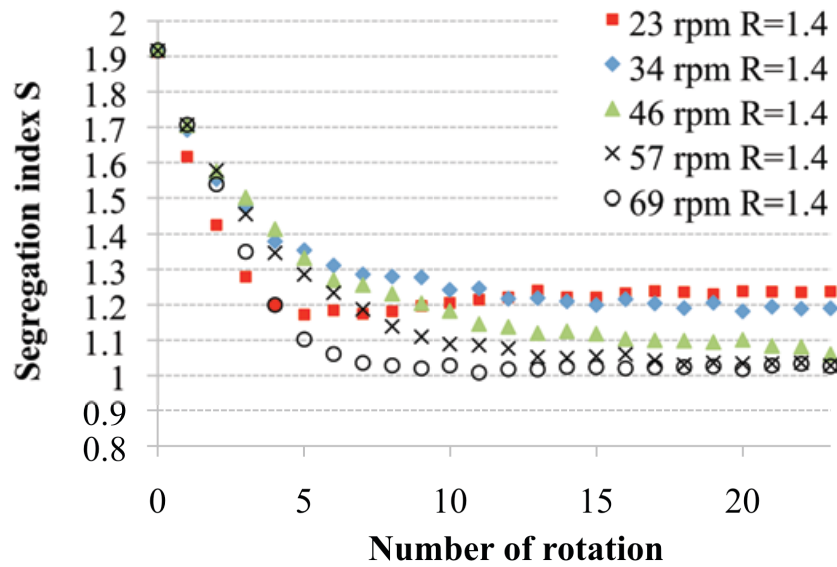


Figure 5.33: Trends for the segregation index from DEM simulations for bidisperse particles ( $R=1.4$ ) at different mixer speeds.

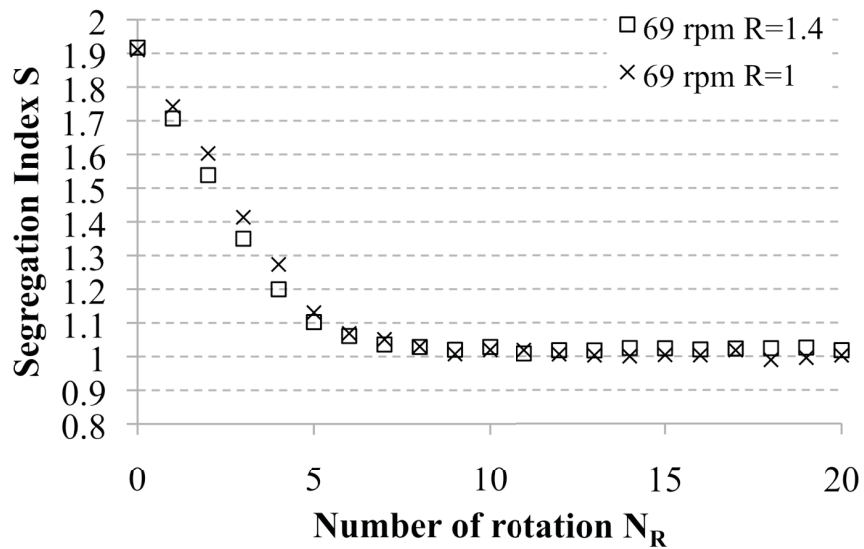


Figure 5.34: Trends for the segregation index from DEM simulations for monodisperse ( $R=1$ ) and bidisperse particles ( $R=1.4$ ) at 69 rpm.

At higher speed, 69 rpm, it can be observed that the effect of different particle sizes on bed ratio was negligible, Figure 5.34, and at higher speed the system with a bed size ratio plateau at about  $S=1$ .

In Figure 5.35, the segregation index at steady state measured by MRI experiments is reported as a function of rotation speed for  $R=2.8$  [7]. It was shown that the residual segregation decreased and mixing improved when the rotational speed increased.

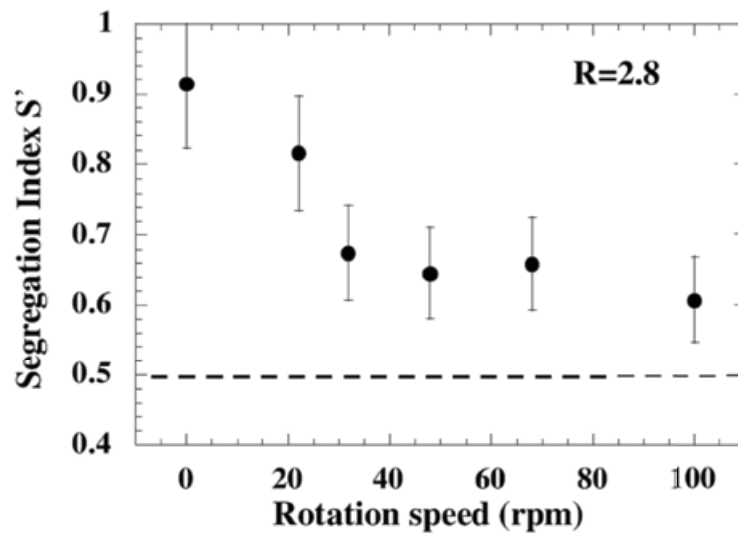


Figure 5.35: Ultimate level of segregation index as a function of mixer speed [7].

In Figure 5.36 the segregation index calculated by DEM simulation for  $R=1.4$ , after 23 total rotations, is reported as a function of operating speed. The increase of operational speed led to an improvement of the mixing quality, indicating good qualitative agreements between the experimental results and the DEM simulations.

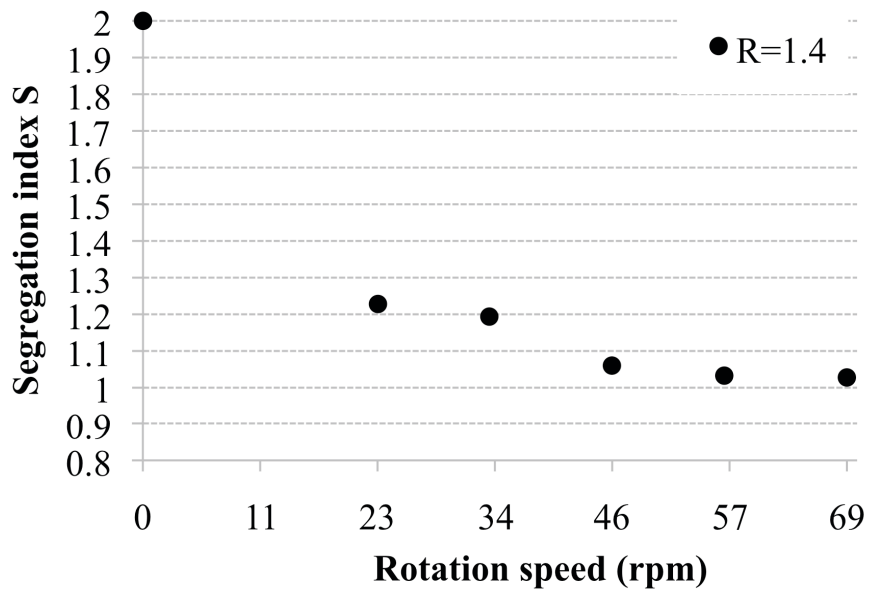


Figure 5.36: Ultimate level of segregation index versus rotation speed from DEM simulations after 23 rotations.

#### 5.4.1 Effect of baffle design: mixing improvement in case of bidisperse particle (R=1.4)

DEM software can help engineers to improve the design of mixing systems. As reported previously for a system comprising a particle bed size ratio, the formation of a segregated core of small particles can occur at low to medium speed. To avoid the formation of the central core of small particles a baffle with a simple geometry was incorporated in the vessel geometry to assess its effect on the mixing quality. Figure 5.37 shows the simple initial design, which consisted of two opposite cones oriented along the longitudinal axes with a cubical element in the centre.

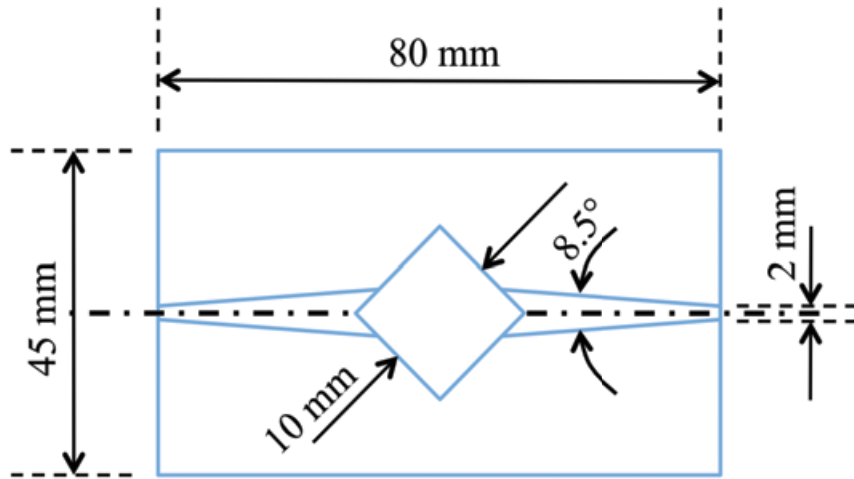


Figure 5.37: Simple baffle design, two opposite cones with a cube into the centre.

The calculated segregation index for the system with baffle and without baffle at different rotational speed is reported in Figure 5.38.

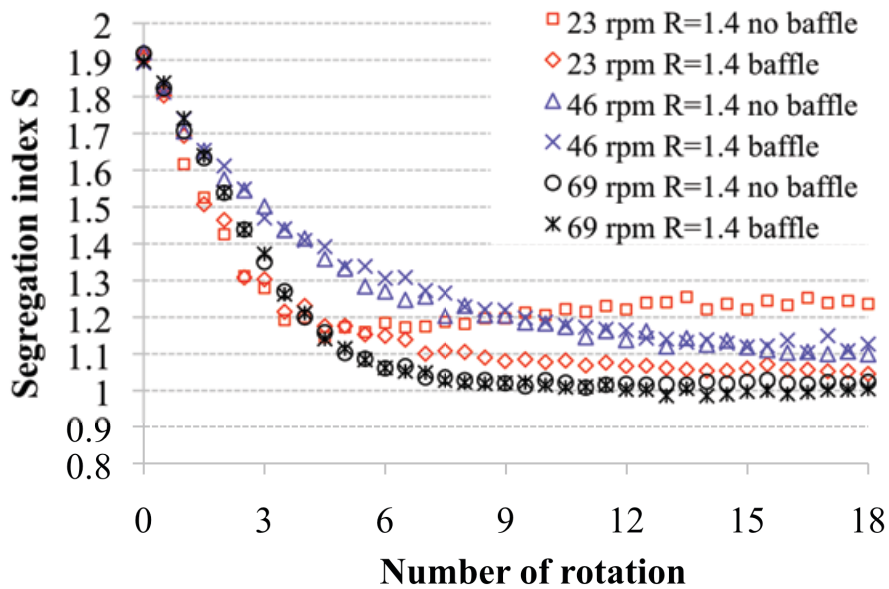


Figure 5.38: Comparison segregation index  $S$  at different rotational speeds of 23, 46, 69 rpm with and without baffle.

It can be observed that at medium and high speed the baffle had no major effect on the mixing efficiency (rate of mixing) as the segregation index,  $S$ , remained almost unchanged. There was, however, a substantial influence at low speed, 23 rpm, with the reduced segregation. It is very interesting to note that with baffle at 23 rpm the mixing was also better than 46 rpm. The effect for the baffle at 23 rpm can be better observed in Figure 5.39 where the segregation index for this speed for three different systems, monodisperse particles ( $R=1$ ), bidisperse particles ( $R=1.4$ ) baffle and no baffle, are compared. It is clear that the baffle improved the mixing as it approached the value of segregation index for the system with monodisperse particles.

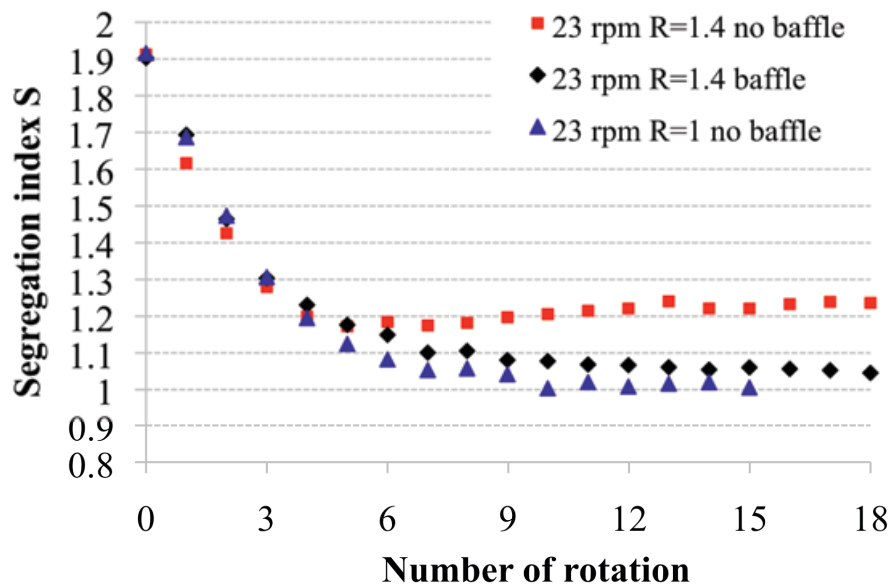


Figure 5.39: Comparison segregation index  $S$  at 23 rpm with baffle and no baffle.

## 5.5 Conclusions

In the last few decades enormous effort had been put into understanding mixing mechanisms in uniaxial mixing systems. The work presented in this chapter is the first attempt of mixing studies by Discrete Element Modelling (DEM) for a complex three-dimensional motion such

as the Turbula mixer. This technique has been employed to calculate both the translational and rotational motions of the solid body of the mixer to recreate the motion in the DEM software. The system has been modelled in order to observe the effect of mixing speed and filling patterns on particle mixing at a constant fill level, with uniform spherical monomodal and bimodal size non-cohesive particles. With monosized particles the effect of a wide range of shaft rotation speeds has been analysed for transverse and axial filling loading patterns. In the bimodal size system the effect of operating speed has been analysed for the axial filling. The results have been presented and discussed in terms of segregation index, characteristic mixing numbers and characteristic mixing time necessary to achieve uniform random mixing of the particles.

Results for the system of monodisperse spheres, for both transverse and axial filling, showed that mixing behaviour changed non-monotonically as a function of mixer speed. It is shown that the characteristic number of rotations, which describes the number of mixer revolutions needed to achieve complete mixing, initially increased with increasing speed and subsequently decreased. The decline in mixing efficiency from 23 to 46 rpm and the subsequent increase as speed increased from 46 to 69 rpm may be indicative of a transition in bed behaviour and mixing mechanisms. The effect of operational speed on the mixing effectiveness has also been shown in terms of axial and radial dispersion coefficients. This decline in mixing efficiency correlated well with a similar trend in axial dispersion coefficient. These trends appear to be indicative of a transition in the flow process and bed behaviour and mixing mechanisms. Changes in particle behaviour in terms of axial travelled distance showed a change in particle behaviour with operating speed. Although DEM modelling has clear potential in giving an insight of a complex system such as the Turbula, difficulties in completely explaining mixing mechanisms still remain due to the high

complexity of the motion. The hypothesised bed behaviour is not fully understood for this multiple axes complex motion and more modelling work is probably required. Confidence in the DEM modelling results presented in this chapter, however, is given by the Positron Emission Particle Tracking (PEPT) mixing experiments presented in Chapter 7. These experiments have shown similar trends to the ones obtained by DEM modelling, for the dispersion coefficients and the distribution of axial travelled distance, under comparable conditions. In addition to the experimental validation an exploration of the mixing efficiency of the Turbula mixer compared to a rotating drum and a hoop mixer will be presented in Chapter 6.

For the system with bimodal sized spheres, good qualitative agreements have been found between DEM simulations and MRI experimental data from Sommier *et al.* 2001 [7]. This confirmed that the mixing quality improved as a function of the operating speed. With lower speed it was demonstrated that a simple baffle could improve the mixing and avoid the formation of the central segregated volume for smaller particles.

## 5.6 References

- [1] Y. Muguruma, T. Tanaka, S. Kawatake, Y. Tsuji, Discrete particle simulation of a rotary vessel mixer with baffles, *Powder Technology* **93** (1997), pp. 261-266.
- [2] P.E. Arratia, N. Duong, F.J. Muzzio, P. Godbole, S. Reynolds, A study of the mixing and segregation mechanisms in the Bohle Tote blender via DEM simulations, *Powder Technology* **164** (2006), pp. 50-57.
- [3] B. Chaudhuri, F.J. Muzzio, M.S. Tomassone, Modeling of heat transfer in granular flow in rotating vessels, *Chemical Engineering Science* **61** (2006), pp. 6348-6360.
- [4] R.Y. Yang, A.B. Yu, L. McElroy, J. Bao, Numerical simulation of particle dynamics in different flow regimes in a rotating drum, *Powder Technology* **188** (2008), pp. 170-177.
- [5] Y. Xu, C. Xu, Z. Zhou, J. Du, D. Hu, 2D DEM simulation of particle mixing in rotating drum: A parametric study, *Particuology* **8** (2010), pp. 141-149.
- [6] P.W. Cleary, M.D. Sinnott, Assessing mixing characteristics of particle-mixing and granulation devices, *Particuology* **6** (2008), pp. 419-444.
- [7] N. Sommier, P. Porion, P. Evesque, B. Leclerc, P. Tchoreloff, G. Couarraze, Magnetic resonance imaging investigation of the mixing-segregation process in a pharmaceutical blender, *International Journal of Pharmaceutics* **222** (2001), pp. 243-258.
- [8] P.A. Cundall, O.D.L. Strack, A discrete numerical model for granular assemblies, *Géotechnique* **29** (1979), pp. 47-65.
- [9] R.Y. Yang, R.P. Zou, A.B. Yu, Microdynamic analysis of particle flow in horizontal rotating drum, *Powder Technology* **130** (2003), pp. 138-146.
- [10] P.E. Arratia, Nhat-hang Duong, F.J. Muzzio, P. Godbole, S. Reynolds, A study of the mixing and segregation mechanisms in the Bohle Tote blender via DEM simulations,

- Powder Technology* **164** (2006), pp. 50-57.
- [11] A. Mehrotra, F.J. Muzzio, Comparing mixing performance of uniaxial and biaxial bin blenders, *Powder Technology* **196** (2009), pp. 1-7.
- [12] M. Kwapinska, G. Saage, E. Tsotsas, Mixing of particles in rotary drums: A comparison of discrete element simulations with experimental results and penetration models for thermal processes, *Powder Technology* **161** (2006), pp. 69-78.
- [13] F. Geng, Z. Yuan, Y. Yan, D. Luo, H. Wang, B. Li, D. Xu, (2009): Numerical Simulation on Mixing Kinetics of Slender Particles in a rotary dryer, *Powder Technology* **193** (2009), pp. 50-58.
- [14] Stambaugh, J.; Smith, Z.; Ott, E.; Losert, W. (2004). Segregation in a monolayer of magnetic spheres. *Physical Review E* **70** (2004), 031304.
- [15] H.P. Kuo, P.C. Knight, D.J. Parker, J.P.K. Seville, Solids circulation and axial dispersion of cohesionless particles in a V-mixer, *Powder Technology* **152** (2005), pp. 133-140.
- [16] A. Mehrotra, F.J. Muzzio, Comparing mixing performance of uniaxial and biaxial bin blenders, *Powder Technology* **196** (2009), pp. 1-7.
- [17] S. Massol-Chaudeur, H. Berthiaux, J. A. Dodds, Experimental study of the mixing kinetics of binary pharmaceutical powder mixtures in a laboratory hoop mixer, *Chemical Engineering Science* **57** (2002), pp. 4053-4065.

## Chapter 6

### **A DEM numerical comparison of mixing efficiencies of solids in a cylindrical vessel subject to a range of motions: rotating drum, hoop mixer and Turbula mixer**

*Although the mixing of solids is a fundamentally important unit operation in the pharmaceutical, food and agricultural industries, as well as many others, considerable uncertainty remains for the optimisation of mixing of solids in different mixer types. Simple laboratory-pilot scale mixers based on the moving vessel, such as the hoop mixer and the Turbula, are commonly used for solids mixing operations and yet also little is understood in terms of performance. These mixers add additional rotational and/or translational movements to the 2D cylindrical rotation of the simple rotating drum with the aim of delivering significant improvements in mixing in the longitudinal axis direction. Mixing by chaotic advection is obtained only in mixers that have a phase space larger than two [1]. 2D steady flows never generate chaos or mixing by advection, but only mixing by diffusion. As an example, consider some sugar in a cup of coffee: mixing by diffusion will require a long time and 2D rotation of the cup around its longitudinal central axis will not improve mixing and sugar dissolution. Conversely complex chaotic motion can be created by the use of a spoon, and this results in the sugar dissolving rapidly. Non-steady 2D flow or 3D steady flows are the minimum requirement to achieve efficient mixing, but the larger the phase space dimension, the more efficient the mixing would be. 2D mixers or mixer with a 3D symmetry*

*should, therefore, be avoided. The idea behind the Turbula mixer is to improve mixing by creating a 3D mixer in non-steady condition, hence a 4D phase space mixer (3D for space motion and 1D for time, non steady state mixing).*

*In this chapter mixing in a simple cylindrical vessel moving according to different motions with different phase space, such as a simple rotating drum, hoop mixer and the Turbula mixer, are compared. For speed and simplicity the modelled system consisted of monosized smooth glass beads. The rate and extent of mixing was shown to depend on equipment motion, operating speed and the initial distribution of the fractions. The well-known characteristics of the horizontal drum operating in rolling mode were demonstrated: excellent transverse mixing and poor axial mixing were seen. Both were observed to improve with speed as the depth of the active layer was shown to increase. The hoop mixer incorporates off-axis rotation, causing periodic tilting of the cylinder axis. This resulted in a considerable improvement in axial mixing. Interestingly, at low speeds the hoop mixer and simple rotating drum exhibited similar transverse mixing but increasing speed had the opposite effect: improved transverse mixing in the drum and poorer transverse mixing in the hoop mixer. Conversely, axial mixing in the hoop mixer improved with speed. The Turbula mixer when compared with the other two mixers in term of characteristic number of rotations (inverse of the rate of mixing) clearly showed a nonlinear relationship with the operating speed. Differently than the other two mixers, the initial filling patterns showed little effect, only for the middle speed the mixing was less efficient in axial direction when compared with the transverse filling pattern.*

## **6.1 Introduction: cylindrical vessels moving with different motion types**

The mixing of particulate material is an important stage in reaching the desired final product quality or the right manufacturing conditions, however it can often be difficult to mix particles homogeneously. Controlling the mixing mechanisms is key to achieving the desired characteristics for a final product. This is difficult to design from first principles since, in spite of considerable research, fundamental understanding remains incomplete. The mixing mechanisms depend on the mixing action of the mixer (a wide range of possible designs) and the flow behaviour of the particles. A variety of solid mixers are available in industry and rotating cylinders for example are widely used as mixers. In batch mode they consist of a horizontal cylinder rotating around the central axis [2,3,4,5,6]. The motion of the granular bed is predominantly rotation about the cylinder axis with a cascading free surface. Mixing occurs predominantly in the cross-section with some axial dispersion [7]. Recent studies have shown that the slow axial mixing can be enhanced by incorporating a rocking motion of controlled amplitude and frequency [8]. This added perturbation accelerates the mixing process. Other types of motion can therefore be applied to try to enhance mixing in the axial direction: the hoop mixer and Turbula mixer are typical examples. In both of these examples the material to be mixed is placed inside a cylindrical mixing vessel, which is then subjected to complex, yet regular motion.

In the hoop mixer the longitudinal axis of the cylindrical container is inclined at an angle to a horizontal axis of rotation. Under this condition the granular bed is subjected to radial and axial movement as a result of the gravitational forces which are acting periodically in the axial direction due to the inclination and the revolving movement of the cylinder [9]. As explained previously (ref. Chapters 4 and 5) the movement of the cylindrical container located within

the Turbula mixer chamber comprises two rotations and a horizontal translation. The material within the vessel is therefore subjected to intensive, periodically pulsating movements.

## 6.2 Geometry and simulations conditions

Three different motions have been applied to a cylindrical container, 45 mm in diameter and 80 mm in length, as shown in Figure 6.1. The cylinder was horizontal and rotation was applied around the horizontal cylindrical axes (rotating drum). In case of the hoop mixer, the cylinder axis was offset from a horizontal axis of rotation by a 30° inclination angle. For the last case the cylinder was driven by a motion corresponding to the motion of a cylinder located inside the chamber of a Turbula mixer.

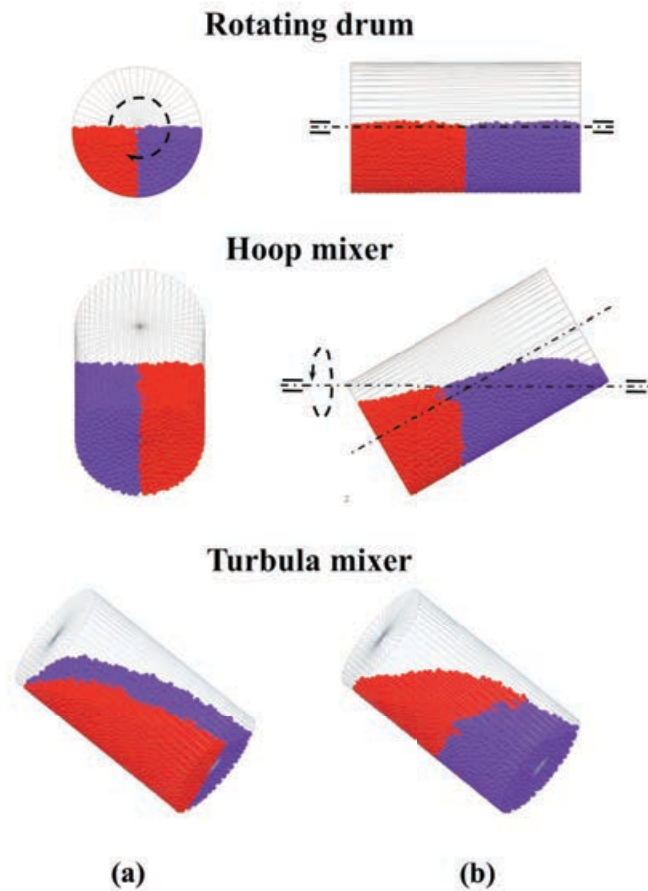


Figure 6.1: (a) Transverse filling. (b) Axial filling.

In these studies, the granular system comprised two differently coloured and initially segregated fractions of otherwise identical monosized spherical particles. Mixing was measured from the intermingling of the two fractions. The distribution of contacts between same and opposite particles within the bed was used to assess the homogeneity (ref. Chapter 5). In order to separately study mixing in the vessel cross section (transverse and radial) and mixing along the vessel length (axial), two different initial filling conditions were considered, transverse and axial filling patterns. In the transverse fill pattern the particles were distributed uniformly in the axial direction but were completely segregated in the cross-section. In this way complete mixing could be achieved by radial mixing alone. By changing the fill pattern it was hoped to reveal the dominant mixing mechanism.

Table 6.1: Parameters used in the simulations.

<b>Parameter</b>	<b>Value</b>
Total particles	9,000
Particle diameter (mm)	2
Particle density ( $\text{g/cm}^3$ )	2.5
Particle shear modulus (Pa)	$2 \times 10^6$
Particle Poisson's ratio	0.3
Vessel density ( $\text{g/cm}^3$ )	1.2
Vessel shear modulus (Pa)	$3 \times 10^9$
Vessel Poisson's ratio	0.3
Particle-particle static friction coefficient	0.5
Particle-particle rolling friction coefficient	0.01
Particle-vessel static friction coefficient	0.35
Particle-vessel rolling friction coefficient	0.005
Particle-particle restitution coefficient	0.73
Particle-vessel restitution coefficient	0.73

The DEM simulations input parameters are reported in Table 6.1 and the simulations conditions are summarised as follows:

- Fill level 50% (9000 particles).
- Mixer operating speed: 23, 46, 69 rpm.
- Loading pattern: axial and transverse loading.
- Cylindrical rotating vessels: rotating drum, hoop mixer and Turbula mixer.

### **6.3 Result and discussion**

In the following section the results for three mixers are compared for the two different filling patterns. The mixers are also simultaneously compared in terms of characteristic number of rotations (inverse of rate of mixing).

#### **6.3.1 Rotating drum**

As shown in Figure 6.2 the effect of rotational speed was investigated in a rotating drum filled by both transverse and axial loading patterns. As expected, it can be noticed that axial filling resulted in very slow mixing due to the purely dispersive mechanism in axial direction. With transverse filling the rate of mixing was faster since for a rotating drum the radial mixing is very effective and higher rotation speeds enhance mixing performance. In both cases there was a small but measurable effect of rotational speed on mixing rate per drum revolution. Transverse mixing per revolution increased with rotational speed while axial mixing decreased.

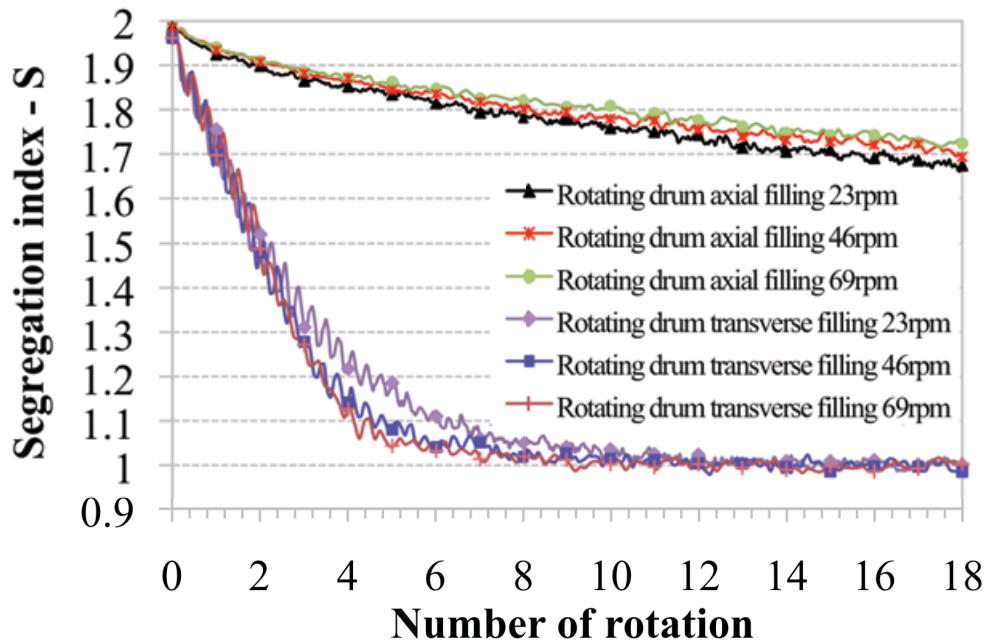


Figure 6.2: Comparison of the segregation index for a rotating drum at different rotational speeds 23, 46 and 69 rpm.

For free flowing granular material in a rotating drum, different types of transverse bed motion have been defined depending on the operational speed: *slipping*, *slumping*, *rolling*, *cascading*, *cataracting* and *centrifuging* [10]. A characteristic criteria for their definition is the Froude number  $Fr$ , Eq.(6.1). This is defined as ratio of centrifugal force to gravity [11].

$$Fr = \frac{\omega_{drum}^2 R}{g} \quad (6.1)$$

Where  $R$  is the drum diameter and  $\omega$  is the drum angular rotational speed. The Froude number for a rotating drum filled greater than 10% operating in rolling mode tends to range between  $10^{-4} < Fr < 10^{-2}$  and in the cascading mode between  $10^{-3} < Fr < 10^{-1}$  [25]. In the present work the  $Fr$  number assumes the following values between  $1.3 \cdot 10^{-2}$  (23 rpm) and  $1.2 \cdot 10^{-1}$  (69 rpm),

which should indicate that the bed was between rolling and cascading mode. In *rolling mode* the bed was characterised by a uniform static flow of particles on a nearly level surface and the majority of the bed was transported upward by solid body rotation [11]. As the rotational speed increased the bed surface started to tilt assuming the typical ‘S’ kidney shape of *cascading mode*. Particles on the upper part of the bed detached from the wall because of the higher kinetic energy and they were thrown to the foot of the bed surface [12]. These typical features for *rolling* and *cascading modes* can be observed in Figure 6.3. At lower speed, 23 rpm, the bed surface was flat and as speed increased the typical kidney shape started to appear, which could start to be observed, 69 rpm. This agreed with the values of the  $Fr$  number previously calculated demonstrating that the rotating drum in this work probably operated in rolling mode at lower speeds and in a transition regime toward the cascading mode for higher speed (69 rpm).

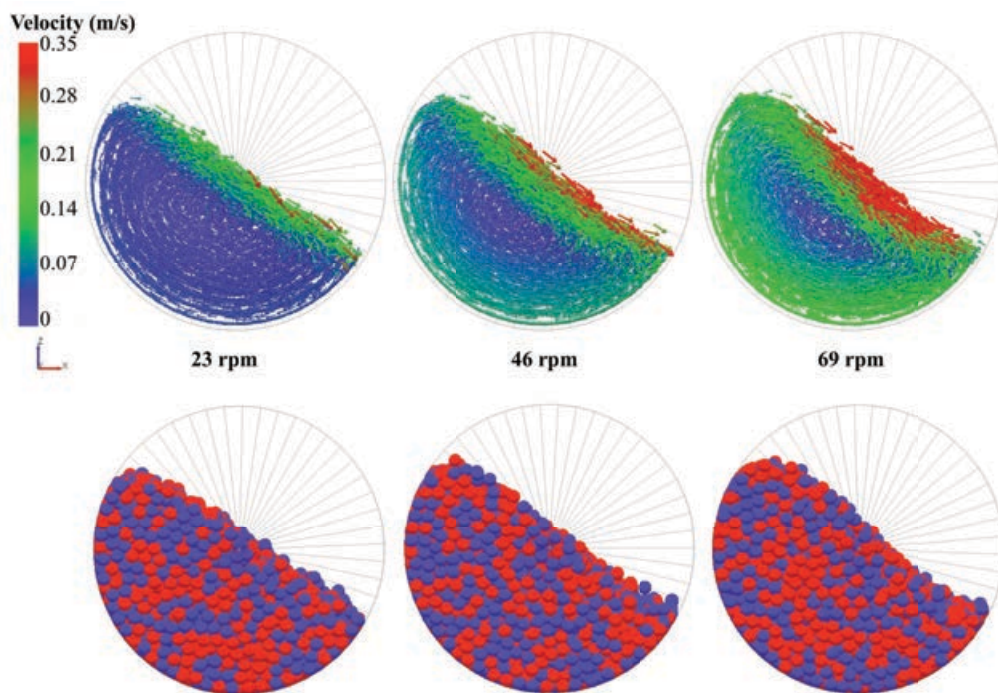


Figure 6.3: Magnitude of velocity in a rotating drum operating at different rotational speeds.

The cross section of the bed in a rotating drum operating in rolling mode can be described according with the scheme in Figure 6.4. Two different regions are defined: an *active region* where particles can mix mainly due to convection and a *passive region* where particles move as rigid body as result of the drum rotation. The particles angular velocity in the passive layer is equal to the drum angular velocity. The diffusion at the active-passive interface is usually negligible compared with the convection in the active region [13].

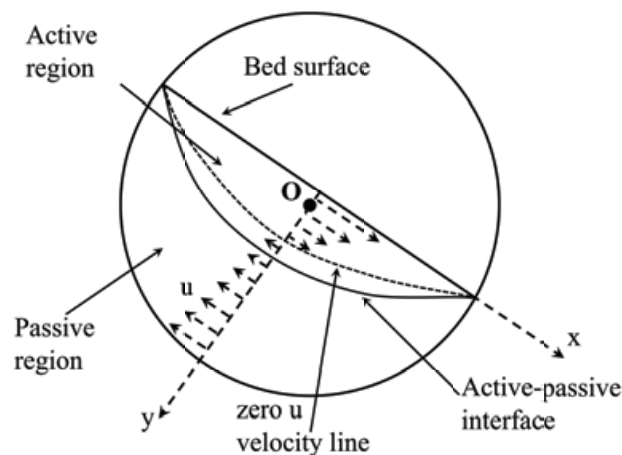


Figure 6.4: Schematic of a rotating drum operating in rolling mode showing the active and passive regions.

Considering the  $y$  direction, along the midchord, normal to the flat surface of the bed ( $x$  direction) the velocity  $u$  equals zero when the flow reverses (zero  $u$  velocity line interface) within the active region. The velocity  $u$  at the active-passive interface equals the  $x$ -direction component of the linear velocity of the solid body at the passive-active [13]. Usually, increasing the speed in rolling mode results in an increase in the size of the active layer and velocity in the  $x$  direction.

In Figure 6.5 the values for the velocity  $u$  along the  $y$  distance from the bed free surface are shown at different drum rotating speeds  $\omega_{drum}$ .

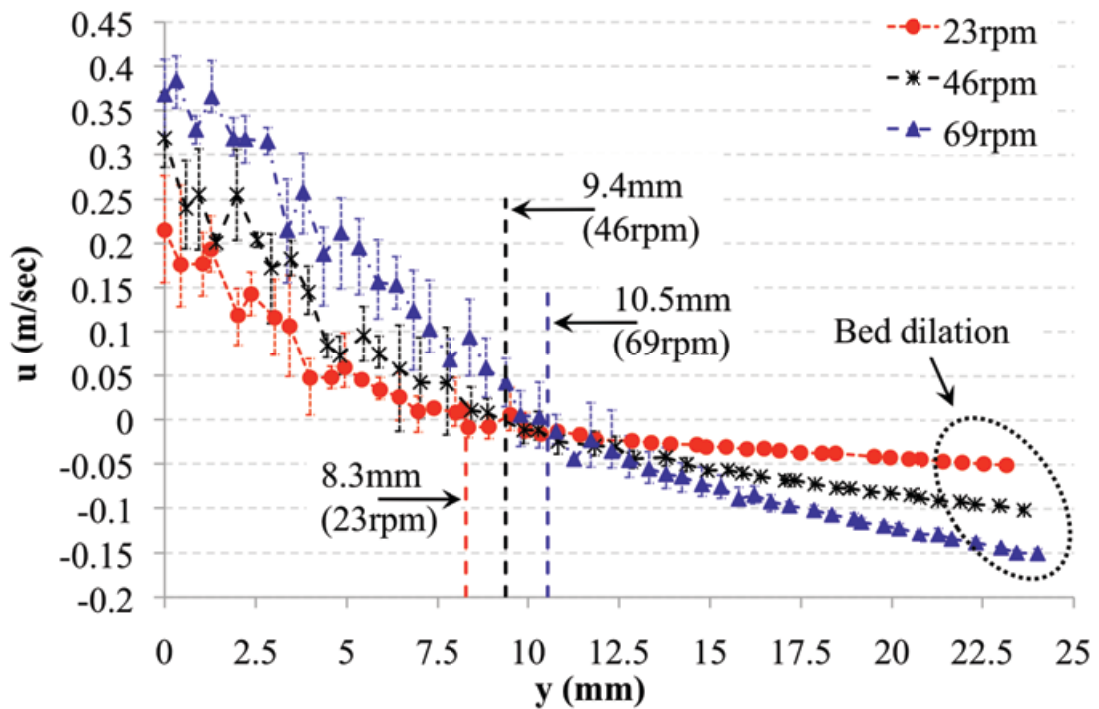


Figure 6.5: Plot of calculated x-direction velocity  $u$  against y-direction distance from the bed surface.

By increasing the operating speed the particle speed through the active layer was increased and the point of zero velocity corresponded to the flow reversal being deeper in the bed. This implied a much deeper and faster moving active layer existed. Furthermore, there was a slight increase in bed dilation with increasing drum speed, presumably accommodated in the active layer. The increase in the rate of mixing with speed with transverse filling can be related to the increased depth, speed and dilation of the active layer. In rolling and cascading mode the particle angular velocity,  $\omega_{particle}$ , in the passive layer was expected to have almost the same magnitude as that of the drum rotational speed since the particles move as a solid body. This was confirmed in Figure 6.6, where the  $\omega_{particle}$ , particles within 10 mm distance from the wall along the bisector line  $y$ , were compared with the angular velocity of the drum,  $\omega_{drum}$ .

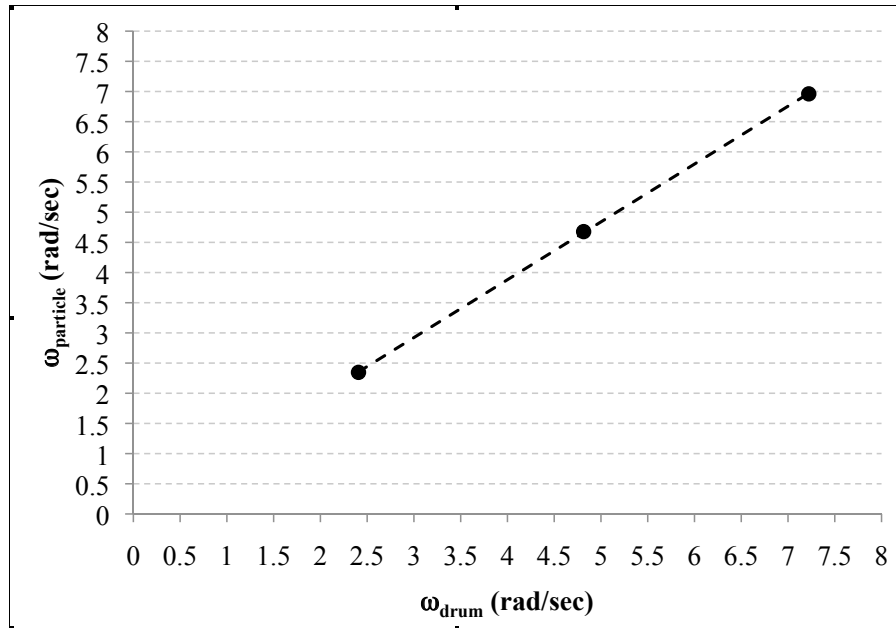


Figure 6.6: Comparison of particle angular velocity  $\omega_{particle}$  with drum angular velocity  $\omega_{drum}$  for particles in the passive layer along the bisector line at 10 mm distance from the wall.

### 6.3.2 Hoop mixer

In the hoop mixer the 3-D movement of the bed is achieved by rotating an inclined drum around a horizontal axes, Figure 6.1.

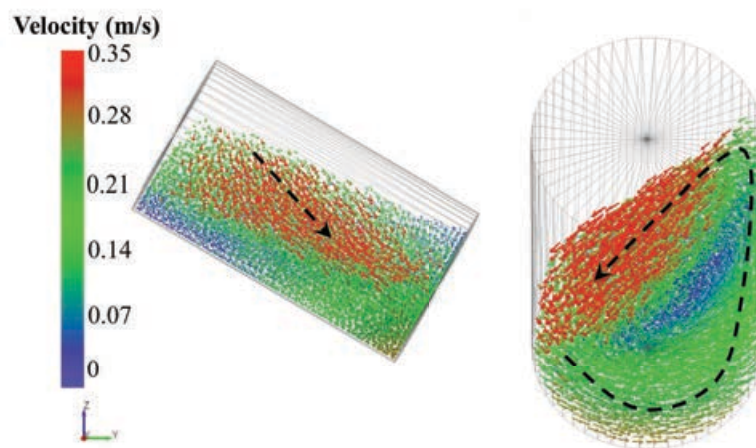


Figure 6.7: Magnitude of velocity in a of hoop mixer. The direction of the flow for a particular drum position is highlighted in black.

The angle of inclination creates a rocking effect, which forces material movement along the longitudinal axes of the container as highlighted by the black arrows in Figure 6.7.

Figure 6.8 shows the segregation index for the two different filling patterns. As with the horizontal rotating drum, the rate of mixing in the transverse direction was greater than in the radial. Comparison with the horizontal drum showed that the rocking mechanism substantially improved the mixing of the material in the axial direction. The operating speed had an effect in terms of mixing efficiency, in particular regarding the axial filling with the rocking effect, which might have played a major role in the axial direction. The hoop motion mixing mechanism, a combination of radial and axial mixing, resulted from a 3-D bed movement. In contrast to the rotating drum, in the hoop mixer the bed developed a bulk movement, which is 3-dimensional, and the effect of axial and radial mixing depended on the operating speed. Mixing in the radial direction declined as the speed was increased. Mixing in the axial direction increased with speed.

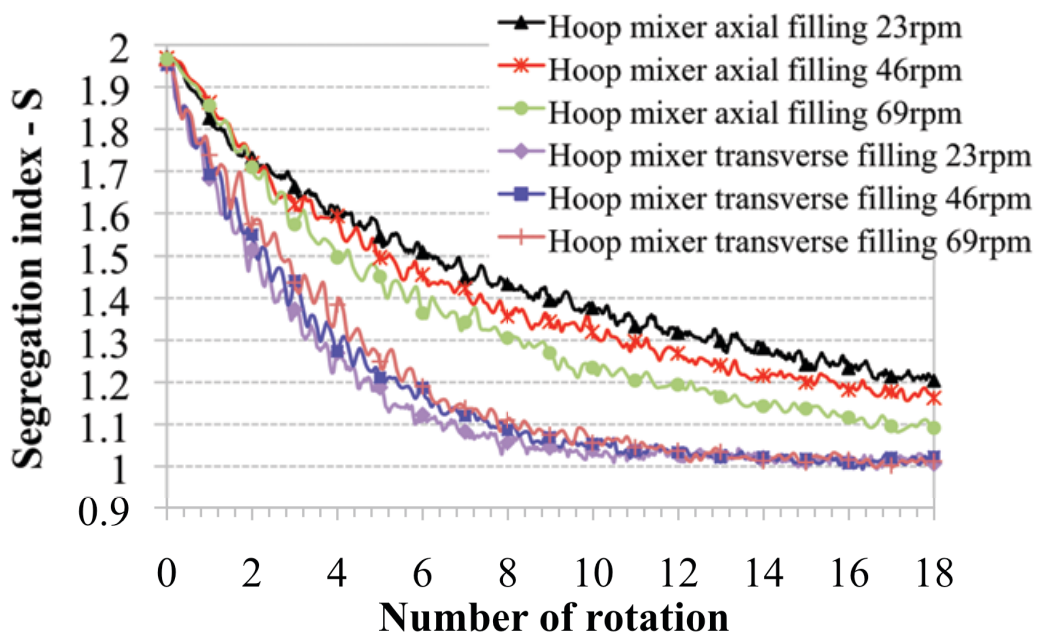


Figure 6.8: Comparison mixing rates for a hoop mixer at 23, 46 and 69 rpm.

### 6.3.3 Turbula mixer

As shown in Chapter 5, the Turbula mixer subjects the mixing vessel to a regular periodic motion that consists of rotation of the vessel about its longitudinal axis and two backward-forward horizontal translational motions during each complete shaft rotation. The vessel moves backwards and forwards, changing its direction of motion at the end of each quarter turn of the shaft. At the same time the inclination of the vessel to the horizontal reverses. The sharp reversal in direction of translation and the rapid change in orientation of the vessel at the end of each quarter revolution give a sharp “kick” to the contents of vessel.

As shown from the segregation indices in Figure 6.9, the number of rotations necessary to achieve the asymptotic value corresponding to random mixing was dependent on the operating speed. At medium and higher speeds the different filling patterns seems to indicate that there was a change in mixing efficiency in axial and radial direction as a function of the filling pattern.

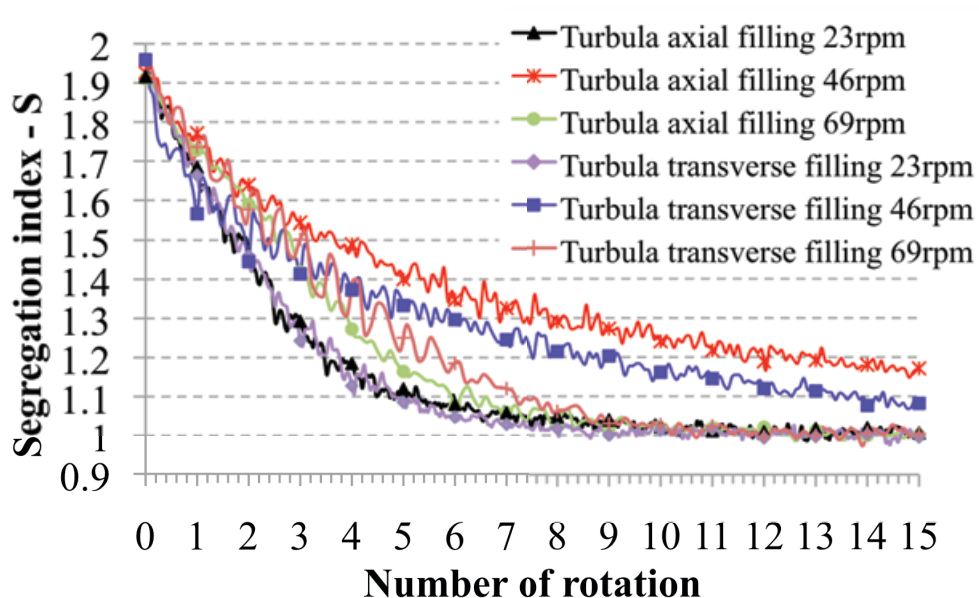


Figure 6.9: Comparison of the segregation index in a Turbula mixer for different rotational speeds for axial and transverse filling.

### **6.3.4 Comparison of characteristic number of rotations for a rotating drum, hoop mixer and Turbula mixer**

The segregation curves obtained from the simulations showed similar trends with rapid decrease of the segregation index corresponding to fast material homogenization, followed by a period with slower homogenization. An exponential decay law can be fitted to the segregation index curves obtained by the numerical simulations to evaluate the kinetics of mixing. The rate of mixing in terms of the number of revolutions to achieve a certain level of mixing can be quantified.

A comparison between the different types of mixers is shown in Figure 6.10. The characteristic number of rotation  $N_{mix}$  (“reciprocal rate of mixing”) was compared between the rotating drum, the hoop mixer and the Turbula mixer rotating at different speeds. The figure also depicts the effect of different loading patterns. For all the three mixers, there was an effect of loading pattern on mixing, however, for transverse filling at 23 rpm there was no appreciable differences between the three mixers and mixing was probably dominated by the mixing mechanisms acting on the cross-section. For the rotating drum with axial filling the characteristic number of rotation was not plotted as mixing would occur over a much longer time than the other cases. For the rotating drum with transverse loading, increasing the speed lead to a decrease of the characteristic number of rotations (increase of the rate of mixing) because mixing in radial direction increased with the speed for a rotating drum operating in rolling mode, as a result of the increase of the depth of the active layer.

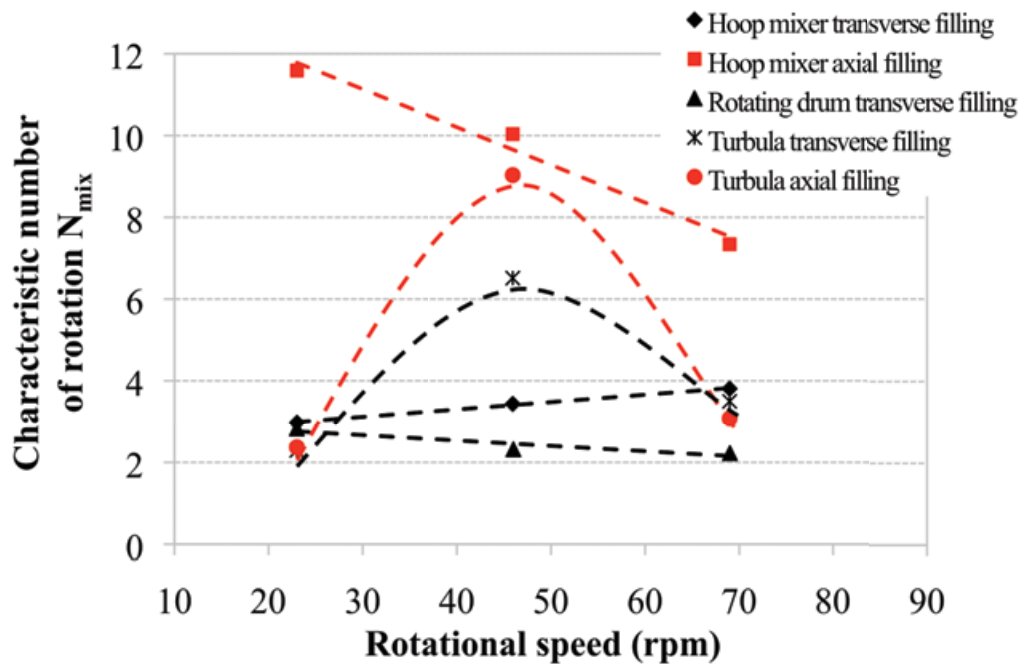


Figure 6.10: Comparison of rate of mixing for a rotating drum, hoop mixer and Turbula mixer at different rotational speed.

Qualitatively the results of the simulation make sense. For the horizontal rotating drum we observe the characteristic high radial dispersion and very low axial dispersion. We also see the clear delineation of the active-passive interface and solid body rotation in the passive layer. We also see a very small increase in the rate of mixing *per revolution* with drum speed. The model of Ding *et al.* (2002) defines a solid exchange coefficient to describe the exchange of material between the active and passive layers [13]. The model predicts that the exchange coefficient per revolution is dependent only on the fill level and the bed dilation. The latter increases with speed and causes a slight increase in mixing rate, as we have seen here.

In the hoop mixer, the overall mixing is a combination of radial and axial mixing. For the hoop mixer there was a considerable difference in terms of number of rotations (rate of mixing) between transverse and axial filling pattern. This was probably mainly related to the size of the vessel (ratio between diameter and length). However, speed had a major influence

in axial filling, where the axial movement probably became more important in terms of mixing as the speed increased. Conversely, the radial mixing declined with speed as shown with the transverse loading. Hence, by increasing the speed the axial movement became more influential than radial and this could explain why mixing with transverse filling was reduced by increasing the speed. There is little work published on the rate of mixing in the hoop mixer, and nothing to the author's knowledge on the effect of speed on mixing rate. Wightman *et al.* (1998) [8] however, have experimentally investigated the effect of combined rotational and rocking motions on mixing in drums. They observed an increase in mixing rate with increasing rate of rocking. This offers some support to the predictions here for the hoop mixer). The effect of rocking was to introduce a convective motion in the axial direction, which we also see with the hoop mixer.

At low rotational speed it probably resembled the effect of a rotating drum with good radial mixing, whereas by increasing the speed the axial effect became more important. From the comparison it is evident that the Turbula mixer did not show a linear relationship between the characteristic number of rotations and operating speed. The initial particle arrangement had little effect at the extremes (23 and 69 rpm) where the mixing was efficient. At 46 rpm, where the efficiency was poor, the effect of loading was quite marked. The effect of the initially uniform axial distribution was to reduce the number of revolutions required to achieve mixing – albeit only by about 20%. At 46 rpm, mixing was still considerably less efficient than at 23 or 69 rpm. With the Turbula mixer at different operating speed the effect of the rotation and the translation probably had different contributions in terms of mixing in radial and axial directions. In transverse filling the mixing efficiency at 46 rpm was higher than axial filling. This indicated that the increasing the speed at 46 rpm worsened the mixing in the axial direction and mixing in axial direction was the dominant mechanism. As with the hoop mixer,

there is very little published on mixing in the Turbula and nothing on the effect of speed. For this reason we have embarked on validation work using Positron Emission Particle Tracking (PEPT). This work is currently being prepared for journal publication. In the meantime, the reader is referred to conference publications [14] that show could qualitative agreement with the trend. In particular, the PEPT work shows a distinct minimum in axial dispersion coefficient at Turbula speed of 46rpm – this corresponds exactly to the DEM prediction.

## **6.5 Conclusions**

This chapter presents an elementary comparison of the effect of axis of rotation and loading pattern on the mixing performances for a cylindrical vessel moving according to different motions. A rotating drum, hoop mixer and Turbula mixer with a drum filled with spherical particles were considered.

An exponential law was used to describe the mixing behaviour in terms of a characteristic number of rotations to achieve mixing. It was observed, as expected, for the rotating drum operating in rolling mode that the axial mixing was very slow and this was driven by a pure dispersive mechanism. Mixing in transverse filling was much faster and radial mixing was the dominant mechanism. With the hoop mixer it was observed that the rocking motion caused mixing in the axial direction and that the overall mixing efficiency depended on the operating speed. The axial mixing in the hoop mixer improved with speed whereas the radial mixing slightly decreased as the speed increased. In the Turbula mixer, a decrease in mixing efficiency from 23 to 46 rpm was observed and a subsequent increase as speed increased from 46 to 69 rpm for both axial and radial mixing. This appears to be indicative of a transition in the bed behaviour and mixing mechanism. For the Turbula mixer, further mixing

experimental work by using Positron Emission Particle Tracking (PEPT) is presented in Chapter 7 to support what was observed from the DEM simulations.

## 6.6 References

- [1] P. Porion, N. Sommier, A.-M. Faugère, P. Evesque, Dynamics of size segregation and mixing of granular materials in a 3D-blender by NMR imaging investigation, *Powder Technology* **141** (2004), pp. 55-68.
- [2] Y.L. Ding, R.N. Forster, J.P.K. Seville, D.J. Parker, Scaling relationships for rotating drums, *Chemical Engineering Science* **56** (2001), pp. 3737-3750.
- [3] Y.L. Ding, R. Forster, J.P.K. Seville, D.J. Parker, Granular motion in rotating drums: bed turnover time and slumping–rolling transition, *Powder Technology* **124** (2002), pp. 18-27.
- [4] M.T. Hardin, T. Howes, D.A. Mitchell, Mass transfer correlations for rotating drum bioreactors, *Journal of Biotechnology* **97** (2002), pp. 89-101.
- [5] A.C. Santomaso, Y.L. Ding, J.R. Lickiss, D.W. York, Investigation of the Granular Behaviour in a Rotating Drum Operated over a Wide Range of Rotational Speed, *Chemical Engineering Research and Design* **81** (2003), pp. 936-945.
- [6] A.-Z.M. Abouzeid, D.W. Fuerstenau, Mixing–demixing of particulate solids in rotating drums, *International Journal of Mineral Processing* **95** (2010), pp. 40-46.
- [7] M. Poux, P. Fayolle, J. Bertrand, D. Bridoux, J. Bousquet, Powder mixing: Some practical rules applied to agitated systems, *Powder Technology* **68**, (1991), pp. 213-234.
- [8] C. Wightman, F.J. Muzzio, Mixing of granular material in a drum mixer undergoing rotational and rocking motions I. Uniform particles, *Powder Technology* **98** (1998), pp. 113-124.
- [9] M. Aoun-Habbache, M. Aoun, H. Berthiaux, V. Mizonov, An experimental method and a Markov chain model to describe axial and radial mixing in a hoop mixer,

- Powder Technology* **128** (2002), pp. 159-167.
- [10] H. Henein, J.K. Brimacombe, A.P. Watkinson, Experimental studies of transverse bed motion in rotary kilns, *Metallurgical and material transactions B* **14B** (1983), pp. 191–205.
- [11] J. Mellmann, The transverse motion of solids in rotating cylinders—forms of motion and transition behavior, *Powder Technology* **118** (2001), pp. 251-270.
- [12] Y. Xu, C. Xu, Z. Zhou, J. Du, D. Hu, 2D DEM simulation of particle mixing in rotating drum: A parametric study, *Particuology* **8** (2010), pp. 141-149.
- [13] Y.L. Ding, J.P.K. Seville, R. Forster, D.J. Parker, Solids motion in rolling mode rotating drums operated at low to medium rotational speeds, *Chemical Engineering Science* **56** (2001), pp. 1769-1780.
- [14] M. Marigo, D.L. Cairns, M. Davies, A. Ingram, E. H. Stitt, DEM Modelling of particle flow in a Turbula mixer, proceedings of *5th International Conference on Discrete Element Methods DEM5 (2010)*, London, UK, 25-26 August 2010.

## Chapter 7

### **Particle motion inside the Turbula mixer: PEPT mixing experiments for a system with irregular moving boundaries**

*Experiments on Turbula mixer to understand the mixing mechanisms are difficult to carry out due to the complex motion. The motion of inversion subjects the contents of the mixing container to two alternating, rhythmic pulsating motions, which causes the material to be swept by an intense “turbulence”. The objective of the present chapter is to develop and present a methodology for tracking particles inside a vessel located in the Turbula chamber and moving with irregular moving boundaries. Hence the motion of particles inside a vessel within the Turbula mixer was investigated using the Positron Emission Particle Tracking technique (PEPT). The aim was to validate the DEM numerical model and predictions presented in Chapter 5 for 2 mm monosized spherical particles, glass beads. Due to the complex vessel motion, the position of the tracer particle within the vessel geometry was related to the irregular moving boundaries by using a tachometer and a two steps approach. Firstly, by tracking the vessel motion by subsequent tracking of the tracer attached on 3 different points of the vessel as a function of the shaft angular position measured by a tachometer attached to the rotating shaft. Secondly, by tracking the tracer particle within the vessel as a function of the shaft angular position. By using this method the particle position within the vessel was related to the vessel position and orientation.*

*PEPT mixing experiments, using a single particle tracer confirmed similar trends for axial and radial dispersion, as previously obtained (ref. Chapter 5) by DEM predictions. For the case using spherical glass beads, the occupancy plots showed a non-linear relationship with the operating speed suggesting a possible bed transition behaviour at about the middle speed as previously hypothesized in Chapter 5. Moreover, qualitative comparison of axial displacement statistics at different operational speeds confirmed similar trend between PEPT experiments and DEM simulations. The full comparison between PEPT experiment results and DEM simulation results is presented in Chapter 8. Mixing experiments were also conducted with zeolite particles with  $d_{50}$  about 338  $\mu\text{m}$  (ref. Chapter 3). Marked differences in terms of occupancy plots and axial and radial dispersion coefficients were shown in comparison of the ideal model glass beads and zeolite particles. This indicates how DEM modeling and prediction of particle behavior for large scale real particle is difficult to relate to other much more idealized systems.*

## **7.1 Introduction: mixing studies and experimental techniques for powder mixing**

Different non-invasive techniques can be used to characterise the bulk behaviour of a powder bed during mixing without interfering with the bulk of material and hence affecting the measurement itself. Computed tomography (CT) and Magnetic Resonance Imaging (MRI) can be employed to get a partially non-disturbed description of the structure of the bed bulk material in a mixer. Usually these techniques rely on the acquisition of stationary images at a given moment in time. This makes it difficult or impossible to observe changes taking place over a very short scale time. Other techniques such as Positron Emission Particle Tracking (PEPT) have been developed for describing the behaviour of a powder bed in real time. This technique allows one to track rapid changes in trajectory of a single particle tracer (PEPT) or multiple tracers (Multiple-PEPT) within the bulk of a powder. The principles behind the technique have been presented in Chapter 4. The single particle behaviour can be used to mimic and infer the behaviour of the bulk of the material if the measurement is carried out for a sufficient period of time, which should be long enough for collecting a statistical representative amount data. This then assumes that the time-averaged behaviour of the particle represents the instantaneous average of the bed. A large number of studies regarding kinematic behaviour of particles in solid mixing have been conducted by using PEPT and many experimental data have been generated for different types of industrial mixers. For example, the motion of individual granular particles has been experimentally observed in a batch ploughshare mixer showing the flow behaviour in terms of axial, radial and angular locations and velocities distributions [1,2]. For a rotating drum, with monosized and binary mixture of particles, operating in rolling mode the active and passive regions in the transverse plane have been described using PEPT [3]. It was shown that the structure of the particle bed consisted of two regions: a relatively thin 'active' region and a 'passive' region near the drum

wall. PEPT was also employed to understand the mechanisms of mixing and study the effect of operational parameters such as volumetric fill level and blade speed in a horizontal rotating cylinder fitted with a single blade [4]. In the case of a V-blender the PEPT was used to show that the direction of the regular circulation motion in the arms of a V-mixer is a function of the volumetric fill level in case of 3 mm glass beads [5]. However, all these are examples of systems with fixed boundaries or boundaries moving around a fixed axes. In these systems the application of PEPT is straightforward since the location of the tracer within the geometry edges is trivial; the tracer position can be easily related to the position of the boundary geometry. If a system has a multiple axis three-dimensional motion, such as the Turbula, the location of the tracer within the vessel geometry walls is much more complex. In this chapter positron emission particle tracking PEPT has been used for tracking the movement of a tracer within a domain irregular moving boundaries such as a cylindrical vessel in a Turbula mixer filled with 2 mm glass beads and zeolite particles. The method involved the use of a two-step procedure by firstly detecting the vessel boundaries motion and secondly relating its position and orientation to the motion of the radioactive tracer placed within the cylindrical vessel.

## 7.2 Materials

The method introduced in the next section was applied to the cylindrical vessel within the chamber of the Turbula mixer to carry out two different mixing experiments: one with ideal model material, glass beads ( $d=2$  mm,  $\rho=2.5$  g cm<sup>-3</sup>), and one with zeolite catalyst support ( $d_{50}=338$   $\mu$ m,  $\rho=2.41$  g cm<sup>-3</sup>). The drum's dimensions correspond to the ones used for the DEM modeling presented in Chapter 5; it consists of a cylindrical vessel with 45 mm inner diameter and 80 mm length. The cylindrical part was constructed with perspex acrylic and the two end plates of the drum were made from polished stainless steel. The fill level was 50% in

volume (including voidage). The speed of the mixer was varied from 22 rpm up to 77 rpm. The tracer particles were activated using the nuclear cyclotron reactor at University of Birmingham (UK). The glass bead tracer was created by direct irradiation and the zeolite particle tracer was created by an Ion exchange technique.

The two sets of experiments were carried out and they are summarized as follows:

1<sup>st</sup> experiment:

- Glass beads: 2 mm
- Vessel size: 45x80 mm
- Fill level 50%
- Rotational speed: 22, 32, 39, 46, 53, 57, 67, 77 rpm

2<sup>nd</sup> experiment:

- Zeolite particles: 338  $\mu\text{m}$ , PSD as in Chapter 3
- Vessel size: 45x80 mm
- Fill level 50%
- Rotational speed: 22, 34, 39, 46, 53, 57, 67, 77 rpm

### **7.3 Experimental set-up: relating particle position with vessel moving boundaries**

In this section the location of the single tracer within the vessel with a 2 step approximated location method will be presented. The experimental setup for the application of PEPT is presented in Figure 7.1. The system consisted of the PEPT measurement equipment with a tachometer positioned on the driving chamber shaft, the PEPT data collection unit and computer for the data processing. A tachometer was employed so that the tracer location was known in relation to the shaft angular position ( $\alpha$  angle) at any given moment in time  $t$ . Considering the current experimental setup, the location of the tracer represented in Cartesian

coordinates by  $\mathbf{P}(X,Y,Z)$  can be defined as a function of time and shaft angular position  $\alpha$  measured by using the tachometer.

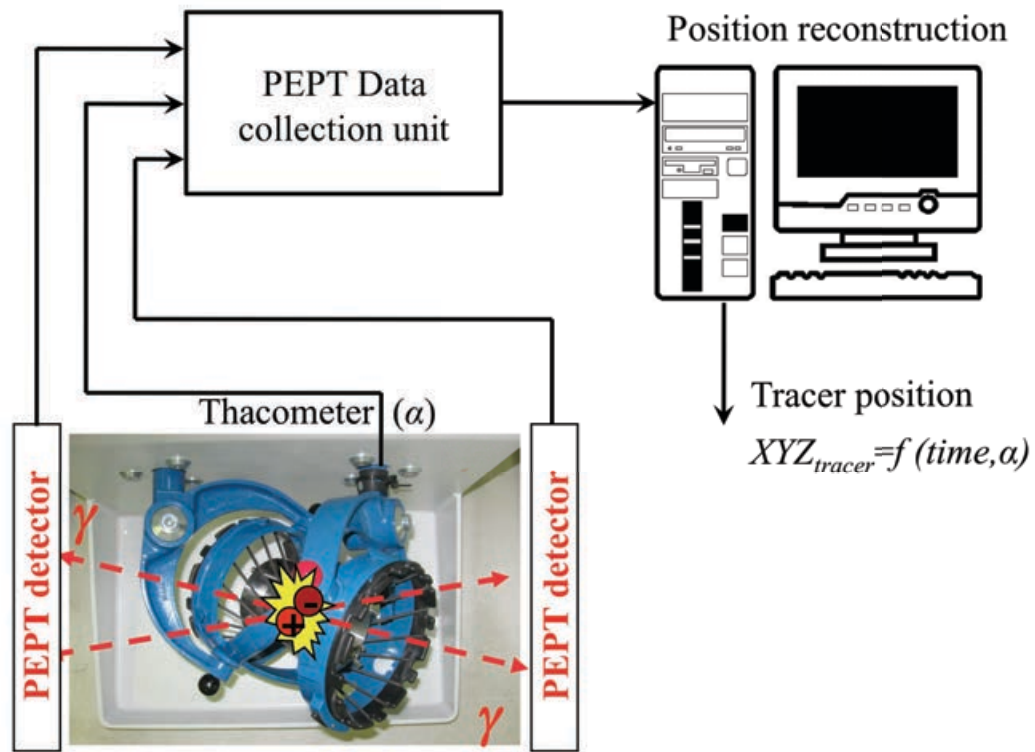


Figure 7.1: Schematic diagram of the experimental system setup the mixing study.

According with the general scheme depicted in Figure 7.2 a 2 step (A and B) procedure was utilised.

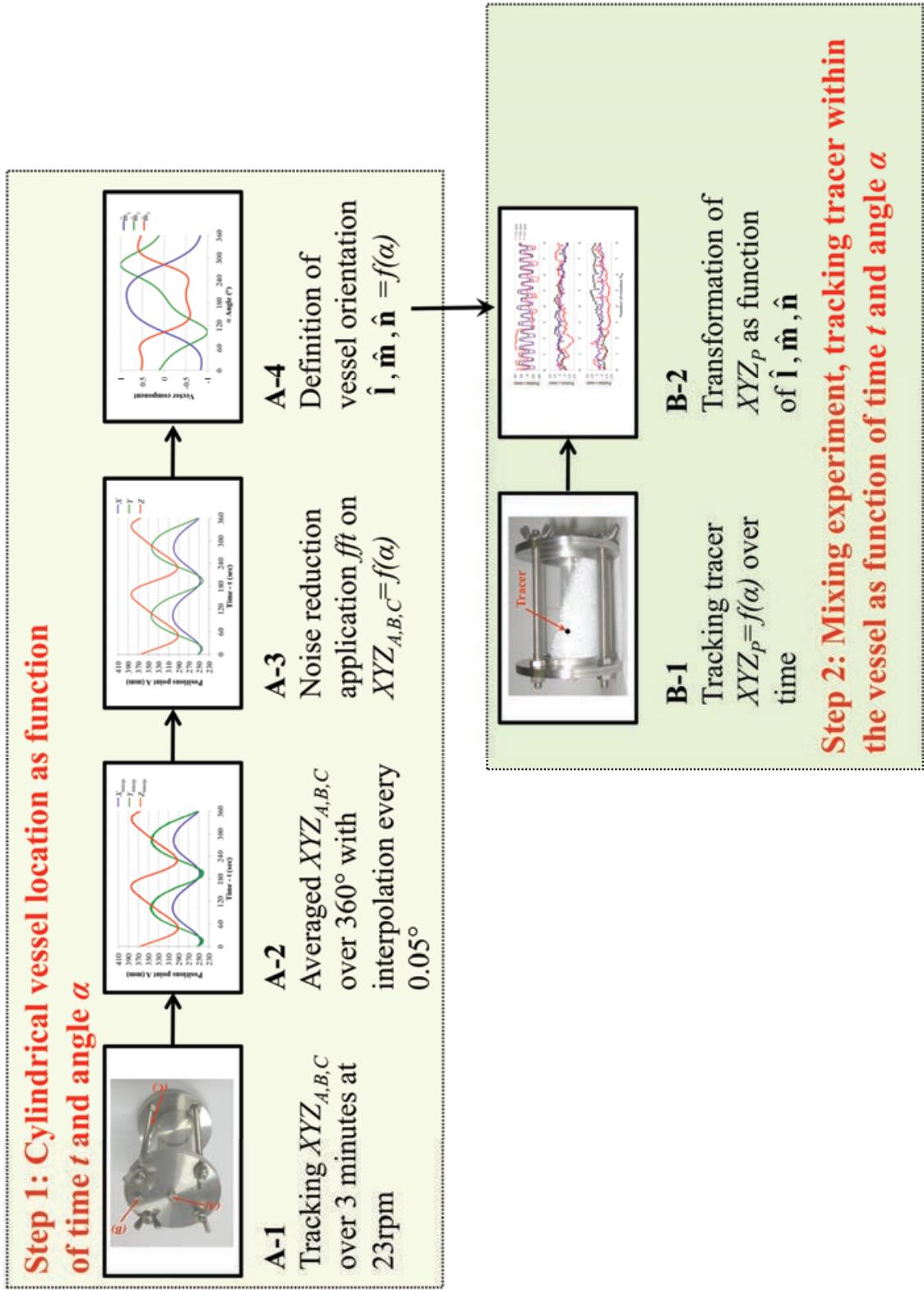


Figure 7.2: General scheme for the methodology used to locate a tracer within the vessel with the moving boundaries. Larger graphs for the steps A-2, A-3, A-4, B-2 are reported in the

next paragraph.

Firstly (Step A) the cylindrical vessel orientations defined by the unit vectors  $\hat{\mathbf{l}}, \hat{\mathbf{m}}, \hat{\mathbf{n}}$  and point  $P_M$ , Figure 7.3, were measured as function of time  $t$  and angle  $\alpha$ .

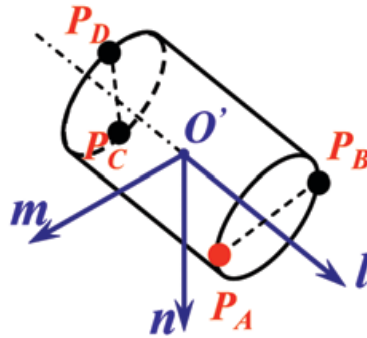


Figure 7.3: Schematic representation of the experimental measurement of the Turbula motion by PEPT.

Secondly (Step B) during the mixing experiments the tracer within the vessel was tracked as a function of time  $t$  and angle  $\alpha$ . By correlating the location of the tracer within the bed as a function of shaft angle  $\alpha$  and the orientation of the vessel as a function of the same angle it was possible to relate the position of the particle within the vessel as function of the moving boundaries position. The following steps were followed according with Figure 7.2:

Step A:

- A-1: three points  $A, B, C$  fixed with the vessel geometry (Figure 7.5) were separately tracked for a total time of 3 minutes as function of angle  $\alpha$ ;
- A-2: the locations  $X, Y, Z$  for the points  $A, B, C$  were averaged over a complete shaft rotation and interpolated every  $0.05^\circ$  angle  $\alpha$ ;
- A-3: fast Fourier transform (*fft*) was then applied for noise reduction (*fft* function Matlab);
- A-4: the unit vector  $\hat{\mathbf{l}}, \hat{\mathbf{m}}, \hat{\mathbf{n}}$  which gives the orientation for the coordinate system  $x, y, z$  fixed with the vessel geometry, could be calculated for every desired angle  $\alpha$ .

Step B:

- *B-1*: mixing experiments, the tracer was inserted within the vessel and located as a function of time  $t$  and angle  $\alpha$ ;
- *B-2*: using the correlation between tracer location and vessel orientation with angle  $\alpha$ , the tracer inside the vessel could be located as function of boundaries orientation  $\hat{\mathbf{l}}, \hat{\mathbf{m}}, \hat{\mathbf{n}}$ .

**7.3.1 Step A: tracking irregular moving boundaries**

As described in Chapter 4 it was shown that both rotational and translational motions of a solid rigid body can be accurately reconstructed by tracking three rigid points located on a solid geometry. The vessel was inserted in to the Turbula mixer chamber during the determination of the vessel motion as shown in Figure 7.4.

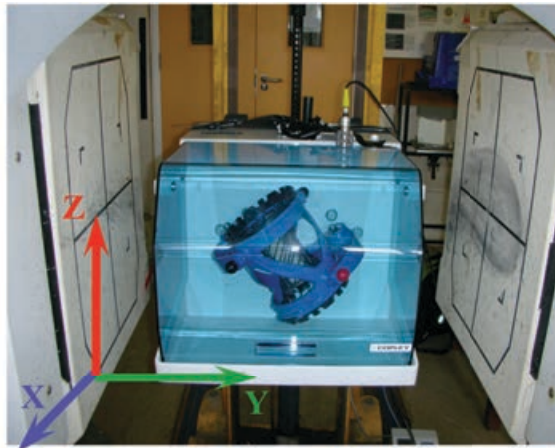


Figure 7.4: Setup for the vessel boundaries orientation measurement.  $X, Y, Z$  directions PEPT coordinate system direction.

The tracer particle (single zeolite particle) was applied to the point  $A$  on the vessel, Figure 7.5, and tracked over a period of time of 3 minutes at a Turbula shaft rotational speed of 22 rpm. This was then repeated for points  $B$  and  $C$ . Particle trajectories were therefore measured as a

function of time and the angle  $\alpha$  recorded by the tachometer.



Figure 7.5: Vessel geometry. Points  $A$ ,  $B$  and  $C$ , where tracer was located for the vessel motion measurement.

An example of tracking for the point  $A$  is given in Figure 7.6.

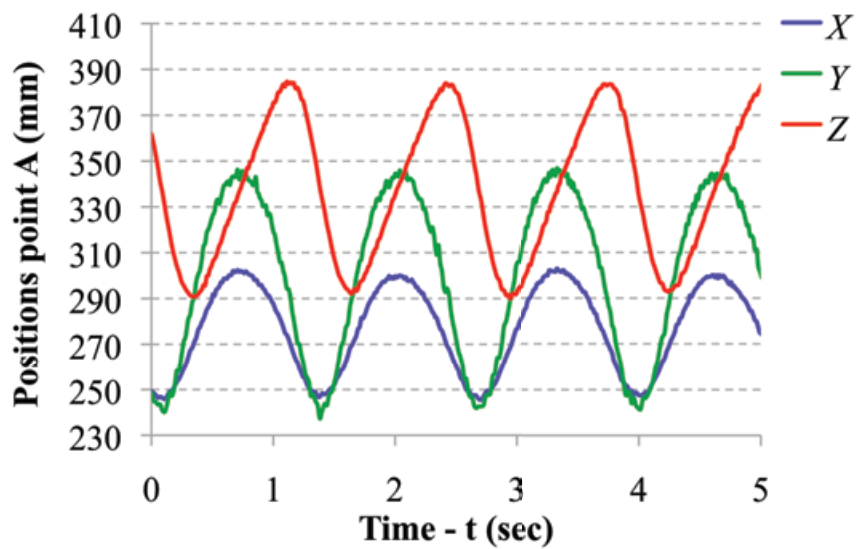


Figure 7.6:  $X, Y, Z$  positions for the point  $A$  determined over 3 minutes time (here only first 5 seconds are reported).

For each point  $A$ ,  $B$  and  $C$  the measured locations  $X$ ,  $Y$  and  $Z$  have been averaged, in increments of the angle  $\alpha$ , over the entire 3 minutes to obtain the average location over the full  $360^\circ$  shaft rotation as a function of the angular position of the shaft measured by the tachometer, Figure 7.7.a.

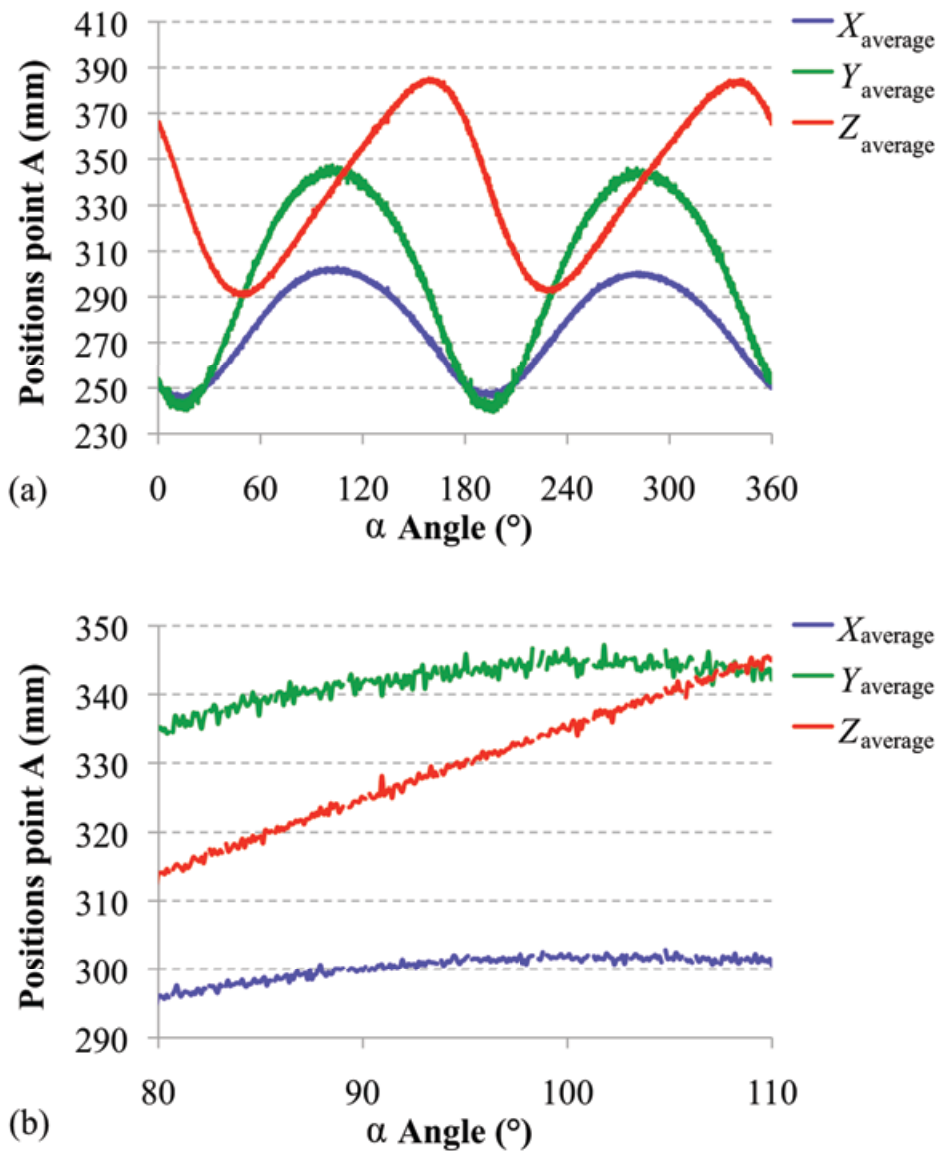


Figure 7.7: (a)  $X, Y, Z$  positions for the point  $A$  averaged over 3 minutes time and full  $360^\circ$  angle. (b) discontinuous data collection.

Over the measured period of time the system produced the position of the tracer with  $0.1^\circ$  as the interval for the angle. However, this angle interval was not constant for some points as can be seen from Figure 7.7.b. This was due to the PEPT algorithm and the way that data is used to compute tracer location: the algorithm uses a fixed number of photon pairs to compute each location, the frequency of these can be variable depending on where the particles are in the field of view. Furthermore, the algorithm rejects computed locations that have high uncertainty, which can give apparent gaps in the data. Therefore the data was filtered (fast Fourier transform, *fft Matlab function*) at a constant angle interval step of  $0.05^\circ$ , for which final result is shown in Figure 7.8.

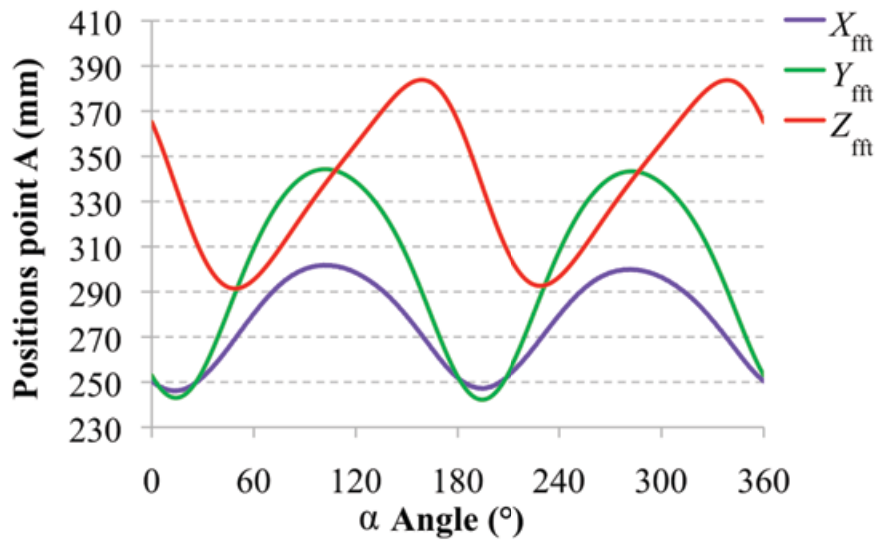


Figure 7.8:  $X, Y, Z$  positions for the point  $A$  after interpolation and *fft*.

By knowing the locations for the three points  $A, B, C$  fixed with the vessel geometry, the position and orientation of the vessel could be defined uniquely for any angle  $\alpha$  by the position vector of its centroid  $\mathbf{P}_M$ , a unit vector along its axis  $\hat{\mathbf{i}}$  and a radial unit vector  $\hat{\mathbf{m}}$ , as shown in Figure 7.9. The unit vector  $\hat{\mathbf{n}}$  was normal to the other two (ref. Chapter 4).

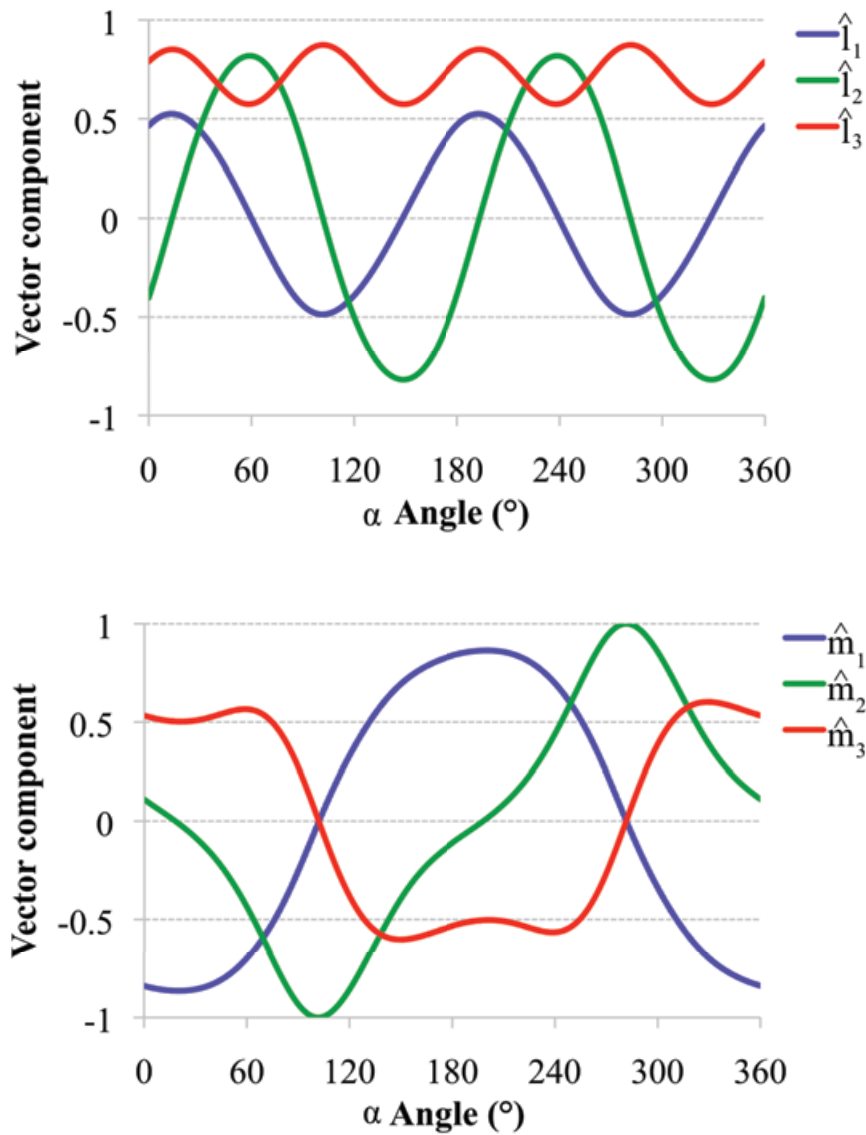


Figure 7.9: Point  $A, B, C$  used to define a unit vector coordinate system  $\hat{\mathbf{i}}, \hat{\mathbf{m}}$  fixed with the vessel geometry (the normal vector  $\hat{\mathbf{n}}$  is given by  $\hat{\mathbf{i}} \times \hat{\mathbf{m}}$ ).

### 7.3.2 Step B: reconstruction of the tracer position relative to the coordinate system fixed to the vessel

The second step (B) consisted of the location of the radioactive tracer within the bulk of material. The tracer particle was inserted into the vessel without taking out the container from the mixer chamber, otherwise the previously measured correlation between the vessel

orientation and the angle  $\alpha$  measured by the tachometer would be lost. To do this, the vessel was designed with a screw (point  $A$  in Figure 7.5), which gave access to the inside of the container.

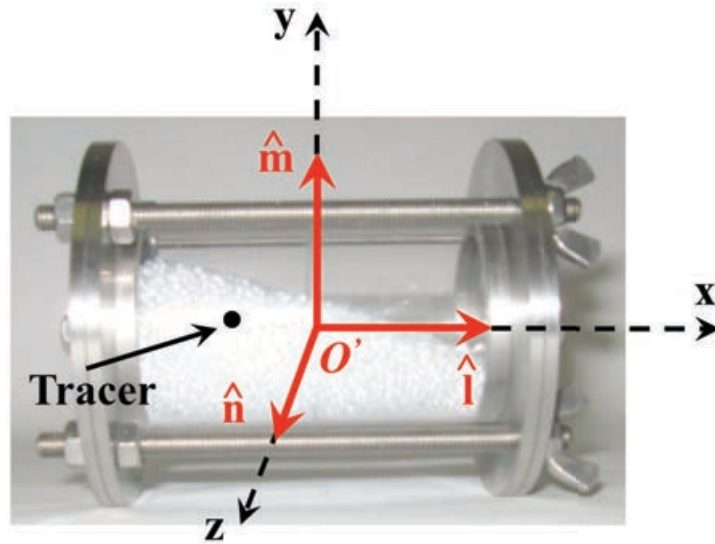


Figure 7.10: Tracer located inside the cylindrical vessel during the PEPT mixing experiments (e.g. glass beads).

The tracer location  $P_{XYZ}$  in terms of PEPT coordinate system was measured over time (for about 1200 complete mixer shaft rotations) and the angle  $\alpha$  measured by the tachometer was also recorded. Figure 7.11 shows the movement of the tracer particle measured in terms of its PEPT coordinates  $X, Y, Z$  for the glass beads at 22, 46 and 67 rpm.

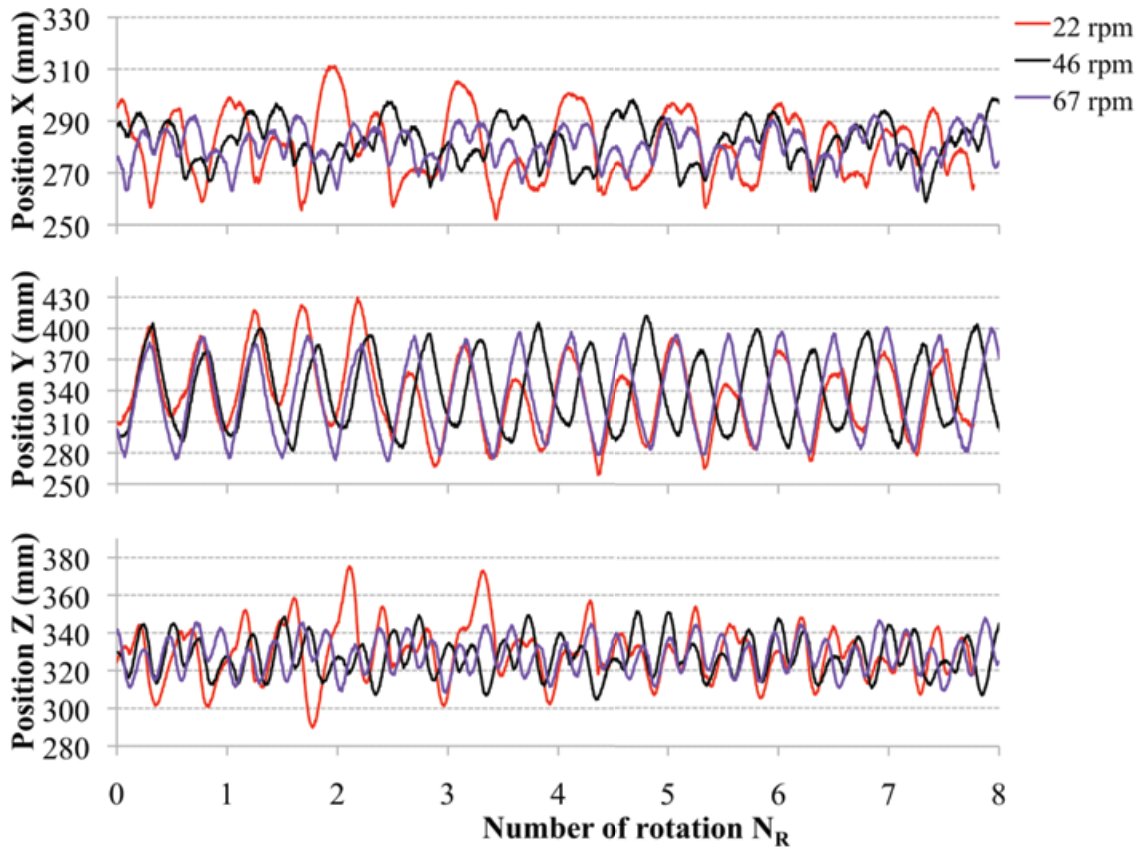


Figure 7.11: Typical particle position ( $X, Y, Z$ ) with respect to the PEPT coordinate system for glass beds at 22, 46 and 67 rpm.

By knowing the orientation of the unit vector  $\hat{\mathbf{l}}, \hat{\mathbf{m}}, \hat{\mathbf{n}}$  and the origin  $\mathbf{O}'$  at any given angle  $\alpha$  it was possible to transform the coordinates of the particle within the vessel from the PEPT fixed coordinate system to the vessel coordinate system ( $x, y, z$ ). The transformation is represented by Eq.(7.1), which was employed to obtain the new particle position ( $x, y, z$ ) from particle position ( $X, Y, Z$ ) at any desired orientation of the drum.

$$\begin{pmatrix} X \\ Y \\ Z \end{pmatrix} = \begin{pmatrix} X_{O'} \\ Y_{O'} \\ Z_{O'} \end{pmatrix} + \begin{bmatrix} \hat{l}_x & \hat{m}_x & \hat{n}_x \\ \hat{l}_y & \hat{m}_y & \hat{n}_y \\ \hat{l}_z & \hat{m}_z & \hat{n}_z \end{bmatrix} \cdot \begin{pmatrix} x \\ y \\ z \end{pmatrix} \quad (7.1)$$

Where  $X, Y$  and  $Z$  are the coordinates of the tracer particle  $P_{XYZ}$  with respect to fixed PEPT coordinate system.  $X_{O'}, Y_{O'}, Z_{O'}$  and  $\hat{l}_{XYZ}, \hat{m}_{XYZ}, \hat{n}_{XYZ}$  are origin position, point  $O'$ , and the unit vector components that define the orientation of the  $x, y, z$  coordinate system fixed with the vessel geometry. Figure 7.12 shows the movement of a the glass bead tracer particle in terms of its coordinates  $(x, y, z)$ , relative to the vessel at 22, 46 and 67 rpm.

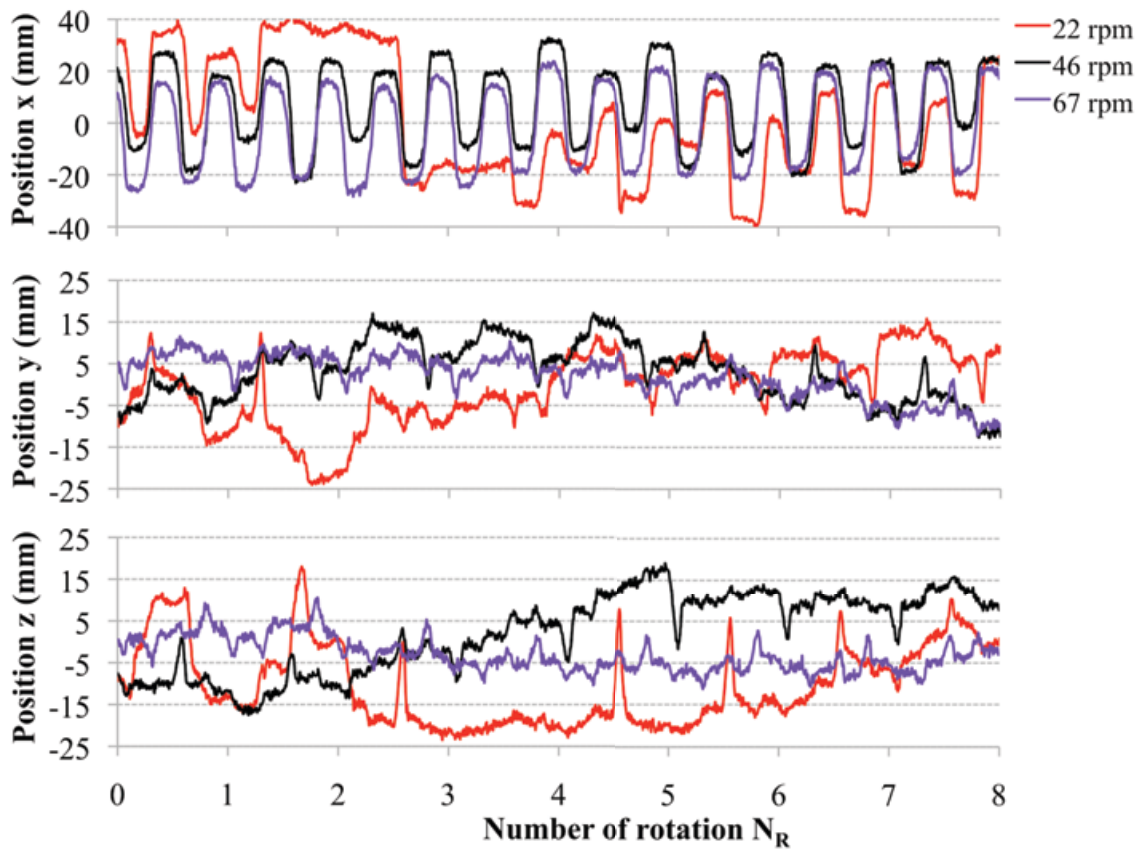


Figure 7.12: Typical particle position  $(x, y, z)$  with respect to the vessel coordinate system for glass beds at 22, 46 and 67 rpm.

For the glass bead particle, the tracer movement was rhythmic, pulsating in the axial direction; this was similar to the results from DEM numerical simulations showed in Chapter 5. The particle spent a relatively long period stationary (relative to the vessel) followed by

rapid movement, repeated twice during each shaft rotation. Despite large displacement of the particle during the rapid movements, the net displacement over the course of a shaft rotation is relatively small; the particle moved and then returned almost to the same position. The  $y$  and  $z$  displacements between the experiment and the DEM simulation were difficult to compare, since the fixed coordinate system in the case of DEM simulation and in the experiment did not have the same direction for a given position and orientation of the vessel. In Figure 7.13 the  $x,y,z$  displacement is shown for zeolite particles, again the tracer particle moved periodically in the axial direction.

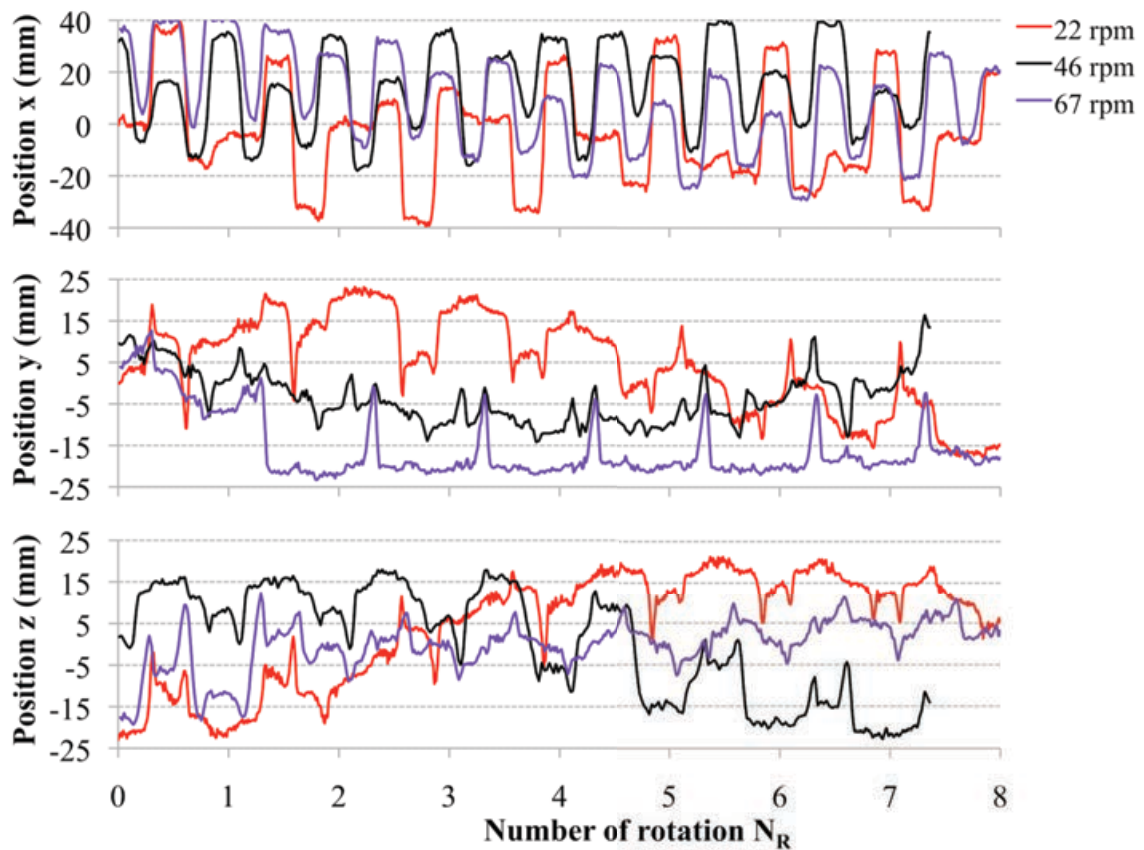


Figure 7.13: Typical particle position ( $x,y,z$ ) with respect to the vessel coordinate system for zeolite particle at 22, 46 and 67 rpm.

## **7.4 Results and discussion**

Due to the Turbula mixer complex 3D+1D motion (ref. Chapter 6), it is difficult to carry out a direct comparison in terms of velocity fields under different experimental conditions. Usually, typical velocity fields from PEPT are obtained as time averaged data points. For example, for a horizontal rotating drum, at steady state the particles would be considered to behave similarly in any transverse plane along the length of the vessel. Therefore, the velocity maps would be obtained by averaging the velocity over time of the tracer obtained on the different transverse plane along the axis [3,6]. Unfortunately, for a Turbula mixer, the bed is periodically changing shape during the shaft rotation without displaying a steady state. The amount of data points that would therefore be necessary to completely characterise the bed velocity in any point for any vessel position during the shaft rotation would be too large. Moreover, the tracer life activity time would probably not last for the required time.

In order to validate the numerical simulations, the parameters calculated from the DEM simulations (ref. Chapter 5): axial peaks length, plateau length in axial direction and dispersion coefficient were also determined by PEPT experiments. Similar trends and values should give the confidence that the simulations' results are trustworthy and also confirm the numerical prediction for the rate of mixing, which otherwise would be difficult to obtain experimentally.

### **7.4.1 Axial displacement analysis for glass bead tracer particle**

The axial movement for the tracer particle at 22 rpm is shown in Figure 7.14. As previously reported in the DEM modeling (ref. Chapter 5) the particle movement in the axial direction (from one peak to the following peak) periodically alternated with a period of no particle movement in the axial direction (plateau) during the inversion of the vessel.

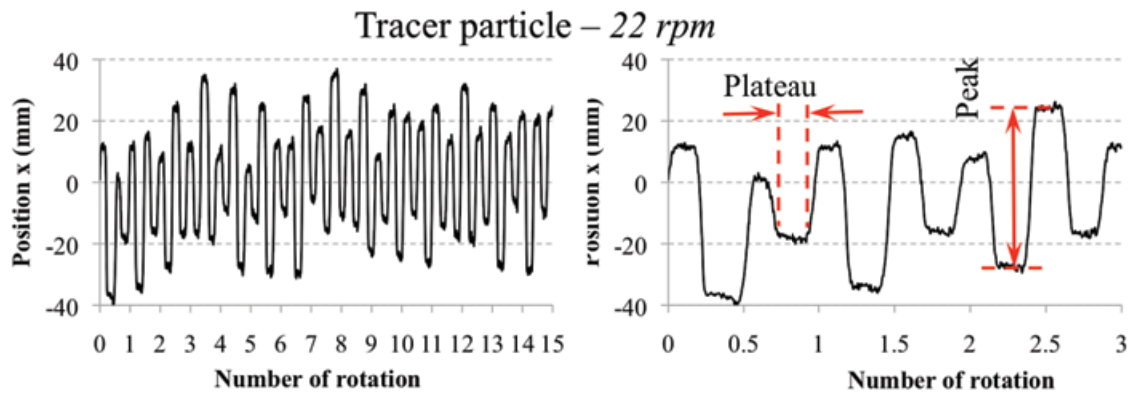
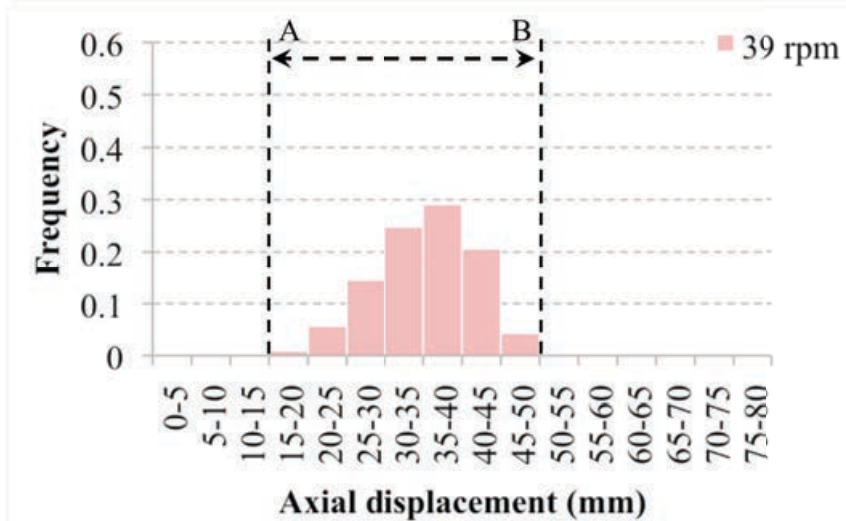
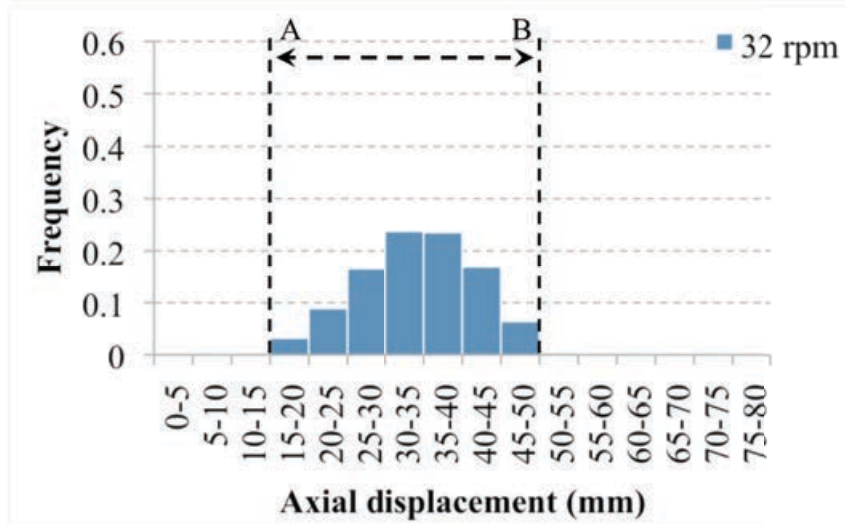
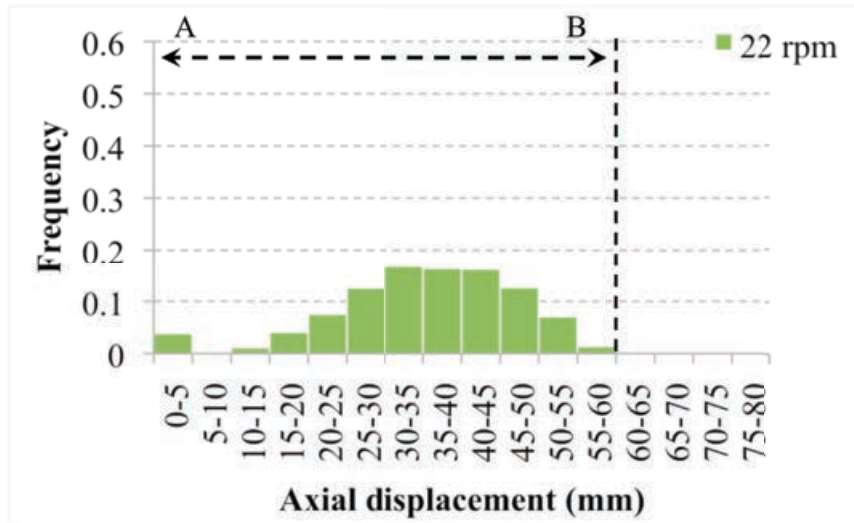
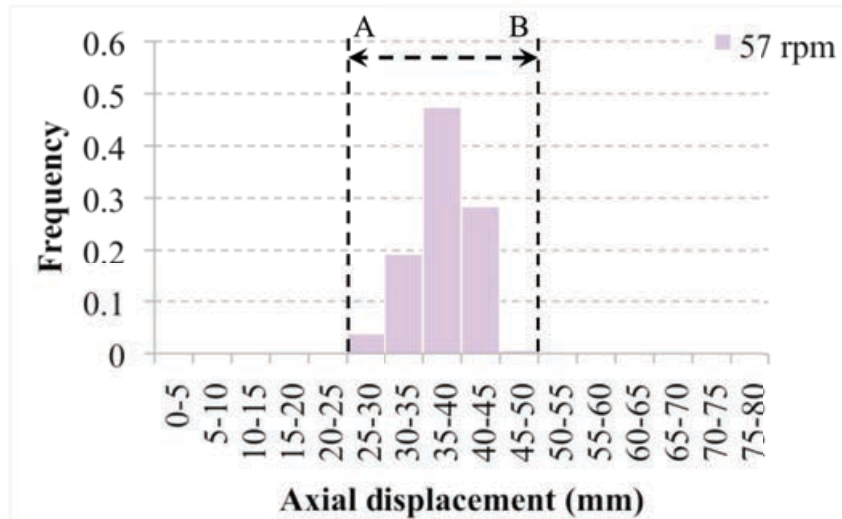
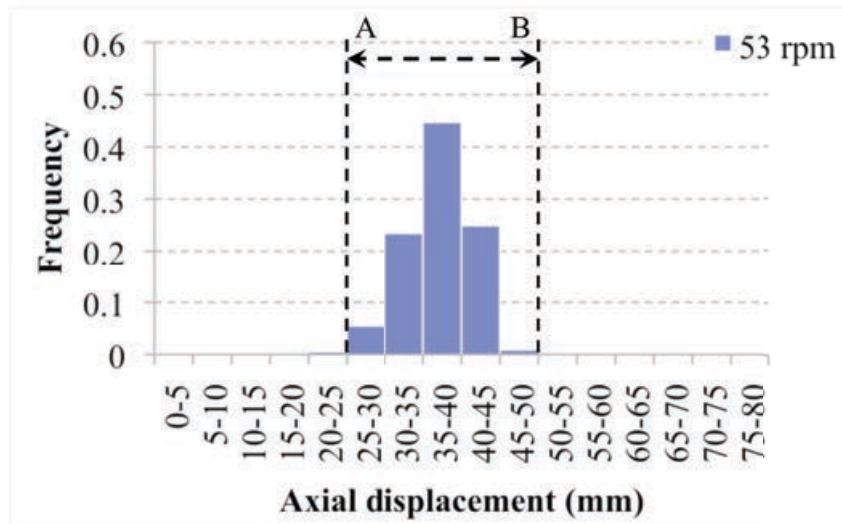
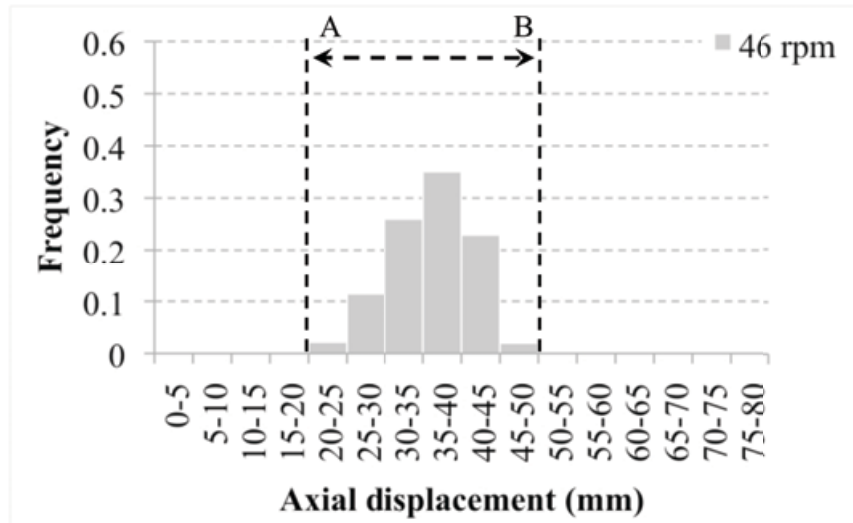


Figure 7.14: Plot of  $x$  position against number of rotation for the tracer particle at 22 rpm for 15 shaft rotations (left) and only for the first 3 rotations (right), definition of peak and plateau.

For the glass bead tracer particle the distance travelled in axial direction  $x$  between each peak “axial displacement” was calculated and the frequency distribution is presented in Figure 7.15.





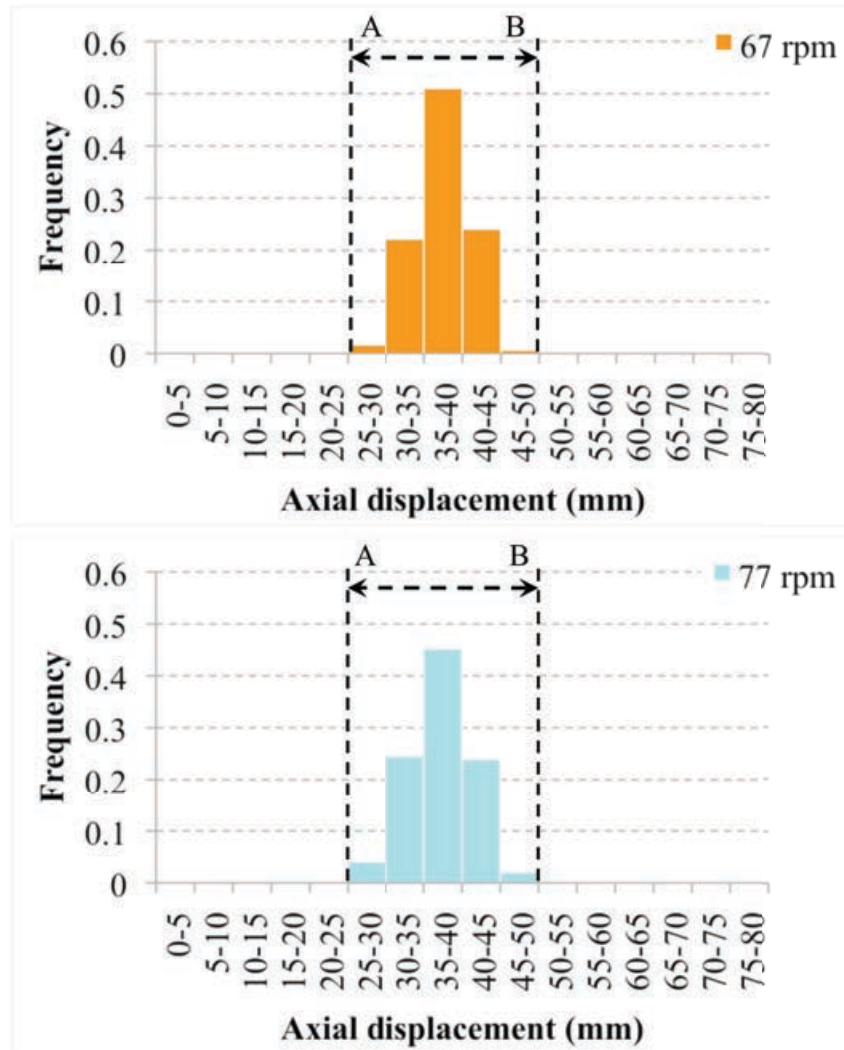


Figure 7.15: Peak frequency distribution during PEPT experiments for glass beads at different speeds.

From the previous plots, it can be noted that by increasing the speed, the distribution of such peaks tended to reduce toward a narrower distribution (line *A-B*) confirming the trends observed by DEM numerical results (ref. Chapter 5). However, in terms of values there were differences between the experimental and the DEM numerical results.

In Figure 7.14 it is illustrated that during the shaft rotation the tracer particle showed a stationary period corresponding to the motion of inversion for the vessel. The average of the

length of time for this static period as a function of the operating speed is shown in Figure 7.16.

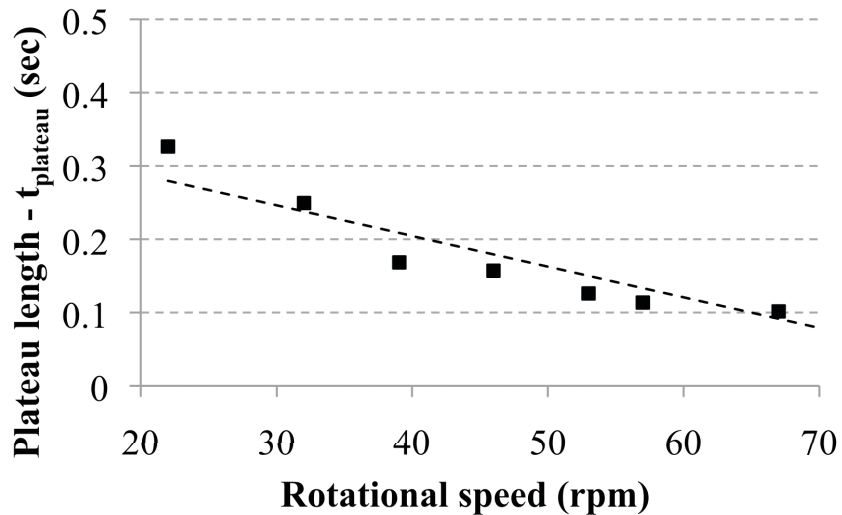


Figure 7.16: Length of average plateau periods in the axial direction for the tracer particle as a function of speed.

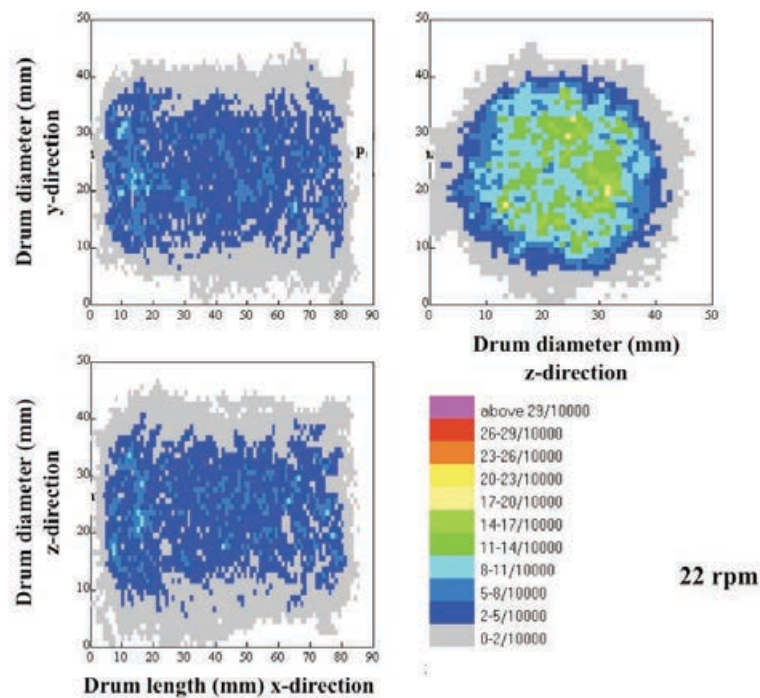
The length of time for the static period decreased with the speed. Again, this trend confirms what was previously reported by DEM simulations.

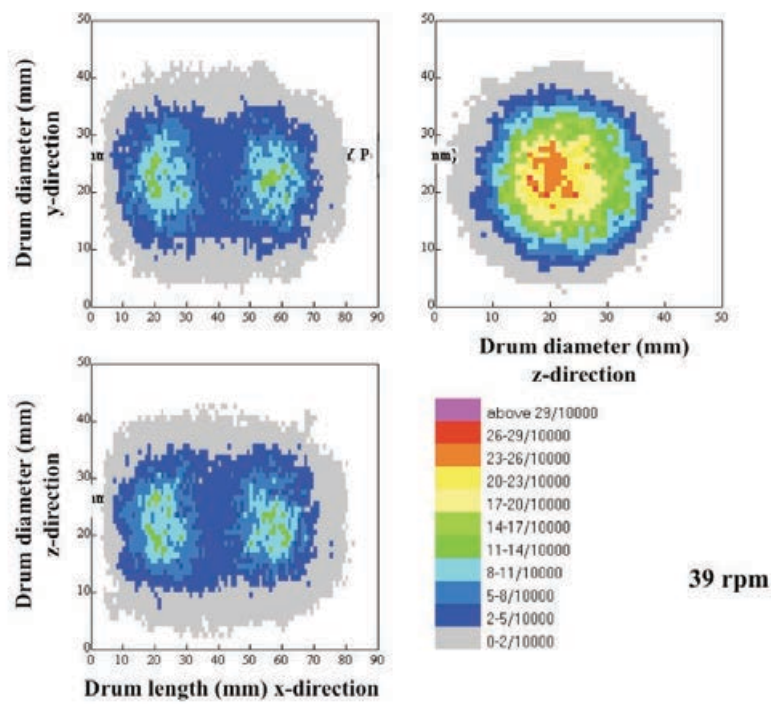
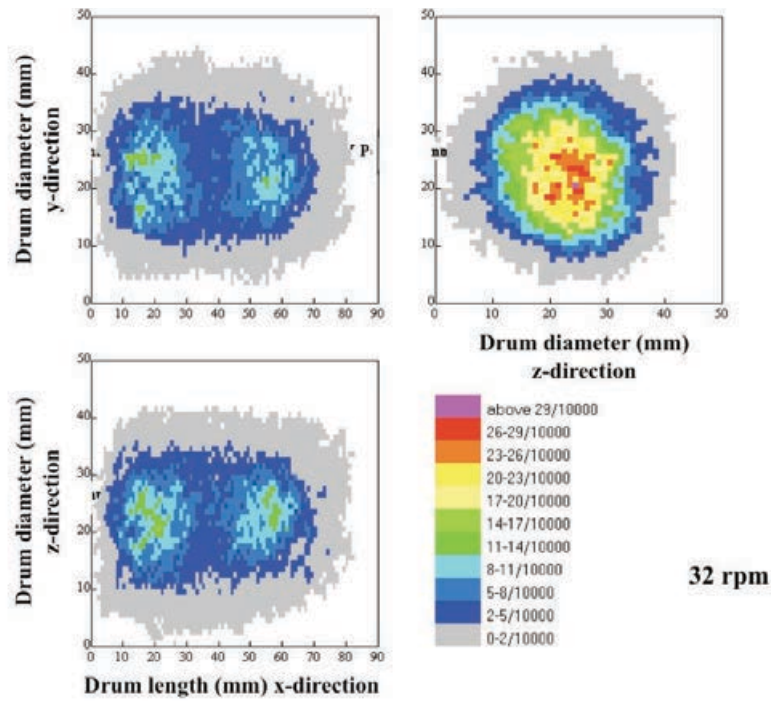
#### 7.4.2 Occupancy plots for glass beads

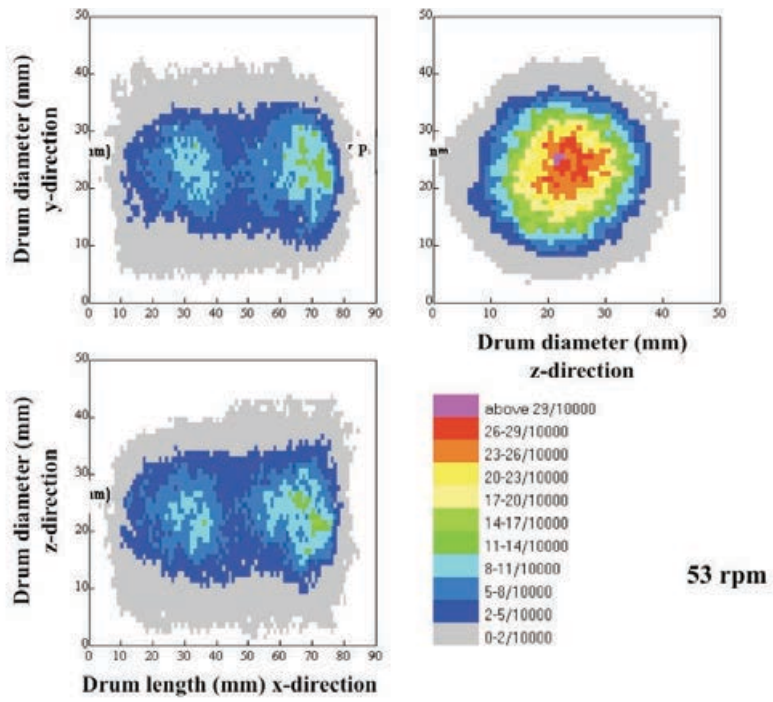
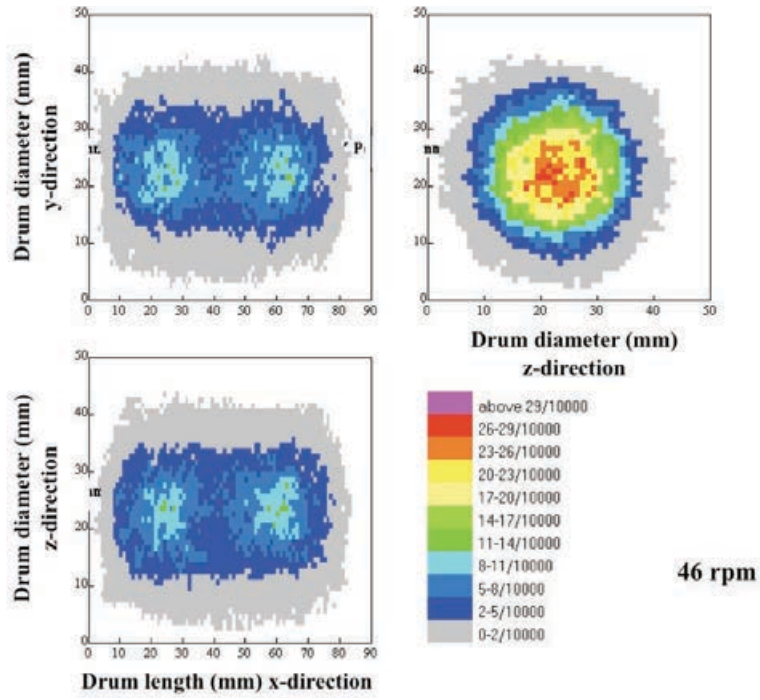
The position of the particle inside the vessel was known over time. Therefore, occupancy, defined as the ratio of time that the tracer spends at a given position to the total tracking time [3], could be calculated.

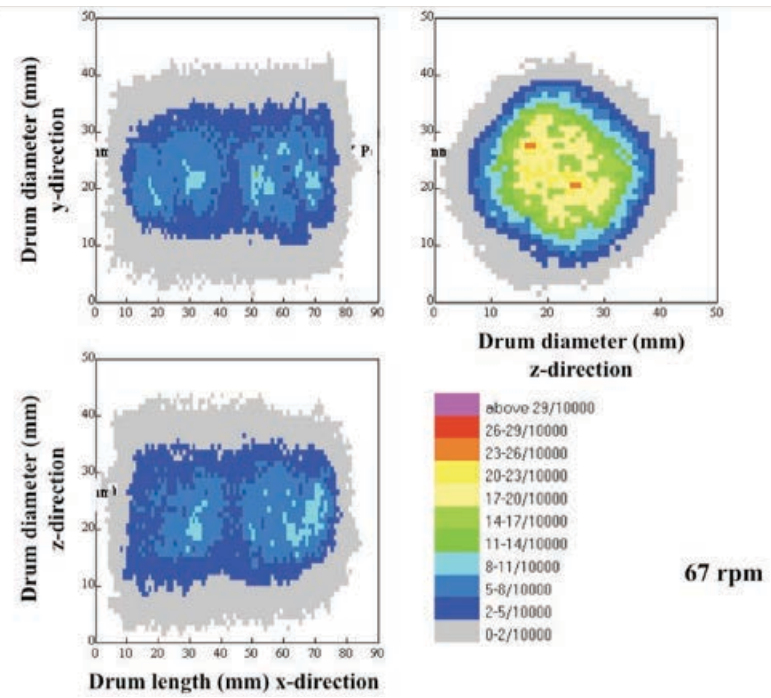
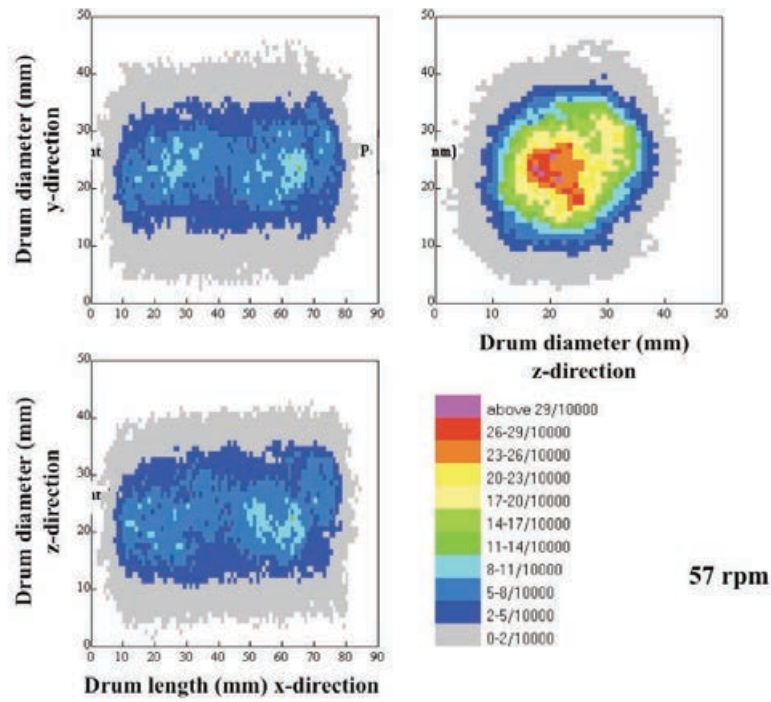
Occupancy plots for the glass bead tracer for the monosized system in the axial and transverse plane are shown in Figure 7.17 for different rotational speeds, (22, 32, 39, 46, 53, 57, 67 and 77 rpm) for a measured period of about 20 minutes. The plots reveal a gradual change in the

occupancies with the speed. By increasing the speed from 22 rpm up to 46 rpm a clear core-shell structure could be seen in the transverse and axial direction. This suggests that the tracer particle tended to occupy two core regions of the bed in the axial direction and the tracer seemed to have difficulty in crossing the middle point. This indicates a change in behaviour for the system occurred when approaching an operational speed of 46 rpm. The core-shell structure is probably bad for mixing operations; the two cores in the axial direction probably explain the decrease in mixing efficiency in the axial direction that was already observed with the numerical simulations when the mixer speed approached 46 rpm. By increasing the speed further the central region in the transverse plane and the two cores tended to disappear again suggesting an improvement in the movement of the tracer in the axial and radial direction.









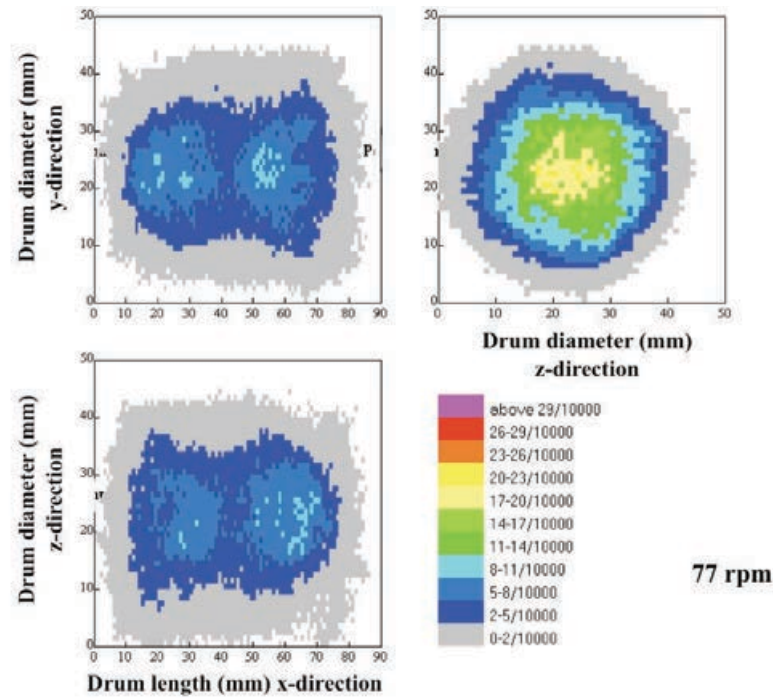


Figure 7.17: Occupancy plots (20 min) for glass bead tracer particle at different speeds.

As seen in the occupancy plots above, the amount of tracer movement in the axial and radial directions, the time spent by the tracer particle within the vessel, did not change linearly as a function of the operational speed. This confirms the idea of a transition behaviour for the powder bed as a function of operating speed.

#### 7.4.3 Dispersion coefficients for glass bead tracer

Again for direct comparison and validation of the results for the DEM numerical simulations (ref. Chapter 5), the “net” movement in the axial and radial directions were monitored by using the coefficients of axial and radial directions ( $D_x$ ,  $D_r$ ). These were calculated for a single particle as the sum of the square of the axial displacement of the tracer particle within the vessel in one shaft rotation averaged over the total number of shaft rotation, Eq.(7.2) and Eq.(7.3). The orientation for the vessel corresponded to the one used in Chapter 5 for the

calculation of the axial and radial dispersion coefficients.

$$D_x = \frac{1}{N-1} \sum_{k=1}^{k=N-1} \frac{(x^{k+1} - x^k)^2}{(t^{k+1} - t^k)} \quad (7.2)$$

$$D_r = \frac{1}{N-1} \sum_{k=1}^{k=N-1} \frac{(r^{k+1} - r^k)^2}{(t^{k+1} - t^k)} \quad (7.3)$$

Where  $x^k$  and  $x^{k+1}$  are the axial positions of the tracer particle at time  $t^k$  and at time  $t^{k+1}$ ; and  $N$  is the total shaft rotation considered for each case (about 1100 shaft rotations). Similarly  $r^k$  and  $r^{k+1}$  are the radial positions of the tracer particle at time  $t^k$  and at time  $t^{k+1}$ .

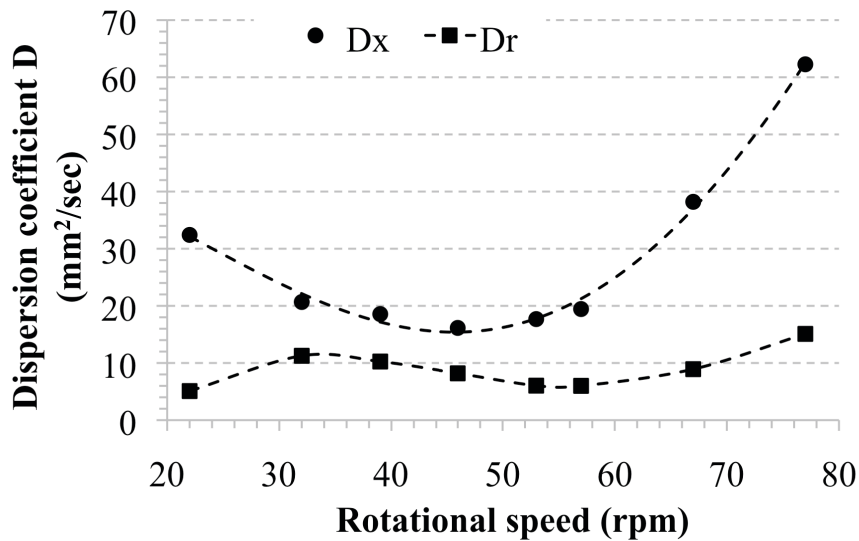


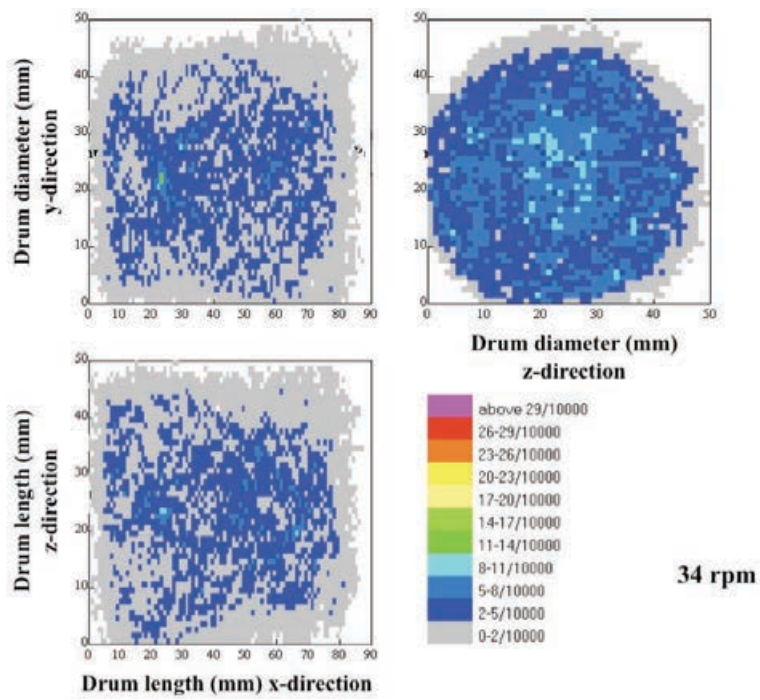
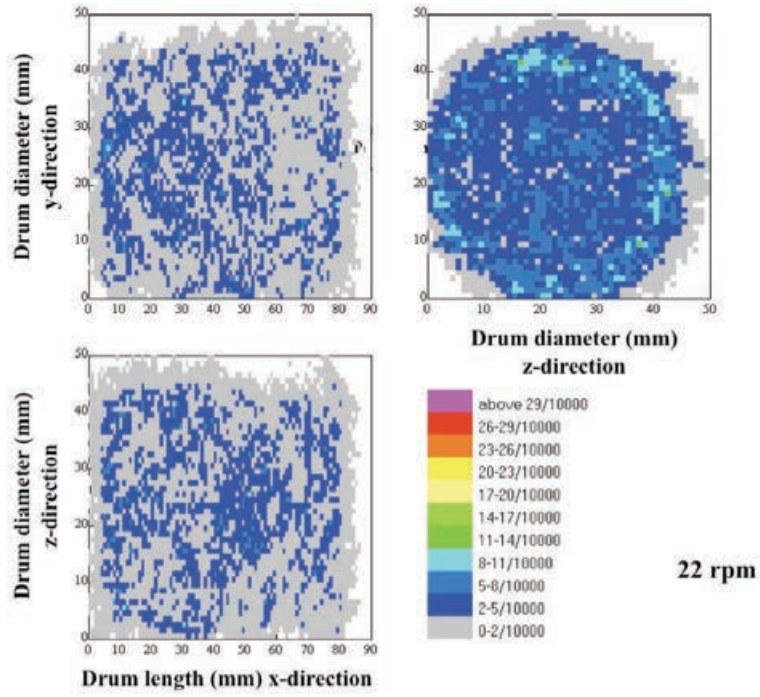
Figure 7.18: Dispersion coefficients  $D_x$  and  $D_r$  for glass bead particles at different speeds.

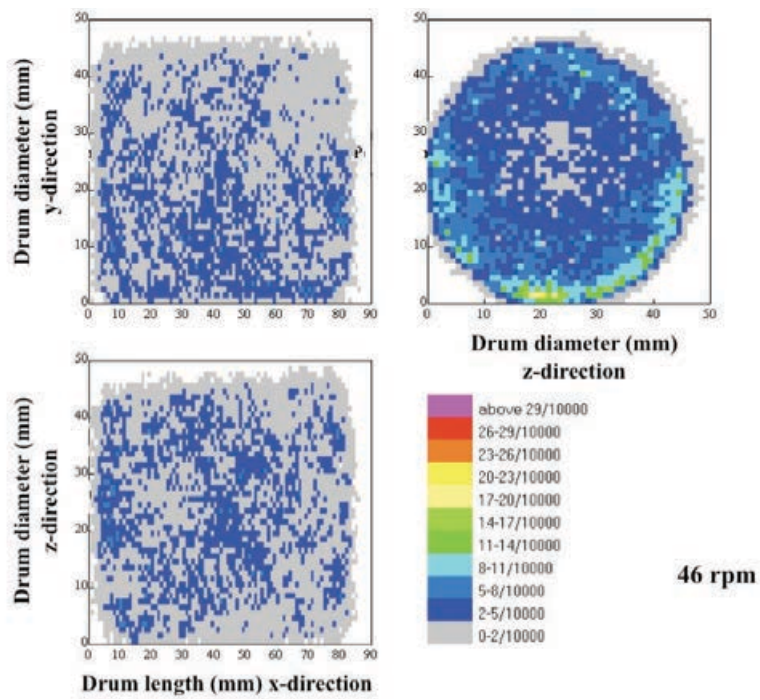
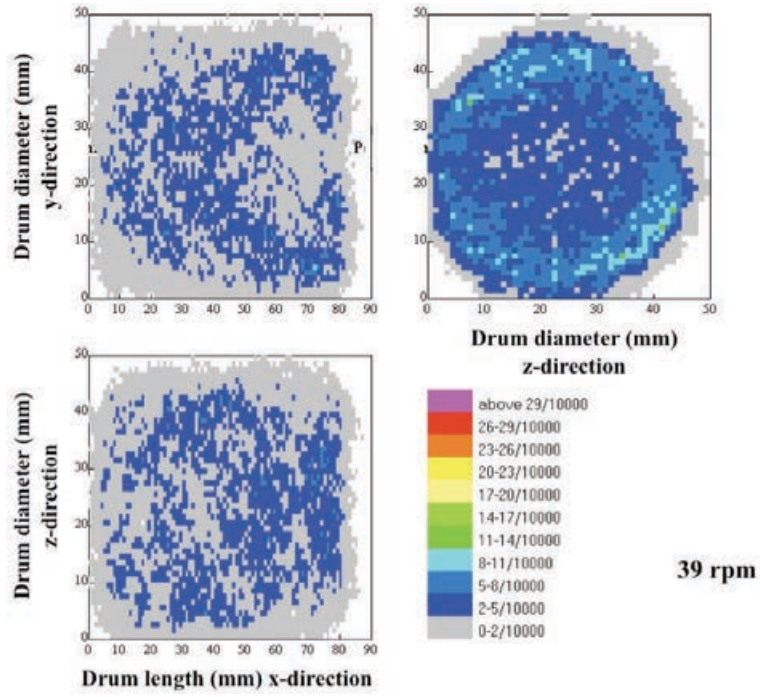
The trend of these data was qualitatively comparable with the results of monosized particles obtained by DEM simulations (ref. Chapter 5) with a minimum value approximately about 46 rpm. However, the magnitude of these results was different than numerical results. It is

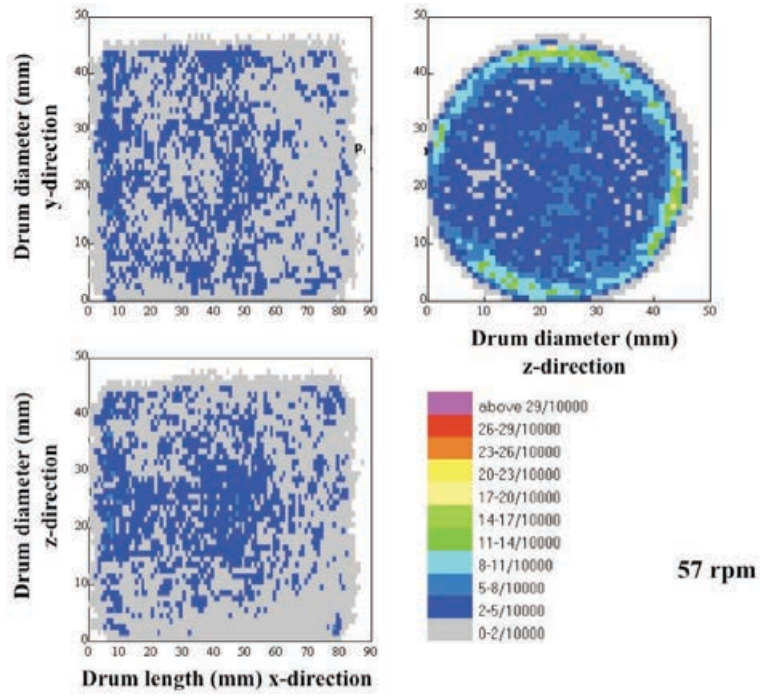
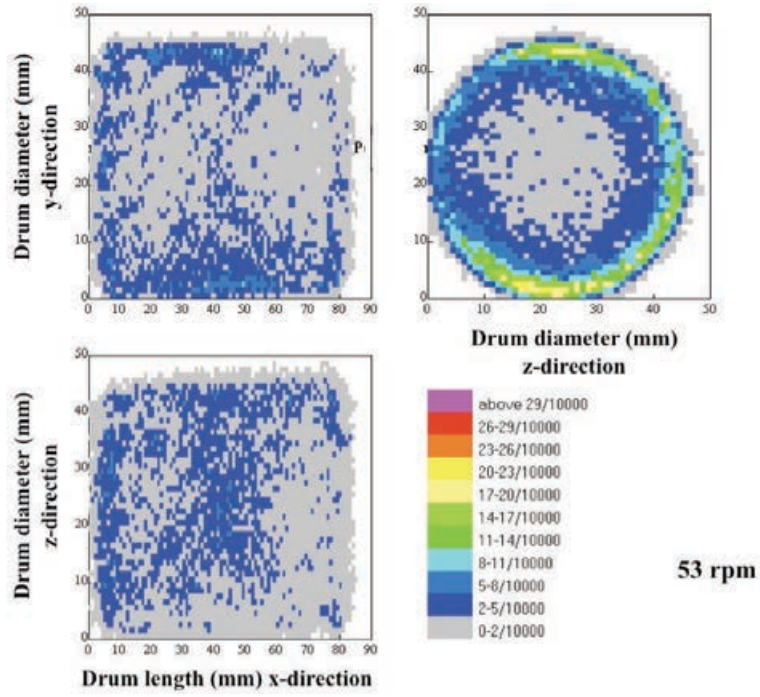
unclear if the comparison between the simulation and experiments is statistically legitimate as the in the PEPT experiment the dispersion coefficients have been calculated by tracing only one particle over about 1200 shaft rotations, whereas in the simulations the same coefficients have been calculated considering all the particles in the system for the 15 total rotations. The difference perhaps could be explained by the definition of the coefficients of dispersion defined by Eq.(7.2) and Eq.(7.3). They were calculated as the time average of the square of the particle displacement. Hence, in the simulations only some of the larger particle movements could strongly influence the averaged values for  $D_x$  and  $D_r$ . Therefore, if some these larger particles movement were not captured from the experiment, the calculated average could show big differences compared with the simulations. In Chapter 8, distributions of axial and radial displacements have been compared instead of  $D_x$  and  $D_r$  between PEPT experiments and DEM simulation results in order to investigate the effect of DEM simulations input parameters.

#### **7.4.4 Occupancy plots zeolite**

In Figure 7.19 the axial and radial occupancy distribution plots are reported for small zeolite particles of which mechanical properties were measured in chapter 3.







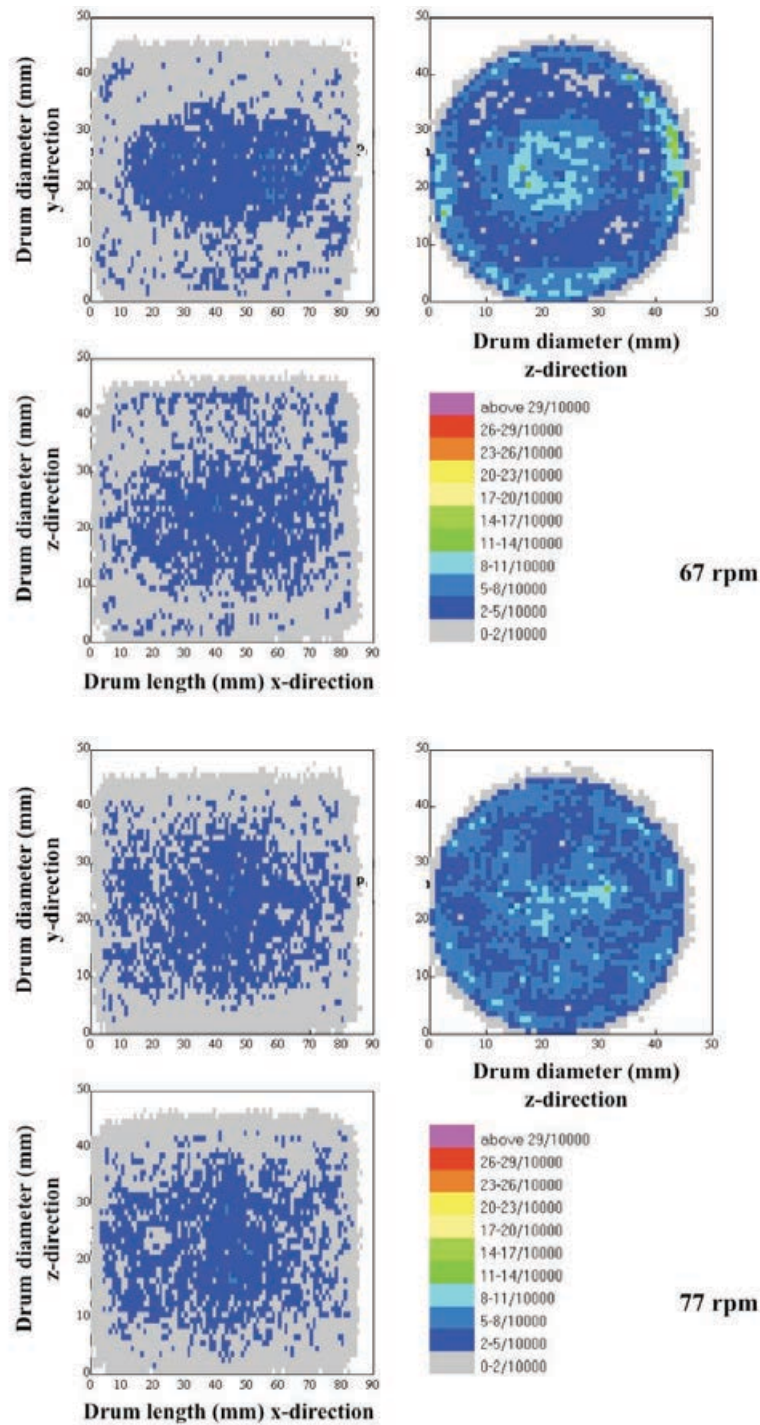


Figure 7.19: Occupancy plots (20 min) for zeolite tracer particle at different speeds.

Compared with glass beads the occupancy plots for the zeolite particles differed as the occupancy inside the vessels was different for the same speed. These differences were expected as the two materials have remarkable differences in terms of size and density. This

would result in a completely different particles kinematics for the two materials. The different particle flow behaviours within the mixer can probably be related to the differences in particle sizes, densities and perhaps the effect of air could have on the dynamics of the remarkably smaller zeolite particles.

#### 7.4.5 Dispersion coefficient for zeolite bead tracer

Dispersion coefficients of a zeolite tracer confirmed different particle behaviour compared with the glass beads, Figure 7.20. It is interesting to note the non-monotonic behaviour for the axial coefficient of dispersion at 67 and 77 rpm shaft speed. This decrease of axial movement can also be observed in the occupancy plots at 67 and 77 rpm, which showed the particle seemed to spend more time in a limited central core region. The reasons for such effect are not totally understood.

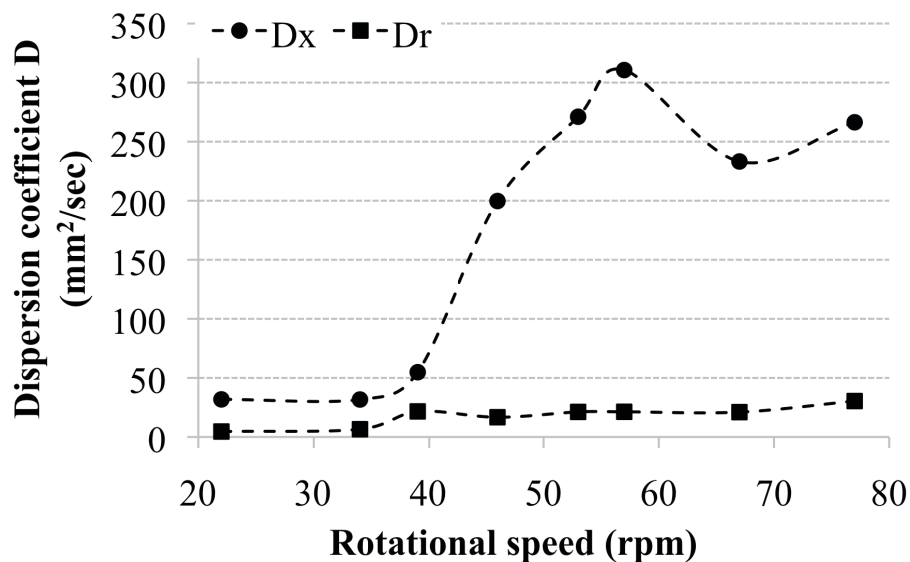


Figure 7.20: Dispersion coefficients  $D_x$  and  $D_r$  for zeolite particle at different speeds.

Differences in particle movement for “real” industrial zeolite particles compared with behaviour of “ideal” material such as large glass beads particles were evident when the dispersion coefficients and occupancy plots were compared for the two materials considered. Therefore, predicting mixing behaviour for a real industrial material from information obtained from a typical model material, such as glass bead, is not ideal. This also implies, that extrapolating information from a DEM model using ideal particles for predicting particles behaviour on a real industrial particles system can be difficult. Hence, in order to be able to predictively model, real industrial particles systems, the DEM limiting issues mainly regarding number of particles, size of particle and shape of particles should be addressed.

## **7.5 Conclusions**

This chapter concerns the Positron Emission Particle Tracking (PEPT) experimental measurement of particle motion within the Turbula mixer. The non-invasive PEPT technique was used to follow particle tracer trajectories within the vessel moving at different operating speeds. PEPT experiments were applied to study the flow of two systems: one consisting of monosized glass beads and one of zeolite catalyst support material (ref. Chapter 3). The overall aim of this chapter was to validate some of the DEM numerical modeling predictions for monosized particles, presented in Chapter 5, and to have a better understanding of mixing occurring within a cylindrical vessel located within the Turbula mixer.

For monosized glass beads, PEPT experiments confirmed similar general qualitative trends observed from the DEM numerical simulations presented in Chapter 5. Similar particle axial displacement behaviour was observed between the experiments and the simulations with axial periodic particle movement alternated with static periods corresponding to the inversion of the vessel. Similar trends for the distribution of the average axial travelled distance were found

between the experiments and DEM simulations. In both cases the movement in axial direction per quarter of shaft revolution decreased with increase in speed. Moreover, similar trends were observed for axial and radial dispersion coefficients. Also, for the experimental case a minimum value for the axial coefficient corresponded to the middle speed of 46 rpm. As said, similar trends were generally observed, but differences in absolute values were seen. Differences could be related to the choice of the DEM input parameters or some statistical error, which could be due to the data analysis comparison between PEPT single particle and DEM entire particle bed. The effect of the choice of the DEM input parameters will be investigated in Chapter 8.

For the glass beads, axial and radial occupancy plots were also presented. Occupancy data showed there was a change in the bed behaviour as a function of operating speed, as generally observed by DEM numerical simulations (ref. Chapter 5). It was observed that the tracer particle tended to concentrate in two core regions of the vessel when the mixer speed was increased from 22 rpm up to 46 rpm. When the speed was further increased these two cores tended to disappear. This is in a good agreement with the DEM numerical predictions, where a decrease in mixing dispersion in the axial direction was observed when the mixer speed was increased up to 46 rpm. The experimental results presented here, therefore confirm the DEM predictions in terms of bed transition behaviour as a function of operating speed for monosized particles. However, there are still difficulties in formulating a clear mechanistic explanation for such effect. This is mainly due to the complex mixer considered in this study and its motion.

In the case of zeolite particles different particle behaviour was observed compared with ideal glass beads. The axial and radial dispersion coefficients showed different trends compared with the ideal material. Specifically a non-monotonic behaviour was observed for the axial

coefficient of dispersion as a function of the operating speed. A decrease of the dispersion coefficient at 67 and 77 rpm was observed. Such non-linear behaviour was also observed in the occupancy plots with a core particle static area into the centre of the vessel at these speeds. The reasons for this is not totally clear.

Difficulties in relating the two materials mixing behaviour are evident. This reinforces the concept that trying to relate or predict particle mixing in real particles systems to ideal systems and a real material can be difficult. Enhanced DEM modelling with a system closer to reality with smaller and higher number of particle with real shapes, is necessary.

## 7.6 References

- [1] C.J. Broadbent, J. Bridgwater, D.J. Parker, S.T. Keningley and P. Knight, Phenomenological study of a batch mixer using a positron camera, *Powder Technology* **76** (3) (1993), pp. 317–329.
- [2] J.R. Jones and J. Bridgwater, Case study of particle mixing in a ploughshare mixer using positron emission particle tracking, *International Journal of Mineral Processing* **53** (1–2) (1998), pp. 29–38.
- [3] Y.L. Ding, R. Forster, J.P.K. Seville, D.J. Parker, Segregation of granular flow in the transverse plane of a rolling mode rotating drum, *International Journal of Multiphase Flow* **28** (2002), pp. 635-663.
- [4] H.P. Kuo, P.C. Knight, D.J. Parker, A.S. Burbidge, M. J. Adams, J.P.K. Seville, Non-equilibrium particle motion in the vicinity of a single blade, *Powder Technology* **132** (2003), pp. 1-9.
- [5] H.P. Kuo, P.C. Knight, D.J. Parker, J.P.K. Seville Solids circulation and axial dispersion of cohesionless particles in a V-mixer, *Powder Technology* **152** (2005), pp. 133-140.
- [6] Y.L. Ding, J.P.K. Seville, R. Forster, D.J. Parker, Solids motion in rolling mode rotating drums operated at low to medium rotational speeds, *Chemical Engineering Science* **56** (2001), pp. 1769-1780.

## Chapter 8

### **Input parameters sensitivity analysis for the comparison of Turbula mixer DEM simulations and PEPT mixing experiments**

*The results presented in Chapters 5 and 7, showed that the DEM model, for the Turbula mixer, captured the major trends for the parameters used to characterize the particle bed motion with monosized 2 mm diameter spherical glass beads. There were analogies between results from the DEM numerical model and the PEPT experimental results in terms of axial and radial dispersion coefficients, distribution of the axial travelled distances and values for the static plateau periods in the axial direction. Although the predicted particle dispersion coefficients and particle movements in axial directions during a shaft cycle had similar trends they differed in terms of absolute values. In particular the dispersion coefficient in the axial direction was double for the DEM simulation compared with the PEPT results. In this chapter a sensitivity analysis has been conducted to investigate the effect of the variation of DEM parameters for the axial and radial displacement and the segregation index in order to compare the DEM simulation predictions with the PEPT experimental results.*

## **8.1 Introduction: comparison between DEM simulation and PEPT experimental results for the Turbula mixer**

In Chapters 5 and 7, particle motion in a cylindrical vessel in a Turbula mixer was studied using discrete element method (DEM) simulations and positron emission particle tracking experiments (PEPT). A cylindrical vessel moving according to the Turbula mixer motion was modeled by numerical simulations. In the DEM simulations, the Hertz Mindlin contact model proposed in the EDEM commercial package was used to model the particle-particle and particle-wall material contact mechanics using some of the input parameters found in literature. The experimental validation using PEPT was conducted by studying the motion of the particle bed by tracking one single tracer particle within the vessel. Due to the complex motion for the Turbula mixer and the “non-steady” state for the bed movement, it was difficult to directly compare DEM simulations with PEPT experimental in terms of velocity field profiles for any given vessel position and orientation. Therefore, other parameters have been compared: the dispersion coefficients in the axial and radial direction, distribution of particle movement in the axial direction and duration of the static period in the axial direction during a shaft rotation cycle. Some differences in terms of quantitative numbers for the compared parameters have been found as PEPT results differed from the simulation results in particular regarding the axial dispersion coefficients. The hypothesised change in bed transition behaviour observed in the DEM simulations and the change of mixing efficiency (characteristic number of rotations) as a function of the operating speed were also observed in the PEPT experiments by comparison of occupancy plot (ref. Chapter 7). It was observed that the middle speed, 46 rpm, seemed to be a critical speed for the mixing behaviour. Hence, the bed transition behaviour dependence on the operating speed has been numerically predicted and experimentally validated. In the next paragraph a comparison between the results

presented in Chapters 5 and 7 is given to highlight the similarities in the trends between the simulation and the experimental results.

### 8.1.1 Comparison of DEM and PEPT axial and radial dispersion coefficients, $D_x$ and $D_r$

In Chapters 5 and 7, the axial and radial dispersion coefficients were calculated according to the equations reported in Table 8.1.

Table 8.1: list of equation used to calculate axial and radial dispersion coefficients in DEM simulations and PEPT mixing experiments.

	<b>DEM</b>	<b>PEPT</b>
<b>Axial dispersion coefficient</b>	$D_x = \frac{1}{N-1} \sum_{k=1}^{k=N-1} \frac{\sum_{i=1}^{i=n} (x_i^{k+1} - x_i^k)^2}{(t^{k+1} - t^k)n}$ (8.1)	$D_x = \frac{1}{N-1} \sum_{k=1}^{k=N-1} \frac{(x^{k+1} - x^k)^2}{(t^{k+1} - t^k)}$ (8.2)
<b>Radial dispersion coefficient</b>	$D_r = \frac{1}{N-1} \sum_{k=1}^{k=N-1} \frac{\sum_{i=1}^{i=n} (r_i^{k+1} - r_i^k)^2}{(t^{k+1} - t^k)n}$ (8.3)	$D_r = \frac{1}{N-1} \sum_{k=1}^{k=N-1} \frac{(r^{k+1} - r^k)^2}{(t^{k+1} - t^k)}$ (8.4)

For the DEM simulations, the coefficients of dispersion were calculated using the displacement in the axial and radial directions, after each period of rotation, for all the particles in the system over a total of 15 periods. For the PEPT experiments a single tracer was used and the dispersion coefficients were calculated by using the displacement in the axial and radial direction considering about 1200 shaft rotations. For the DEM simulation spherical particles were modelled with DEM input parameters considered to be representative of the glass beads used in the PEPT mixing experiment. In Figure 8.1 the results from DEM simulations and the PEPT experiments are compared.

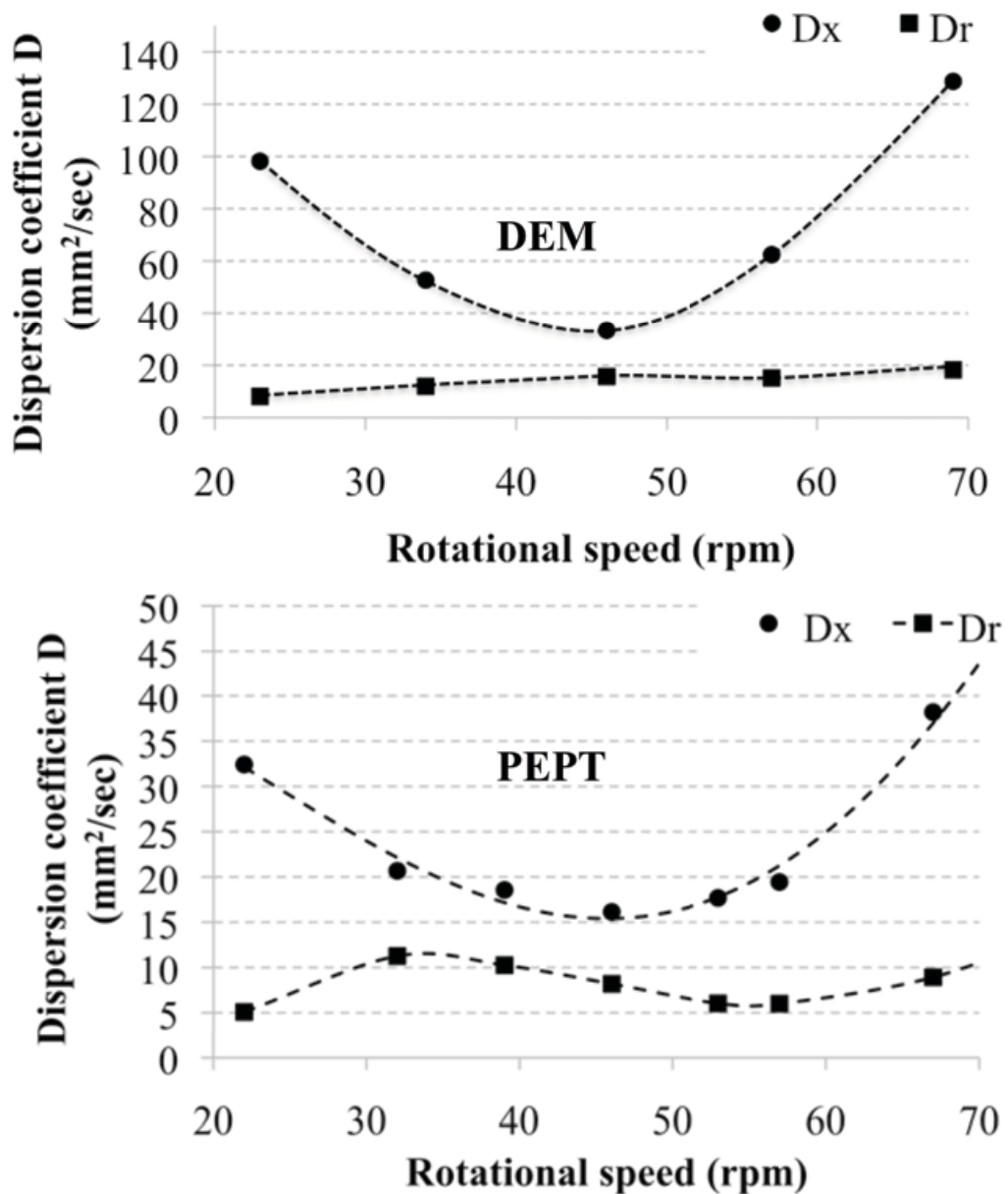


Figure 8.1: Comparison of axial and radial dispersion coefficients,  $D_x$  and  $D_r$ , for DEM and PEPT as a function of speed.

Similar trends for both axial and radial dispersion coefficients were seen between DEM simulations and PEPT experiments. In both cases the axial dispersion coefficients was always much greater than the radial. One of the reasons could be the choice of the DEM input parameters, hence a sensitivity analysis for the input parameters was carried out. Also, the

differences between the DEM simulation and the PEPT experiments might be magnified by the square of the difference in the calculation for the dispersion coefficients. Therefore, the net displacements in the axial and radial directions,  $x'-x$  and  $r'-r$ , after each period of rotation were used.

### **8.1.2 Comparison of particle movement in axial direction: peak frequency distribution and average plateau periods length**

As previously reported the particle movement in the axial direction (from one peak to the following peak) periodically alternated with a period of no particle movement in the axial direction (plateau) during the inversion of the vessel for both DEM simulations and PEPT mixing experiments. As shown in Chapters 5 and 7, in the DEM simulations the axial position for 10 selected particles was recorded at different speeds and the peak frequency distributions were calculated (peak calculated as “axial displacement”) over 15 shaft rotations. In the PEPT experiments, the single glass bead tracer particle was followed and the distance travelled in axial direction  $x$  between each peak “axial displacement” was also calculated over about 1200 shaft rotations. The comparison between peak frequency distributions is presented in Figure 8.2.



From these previous plots, some differences in values can be highlighted. However, it can be noted that for both the DEM simulation and the PEPT experiments, increasing the speed resulted in a narrower distribution for such peaks. The differences might be related to the nature of the comparison between the DEM simulations, where 10 particles are selected and followed for 15 rotations, and the PEPT experiment where one single glass bead tracer was employed over about 1200 shaft rotations.

For both DEM simulations and experimental results, during the motion of the vessel, there were periods during which the particles alternated between axial movement, relative to the cylinder axes, and static periods. In Figure 8.3, the average length of such static periods for the 10 selected particles in DEM and PEPT single tracer particle is plotted as a function of speed. It can be observed that by increasing the speed the bed movement in the axial direction resulted in shorter static periods for both DEM simulations and PEPT experiments.

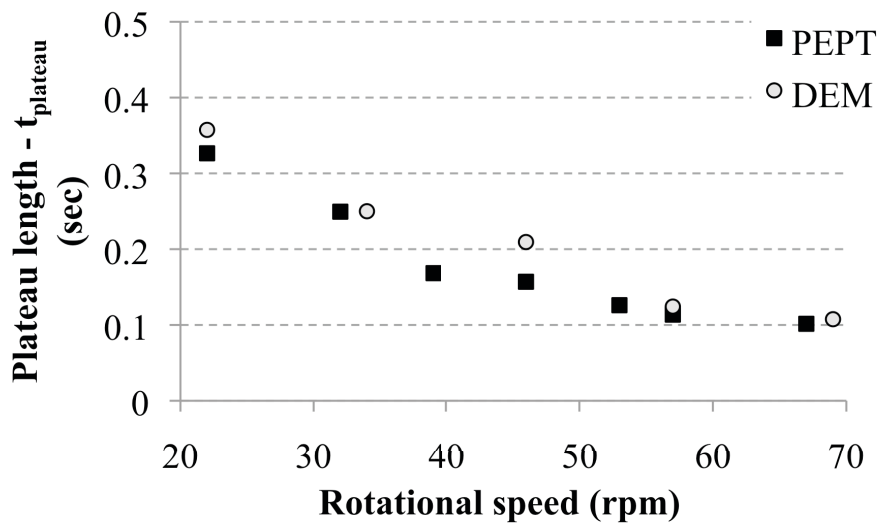


Figure 8.3: Average length of plateau periods for DEM simulations and PEPT experiments.

## 8.2 DEM input parameters sensitivity analysis for operating 3 speeds: 23, 46 and 69 rpm

It has been shown that some similarities exist between the DEM simulations and the predictions, however, differences were shown in terms of absolute values. DEM input parameters were varied in order to assess their influence on the magnitude of discrepancies between the simulations and experimental data. The analysis of the influence of the input parameters should also give some indications regarding the hypothesised change in bed behaviour with the operating speed, since their influence should be different as a function of the mixing mechanisms occurring. A number of simulations have been run in order to investigate the effect of the choice for the EDEM input parameters. Table 8.2 lists the set of EDEM input parameters for simulation using 2 mm monosized and three operating speeds: 23, 46 and 69 rpm.

Only the static and rolling friction coefficients and particle-particle coefficient of restitution were varied in the simulations *A* to *G*. The rest of DEM input parameters were the same used in Chapters 5 and 6.

Table 8.2: EDEM input parameters for sensitivity analysis.

<b>Parameter</b>	<b>Base</b>	<b>A</b>	<b>B</b>	<b>C</b>	<b>D</b>	<b>E</b>	<b>F</b>	<b>G</b>
$\mu_{s,pp}$	0.5	0.5	0.5	<u>0.7</u>	<u>0.25</u>	<u>0.25</u>	<u>0.25</u>	<u>0.25</u>
$\mu_{r,pp}$	0.01	<u>0.1</u>	<u>0.001</u>	0.01	0.01	<u>0.001</u>	<u>0.001</u>	<u>0.001</u>
$\mu_{s,pw}$	0.35	0.35	0.35	0.35	0.35	<u>0.25</u>	<u>0.25</u>	<u>0.25</u>
$\mu_{r,pw}$	0.005	0.005	0.005	0.005	0.005	<u>0.001</u>	<u>0.001</u>	<u>0.001</u>
$\epsilon_{pp}$	0.75	0.75	0.75	0.75	0.75	0.75	<u>0.85</u>	<u>0.45</u>
$\epsilon_{pw}$	0.75	0.75	0.75	0.75	0.75	0.75	0.75	0.75
<i>Speed</i> (rpm)	23,46, 69							

The term “*base*” refers to the original input parameters used in the simulations reported in Chapters 5 and 6.

### 8.2.1 Effect of input parameters on distribution of $x'-x$ and $r'-r$

The distribution of the net displacements,  $x'-x$  and  $r'-r$ , used in Eq.(8.1), Eq.(8.2), Eq.(8.3) and Eq.(8.4), were compared between the PEPT experiments and DEM simulations using different values for the input parameters.

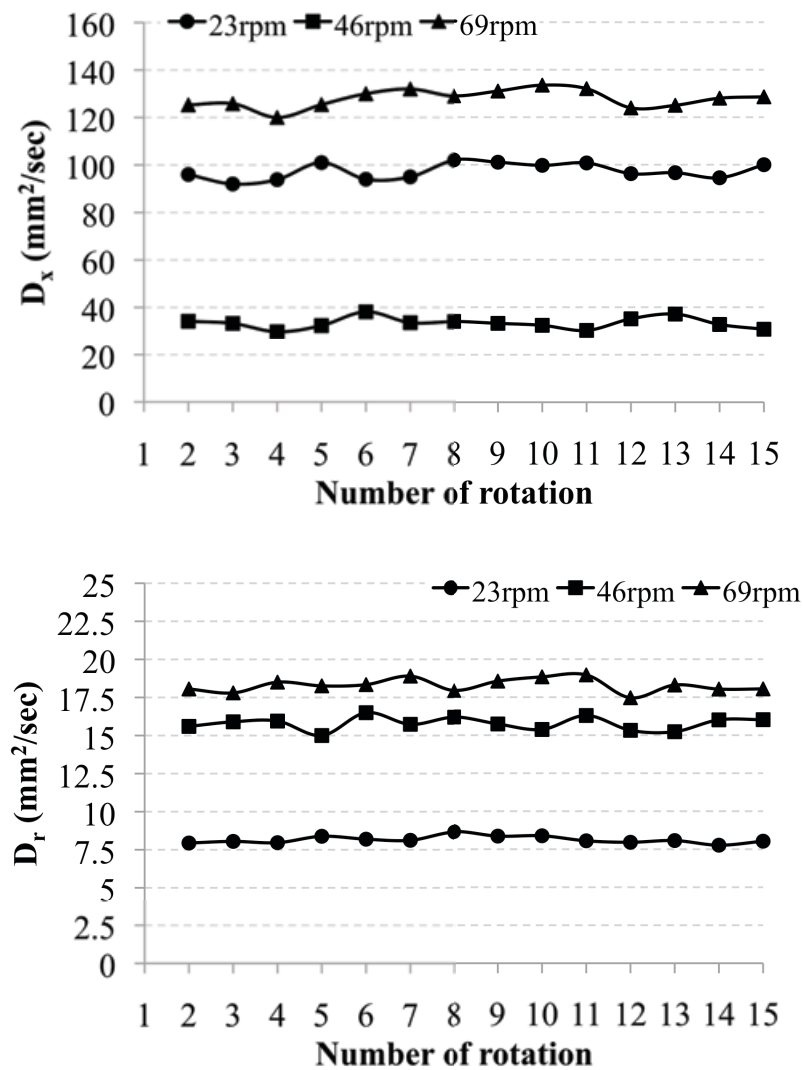


Figure 8.4:  $D_x$  and  $D_r$  from rotation 2 and 15 for the “*base*” case.

Due to computational time restrictions only three periods of motion, between rotation 2 and 5, were used to compare the statistics for the distribution  $x'-x$  and  $r'-r$  from the DEM simulation for the different input parameters versus the PEPT results.

The coefficients of dispersion  $D_x$  and  $D_r$ , for the “base” simulation, were plotted between rotations 2 and 15 in Figure 8.4. The two dispersion coefficients seemed to be fairly constant; therefore indicating that using only three periods of rotation was acceptable for the determination of  $x'-x$  and  $r'-r$  distributions. In the first rotation the particle bed started from a static position, and therefore this part of the cycle would not be representative. Thus, the first cycle was not used for these calculations.

For the simulations with the different sets of input parameters and the PEPT experimental results the distribution of  $x'-x$  and  $r'-r$  are plotted for the different speeds in Figure 8.5 and Figure 8.6. For all the cases considered the results for the DEM simulations never matched the ones obtained in the experiments, particularly for the distribution of  $x'-x$ . The distribution of  $x'-x$  and  $r'-r$  were narrower for the PEPT experiments when compared to the DEM simulations. This led to the high difference between DEM and PEPT results when Eq.(8.1), Eq.(8.2), Eq.(8.3) and Eq.(8.4) were used to calculate  $D_x$  and  $D_r$ .

Although these differences existed, again the distribution of  $x'-x$  and  $r'-r$  showed some comparable trends between DEM simulations and PEPT experiments, as later discussed. At 23 rpm and 46 rpm, the choice of a higher value of the coefficient of rolling friction seemed to have a major impact in terms of net displacement  $x'-x$  after each period of rotation. This also had implications on the mixing efficiency (characteristic number of rotation) as later demonstrated.

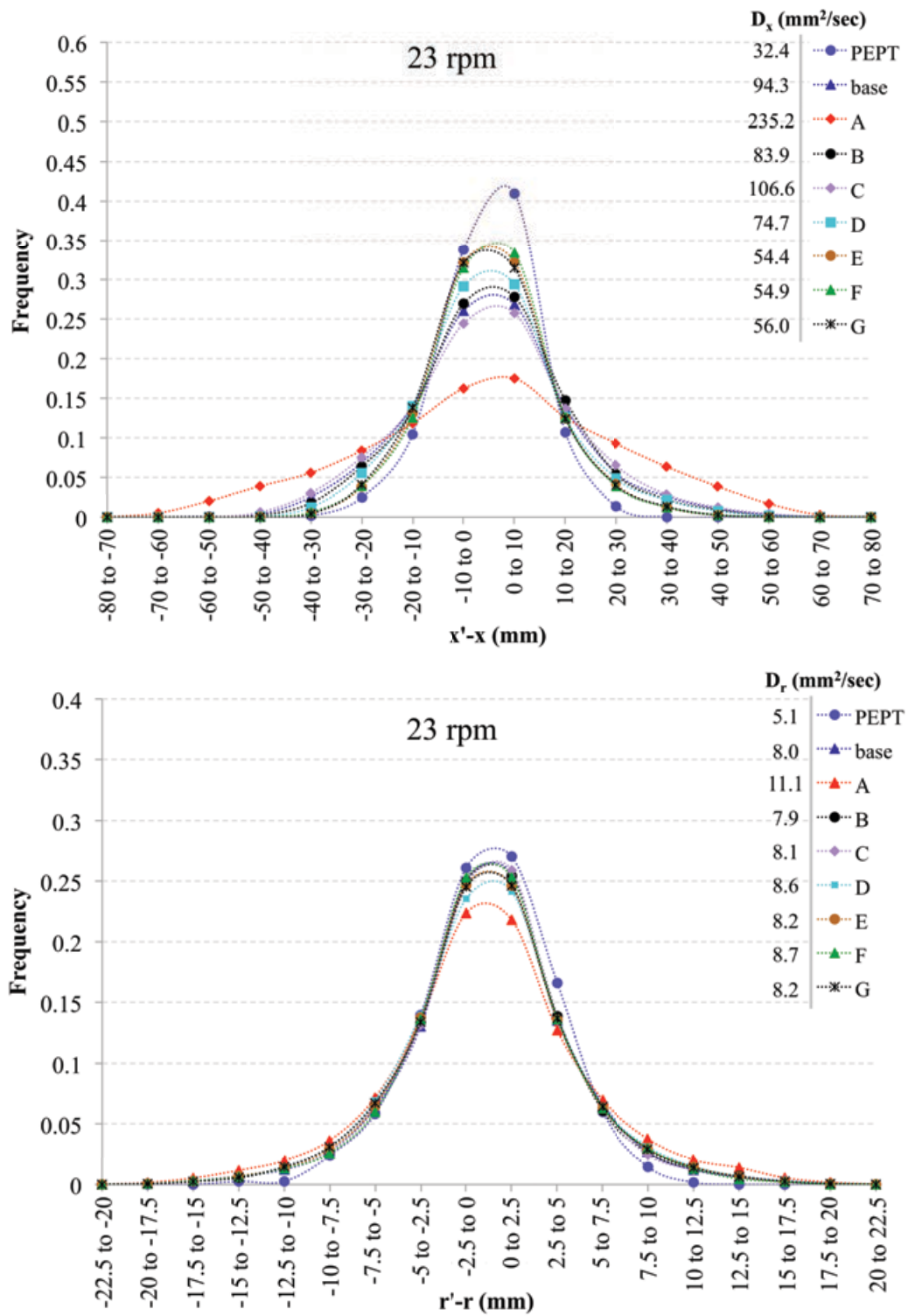


Figure 8.5: Comparison of  $x'-x$  and  $r'-r$  distributions, DEM simulations and PEPT at 23 rpm.

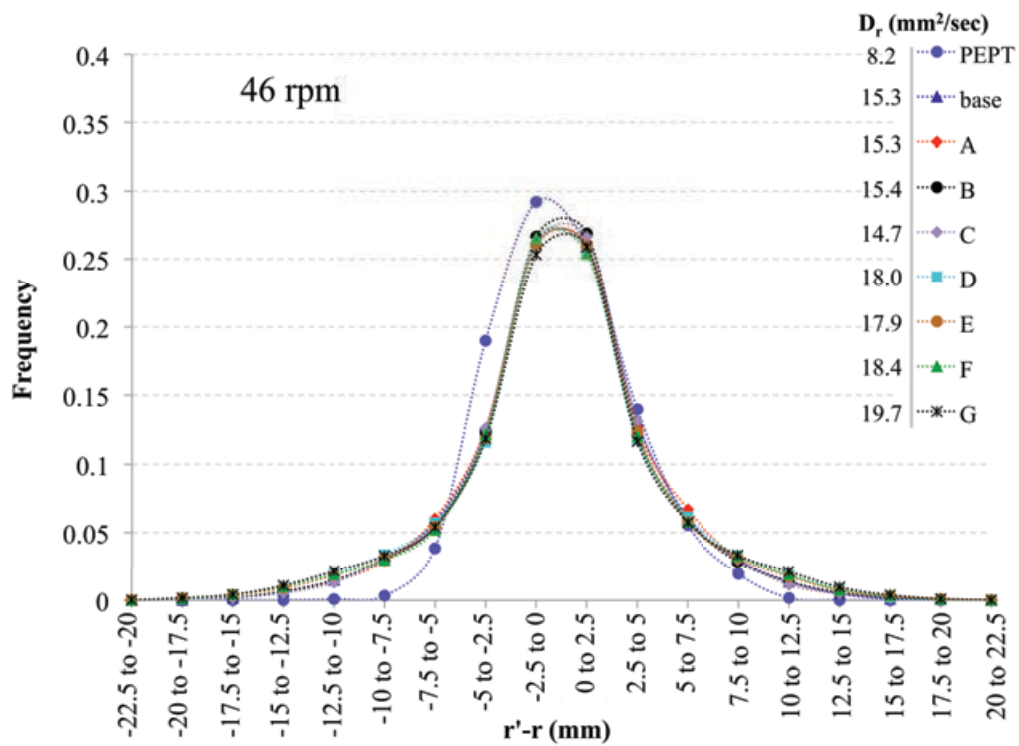
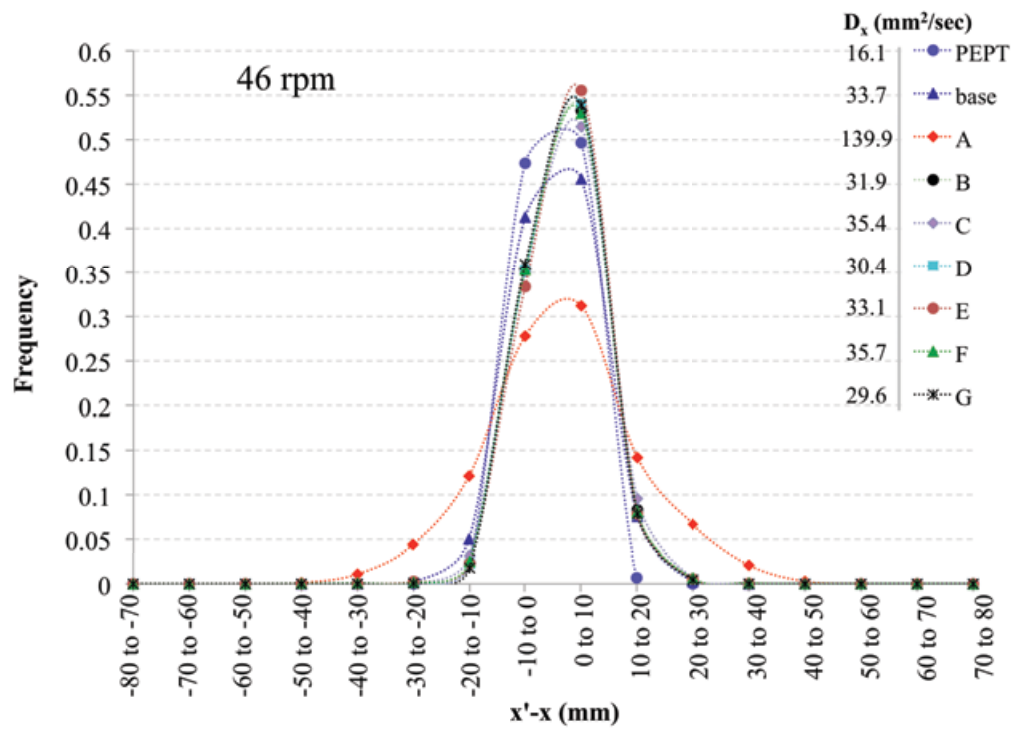


Figure 8.6: Comparison of  $x'-x$  and  $r'-r$  distributions, DEM simulations and PEPT at 46 rpm.

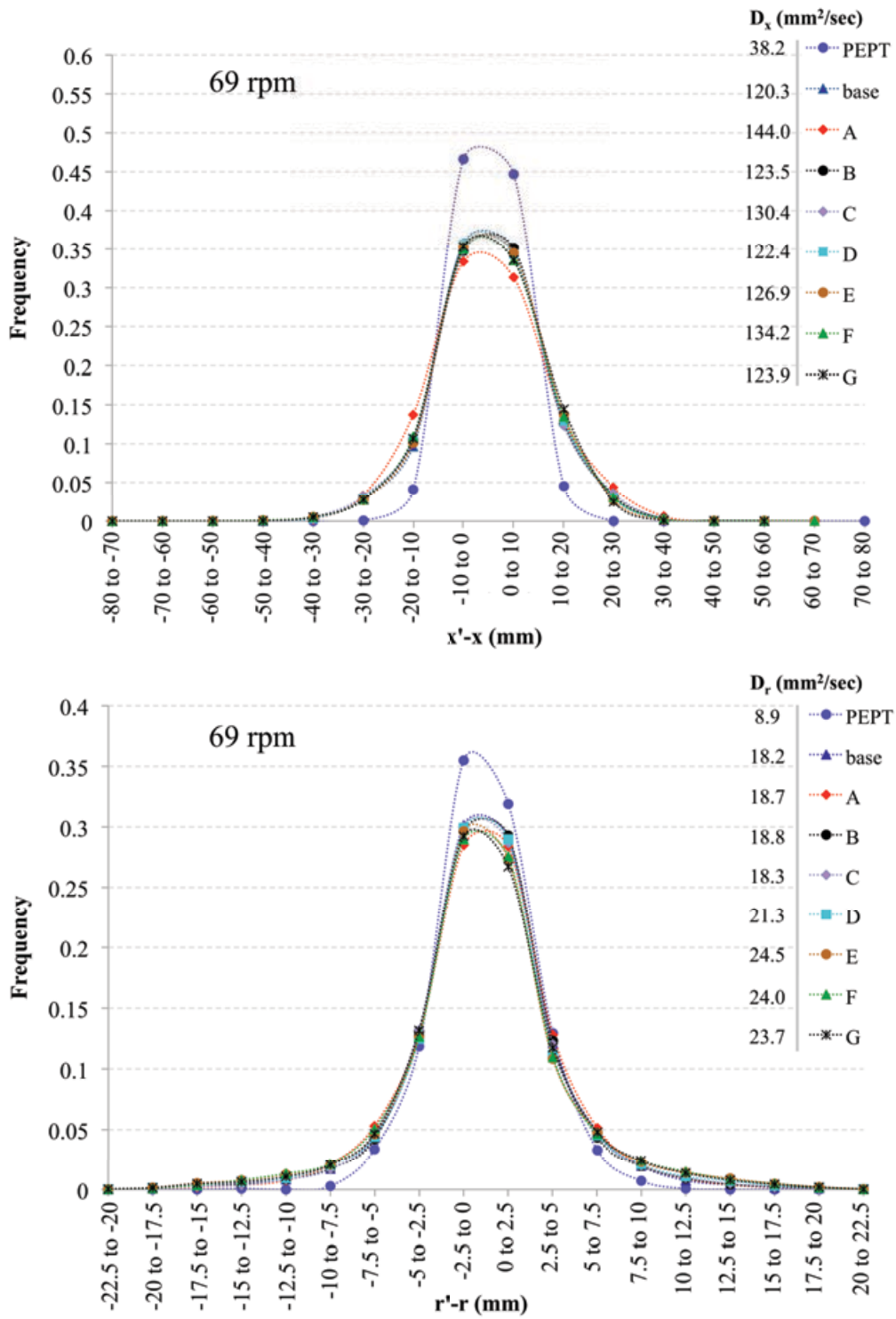


Figure 8.7: Comparison of  $x'-x$  and  $r'-r$  distributions, DEM simulations and PEPT at 69 rpm.

The actual values obtained for  $x'-x$  and  $r'-r$  were again different between PEPT experiments and DEM simulations. Again however, the trends seen when comparing  $x'-x$  and  $r'-r$  at

different rotational speeds were similar between PEPT experiments and DEM simulations as illustrated in Figure 8.8 and Figure 8.9.

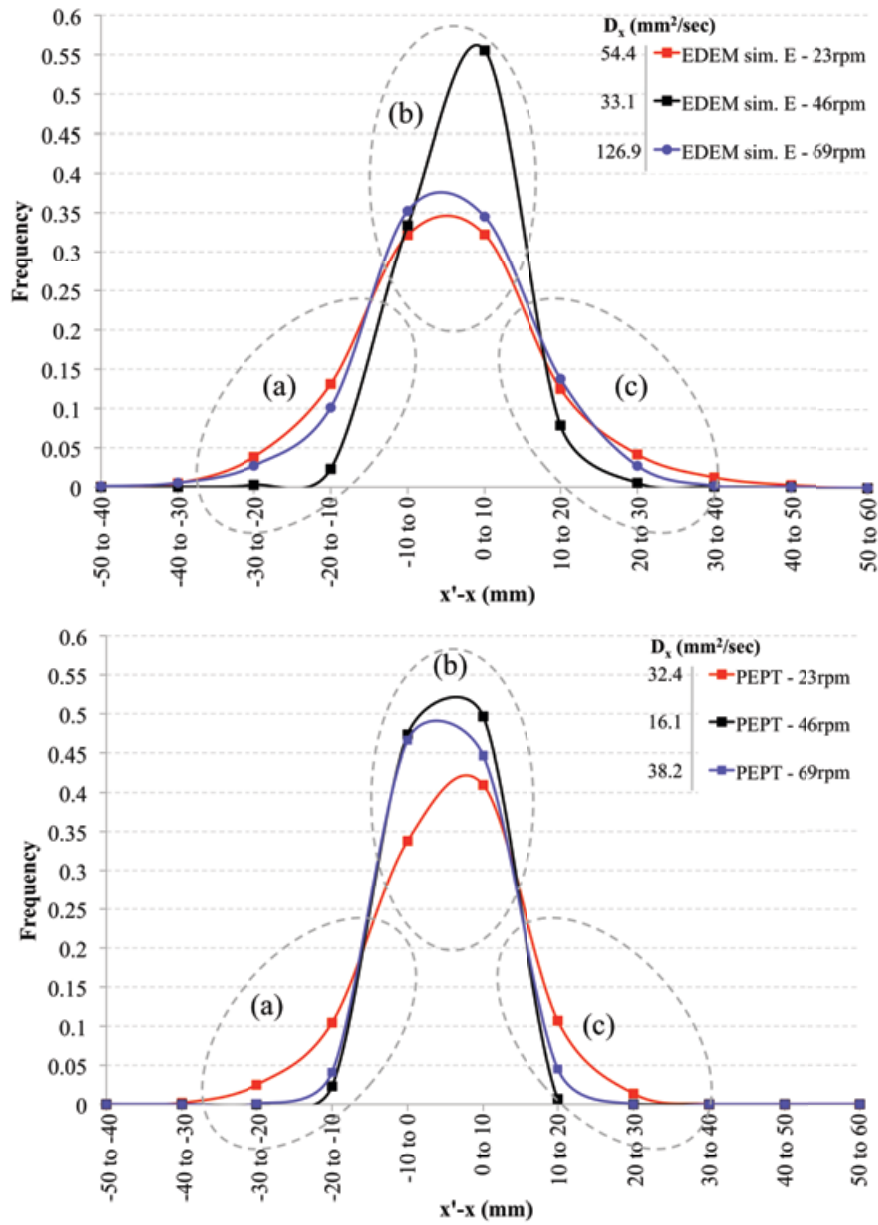


Figure 8.8: Comparison of  $x'-x$  distributions for DEM simulations (*case E*) and PEPT.

In Figure 8.8, the trends for  $x'-x$  for the case *E* in the DEM simulations and PEPT experiments are similar in the three regions (a), (b) and (c) highlighted. For both simulation

and experiments, 46 rpm presented the highest peak and narrower distribution for  $x'-x$ , followed by 23 rpm and 69 rpm. Similar trends can also be observed regarding the tails of the distributions. The wider distribution for the 23 rpm and 69 rpm corresponded to a much larger value for the coefficient  $D_x$  for the 23 rpm and 69 rpm when compared with the 46 rpm case.

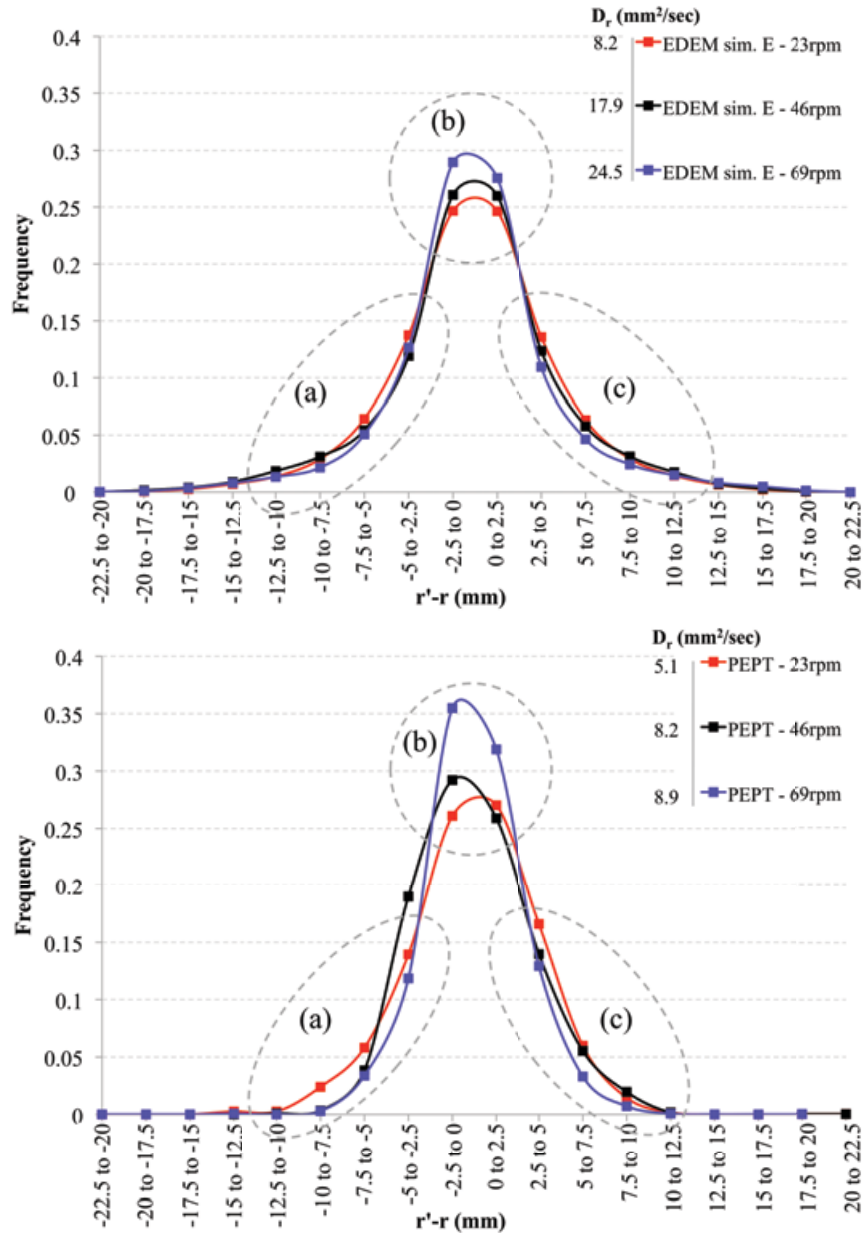


Figure 8.9: Comparison of  $r'-r$  distributions for DEM simulations (*case E*) and PEPT.

In Figure 8.9 the trends for  $r'-r$  for the case  $E$  in the DEM simulations and PEPT experiments are compared. In region (a) there are some differences between the simulations and the experiments. However, in region (b) the maximum frequency reached is highest at 69 rpm, followed by 46 rpm then 23 rpm, for both the simulations and the experimental results. Similarly in region (c) the trends are comparable with the 69 rpm presenting the narrowest distribution followed by the 46 rpm.

### 8.2.2 Effect of input parameters on the segregation index $S$

The effect of the choice for the DEM input parameters were investigated in terms of segregation index and mixing efficiency. As showed in Chapter 5, for monosized particle the segregation index can be fitted with an exponential law, Eq.(8.5). For the considered system, when random mixing was achieved the segregation index plateaued to a value,  $S_\infty$ , that equals to 1.

$$S_{fit} = S_\infty + (S_0 - S_\infty)e^{-N_R / N_{mix}} \quad (8.5)$$

The previous equation can be plotted in a linear form by taking the logarithm of both sides of the equation.

$$\ln(S_{fit} - S_\infty) = \ln(S_0 - S_\infty) - \frac{N_R}{N_{mix}} \quad (8.6)$$

Therefore, from Eq.(8.6),  $\ln(S_{fit}-S_\infty)$  can be plotted against number of rotation  $N_R$  to compare the effect of the choice for the DEM input parameters for the first three periods of motion. In Figure 8.10, Figure 8.11 and Figure 8.12 the comparison between the segregation indices for the different choice of input parameters are shown for the different speeds. Only the first three periods of rotations were considered for the comparison since fast macro mixing occurred as

shown in Chapter 5. The characteristic number of rotation  $N_{mix}$ , inverse of mixing efficiency (ref. Chapter 5), was determined by minimisation of the sum of squares of the difference between the segregation index determined from the simulation during the first three period of rotation and the exponential decay law Eq.(8.6). For the calculation the value of  $S_\infty$  was superimposed to be equal to 1.

It is interesting to highlight that the choice of input parameters had a different effect depending on the speed. From the comparison, it seemed that for the lowest speed, 23 rpm, the choice of input parameters had a major effect. In particular, the choice of a high value for the coefficient of rolling friction seemed to improve the rate of mixing.

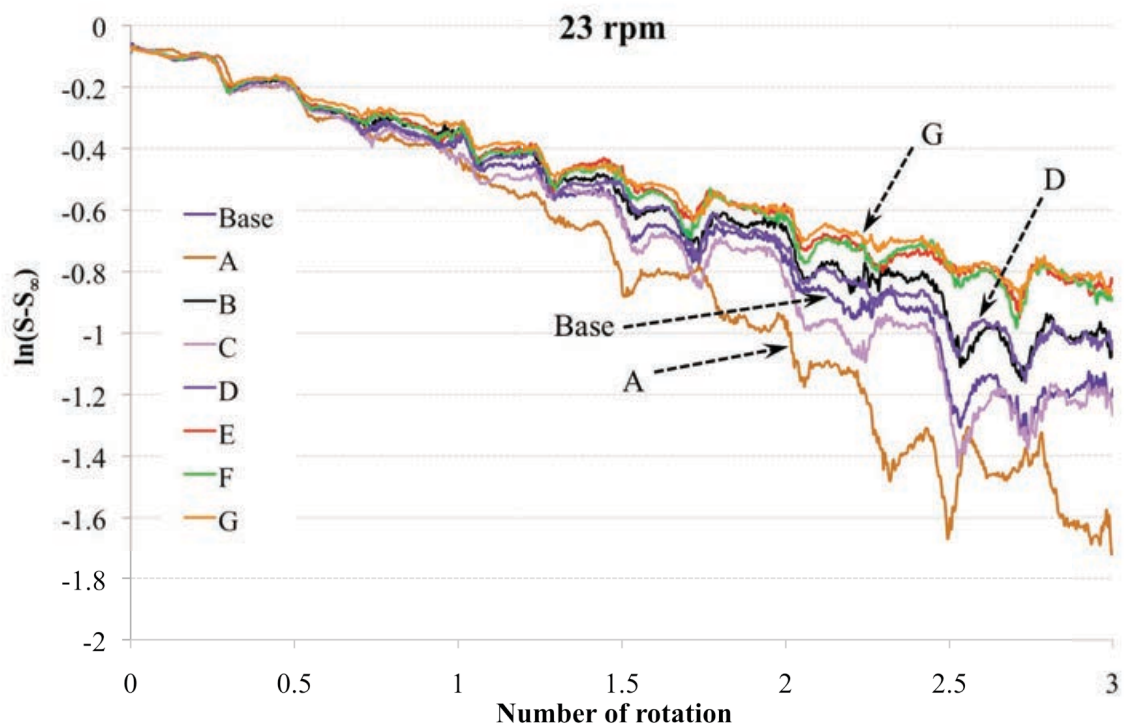


Figure 8.10: Effect of DEM parameters on  $\ln(S_{fit} - S_\infty)$  with number of rotation  $N_R$  for 23 rpm.

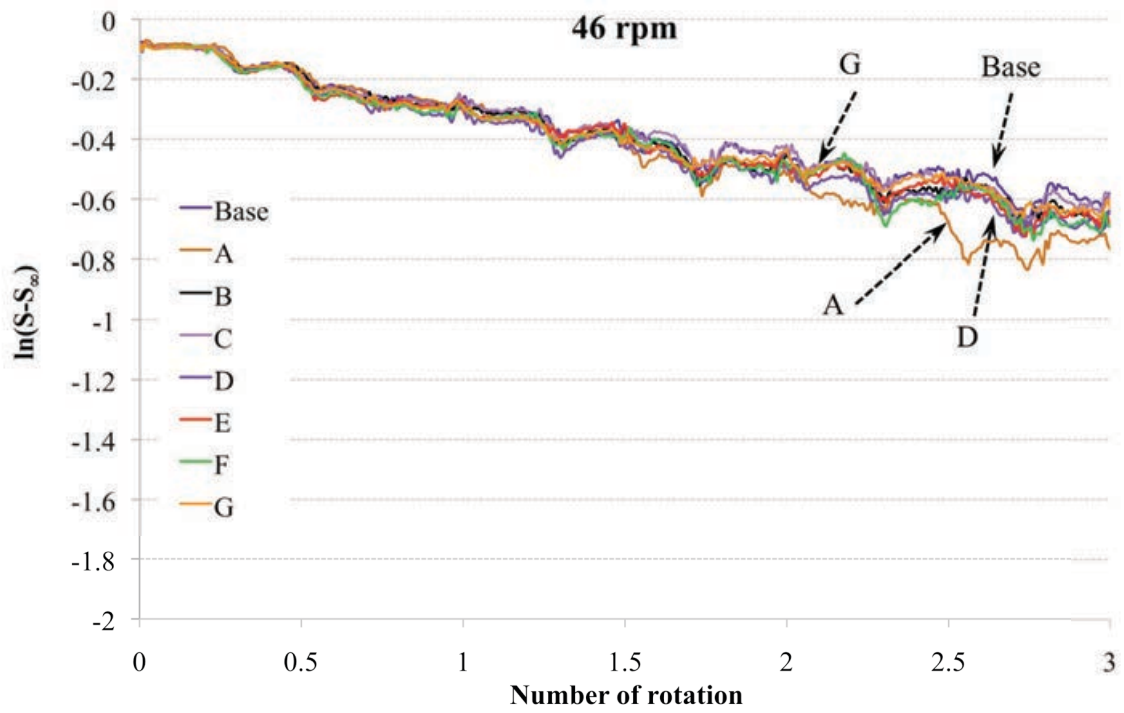


Figure 8.11: Effect of DEM parameters on  $\ln(S_{fit} - S_{\infty})$  with number of rotation  $N_R$  for 46 rpm.

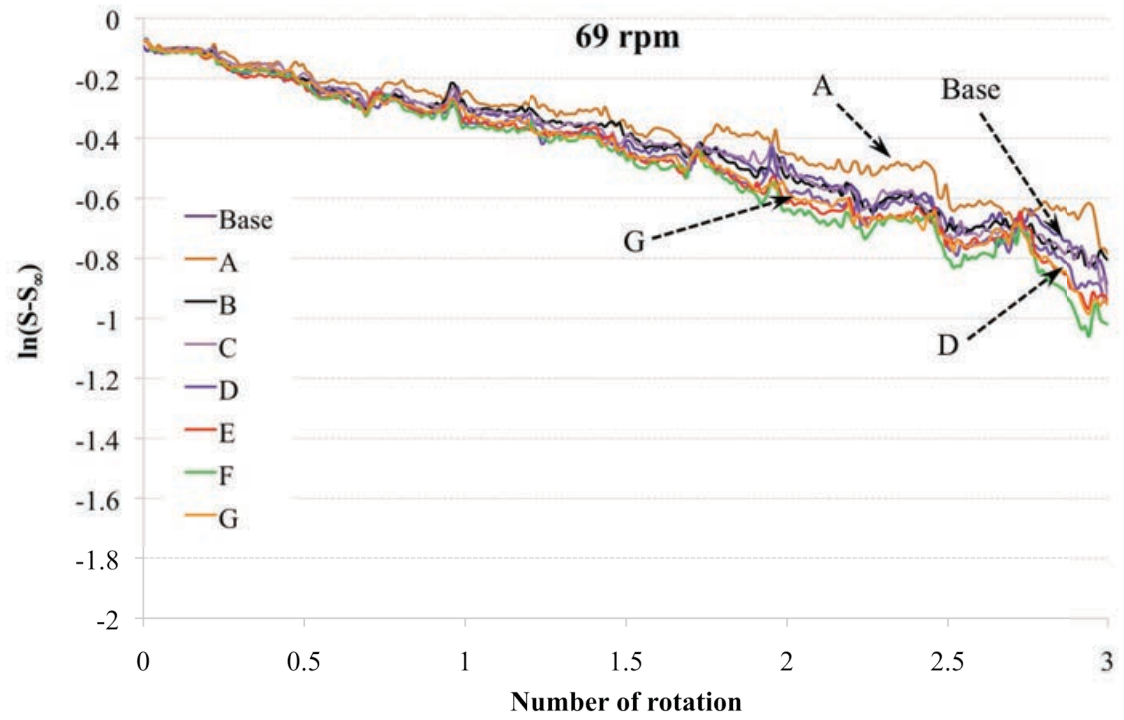


Figure 8.12: Effect of DEM parameters on  $\ln(S_{fit} - S_{\infty})$  with number of rotation  $N_R$  for 69 rpm.

As visually seen in the previous plots, varying the DEM input parameters within the selected range resulted in a change of the segregation index (in terms of characteristic number of rotation  $N_{mix}$ ) for the different speeds considered.

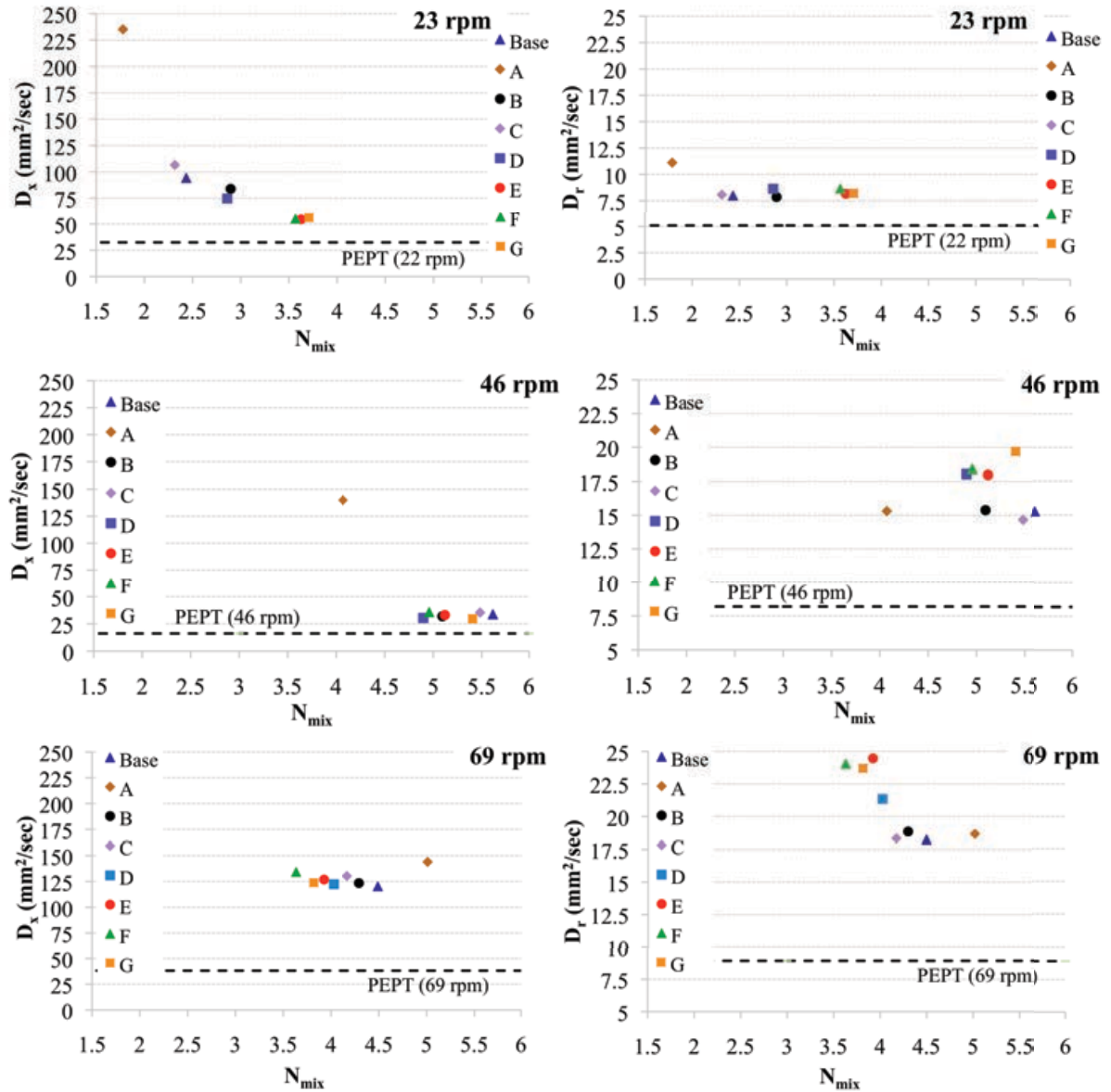


Figure 8.13: Effect of DEM input parameters for the axial and radial coefficients of dispersion,  $D_x$  and  $D_r$ , against characteristic number of rotations for different operating speeds. The dotted line represents the PEPT experimental values for  $D_x$  and  $D_r$ .

The choice of input parameters clearly had a different effect for the three speeds. This probably indicated that the mixing mechanisms in axial and radial directions were different and were functions of the operating speed. Figure 8.13 shows the effect of the choice of DEM input parameters for the coefficients  $D_x$  and  $D_r$  against the characteristic number of rotations  $N_{mix}$  (inverse of the mixing efficiency). The value for the coefficients of dispersions for the PEPT results is also shown as dotted line. For the PEPT results it is not possible to calculate the corresponding characteristic number of rotations, hence for this comparison the dotted line was plotted over the all values for  $N_{mix}$  shown in the graph.

In all of the cases analysed the coefficients of dispersions predicted by DEM simulations did not have values comparable with the PEPT experimental results. Only  $E$ ,  $F$  and  $G$  at 23 rpm, the choice of input parameters seemed to give a value of the coefficient of dispersion  $D_x$  similar to the PEPT results. However, that was not valid for the coefficient  $D_r$ . For the different operational speeds the effect of changing the input parameters had a different impact on the coefficient of dispersion and mixing efficiency. It is interesting to note that for the 23 rpm operational speed, the coefficient of dispersion increased and the mixing efficiency increased, if compared to the base case, when the highest value for coefficient of rolling friction was chosen, *case A*. For the highest rolling friction, *case A*, at 46 rpm, the dispersion coefficient in the axial direction increased if compared to the *base case*. For the other cases considered the dispersion coefficient was quite similar to the *base case*. However, at 46 rpm the coefficient of dispersion in the radial direction became much larger compared with the *base case*. At 69 rpm, the different choice for the DEM input parameters did not have much effect on the axial dispersion coefficient. Conversely, there was again a difference in the pattern for the coefficient in the radial direction at the 69 rpm speed. Again, there were differences in the influence of the DEM input parameters between operating speeds This

might indicate that there was change in the bed behaviour and mixing mechanisms since the choice of the input parameters had different influences. However, the dispersion coefficients predicted by DEM simulations still not match the experimental results. The summary for all the dispersion coefficients  $D_x$  and  $D_r$  for the base case, PEPT and sensitivity analysis is reported in Table 8.3.

Table 8.3: Summary dispersion coefficients  $D_x$  and  $D_r$  from sensitivity analysis.

Speed (rpm)		PEPT	Base	A	B	C	D	E	F	G
23	$D_x$ (mm <sup>2</sup> /sec)	32.4	94.3	235.2	83.9	106.6	74.7	54.4	54.9	56.0
	$D_r$ (mm <sup>2</sup> /sec)	5.1	8.0	11.1	7.9	8.1	8.6	8.2	8.7	8.2
46	$D_x$ (mm <sup>2</sup> /sec)	16.1	33.7	139.9	31.9	35.4	30.4	33.1	35.7	29.6
	$D_r$ (mm <sup>2</sup> /sec)	8.2	15.3	15.3	15.4	14.7	18.0	17.9	18.4	19.7
69	$D_x$ (mm <sup>2</sup> /sec)	38.2	120.3	144.0	123.5	130.4	122.4	126.9	134.2	123.9
	$D_r$ (mm <sup>2</sup> /sec)	8.9	18.2	18.7	18.8	18.3	21.3	24.5	24.0	23.7

### 8.3 Conclusions

This chapter is concerned with the comparison between DEM simulation using different input parameters and PEPT experimental result for the particle behaviour in a Turbula mixer. The DEM simulations using the Hertz Mindlin contact model captured the major features for the particles motion regarding the parameters used for the comparison. However, the DEM predicted dispersion coefficients always exceed the measured ones. The values obtained from the simulations were about 50% higher than the PEPT when using physically reasonable

simulations input parameters. An investigation of the effect for the choice for such parameters was carried out. Although, some of the experimental trends were reproduced with the simulations there was still a lack of agreement between the absolute values. It seemed that the DEM simulation always exceeded the PEPT results in terms of particle movement in axial and radial directions. However, by using different input parameters some interesting observations were made regarding the change of their effect as a function of speed. It was observed that depending on the speed their influence on the dispersion coefficients in axial and radial direction was different. This could be indicative that different mixing mechanisms were occurring in axial and radial directions as consequences of the different mixing flows, probably dilated granular flow at lower speed and inertial chaotic flow at the higher speed.

## Chapter 9

### Conclusions: results and summary

*The main objective of this project was to understand the capabilities and the limitations of applying Discrete Element Method (DEM) to real industrial applications. This was done by comparison between a computational approach to study particle mixing and experimental results obtained from single particle tracking in a laboratory scale mixer, the Turbula mixer, which presented a challenge regarding the complex motion. Here, the outcomes from a preliminary investigation of solids mixing modelled using a DEM approach has been presented. The data suggest some interesting and as yet unpredicted behaviour on the basis of different mixing motions. The study of the particle motion within the vessel has been carried out through the radioactive PEPT technique and the DEM numerical simulations technique, considering each particle as a single element.*

#### 9.1 Results

The use of Discrete Element Method (DEM) to study and understanding complex particulate systems has increased considerably over the last few decades. The use of such technique has been exploited in a number of applications, both academically and industrially. In some occasions DEM has proved to be an exceptional tool for equipment design, where for example, the use of different equipment geometry designs were studied. However, the full application of DEM as a predictive tool for real scale industrial systems is not possible yet

due to the intrinsic DEM limitation such as particle size, particle shapes and often simplistic contact models which do not consider interparticle forces (capillary forces, electrostatic forces, Van der Waals forces). Another important issue for the DEM application regards the definition of the simulation input parameters. In the literature a methodology for determining the DEM input parameters is not clearly reported, in particular, for small particles. In this work, an example of material mechanical characterisation for the small ZSM5 zeolite particles was carried out. Different powder characterisation techniques were employed to characterise the flow behaviour for the material, showing exceptional flowability. Single particle compression and indentation techniques showed the high value for the reduced elastic Young's modulus, strength and hardness for the material considered. Bulk compression for the material showed its low compressibility. Some of the determined properties for the zeolite were used to show the computational limitations and the unfeasible simulation time for the modelling of mixing of zeolite particles in a Turbula mixer, when a high number of small particles with high shear modulus were considered. Therefore, a model system using larger spherical particles was used to simulate the mixing, and the simulations were compared with PEPT mixing experiments using "model" spherical glass beads. The Turbula motion was measured by PEPT and it was imported into the DEM code. It has been shown that both rotational and translational motions of the cylindrical vessel within the mixer can be reconstructed through tracking three rigid points on the corners of the solid cage. It was also shown that only one tracked point was sufficient to describe the motions as a result of the geometrical symmetry in the Turbula motion. The complex measured motion was used to carry out DEM simulations under different conditions by looking at the effect of mixing speed and filling patterns on particle mixing at a constant fill level, with uniform spherical monomodal and bimodal sized spherical particles.

For the monosized particles the influence of a range of operational speeds revealed that the mixing behaviour changed non-monotonically as a function of mixer speed. The segregation index calculated from DEM simulations was used to determine the characteristic number of rotations and mixing time. These experiments revealed that the number of mixer revolutions needed to achieve complete mixing, initially increased with the increase in speed (from 23 rpm to 46 rpm) and subsequently decreased with the further increase in speed. This was probably indicative of a transition in the bed behaviour with speed (from 46 rpm to 69 rpm). The decline in mixing efficiency with the initial increase in speed correlated well with a similar trend in axial dispersion coefficient. However, due to the complexity of the Turbula motion, difficulties still remained in the formulation of a complete explanation for the interesting unpredicted behaviour. The results from the Turbula simulations were also compared with a cylindrical vessel undergoing two simpler motions, such as a rotating drum and a hoop mixer. As extensively reported in literature for the rotating drum, the radial mixing was observed to be the dominant mixing mechanism whereas axial mixing was very slow, being purely a dispersive mechanism. With the hoop mixer it was observed that the rocking motion caused mixing in the axial direction and that the overall mixing efficiency depended on the operating speed. The axial mixing in the hoop mixer improved with speed whereas the radial mixing slightly decreased as the speed increased.

Positron Emission Particle Tracking (PEPT) was then used to follow particle tracer trajectories during mixing experiments using the Turbula mixer under comparable conditions used in the Turbula DEM simulations. As with DEM, monosized glass bead particles were used. PEPT showed narrower distributions of the net axial displacement per shaft rotation with increasing speed. Axial periodic particle movements alternated with static periods were also observed. These observations from PEPT experiments were qualitatively in agreement

with DEM simulations. Also, for the experiments, a minimum value for the axial coefficient was measured at the middle speed of 46 rpm, confirming the DEM observations. The axial and radial occupancy plots from the PEPT experiment, also revealed that the tracer particle tended to concentrate in two core regions of the vessel when the mixer speed was increased from 22 rpm to 46 rpm. When the speed was further increased these two cores tended to disappear. The experiments, therefore, showed a non-linear pattern for the occupancy plots with speed, implying a possible transition in the bed behaviour. The experimental results, therefore, validated the DEM predictions in terms of possible bed transition as a function of operating speed for monosized particles. As stated, the DEM model, for the Turbula mixer, captured the major trends for the parameters used to characterise the particle bed motion but differences in absolute values were seen, with the predicted dispersion coefficients being always higher than those measured by PEPT. The change of the choice for the DEM input parameters revealed some effects on the characteristic number of rotations and dispersion coefficients in particular regarding their different effect for the different speeds, probably confirming the idea of different mixing mechanisms occurring in axial and radial directions as a function of speed. Changing the DEM input parameters never resulted in achieving coefficients which matched the PEPT values, but trends were generally reproduced between simulations and experiments. PEPT experiments were also applied to study the flow of a system using zeolite catalyst support material, which revealed a quite different mixing behaviour if compared to the “model” glass beads. The axial and radial dispersion coefficients together with the occupancy plots showed different trends compared with the model material. A much greater value for the dispersion coefficient in the axial direction was also observed. This could perhaps be associated with a much higher mobility for the tracer particle for this particle bed. There are clear difficulties in relating the behaviour for the two materials. This

reinforces the idea that, modelling ideal systems and extending some understanding to a more complex system can be challenging. In order to tackle the issue of particle mixing for real particles it is necessary to enhance DEM modelling capabilities by being able to model systems with smaller, larger number of particles and with real shapes.

DEM simulations were also used to model a system considering bimodal sized spherical particles and the effect of operating speed was analysed for the axial filling. For this system, good qualitative agreements were found between DEM simulations and MRI experimental data from literature with a formation of a core of small particles within the centre of the bed. It was also shown, as previously reported in the literature, that the mixing quality improved as a function of the operating speed. In addition, it was demonstrated that the design of a simple baffle could improve the mixing and avoid the formation of the small particle central segregated volumes within the particle bed.

## **9.2 Summary**

Particle technology is critical in many industries. In the chemical industry, about 75% of manufacturing processes involve the use of solid particles. As in many other parts of the chemical industry, in Johnson Matthey a number of different operations involve particle technology, for example, mixing, precipitation, impregnation, filtering, washing, drying, forming and thermal processing. Often systems involving particulate systems show difficult and unpredictable behaviour resulting in inefficiencies. Improving processes involving complex particulate systems could result in higher product yield, more consistent quality products, faster production, lower energy usage and economical improvements.

One of the most interesting tools, which may be used to address some of the problems related to particle processing is probably the DEM numerical technique. Some comments regarding its application are as follows.

- DEM can be used to describe granular problems considering each particle as a discrete discontinuous element within the system. DEM simulations are widely reported for large scale particles. Limitations of particle size are mainly due to computational limitations due to the combination of the high number of particles to be considered and the effect of the small timestep.
- There are some limitations regarding the representation of particles with simplified spherical discrete elements. Different approaches using representation of complex shapes are being developed, however, there is still a need to develop and validate relationships between the local constitutive laws depending on the shapes of the discrete elements. By using a multiple sphere approach there is a limitation on computational effort due to the increased complexity due to the large number of spheres considered in the simulations.
- Clear limitations regarding the determination or the choice of the input parameters for the simulations with different materials still make DEM a tool for simplified systems which user consider “model” particles such as glass beads. A methodology for gathering the input parameters is not clearly defined, especially for small particles.

Regardless the issues reported above, this modelling technique for granular materials is growing considerably, mainly in academic research but also in industry. Many DEM modelling results have shown that these kind of simulations reproduce experimental results well, giving new understanding of the behaviour of granular systems. This is mainly true for simpler systems that consider large spherical particles. However, new developments and advancements of both computer hardware and DEM software is resulting in a continuously

more extensive applications of this modelling technique for the exploration of more complex applications.

In this thesis, it has been demonstrated that the DEM simulation technique can be used for complex granular motion of particles in mixing vessels. The capability of DEM to model the mixing in complex systems such as the Turbula mixer was examined. A DEM numerical evaluation and a PEPT experimental validation have been made for the first time for a cylindrical vessel moving according to a 4D phase space mixer motion (3D for space motion and 1D for time, non steady state mixing) such as the Turbula mixer. Due to inherent DEM computational limitations the modelling could not be carried out on real industrial sized particles such as the ZSM5 zeolite. Therefore, the particles used in the DEM simulation were large ideal spherical model particles and the modified Hertz Mindlin contact model was employed. Based on the DEM simulations and PEPT qualitatively experimental validation, it can be generally stated that DEM simulations approach is capable of modelling the major features of complex systems such as the Turbula mixer using the ideal spherical particles material. Given that this is novel work considering such complex motion and its aims include increasing confidence in the use of DEM for this type of work, the outcomes and conclusions from the work are interesting and provide some clues for further work, both by experimental and computational methods. Computational results provided qualitative evidence regarding the unpredictable bed behaviour, which was also observed by PEPT experiments. However, although the simulations were useful to observe the non-linearity for the rate of mixing as a function of the operating speeds and different speculative hypothesis were made, there was not a transparent and rational explanation. This presents the additional challenge for the DEM results analysis to be able to extract and present the data with the aim of giving a mechanistic explanation for the mixing mechanisms within the vessel. To gain a better understanding on

the flow within the vessel and to improve the understanding of mixing mechanisms, more simulations are probably necessary, for example, by analysing the effect of different fill levels and systems with different particle sizes. Moreover, a more meticulous comparison between the DEM simulations and the PEPT experiments should be made. For example, the actual PEPT experiment could be modelled using DEM. This would involve only looking at the movement of one particle, as was done in PEPT, rather than all the particles as was done in the simulations presented in this thesis. However, in order to do this simulation, the DEM modelling would need to be conducted over time periods that correspond with the PEPT experiments, which are far greater than those used in the presented DEM simulations. A more detailed analysis of data regarding particle velocities from PEPT and DEM may also be beneficial. This data analysis may allow ascertainment of greater information regarding mixing mechanisms in the axial and radial directions for the considered mixer.

Many problems still remain and many challenges need to be addressed to transform DEM from a largely academic tool into a full industrial predictive tool for real commercial systems, considering for example small complex particles such as the Zeolite. Future work may involve the following subjects/topics:

- Development of methodologies for definition of DEM input parameters, from bulk as well as individual particle measurements, for both model material particles and real particles.
- Ability of modelling real industrial particles size and shapes representations.
- Develop models to include other interparticle forces such as capillary forces, electrostatic forces, Van der Waals forces; especially for the modelling of small particles.
- Detailed validation of simulations results closely matching experimental to obtain quantitative results rather than qualitatively.
- Moving from qualitatively simulations to quantitative predictive simulations.

## Appendix

### List publications

#### Journals

*M. Marigo, D. L. Cairns, M. Davies, M. Cook, A. Ingram, E. H. Stitt*

Developing Mechanistic Understanding of Granular Behaviour in Complex Moving Geometry using the Discrete Element Method. Part A: Measurement and Reconstruction of TurbulaMixer Motion using Positron Emission Particle Tracking, CMES: Computer Modeling in Engineering & Sciences, Vol. 59, No. 3 (2010), pp. 217-238.

*M. Marigo, D. L. Cairns, M. Davies, A. Ingram, E. H. Stitt*

Developing Mechanistic Understanding of Granular Behaviour in Complex Moving Geometry using the Discrete Element Method. Part B: Investigation of Flow and Mixing in the Turbula® mixer, Powder Technology 212 (2011), pp. 17-24.

*M. Marigo, D. L. Cairns, M. Davies, A. Ingram, E. H. Stitt*

A numerical comparison of mixing efficiencies of solids in a cylindrical vessel subject to a range of motions, Powder Technology, Powder Technology 217 (2012), pp. 540-547.

**Conferences:**

***M. Marigo, D. L. Cairns, M. Davies, A. Ingram, E. H. Stitt***

Comparison of the mixing efficiencies in a cylindrical vessel under different motions: rotating drum, hoop mixer and Turbula mixer, Particulate Processes in the Pharmaceutical Industry III, Brisbane (2011), *presentation*.

***M. Marigo, A. Ingram, C. Y. Wu, E. H. Stitt, D. L. Cairns***

DEM modelling of cohesionless particles flow in a Turbula mixer, 10th UK Particle, Technology Forum, Birmingham University, Birmingham, *poster*.

***M. Marigo, D. L. Cairns, M. Davies, A. Ingram, X. Fan, Z. Yang, E. H. Stitt***

DEM Modelling of Particle Flow in a Turbula T2F Mixer, 8th World Congress of Chemical Engineering, Montreal (2009), *presentation*.

***M. Marigo M., D. L. Cairns, M. Davies, A. Ingram, C. Y. Wu, X. Fan, Z. Yang, E. H. Stitt***

EDEM modelling of particle flow in a tubular mixer, 2nd UK-China Particle Technology Forum, Guiyang China (2009), *presentation*.

***M. Marigo, D. L. Cairns, A. Ingram, C. Y. Wu, E. H. Stitt***

Challenges in Applying DEM to Commercially Relevant Particles and Processes, 9th UK Particle, Technology Forum, Herriot Watt University, Edinburgh, *poster*.

## Developing Mechanistic Understanding of Granular Behaviour in Complex Moving Geometry using the Discrete Element Method. Part A: Measurement and Reconstruction of Turbula<sup>®</sup> Mixer Motion using Positron Emission Particle Tracking

M. Marigo<sup>1,2</sup>, D. L. Cairns<sup>1</sup>, M. Davies<sup>1</sup>, M. Cook<sup>3</sup>  
A. Ingram<sup>2,4,5</sup> and E. H. Stitt<sup>1</sup>

**Abstract:** In this work the complex motion of the Turbula<sup>®</sup> mixer has been measured by Multiple-Positron Emission Particle Tracking (Multiple PEPT) in order to set-up a DEM numerical model. Positron emitting radioactive tracers were attached to three of the pivot bearings on the shaft of the mixer to enable the rotation and translation of the mixer chamber to be tracked in the PEPT camera. The measured movement was mathematically reconstructed and imported into DEM in order to apply the same movement to the modelled vessel.

The three-dimensional motion of particles in a vessel located in the Turbula mixer was then calculated using Discrete Element Modelling (DEM). The DEM code used in this work is a commercially available package provided by DEM-Solutions (EDEM).

Good qualitative agreements have been found between the DEM simulations and experimental data from the literature for the degree of segregation in bi-disperse particle mixtures at long mixing times.

**Keywords:** Turbula mixer, particle mixing, PEPT, granular blending, DEM.

---

<sup>1</sup> Johnson Matthey Technology Centre, P.O. Box 1, Belasis Avenue, Billingham, Cleveland, TS23 1LB, United Kingdom

<sup>2</sup> Centre for Formulation Engineering, Chemical Engineering, School of Engineering, The University of Birmingham, B15 2TT, United Kingdom

<sup>3</sup> DEM Solutions, Edinburgh, EH2 3NH, United Kingdom

<sup>4</sup> Positron Imaging Centre, School of Physics and Astronomy, The University of Birmingham, B15 2TT, United Kingdom

<sup>5</sup> Corresponding author. Tel.: (+44) (0) 121 414 4548; fax: (+44) (0) 121 414 5324; E-mail: a.ingram@bham.ac.uk.



# Developing mechanistic understanding of granular behaviour in complex moving geometry using the Discrete Element Method

## Part B: Investigation of flow and mixing in the Turbula® mixer

M. Marigo<sup>a,b</sup>, D.L. Cairns<sup>a</sup>, M. Davies<sup>a</sup>, A. Ingram<sup>b,c,\*</sup>, E.H. Stitt<sup>a</sup>

<sup>a</sup> Johnson Matthey Technology Centre, P.O. Box 1, Belasis Avenue, Billingham, Cleveland, TS23 1LB, United Kingdom

<sup>b</sup> Centre for Formulation Engineering, Chemical Engineering, School of Engineering, The University of Birmingham, B15 2TT, United Kingdom

<sup>c</sup> Positron Imaging Centre, School of Physics and Astronomy, The University of Birmingham, B15 2TT, United Kingdom

### ARTICLE INFO

*Article history:*

Received 31 August 2010  
Received in revised form 23 February 2011  
Accepted 14 April 2011  
Available online 20 April 2011

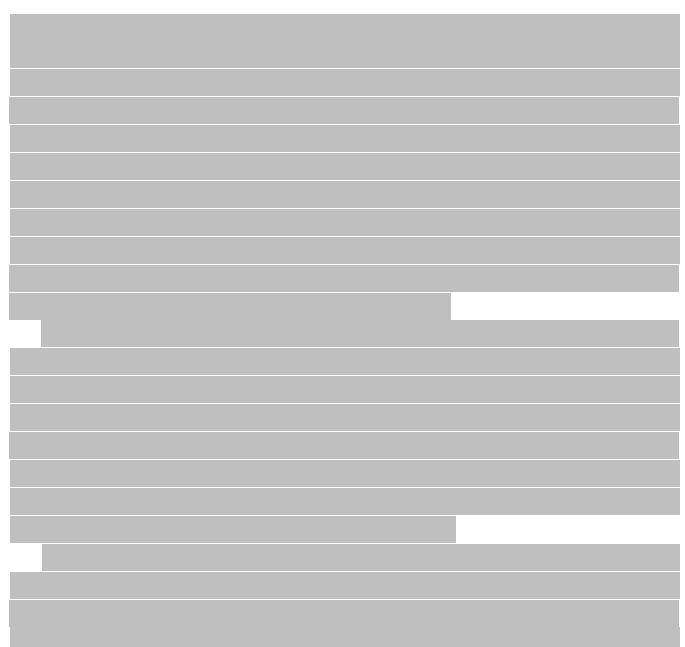
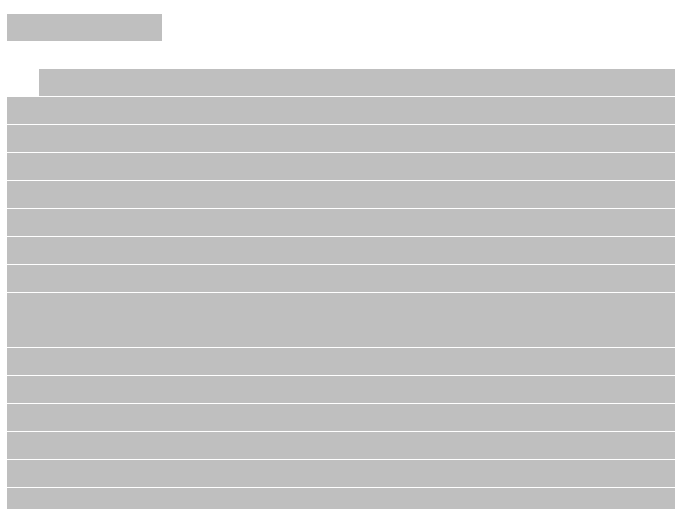
*Keywords:*

Turbula mixer  
Particle mixing  
Granular blending  
DEM

### ABSTRACT

As a consequence of increasing computer power and more readily useable commercial codes, the Discrete Element Method is being used in an increasing range of applications to simulate increasingly complex processes, often for evaluation of machinery prototypes. This presents the additional challenge of analysis of results, in particular to extract flow and mixing mechanisms with a view to improving design or operation. The Turbula mixer is a laboratory scale mixer, which is widely used in industry for the development or testing of new granular products. It comprises a simple vessel geometry (cylinder) that moves with a complex, yet regular, 3D motion giving rise to rapid and thorough mixing of the contents. The mixer presents an ideal system for evaluation of the power of DEM to simulate complex processes and to develop protocols for processing the results of the simulation. Initial results of this investigation, presented in this paper, show that mixing behaviour changes non-monotonically as a function of mixer speed. For the system of monodisperse glass spheres it is shown that mixing rate (in terms of number of mixer revolutions to achieve complete mixing) initially decreases with increasing speed and subsequently increases. The behaviour is suggestive of a transition in the flow process and is the subject of further investigation.

© 2011 Elsevier B.V. All rights reserved.



\* Corresponding author at: Centre for Formulation Engineering, Chemical Engineering, School of Engineering, The University of Birmingham, B15 2TT, United Kingdom. Tel.: +44 121 414 4548; fax: +44 121 414 5324.

E-mail address: [a.ingram@bham.ac.uk](mailto:a.ingram@bham.ac.uk) (A. Ingram).



## A numerical comparison of mixing efficiencies of solids in a cylindrical vessel subject to a range of motions

M. Marigo<sup>a,b,\*</sup>, D.L. Cairns<sup>a</sup>, M. Davies<sup>a</sup>, A. Ingram<sup>b,c</sup>, E.H. Stitt<sup>a</sup>

<sup>a</sup> Johnson Matthey Technology Centre, P.O. Box 1, Belasis Avenue, Billingham, Cleveland, TS23 1LB, United Kingdom

<sup>b</sup> Centre for Formulation Engineering, Chemical Engineering, School of Engineering, The University of Birmingham, B15 2TT, United Kingdom

<sup>c</sup> Positron Imaging Centre, School of Physics and Astronomy, The University of Birmingham, B15 2TT, United Kingdom

### ARTICLE INFO

#### Article history:

Received 27 February 2011

Received in revised form 7 November 2011

Accepted 12 November 2011

Available online 26 November 2011

#### Keywords:

Rotating drum

Hoop mixer

Turbula mixer

Particle mixing

DEM

### ABSTRACT

The mixing of solids is a fundamentally important unit operation in the pharmaceutical, food and agricultural industries, as well as many others. The efficiency and quality of mixing can have a significant bearing on downstream processability and product quality. In spite of the fact that the equipment, usually batch blenders without impellers such as tumbling bins and V-Blenders or with impellers such as ploughshare mixers, is well established, there remains considerable uncertainty in the optimisation of mixing. Simple laboratory/pilot scale mixers based on the rotating drum, such as the hoop mixer and the Turbula, are commonly used and yet also little understood in terms of performance. These mixers add additional rotational and/or translational movements to the cylindrical rotation of the drum to deliver significant improvements in mixing, particularly in the longitudinal axis.

Discrete Element Modelling (DEM), in which a flowing or deforming granular system is modelled by considering the movement of each individual particle and its interaction (momentum and energy exchange) with neighbours and boundaries, has recently become accessible to relatively non-expert users. The reasons for this include: increasing confidence in its capability; user-friendly graphical interfaces of commercial software packages; and the fact that top end personal computers now have sufficient memory and computational speed to enable many problems to be solved in weeks rather than months.

The purpose of the work reported here is to evaluate the power of DEM to help understand flow processes and explain mixing mechanisms in mixing equipment based on the rotating drum. The commercial package EDEM (from DEM Solutions) was used. For speed and simplicity the modelled system comprised monosized smooth glass beads. Three mixers were selected: horizontal rotating drum, the hoop mixer and the Turbula. The rate and extent of mixing, quantified using a “segregation index” based on contacts between two discretely labelled but otherwise identical fractions, was shown to depend on equipment motion, operating speed and the initial distribution of the fractions. The well known characteristics of the horizontal drum operating in rolling mode were demonstrated: excellent transverse mixing and poor axial mixing; both improving with speed as the depth of the active layer is shown to increase. The hoop mixer incorporates off-axis rotation, causing periodic tilting of the cylinder axis. This results in a considerable improvement in axial mixing. Interestingly, at low speeds the hoop mixer and simple rotating drum exhibit similar transverse mixing but increasing speed has the opposite effect: improving transverse mixing in the drum while worsening it in the hoop. Axial mixing in the hoop mixer, on the other hand improves with speed. The Turbula displays a very interesting relationship with speed. At low speeds, its transverse mixing performance is the same as the horizontal drum and hoop mixer but decreases significantly with increasing speed, going through a minimum at medium speed before recovering completely at high speed. Axial mixing is comparable, showing the same trend. It appears that the motion in the Turbula goes through some sort of transition that has a profound effect on mixing performance. The implication is that unless this is understood, it will be difficult *a priori* to identify optimum operating conditions.

The power of DEM lies in the fact that the complete trajectory of each particle is recorded: it is possible to follow the movement, deformation and breakup of clusters of particles. From this it should be possible to elucidate the dominant flow mechanisms and to identify those that have the most impact on mixing. This presents a challenge to develop methodologies for cluster analysis and visualisation and is the subject of on-going work. Other work is focussed on experimental validation of the DEM predictions.

© 2011 Elsevier B.V. All rights reserved.

\* Corresponding author at: Johnson Matthey Technology Centre, P.O. Box 1, Belasis Avenue, Billingham, Cleveland, TS23 1LB, United Kingdom. Tel.: +44 1642 522 2245.  
E-mail address: [Michele.Marigo@matthey.com](mailto:Michele.Marigo@matthey.com) (M. Marigo).